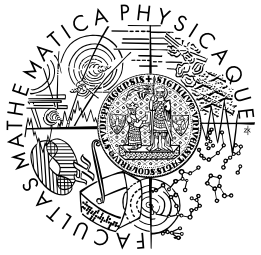

FACULTY
OF MATHEMATICS
AND PHYSICS
Charles University

DOCTORAL THESIS

Mgr. Štěpán Vyhlídka

Dispersion management of a 10 PW laser system

Department of Chemical Physics and Optics

Supervisor of the doctoral thesis: Ing. Bedřich Rus, PhD.
Study programme: Physics
Study branch: Quantum Optics and Optoelectronics

Prague 2019

I declare that I carried out this doctoral thesis independently, and only with the cited sources, literature and other professional sources.

I understand that my work relates to the rights and obligations under the Act No. 121/2000 Sb., the Copyright Act, as amended, in particular the fact that the Charles University has the right to conclude a license agreement on the use of this work as a school work pursuant to Section 60 subsection 1 of the Copyright Act.

In ..... date ..... signature of the author

I am extremely grateful to Daniel Kramer for providing me guidance and for introducing me into the foundations and methods of the optical simulation, my supervisor Bedřich Rus for allowing me to work on this thesis and for allowing me to pursue the aspects of this work which I found most interesting and Erhard Gaul for his insight and that he willingly shared his rich experience with high power laser systems. Their good-natured friendly attitude fosters pleasant and creative working environment which allowed me to enjoy every aspect of this work.

I had a great pleasure to work everyday with Pavel Trojek, Jan Hubáček and Jan Bartoníček, who helped me with practical tasks of this thesis and who made every work-day enjoyable and fun. I also very appreciate all the support and constructive advice during writing publications from Pavel. Many thanks goes to all my other colleagues, who helped me, such as Galina Kalinchenko, František Batysta, Roman Antipenkov, Davorin Peceli, Martin Šolc, Gilles Cheriaux, Gavin Friedman, Matt Keppler, Jeff Jarboe, David Snopek, Jack Naylon, Alexander Meadows and others.

I would like to thank my band Keysmoon, Ondřej and David for letting me escape from this reality and allowing me to clear my mind from physics.

Finally, my biggest thanks goes to my parents, my brother, my wife and my small daughter for being such wonderful people, supporting me and uplifting me every day.

I would also like to acknowledge the following grants:

- CZ.1.05/1.1.00/02.0061
  ELI: EXTREME LIGHT INFRASTRUCTURE
- CZ.1.07/2.3.00/20.0091
  Výzkum a vývoj femtosekundových laserových systémů a pokročilých optických technologií
- CZ.02.1.01/0.0/0.0/15_008/0000162
  ELI: EXTREME LIGHT INFRASTRUCTURE - fáze 2

Title: Dispersion management of a 10 PW laser system

Author: Mgr. Štěpán Vyhlídka

Department: Department of Chemical Physics and Optics

Supervisor: Ing. Bedřich Rus, PhD., Institute of Physics of the Czech Academy of Sciences)

Abstract: This thesis deals with the design of a stretcher and compressor systems used for the chirped pulse amplification method for the L4 beamline. The L4 beamline is being developed for the ELI Beamlines project and aims to deliver pulses with peak power of 10 petawatt, central wavelength of 1060 nanometers, pulse duration of 150 femtoseconds and energy of 1500 Joules. Since the laser induced damage threshold and aperture of commercial diffraction gratings is currently a limiting factor in reaching higher peak powers, it was necessary to increase the effective aperture of the compressor using either tiled grating or object-image-grating self tiling methods. These two methods are compared for two compressor configurations using either 1740 ln/mm or 1136 ln/mm diffraction gratings, methods for their alignment are discussed and the selected alignment method is experimentally tested. Moreover, an analytical theory connecting the Seidel aberrations of the stretcher imaging system with the spectral phase deviation of the stretched pulse is presented. This theory is applied to commonly used Banks and Offner stretcher designs and it is demonstrated how it can be employed for the suppression of the residual spectral phase of compressed pulses. Next, the design of the stretcher for the L4 beamline based on this theory is presented and its implementation together with a sub-aperture compressor is discussed.

Keywords: ultrashort pulses, dispersion, chirped pulse amplification, compressor, stretcher

Contents

Introduction

It has been nearly one hundred years since Albert Einstein introduced the idea of stimulated emission which gradually culminated into the theoretical concept of a laser. About forty years later the first laser emission was successfully demonstrated and a whole new branch of optics dealing with properties of intense coherent light was unveiled. The advancement of lasers was quickly followed by the theoretical foundation and practical implementation of the mode locking technique enabling generation of ultra-short laser pulses. A femtosecond is equal to a fraction 10^{-15} of a second and it represents a timescale on which dynamics of chemical reactions or molecular movement can be studied. It is also the limit of the shortest pulse duration generated with visible light, since the period of oscillation of visible light is 1-3 fs. Such properties of femtosecond pulses are very valuable as they enable to study processes at timescales which are unreachable by any other methods. Applications of femtosecond lasers gave birth to the new fields of physics such as ultrafast spectroscopy or femtochemistry. The ultrafast lasers also yield another advantage because their output energy can be squeezed into a very short time interval. Their high peak power combined with excellent focusability of laser beams has proved to be irreplaceable for the study of so-called extreme physics [1], which aims at the understanding of behavior of matter under extreme pressure, temperature and electric fields such as is the environment in cores of stars. The extreme physics mostly connects the areas of plasma, particle, relativistic and quantum physics and is crucial for the better understanding of the fundamental physical laws [2]. Moreover, experimental results have already pointed out at the applicability of the lasers for the generation of secondary sources of radiation such as x-ray or proton beams [3]. The high-intensity ultrafast lasers could be employed as tabletop particle accelerators reducing the size and cost of such devices and making them widely available for biomedical applications such as tumor treatment, coherent high resolution single-shot 3D scanning, etc. [4].

The Extreme Light Infrastructure (ELI) project was established to boost up the progress in this field. It comprises three pillars located in the Czech Republic, Hungary and Romania, each of them specializing in a different field. The Eli-Beamlines pillar based in the Czech Republic specializes in the generation of secondary sources of radiation and it will host both high-repetition rate petawatt-class laser L3 and laser system L4 with unprecedented peak power 10 PW [A7]. The L4 system aims to deliver 150 fs pulse with 1500 kJ energy with central wavelength 1060 nm. The pulses are amplified using the chirped pulse amplification technique [5], where the pulses are broadened prior to their amplification in a stretcher and they are compressed in a compressor before the experimental chamber. Such a technique is necessary to avoid possible optical damage and nonlinear effects which start to occur at GW/cm^2 intensity scale. Therefore, the pulse duration has to be increased roughly 20 000 times to reach 3 ns prior to their amplification to limit peak intensity. The individual spectral components of the pulse have to be de-phased with respect to each other. This can be achieved when a pulse propagates through a dispersive component, such as a pair of diffraction gratings [6]. To reach maximal intensity at focus it is critical that the compressed pulse has shortest pulse duration possible. To achieve that the induced spectral phase change by the stretcher and compressor has to be matched appropriately and well controlled. However, with increasing peak power of lasers the requirements on the design and alignment of these subsystems become more stringent [7].

Even with recent advances in multilayer dielectric coatings, the laser induced damage threshold of diffraction gratings is the main limiting factors in reaching higher peak

powers [8]. The threshold is given by the fluence, which inversely scales with pulse duration [9] and which is currently on the order of hundreds mJ/cm^2 beam normal for femtosecond pulses. The only means how to increase the pulse peak power without damaging the gratings is then to increase the beam size to tens of centimeters depending on the specific grating design. However, as the maximal commercially available grating size is currently limited to approximately 1 m in diameter, a tiled grating scheme was proposed to increase the effective aperture of the compressor [10]. There is also an alternative object-image-grating self-tiling method (called grating-mirror method in the following text for brevity), in which the grating is aligned with a perpendicularly positioned plane mirror effectively doubling its aperture [11, 12]. The tiled grating scheme has been successfully implemented in 500 fs 1 PW [13] and 100 fs 25 TW laser systems [14] but the grating-mirror scheme has been only tested in low power small aperture laser systems so far [15, 16]. Compared to the mentioned systems, the L4 system possesses short pulse duration combined with large beam aperture, which puts strict requirements on the alignment of tiled gratings in submicroradian range and also on the surface and holographic quality of the gratings. Here, 1740 ln/mm and 1136 ln/mm compressor designs were compared both utilizing either tiled grating or grating mirror scheme. Also, since the grating-mirror configuration has not yet been experimentally tested for the state-of-the-art laser systems, a thorough analysis was necessary to check its applicability for the L4 system.

Another challenge in the development of the L4 system was posed by the design of the stretcher. Since the low line density compressor design was favoured, the grating distance in the compressor had to be set to 15 m to reach sufficient pulse broadening. A large stretch ratio then leads to a big footprint and residual spectral phase induced by the aberrations of the imaging system of conventional stretcher designs. A multi-pass stretcher with a modified Offner triplet was proposed to overcome these limitations and a theory calculating the change in the induced spectral phase by the aberrations was deduced to bring more insight into the stretcher design.

Goals

The topic of this thesis is dispersion management of the L4 laser system which mostly encompasses the design and the analysis of the stretcher and compressor. The first goal was to analyze and compare two compressor designs using analytical and numerical methods. Since both designs require the utilization of either tiled grating or grating-mirror method, both of these methods had to be examined as well. The second goal was to choose an appropriate method for the alignment of the tiled grating/grating-mirror assemblies and to test it. The third goal was to make an optical design of a stretcher matching the selected compressor design and to find a passive method for the suppression of the stretcher's residual spectral phase. The next step was to propose an alignment procedure and to implement the stretcher into the L4 laser system. The fourth goal was to install a diagnostic sub-aperture compressor to verify the compressibility of the amplified stretched pulses.

Outline

The first chapter provides the theoretical foundation necessary for the numerical and analytical analysis of the stretcher and compressor discussed in the following sections. Theoretical treatment of ultrashort pulses, dispersion and spatio-temporal couplings is presented and the methods for numerical simulation of ultrashort pulse propagation are discussed.

The second chapter provides an overview of the CPA technique. Sections 2.1-2.3

summarize the theory of grating compressors, stretchers and methods for the alignment of tiled grating and grating-mirror pairs. Section 2.4 presents the first outcome of this thesis, which is a method for the analytical calculation of spectral phase deviation induced by the Seidel aberrations present in the stretcher imaging system. The theory is demonstrated on the commonly employed Banks and Offner stretcher designs in subsections 2.4.1-2.4.2 and its applicability is further discussed in subsection 2.4.3. Section 2.5 then examines general dispersion management and points out several possibilities on how to compensate residual spectral phase in the CPA systems.

The third chapter introduces the ELI Beamlines project and especially the L4 laser system in more detail.

The fourth chapter presents an analytical and numerical analysis of the compressor designs. Section 4.1 and 4.2 deals with 1740 ln/mm and 1136 ln/mm compressor designs in either tiled gratings or grating-mirror configuration respectively. The outcomes of a tolerance analysis, optimization of spectral throughput, simulation of intensity modulations induced through the diffraction on tiled grating gaps are presented. The sections also entail a novel analysis of line density variation within tiled grating compressors. The analysis points out that the line density variation can significantly decrease focused peak intensity for tiled grating compressors. Pre-pulses and post-pulses originating from specular reflections off the grating-mirror assemblies are examined as well.

In the fifth chapter established methods for the alignment of tiled grating and grating-mirror configurations are compared, experimental results are presented and an alignment system is proposed for the L4 compressor.

The sixth chapter describes the evolution of the L4 stretcher design. In section 5.1 an optimization method reducing residual spectral phase and footprint of the stretcher is discussed for both Offner and Banks designs. Section 5.2 encompasses the implementation of the final stretcher design into the L4 beamline, mostly discussing the alignment procedure and the output characteristics.

In the seventh chapter, an implementation of the sub-aperture compressor is presented. The sub-aperture compressor is a miniaturized version of the main compressor for small beam aperture yielding the same dispersion properties and was used to compress the stretched pulse amplified by the OPCPA section.

Finally, the work and its impact on the current state in this field are summarized in the conclusion.

1. Ultrashort pulses

1.1 Ultrashort pulses

Ultrashort pulses can be described as electromagnetic wave-packets with duration in femtosecond to picosecond scale. The pulses are usually generated using mode-locking technique [17]. Their ultrashort duration is achieved via interference of their individual spectral components and is therefore inversely proportional to their spectral width. The complete theoretical description can be found in Ultrashort Pulse Phenomena [18].

To begin with, it is convenient to decouple their temporal and spatial characteristics and treat them separately. However, as it will be shown later, such separation is not entirely accurate when spatio-temporal couplings are present. Here, we review basic formulae relevant for the following chapters and numerical simulations. Ultrashort pulses are usually treated in the complex representation to allow exponential notation as they are fully characterized by the electric field. The complex spectrum $E(\omega)$ of a pulse is connected with its real electric field $E_R(t)$ through the Fourier transform:

$$E(\omega) = \int_{-\infty}^{\infty} E_R(t) e^{-i\omega t} \mathrm{d}\omega = |E(\omega)|\, e^{i\varphi(\omega)}, \tag{1.1}$$

where $|E(\omega)|$ is the spectral amplitude and $\varphi(\omega)$ is the spectral phase of the pulse. The complex electric field $E(t)$ is defined as the Fourier transform of the positive part of the spectrum only:

$$E(t) = \frac{1}{2\pi} \int_{0}^{\infty} E(\omega) e^{i\omega t} \mathrm{d}\omega = |E(t)|\, e^{i\varphi(t)} e^{i\omega_0 t}, \tag{1.2}$$

where $|E(t)|$ denotes temporal amplitude, $\varphi(t)$ is temporal phase and ω_0 is the central frequency of the pulse. The real electric field of a pulse is obtained from the real part of its complex amplitude $E_R(t) = \mathrm{Re}\{E(t)\}$. The temporal intensity $I(t)$ can be derived by substituting the electric field into the Poynting vector:

$$I(t) = 1/2\epsilon_0 cn |E(t)|^2 \tag{1.3}$$

and it is connected with the energy of the pulse $\mathcal{E}$ and its spectral intensity $S(\omega)$ through Parseval's theorem:

$$\mathcal{E} = \int I(t) \mathrm{d}t = \int S(\omega) \mathrm{d}\omega, \tag{1.4}$$

with

$$S(\omega) = \frac{\epsilon_0 cn}{\pi} |E(\omega)|^2 . \tag{1.5}$$

The temporal profile of a pulse is usually estimated from its measured spectrum. A Gaussian pulse shape is most commonly used due to its mathematical simplicity and because it resembles the output spectrum of mode-locked lasers. Temporal and spectral amplitudes of a Gaussian pulse are described with a Gaussian function:

$$|E(t)| = \frac{I_0}{\sqrt{2\epsilon_0 cn}} \exp\left(-\frac{t^2}{2\tau_e^2}\right) \qquad |E(\omega)| = \frac{I_0 \tau_e}{\sqrt{\pi\epsilon_0 cn}} \exp\left(-2\tau_e^2 t^2\right) \tag{1.6}$$

where I_0 is the peak intensity of the pulse and τ_e^2 is the pulse duration half width. Experimentally, it is more convenient to define the pulse duration corresponding to the full width at half maximum $\tau_{FWHM} = 2\sqrt{\ln(2)}\tau_e$. Since high-power laser systems

usually operate with limited spectral bandwidth, it is desirable to generate the spectral profile that maximizes the peak power within the given bandwidth. A super-Gaussian spectral profile of the order N can be analytically described as:

$$|E(\omega)| = \frac{\mathcal{E}}{c_n}\exp\left(-\left(\frac{|\omega-\omega_0|^N}{2\ (\Delta\omega_N)^N}\right)\right) \tag{1.7}$$

where c_n is a normalization constant and ω_N is the spectral half-width. Because of the Fourier transform relationship between the complex electric field and the complex spectrum, there exists a connection between the pulse duration τ_{FWHM} and its spectral width $\Delta\omega_{FWHM}$

$$\tau_{FWHM}\Delta\omega_{FWHM} \geq 2\pi c_p, \tag{1.8}$$

where c_p is a constant depending on the shape of the pulse profile. The equality holds when the pulse is transform-limited. Such pulses do not exhibit any kind of chirp and have constant carrier frequency.

1.2 Dispersion

Dispersion is the phenomenon that the phase velocity of a wave depends on frequency. Generally, when an ultrashort pulse propagates through a medium, its phase velocity ω/k differs from its the group velocity $\delta\omega/\delta k$ due to the presence of absorptive resonances of the medium. Dispersion properties of the medium are described by the frequency dependence of its refraction index $n(\omega, z)$. The propagation of the optical pulse through the medium has a form of the linear wave equation:

$$\left[\frac{\delta^2}{\delta z^2} + \frac{\omega^2}{c^2}n(\omega,z)^2\right]E(\omega,z) = 0, \tag{1.9}$$

with a solution:

$$E(\omega,z) = E(\omega,0)\exp(-ik(\omega)z) = E(\omega,0)\exp(-i\varphi(\omega)). \tag{1.10}$$

The spectral phase $\varphi(\omega)$ represents both the delay of pulse due to its propagation through the medium as well as possible distortion of the pulse temporal envelope. The solution can be further generalized by using a linear transfer function $H(\omega)$:

$$E(\omega,z) = H(\omega)E(\omega,0); \qquad H(\omega) = (1-R(\omega)-A(\omega))\exp(-i\varphi(\omega)), \tag{1.11}$$

where $A(\omega)$ is absorption and $R(\omega)$ is total reflection loss. To add some physical insight into how the induced spectral phase influences the temporal profile of the pulse, it is convenient to expand it into a Taylor series around the central frequency of the pulse ω_0:

$$\begin{aligned}\varphi(\omega) &= \varphi_0 + \frac{\mathrm{d}\varphi}{\mathrm{d}\omega}|_{\omega_0}(\omega-\omega_0) + \frac{\mathrm{d}^2\varphi}{\mathrm{d}\omega^2}|_{\omega_0}\frac{(\omega-\omega_0)^2}{2} + \frac{\mathrm{d}^3\varphi}{\mathrm{d}\omega^3}|_{\omega_0}\frac{(\omega-\omega_0)^3}{3!} + \frac{\mathrm{d}^4\varphi}{\mathrm{d}\omega^4}|_{\omega_0}\frac{(\omega-\omega_0)^4}{4!} + ... \\ &= \varphi_0 + \mathrm{GD}(\omega-\omega_0) + \frac{\mathrm{GDD}}{2}(\omega-\omega_0)^2 + \frac{\mathrm{TOD}}{3!}(\omega-\omega_0)^3 + \frac{\mathrm{FOD}}{4!}(\omega-\omega_0)^4 + ... \ .\end{aligned} \tag{1.12}$$

The first term φ_0 represents carrier envelope offset. Its control is important mostly for metrology and few-cycle optical pulses. This thesis deals with optical pulses with $\sim$ 130 fs duration and its impact can be therefore neglected. The second term $\frac{\mathrm{d}\varphi}{\mathrm{d}\omega}$ is equal to the product of the inverse of the group velocity and the length of the

medium z. Therefore, it describes the group delay (GD) of the pulse with respect to its initial state. The group delay dispersion (GDD) homogeneously broadens the pulse envelope. It represents linear change of the group delay with respect to the individual spectral wave-packets which make up the pulse. The third order dispersion (TOD) induces quadratic group delay dependence and therefore it distorts either the front side or the back side of the pulse envelope depending on the sign of the TOD. It also creates characteristic ripples in time intensity. The fourth order dispersion (FOD) is cubic in the group delay and therefore induces additional pulse broadening and degrades temporal contrast as well. ∼130 fs pulses are not usually influenced by higher dispersion orders than FOD and thus they will be neglected here. The impact of the individual dispersion orders on the temporal profile of a Gaussian pulse is shown in Figure 1.1. The duration of a Gaussian pulse increases with the residual group delay dispersion as:

$$\tau_{FWHM} = \tau_{0FWHM}\sqrt{1 + \frac{(4\ln(2)\ \mathrm{GDD})^2}{\tau_{0FWHM}^4}} \tag{1.13}$$

Generally, pulses with super-Gaussian profiles have lower dependence of their pulse duration on the GDD as the super-Gaussian function decays more quickly at the edges compared to the Gaussian function. In reality, measured spectra deviate from the perfect analytical curves. To evaluate the impact of residual spectral phase on the pulse envelope, it is always necessary to calculate the Fourier transform of the measured spectrum according to Eq. (1.2). However, for the simulations aiming at minimization of pulse duration, it is convenient to use the Gaussian profile as the worst case scenario.

It is also important to note that the Taylor expansion from Eq. (1.12) is valid only for systems with smooth and slowly varying phase profile such as the systems using diffraction grating compressors and stretchers. In the case of multilayer dielectric struc-

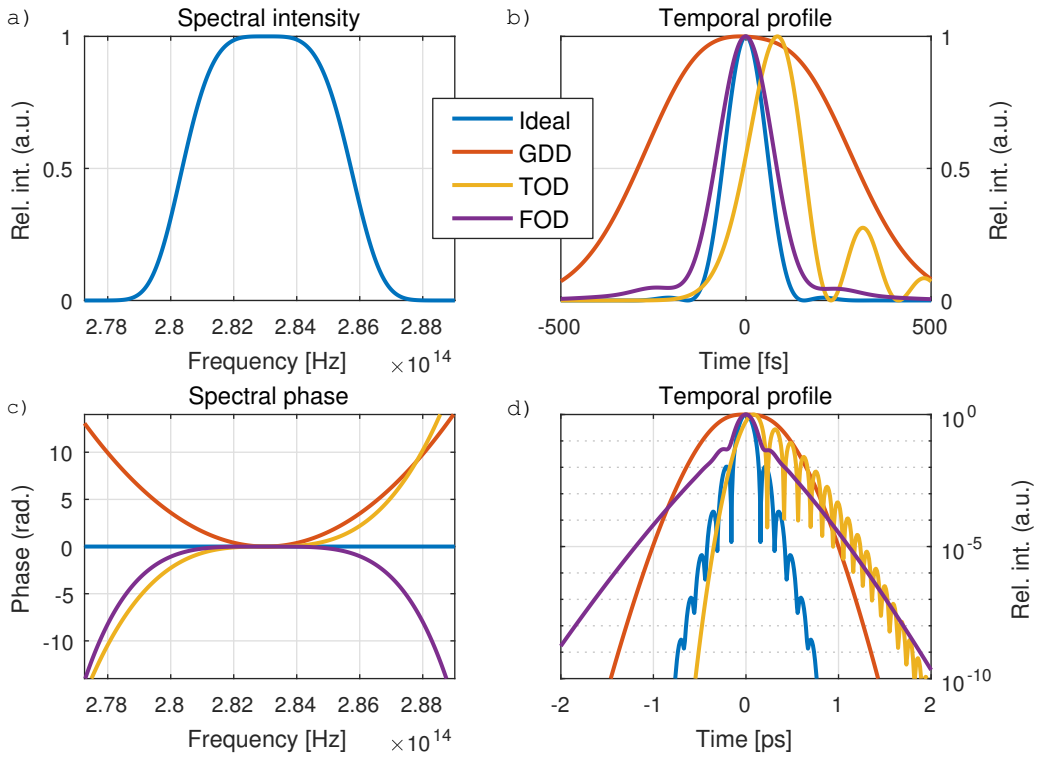

Figure 1.1: Impact of residual dispersion on the temporal profile of a Gaussian pulse with 130 fs FWHM duration having GDD=20 000 fs^2, TOD=200 000 fs^3 or FOD = -2 000 000 fs^4)

tures exhibiting sinusoidal phase modulations and narrow peaks, the Taylor expansion approximation is not accurate and it might be necessary to abandon this approach.

1.3 Temporal intensity contrast

Temporal intensity contrast is defined as a ratio of the intensity at a given time to the peak pulse intensity. The modern state-of-the-art laser systems reach focused intensity as high as $\sim 10^{23}$ W/cm^2. Time intensity contrast plays a crucial role in the majority of experiments as the ionization and formation of pre-plasma at the target can occur at intensities $\sim 10^{12}$ W/cm^2. Therefore if the intensity rises above this level before the arrival of the main peak, the induced pre-plasma can change the experimental conditions and ruin the experiment. Therefore, the time intensity contrast of 10^{-11} in ps-scale is necessary for the highest peak power laser systems. A typical contrast trace is sketched in Figure 1.2. Temporal contrast degradation can occur due to many different reasons. First, the contrast is closely connected with the shape of the spectral intensity and phase of the pulse. Because the temporal and spectral domain are connected through the Fourier transform, any high-frequency content present in the spectral domain should be avoided. Any abrupt variations of the spectral intensity create pedestal around the main peak. Such variations are usually induced through the spectral clipping in the stretchers and compressors when the aperture of diffraction gratings is not sufficient for a given spectral bandwidth [19]. The same argument can be applied for abrupt variations of the spectral phase where discontinuities are very rare. However, more often the spectral phase exhibits rapid sinusoidal variations which can originate from dielectric coatings or high frequency noise. The high frequency noise can be induced by the surface quality of mirrors placed in the focal plane of grating stretchers [20] and it has been shown that it leads to contrast degradation [21]. For a single frequency component, it leads to the creation of pre-pulse and post-pulse with delay equal to the period of the modulation. Noisy spectral phase profile $\Delta\varphi(\omega) \ll 1$ generates a pedestal around the main peak of the pulse. The intensity of the pedestal can be estimated as:

$$I(t) = I_0(t) + \epsilon|\Delta\varphi(t)|^2, \tag{1.14}$$

where $I_0(t)$ is the temporal profile of a pulse without phase modulation, ϵ is the energy of the pulse and $\Delta\varphi(t)$ is the temporal Fourier transform of $\Delta\varphi(\omega)$. Second, a

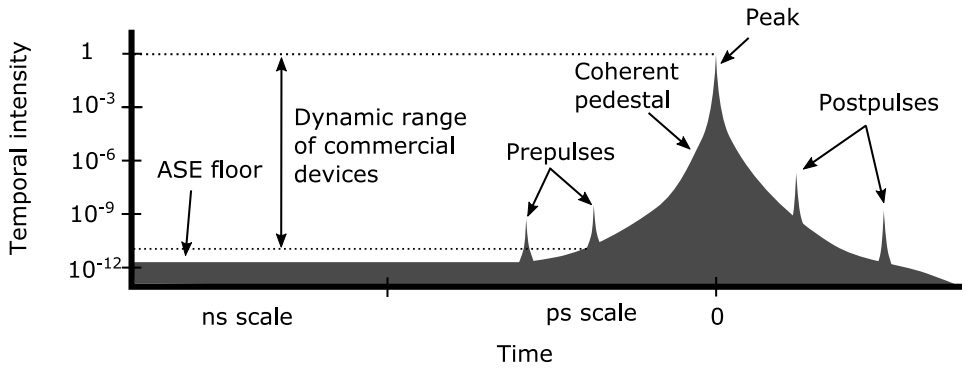

Figure 1.2: Example of a typical temporal contrast trace. The area around the main peak in the ps scale is called a coherent pedestal and is mainly induced through the effects discussed in this section. The temporal contrast in the ns scale is usually mostly degraded by amplified spontaneous emission.

pulse passing through transmissive optics such as beam-splitters, polarizers or vacuum windows undergoes multiple reflections which are delayed with respect to the main peak. These post-pulses can be then converted to pre-pulses in the nonlinear regime [22]. Third, scattering on the optics in the multi-pass designs of stretchers, amplifiers or compressors can degrade the temporal contrast as well [23]. This can happen when a pulse is double scattered so that the scattered light gets at the output of the system before the main peak.

1.4 Gaussian beams

Gaussian beams are the solution of the Helmholtz equation in paraxial approximation and are the most commonly encountered spatial beam profiles. Only a fundamental TEM_{00} mode is discussed here as it offers the best spatial properties compared to the other modes. Its spatial profile is given by:

$$E(x,y,z) = E_0 \frac{w_0}{w(z)} \exp\left(\frac{-(x^2+y^2)}{w(z)^2}\right) \exp\left(-i\left(kz + k\frac{(x^2+y^2)}{2R(z)} + \arctan(z/z_R)\right)\right), \quad (1.15)$$

where w_0 is the waist size, $w(z)$ is the beam size at a given distance from the waist, z_R is the Rayleigh length and R(z) is the wavefront curvature. These parameters are defined as:

$$z_R = \frac{\pi w_0^2}{\lambda_0}, \quad w(z) = \sqrt{1 + \left(\frac{z}{z_R}\right)^2}, \quad R(z) = z\left(1 + \left(\frac{z_R}{z}\right)^2\right). \quad (1.16)$$

For high-energy laser systems, super-Gaussian profiles are preferred because they effectively fill the aperture of optics and thus they maximize the energy at a fixed beam size. Such profiles can be generated using serrated apertures combined with far-field filtering or custom collimators. Their spatial profile in the 2D is given by (similarly to Eq.1.7):

$$|E(x,y)| = \frac{\mathcal{E}}{c_n} \exp\left(-\left(\frac{|x|^N + |y|^N}{w_0^N}\right)\right), \quad (1.17)$$

where $\mathcal{E}$ is the total energy and c_n is the normalization constant. While Gaussian beams have approximately two times higher intensity at focus for the same FWHM width (Fig 1.3 a,b), the super-Gaussian beams have superior focused peak intensity when the beam size is limited by the aperture of optics (Fig 1.3 c,d). Due to high spatial frequencies, which are present in super-Gaussian beam profiles, it is necessary to relay image the position of a waist through the system to avoid amplitude modulations (Fig. 1.4). Usually, the beam is imaged to the center of an amplification medium at each amplification stage and on the optics such as deformable mirrors and diffraction gratings, which could be damaged through the amplitude modulations.

During its propagation through an optical system, a laser beam passes through and reflects off many optical components. This can induce additional wavefront deviation with respect to the phase of the ideal beam. The deviation is usually described by the set of orthogonal Zernike polynomials $Z_n^m(\rho,\phi)$ [24]:

$$Z_n^m(\rho,\phi) = R_n^m(\rho)\cos(m\psi) \qquad Z_n^{-m}(\rho,\phi) = R_n^m(\rho)\sin(m\psi) \quad (1.18)$$

with the radial polynomials $R_n^m(\rho)$ defined as:

$$R_n^m(\rho) = \sum_{k=0}^{\frac{n-m}{2}} \frac{(-1)^k (n-k)!}{k!(\frac{n+m}{2}-k)!(\frac{n-m}{2}-k)!} \rho^{(n-2)k} \quad (1.19)$$

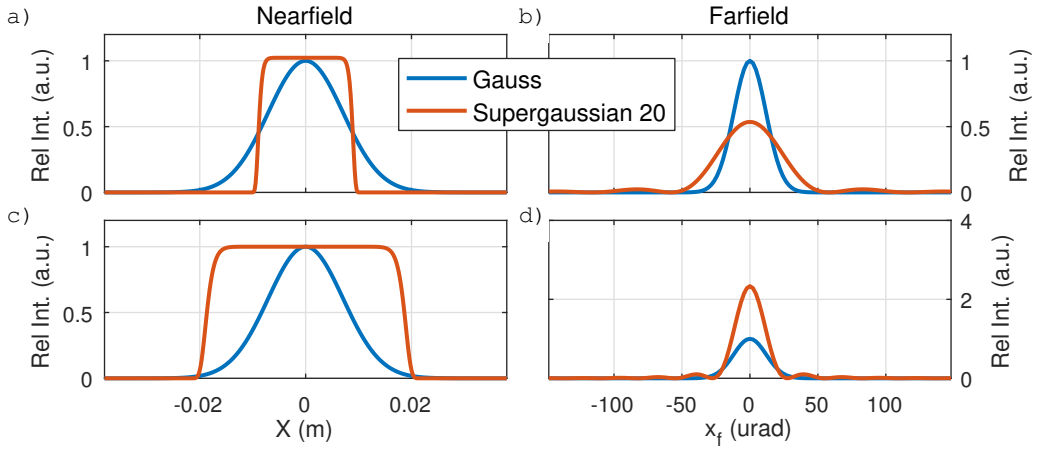

Figure 1.3: Comparison of a Gaussian and super-Gaussian profile in nearfield and farfield. a,b) Comparison of the profiles having same FWHM and peak intensity in nearfield. c,d) Comparison of the profiles having the same peak intensity and filling a given aperture in nearfield.

Focusability of a laser beam can be described by the Strehl ratio which is defined as the ratio between the peak intensity of a real distorted beam to the peak intensity of the ideal beam:

$$S_x = \exp(-(2\pi\sigma)^2) \approx 1 - (2\pi\sigma)^2, \tag{1.20}$$

where S_x is the spatial Strehl ratio and σ is the RMS of the wavefront deviation. According to the Marechal criterion, the optical system is regarded as well corrected for $S_x > 0.8$, which is equivalent to RMS wavefront deviation $\leq \lambda/14$.

1.5 Spatio-temporal couplings

In reality, it is not possible to separate the spatial and temporal/frequency characteristics $E(\omega, x, y, z) \neq E(\omega)E(x, y, z)$ of ultrashort pulses. Such separation is often desired for simplification and to illustrate some basic approaches. However, generation and manipulation of high-power ultrashort pulses requires to temporarily induce some spatio-temporal couplings, such as in the pulse stretchers and compressors, for

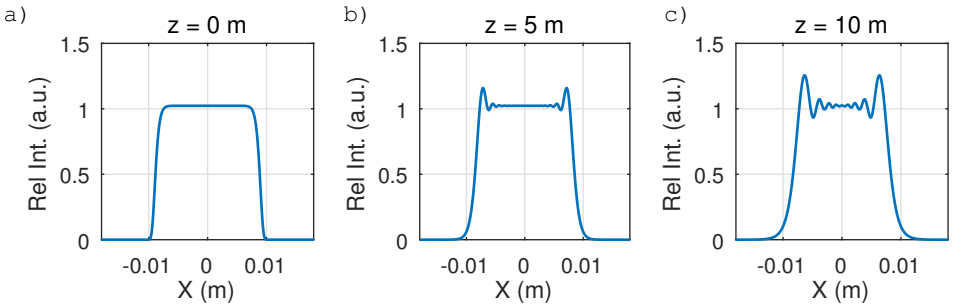

Figure 1.4: Evolution of super-Gaussian beam profile propagated in space. The amplitude modulation makes it necessary to relay image the beam profile. a) Spatial profile at the waist, b) spatial profile after 5m of propagation, c) spatial profile after 10m of propagation.

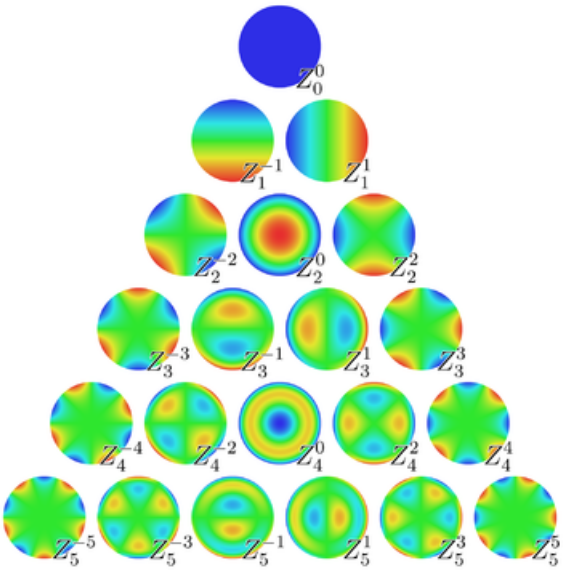

Figure 1.5: Spatial representation of Zernike polynomials

which is such approximation inadequate. These spatio-temporal couplings then may not be entirely compensated at the end of chain or in some cases they can be used to advantage like in broadband OPCPA. Principally, we can distinguish amplitude and phase couplings. General spatio-temporal couplings in the first order approximation are summarized in Table (1.1) [25]:

Table 1.1: Classification of spatio-temporal couplings

Domain	**Amplitude**	**Phase**
x - t	pulse front tilt	wave-front rotation
x - ω	spatial chirp	wavefront tilt dispersion
k - t	time versus angle	angular temporal chirp
k - ω	angular dispersion	angular spectral chirp

The couplings are not mutually independent. When pulse characteristics are determined in one domain, the characteristics in the other domains can be calculated using appropriate Fourier transforms. For the complete characterization of the pulse, it is sufficient to measure the amplitude and phase profile in only one domain. For example, to completely characterize pulse in the x-t domain, it is necessary to measure its spatial profile, wavefront, temporal profile, temporal phase, pulse front tilt angle and wavefront rotation. However, due to the fact that duration of ultrashort pulses is shorter than the response time of electronics devices, it is usually more convenient to measure the couplings in the spectral domain and to recalculate their impact to the $x - t$ domain. The characterization of the output pulse in both x-ω (near-field) and k-ω (far-field) domains is also very useful for the alignment of dispersive devices such as grating stretcher and compressors.

Angular dispersion

Angular dispersion is a well-known phenomenon discovered by Isaac Newton in his famous prism experiment in the 17th century. When angular dispersion is present, spectral components of light propagate in different directions. Mathematically, this

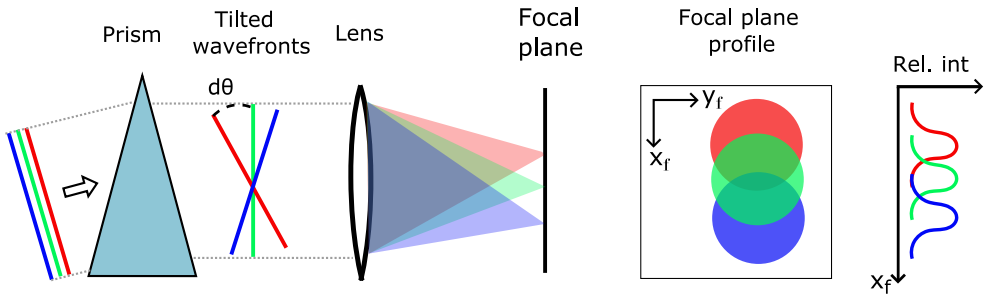

Figure 1.6: Illustration of angular dispersion

can be expressed through the frequency dependency of k-vectors:

$$E(k_x, k_y, k_z, t) = E(k_x(\omega), k_y, k_z, t) \tag{1.21}$$

There is also a second definition, defining the angular dispersion as the angle between individual phase fronts. These two definitions coincide for plane waves, but they can yield different results for Gaussian beams [26]. Here, we stick with the first definition as we will deal mostly with collimated beams. Residual angular dispersion is closely connected with distortions of a pulse front [27]. Usually, the linear term of the angular dispersion $k_x(\omega) = k_{0x} + \frac{\mathrm{d}k_x}{\mathrm{d}\omega}(\omega - \omega_0)$ is dominant. In the $x - \omega$ domain, the linear angular dispersion can be described by a linear phase term scaling with both x and ω:

$$E(x, y, z, t) = E_0(x, y, z, t)\ \exp\left(i\frac{2\pi}{\lambda}\frac{\mathrm{d}\theta}{\mathrm{d}\omega}|_{\omega_0}(\omega - \omega_0)\vec{x}\right), \tag{1.22}$$

where $\frac{\mathrm{d}\theta}{\mathrm{d}\omega}|_{\omega_0}$ is the linear angular dispersion at ω_0. Free space propagation of a pulse with residual linear angular dispersion leads to a residual GDD offset [28]:

$$\mathrm{GDD} \approx -L\frac{\omega_0}{c}\left(\frac{\mathrm{d}\theta}{\mathrm{d}\omega}|_{\omega_0}\right)^2 \tag{1.23}$$

The linear term usually originates from wedged optics or misaligned gratings in stretchers or compressors. However, in some cases quadratic or cubic terms can be present. They are induced by the Seidel aberrations of imaging systems of grating stretchers [A1] or they can be induced by misaligned compressors having line density variation of the gratings. Residual angular dispersion reduces the peak power of the focused pulse by two mechanisms as it is shown in Figure 1.6. It increases the focal spot size and it locally broadens the pulse by limiting the spectral bandwidth at each focal point [29].

Spatial chirp

Spatial chirp is a spatio-temporal coupling for which the position of a beam centroid varies with frequency:

$$E(x_0 + \frac{\mathrm{d}x}{\mathrm{d}\omega}|_{\omega_0}(\omega - \omega_0), y, z, t) \tag{1.24}$$

The spatial chirp $\frac{\mathrm{d}x}{\mathrm{d}\omega}|_{\omega_0}$ is generally induced by a pulse propagating distance L with angular dispersion:

$$\frac{\mathrm{d}x}{\mathrm{d}\omega}|_{\omega_0} = L\frac{\mathrm{d}\theta}{\mathrm{d}\omega}|_{\omega_0}. \tag{1.25}$$

Spatial chirp prolongs pulse duration in the near-field by reducing the spectral bandwidth of the pulse at each point. It has minimal effect on pulse duration in focus as all spectral components overlap there. Spatial chirp is mostly connected with the spectral

spread of the beam on the second grating or prism in the pulse stretchers and compressors. However for ultrashort pulses with broad bandwidths, it can be easily introduced when a pulse propagates through a tilted window as it is illustrated in Figure 1.7.

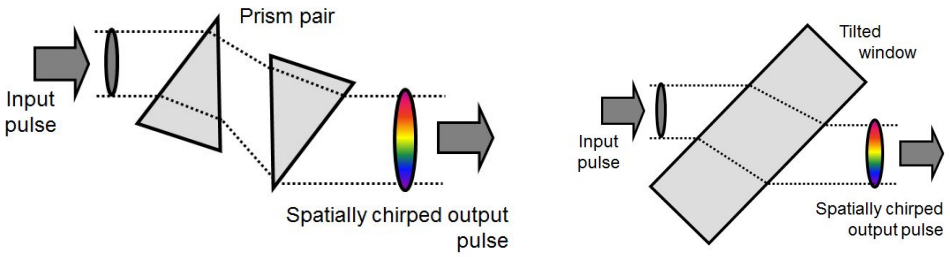

Figure 1.7: Illustration of spatial chirp after propagation through a pair of dispersive components and a tilted window [30].

Pulse front distortion

Ideally, a pulse front should coincide with the wavefront of all spectral components. When some distortion is present, the individual wavefronts no longer overlap and the position of the intensity maxima is shifted in time to a position, where all spectral components constructively interfere. Mathematically, the pulse front distortion can be expressed as the spatial dependence of the arrival time of the pulse maxima t_0 (equivalent to the group delay in spectral domain):

$$E(x, y, z, t) = E(x, y, z, t - t_0(x, y)) \tag{1.26}$$

The origin of the majority of pulse front distortions is closely connected with angular dispersion. When a pulse passes through a dispersive component like a prism in Fig. 1.8a, the top and the bottom part of the beam undergo different optical paths. Since they are identical, the bottom part of the beam has to delayed with respect to the top part. However, this also means that the beam exhibits angular dispersion $k - \omega$ domain [27]. This is true for every dispersive component - prism, gratings or etalons. It can be also proved using basic Fourier transform theorems in linear approximation, since the field having angular dispersion can be transformed as follows:

$$E(k_x - a\omega, k_y, \omega) \rightarrow E(x, y, \omega)\exp(-iax\omega) \rightarrow E(x, y, t - ax) \tag{1.27}$$

Pulse front distortion can be also induced by the combination of spatial and temporal chirp. The spatial chirp yields spectral spread in the x-y plane, while the temporal chirp shifts the maxima of the individual spectral wave-packets along the time and z-axis. Combination of chirps tilts the pulse front as in Fig. 1.8b.

Pulse front tilt

A pulse front tilt represents linear dependence of the arrival time of a pulse on its spatial coordinate. It is equivalent to constant linear angular dispersion across the beam profile in the absence of either spatial or temporal chirp. The dependence of tilt angle ψ on the angular dispersion can be easily expressed as [31]:

$$\text{tg } \psi = \omega_0 \frac{\mathrm{d}\theta}{\mathrm{d}\omega}|_{\omega_0} \tag{1.28}$$

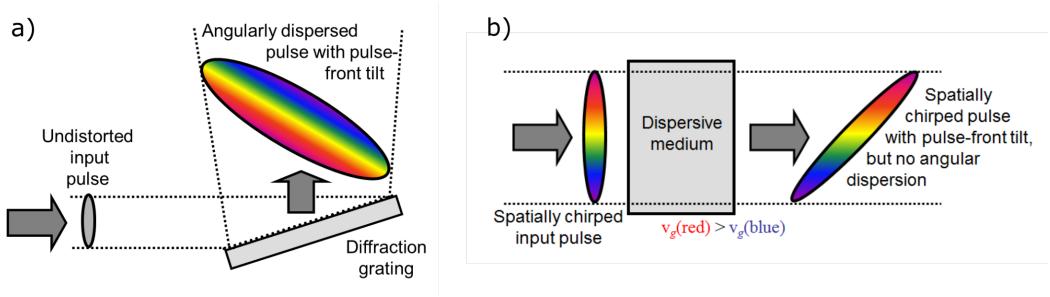

Figure 1.8: Pulse front tilt originating from angular dispersion (a) and the combination of spatial and temporal chirp (b) [30].

The delay between the top and bottom part of a beam can be then calculated as:

$$\tau_{PFT} = \omega_0 \frac{2w_x}{c} \frac{\mathrm{d}\theta}{\mathrm{d}\omega}|_{\omega_0} \tag{1.29}$$

The combination of temporal and spatial chirp can also yield a pulse front tilt 1.8. In focus, the pulse-front tilt vanishes. However, its impact on the focused pulse peak intensity is transferred through the angular dispersion (Figure 1.6)

1.6 Ultrashort pulse propagation

Generation and manipulation of ultrashort pulses requires a laser beam to propagate them through linear and nonlinear media. Since an analytical solution can be often found only for the simplest systems, numerical modeling is usually necessary. For linear systems, it is usually more convenient to propagate ultrashort pulses in the spectral domain. Their temporal profile can be decoupled into individual spectral components using Eq. (1.1) and the spatial profile of each component can be then propagated through the system separately. Nonlinear parts of the system have to simulated in time domain since the response of the medium can no longer be described by the linear transfer function (Eq. 1.11) [18]. This thesis focuses on the linear systems only.

Generally, ultrashort pulses can be propagated by solving the linear Helmholtz equation (Eq. (1.9)). Numerically, it is more feasible to use either the Fresnel-Kirchoff integral, which is an approximate solution of the Helmholtz equation using spherical waves, or to use the angular spectrum propagation method based on plane wave decomposition. For Gaussian laser beams, it is in most cases sufficient to consider their propagation under paraxial approximation. That leads to the exactly same formulae using both methods [32]. The angular spectrum propagation method will be discussed here, since it is more robust, easier to implement numerically and has less boundary conditions.

Angular spectrum propagation method

In the angular spectrum propagation method, the spatial profile of a complex electric field $E(\omega, x, y, 0)$ at the given z position $z = 0$ is 2D Fourier transformed into the k-domain:

$$E(\omega, k_x, k_y, 0) = \frac{1}{2\pi} \iint E(\omega, x, y, 0) \exp(-i(k_x x + k_y y)) \mathrm{d}k_x \mathrm{d}k_y, \tag{1.30}$$

where $E(\omega, k_x, k_y, 0)$ represents a plane wave propagating along the wave vector $\vec{k} = (k_x, k_y, k_z)$ with

$$k_z = \sqrt{\left(\frac{2\pi}{\lambda}\right)^2 - k_x^2 - k_y^2}. \tag{1.31}$$

The input field can be therefore described as a projection of many plane-waves propagating along the k-vector $\vec{k}$ with amplitude $|E(\omega, k_x, k_y, 0)|$. After free space propagation along the z-axis over a distance z, the electric field acquires an additional phase factor $\exp(-ik_z z)$. The output field can be then calculated as the inverse Fourier transform of the input field times the acquired phase factor:

$$E(\omega, x, y, z) = \iint E(\omega, k_x, k_y, 0)\exp(-i(k_x x + k_y y + k_z z))\mathrm{d}k_x\mathrm{d}k_y, \tag{1.32}$$

Under the paraxial approximation, the k_z component can be simplified by performing the Taylor expansion of the square root from Eq. (1.31):

$$k_z = \frac{2\pi}{\lambda} - \frac{k_x^2 + k_y^2}{2(\frac{2\pi}{\lambda})^2} \tag{1.33}$$

The Eq. (1.32) can be then rewritten to:

$$E(\omega, x, y, z) = \exp(-ikz) \iint E(\omega, x, y, 0)\exp(-i\frac{k_x^2 + k_z^2}{2k}z))\exp(-i(k_x x + k_y y))\mathrm{d}k_x\mathrm{d}k_y, \tag{1.34}$$

which is equivalent to Fresnel propagation. Eq. (**??** can be also reformulated so that the output field can be regarded as a convolution of the input field with a point spread function represented by the acquired phase factor:

$$E(\omega, x, y, z) = E(\omega, x, y, 0) * \mathrm{PSF}; \quad \mathrm{PSF} = \exp(-i\frac{k_x^2 + k_y^2}{2k}z)) \tag{1.35}$$

Focusing

In general, there are several ways of calculating the propagation of the electric field from the exit pupil of the optical system into the focal region [33]. The Fraunhofer integral is usually calculated as it based on the Fourier transform and can be easily numerically implemented. Since it is derived under the scalar approximation, it is more suitable for calculation of the focusing with large f-numbers, where the amplitude of the neglected longitudinal E_z component is very small. The distribution of the electric field in the focal plane $E(\omega, x_f, y_f)$ can be calculated as:

$$E(\omega, x_f, y_f) \approx \omega \iint E(\omega, x, y)\exp(i(x x_f + y y_f))\mathrm{d}x\mathrm{d}y \tag{1.36}$$

After applying the Fourier transform spatially for each frequency component, the temporal profile at each point can be obtained doing the inverse Fourier transform from frequency into the time domain at each x_f, y_f focal point (Eq. (1.2)). If the electric field distribution close to the focal plane is in the area of interest, the field distribution can be obtained by introducing small defocus spatial phase term before applying Eq. (1.36) [33]. In case that calculation of focal spot distribution with small f-number is required, commercial software such as Wyrowski VirtualLab Fusion [34] can be used.

Ray-tracing

For complex linear systems such as laser pulse compressors and stretchers, proper diffraction propagation even under the paraxial approximation is too CPU intensive due sampling requirements in both spatial and time domains. Therefore, it is advantageous to obtain the transfer function of the system by some other simpler method such as ray-tracing. Since ray-tracing neglects any diffraction/interference induced effects, it can be performed under the assumption that there is no pronounced clipping of the beam and that the propagation distance is within the Rayleigth range of the beam. On the other hand, ray-tracing allows much faster optimization since its calculation is based on matrix multiplication.

Propagation of a pulse through an optical system induces both amplitude $|E(x, y, \omega)|$ and phase changes $\varphi(x, y, \omega)$ according to Eq. (1.11). The amplitude $|E(x, y, \omega)|$ can be modified locally taking into account the vignetting of individual rays and transmittance and reflectance curves of each optical component within the optical system. It is also possible to estimate energy loss due to scattering on the optics. The induced spectral phase change $\varphi(x, y, \omega)$ is then calculated from the optical path of the individual rays. Recently, a new term "Phase-tracing" was coined to describe this method. Its process is shown in Fig. 1.9.

First, a spatio-temporal x-y-ω grid is created and an input electric field is established. Each grid point represents object plane coordinates and frequency of a ray. Rays corresponding to a grid point with non-zero electric field amplitude are then propagated from the object to the image plane using the laws of geometrical optics. The position and phase of the output rays is then interpolated to match the output x-y-ω grid. From the vignetting and optical path of the rays, the transfer function of the system $H(\omega)$ is recovered. The input electric field is then multiplied by the transfer function and can be then transformed to farfield and time domain using Eqs. (1.36) and (1.2).

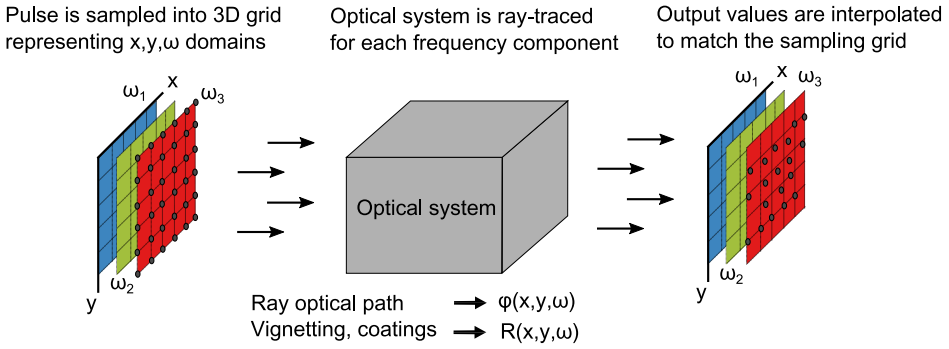

Figure 1.9: General schematic of phase-tracing

Ray-tracing can be performed using either an extended ABCD matrix formalism or dedicated software. In the case of this thesis, ZEMAX Optic Studio was used in connection with Matlab using ZOSAPI link. The seamless integration of ZEMAX into Matlab allowed simple manipulation of large arrays of data and their further processing. Even though ray-tracing is now commonly integrated into commercial software, a great care must be taken to avoid systematic errors such as inexact definition of the optical system, sub-sampling and others.

For fast optimization of dispersive systems, a macro calculating GD and higher dispersive orders can be programmed [35]. According to Eq. (1.12), the group delay is

calculated as a frequency derivative of the acquired phase through the system:

$$\mathrm{GD}(x,y) = \frac{\mathrm{d}\varphi(x,y,\omega)}{\mathrm{d}\omega} = \frac{1}{c}\left(nL + L\frac{\mathrm{d}n}{\mathrm{d}\omega} + n\frac{\mathrm{d}L}{\mathrm{d}\omega}\right) \tag{1.37}$$

Undoubtedly, Eq. (1.37) holds only when rays with different wavelengths originating from the same point in the object plane meet each other at one point in the image plane [36] or are collinear at the output. Therefore, Eq. 1.37 is valid only for aberration-free imaging systems or afocal systems like pulse compressors with no residual angular dispersion. Since rays represent infinite plane waves, the optical path of each ray can be corrected so that their wavefronts intersect at the image point for aberrated systems (shown in Fig. 1.10) [36]. A correction factor ΔL is then:

$$\Delta L = \sin\theta_x^\lambda x^\lambda + \sin\theta_y^\lambda y^\lambda, \tag{1.38}$$

where θ_x^λ and θ_y^λ is the angular deviation of a ray with respect to the z-axis. x^λ and y^λ is the lateral distance between the point where the ray intersects the image plane the image point. When the entire entrance pupil is scanned with rays such as in Fig. 1.9, the correction factor has to be omitted.

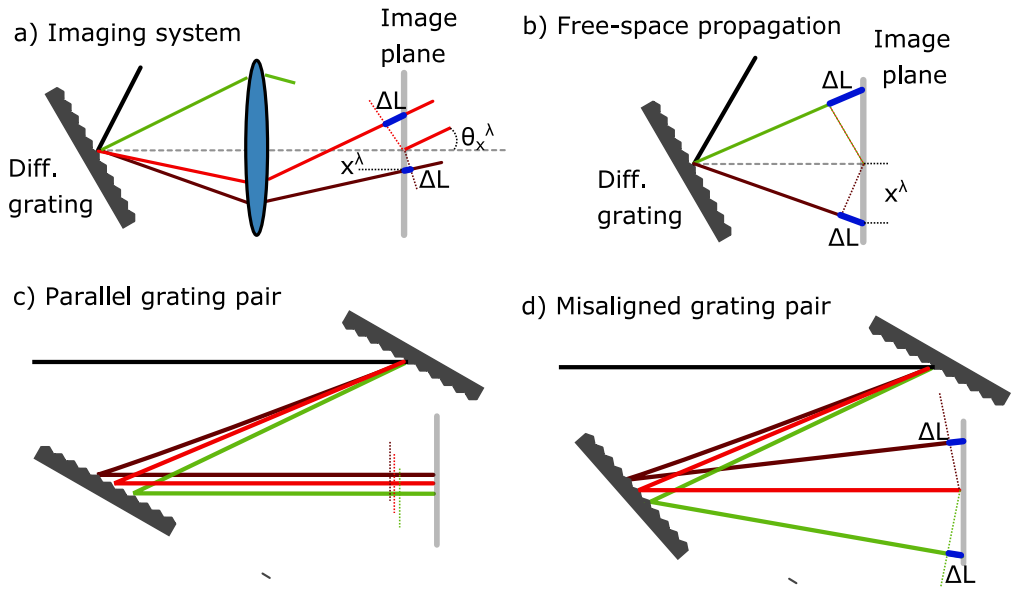

Figure 1.10: Optical path length correction factor for aberrated optical systems

Sampling considerations

Frequency content of a sampled signal is constrained by the Nyquist-Shannon sampling theorem stating that the highest measurable frequency is given by the half of sampling frequency (i.e., the inverse of a sampling step). This can be directly applied to the sampling of amplitude and phase profiles of ultrashort pulses. The highest sampling frequency determines the resolution in the time domain. The sampling step in the frequency domain then determines the width of the temporal window. Dependency of sampling resolution and window in conjugate domains are shown in Table 1.2. It has to be noted that the Nyquist-Shannon sampling theorem was formulated for the continuous signals. From Table 1.2 it might seem that even with a limited beam size, the increase of $x_{\max}$ can increase resolution. Such a technique is called zero-padding. In reality, it only decreases the sampling step of the transformed signal while the real

Table 1.2: Resolution and boundaries of the fast Fourier transform algorithm

Spatial	**Spatial freq.**	**Frequency**	**Temporal**
$\mathrm{d}x$	$\max(\lvert k_x \rvert)$	$\mathrm{d}\omega$	$t_{\max}$
$x_{\max}$	dk_x	$\omega_{\max}$	$\mathrm{d}t$

resolution remains limited by the actual beam size. The zero-padding technique is equivalent to sync interpolation of the signal.

Nyquist-Shannon sampling theorem also entails aliasing of an analytic signal. Ultrashort pulses often acquire large amounts of quadratic phase either when spatially focused or chirped in stretcher or compressor. If the neighbouring points in x-y-ω domains have bigger than π phase difference, the profile of the unwrapped phase is ambiguous and its alias can be recovered (Fig. 1.11). This can be very tricky to notice and has to be carefully monitored, since the phase in the first image of Fig 1.11 seems to be well sampled. Moreover, there are no apparent high-frequency modulations present so the sampling step might seem adequate according to Nyquist-Shannon criterion.

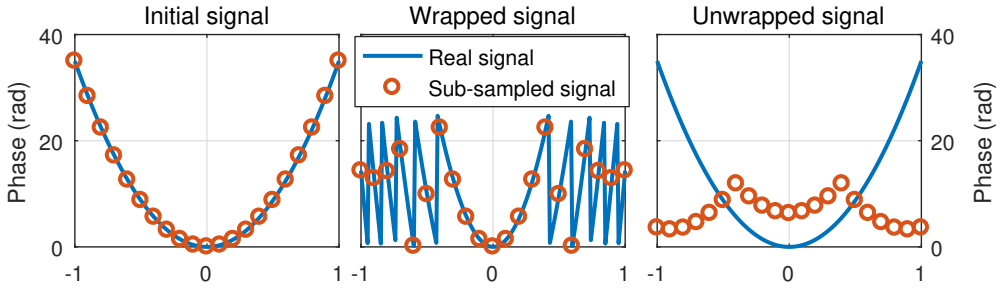

Figure 1.11: Example of the aliasing error due to sub-sampling. An analyzed signal is sub-sampled so that significant amount of information is lost when the signal is wrapped to 2π interval. When the signal is unwrapped back, the alias of the initial signal is recovered.

The other type of errors originate from the discrete nature of the FFT algorithm such as a picket fence effect and spectral leakage. The picket fence effect can distort the position and maximal amplitude of a peak as it is illustrated in Fig. 1.12. Spectral

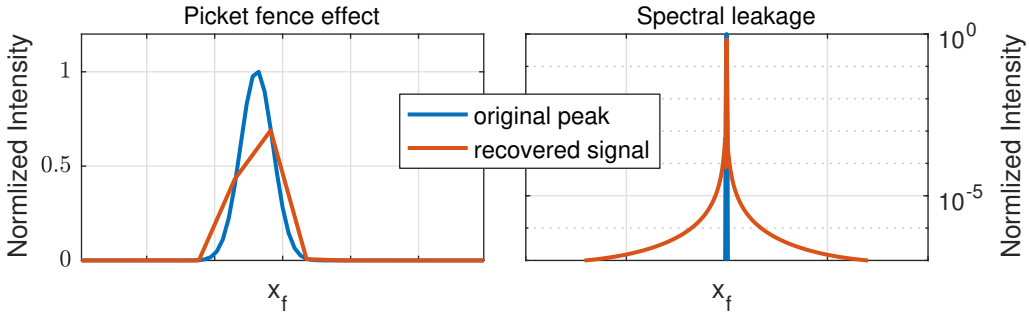

Figure 1.12: Demonstration of a picket fence effect (a) and spectral leakage (b) in farfield domain. The original and recovered signal are represented by identical functions in nearfield with the same sampling interval $\mathrm{d}x$. The recovered signal has 3 times smaller x_{max} than the original signal which results in a smaller step in the x_f domain (a) and bigger information loss at the edges of its x range leading to more pronounced clipping of the signal (b).

leakage can increase the noise floor of the simulated temporal contrast. Mathematically, the spectral leakage is the convolution of the Fourier image of the input function with the Fourier image of the windowing function. The windowing function is usually a rectangular window with width equal to the sampling range.

The number of sampling points is limited by computational power. If smaller sampling step is needed to increase resolution, the width of the window in which the calculation is performed has to be decreased. This makes difficult to numerically evaluate spatio-temporal properties of ultrashort pulses in compressors and stretchers using diffraction propagation methods. A quadratic temporal chirp demands small sampling step in the time domain to avoid aliasing effect. On the other hand, it broadens the pulse and therefore it requires a wide temporal window. The same holds for the spatial domain due to angular dispersion and spatial chirp. At the output of a well-aligned compressor or stretcher, the angular chirp is usually small. If the compressor is examined in the combination with the stretcher, the output temporal chirp is also very small. Diffraction propagation methods require to have the beam well sampled at each stage compared to the phase tracing method, where the sampling as to be sufficient only at the object and image plane. Sampling requirement is then much smaller for the phase tracing method as the numerical analysis is usually done to study small deviations from the ideal system. For this reason, it much more efficient to phase trace the stretcher and compressor systems when spatio-temporal information is required.

2. Chirped pulse amplification

Since the invention of Q-switching and mode locking techniques, laser community tirelessly worked on increasing energy and peak power of lasers every year, motivated by the possibility of laser induced nuclear fusion enabling the production of free fusion energy (Figure 2.1). The peak power of systems using a master oscillator power amplifier configuration rapidly grew. It culminated in the eighties when the peak power reached a gigawatt-scale. At this power, nonlinear effects start to occur even for non-focused beams. Notably, self-focusing leads to optical damage of amplifiers accompanied by self-phase modulation causing distortion of the pulse profile preventing further progress of direct amplification scheme. This lead to the adaptation of a chirped pulse amplification (CPA) technique [5], which was initially discovered in order to increase the power of radar. With this technique, pulses are temporally stretched in a device with positive dispersion prior to their amplification to reduce their peak power. Then, pulses are compressed to their initial duration in a device with opposite dispersion, which is usually a compressor comprising a pair of diffraction gratings (Fig. 2.2). The CPA technique allowed to increase the peak power of laser pulses up to several petawatts during the last two decades and its potential has not been yet depleted [37, 38].

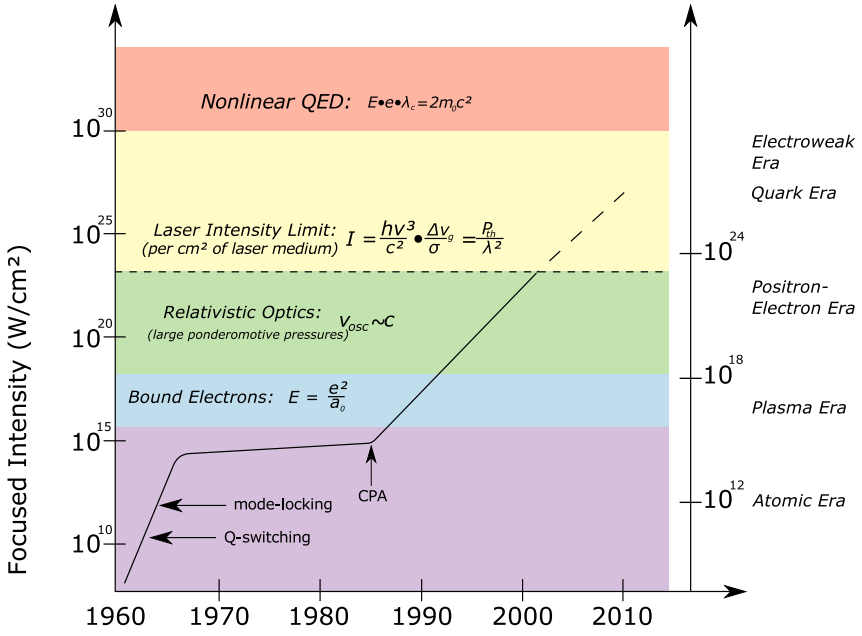

Figure 2.1: Schematic of the evolution of laser peak power

Soon, it was recognized that the concept of the CPA is also very useful for an optical parametric amplification process (OPCPA), where nanosecond pulse duration of a seed allows to apply much higher pump energies and therefore to reach much higher overall gain (Fig. [2.2]). Compared to the CPA, the OPCPA offers better quality of the amplified pulse at the price of a more complicated setup. In general, it allows to achieve large single pass gain and to get very broad gain bandwidth under certain phase-matching conditions. Small absorption of a pump limits the heating of a crystal and therefore reduces thermal lensing effects. It eliminates the need to cool the crystal and enhances the quantum efficiency of the process. Also, as the amplification occurs only when both pump and seed pulses propagate through the crystal, amplified spontaneous emission is not present. On the other hand, it is necessary to well synchronize the

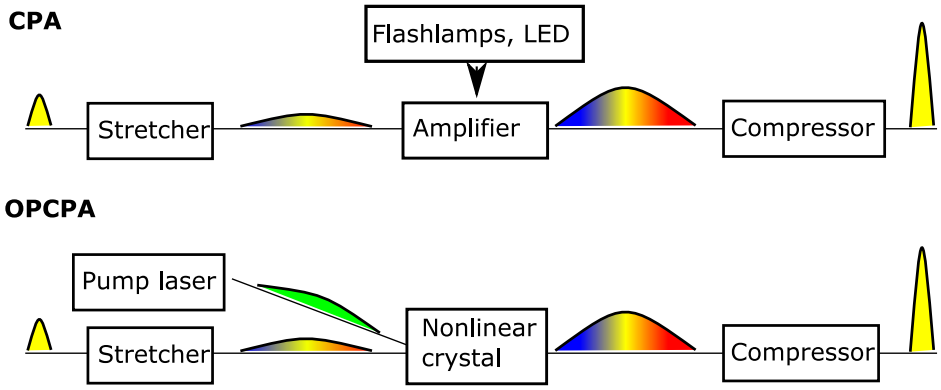

Figure 2.2: In the CPA, the seed pulse extract the energy from the excited crystal pumped by either optically or electrically. In the OPCPA, the energy of the pump pulse is directly transferred to the seed pulse by the nonlinear optical parametric amplification phenomena.

pump and the seed and match their pulse durations. The pump and the seed have to be also appropriately phase-matched to allow energy transfer. The spatial quality of a pump is imprinted into a seed, so it is required even for the pump to exhibit excellent spatial uniformity.

2.1 Compressor

In 1968 E.B. Treacy discovered that propagation of a pulse through a pair of parallel diffraction gratings induces negative group-delay dispersion [39]. 16 years later Martinez clarified that the mechanism behind which leads to negative group-delay dispersion is angular dispersion [40] regardless of its origin - whether it is refraction, diffraction or interference. Based on that, new types of devices with the ability to compress pulses were proposed such as a prism compressor, grism compressor, multi-layer dielectric structures, acousto-optics modulators [41]. However, only diffraction gratings are able to provide sufficient dispersion, large aperture and high laser induced damage threshold necessary for their successful implementation in state-of-the-art high power laser systems (Table 2.1). Therefore, this chapter will mainly focus on the treatment of dispersion induced by diffraction gratings.

For an arbitrary incidence, the k-vector of the diffracted beam $\vec{k}_d$ from a diffraction

Table 2.1: Comparison of basic parameters between different compressor types.

Type	**Dispersion**	**Aperture**	**LIDT**	**Alignment**
Gratings	high	$\sim$ 1m	high	hard
Prisms & grisms	low	$\lesssim$ 10 cm	low	moderate
MLD structures	low	$\sim$ 1 m	high	easy
A-O modulator	medium	$\lesssim$ 1 cm	low	easy

grating has to fulfill the following condition:

$$\vec{n_r} \times (\vec{k_d} - \vec{k_i} - m\vec{K}) = \vec{o} \tag{2.1}$$

where $\vec{n_r}$ is the grating normal vector, $\vec{k_i}$ is the k-vector of the incident beam, $\vec{K}$ is the grating vector and $\vec{o}$ is the null vector. Eq. (2.1) can be further simplified to a more common form known as the grating equation:

$$\sin\,\alpha + \sin\,\beta = \frac{mN\lambda}{\cos\,\gamma} \qquad\qquad \sin\,\gamma = -\sin\,\delta, \tag{2.2}$$

where α is the angle of incidence, β is the diffraction angle, m is the diffraction order, N is line density of the grating, λ is the wavelength of the incident wave, γ is the off-plane angle of the incident wave and δ is the off-plane angle of the diffracted wave. Fig. 2.3 shows how are these angles related to each other. We define the diffraction plane as a plane which is perpendicular to the grating grooves (e.g. the grating $\vec{K}$ vector lies in this plane).

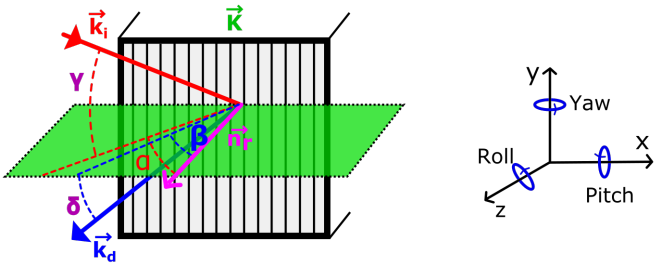

Figure 2.3: Schematic of diffraction of light on a grating. $\vec{n_r}$ is the normal vector to the grating surface. $\vec{K}$ is the grating k-vector. The diffraction plane, perpendicular to the grating grooves, is marked with green. α is then the angle between the projection of the incident k-vector into the diffraction plane and the grating normal $\vec{n_r}$, β is the angle between the projection of the diffracted k-vector into the diffraction plane and grating normal $\vec{n_r}$, γ is the angle between the incident k-vector and the diffraction plane (inclination angle), δ is the angle between the diffracted k-vector and the diffraction plane. The rotation about the axis parallel with grooves ($\vec{y}$) is named yaw, the rotation about the grating normal ($\vec{z}$) is called roll and the rotation about the axis perpendicular to the grating grooves and lying in the grating plane ($\vec{x}$) is named pitch.

A grating pulse compressor as proposed by Treacy consists of 2 grating pairs, where each pair is composed of two diffraction gratings aligned with parallel faces and grooves as in Fig. 2.4. In this configuration, higher frequency components of a pulse propagating through the grating pair have shorter optical path compared to lower frequency components. The second pair of gratings then ensures that all frequency components spatially overlap at the output. The phase accumulated by the pulse propagating through a pair of parallel diffraction gratings can be calculated as [41]:

$$\varphi(\omega) = \vec{k_d} \cdot \vec{G} = \frac{\omega}{c} G \frac{\cos(\alpha - \beta)}{\cos\,\alpha}, \tag{2.3}$$

where $\vec{L}$ denotes the vector representing grating distance for the central wavelength of the pulse and G is the perpendicular grating distance. Analytic expressions for group

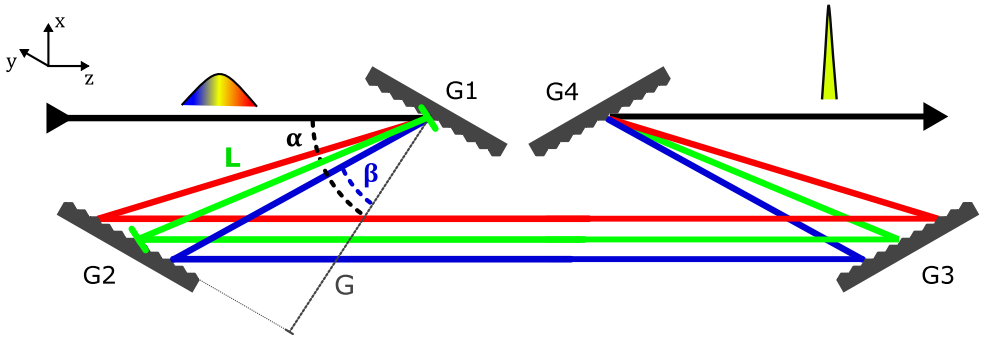

Figure 2.4: Schematic of a grating compressor. α is the angle of incidence, β is the diffraction angle, G is perpendicular grating distance, L is grating spacing for the central wavelength of the pulse. The diffraction plane lies in the xz plane and we assume that it is horizontal in following chapters. The vertical plane is then perpendicular to the diffraction plane and parallel with the gravity.

delay dispersion can be then calculated as a derivative of Eq. (2.3) with respect to frequency according to Eq. (1.12):

$$\begin{aligned} GDD_{cmpr} &= -\frac{\lambda_0^3 G N^2}{2\pi c^2 \cos^3(\beta_0))}; \qquad TOD_{cmpr} = -\frac{3\lambda}{2\pi c} GDD_{cmpr}\left(1+\frac{\sin\,\alpha}{\cos^2\,\alpha}\right); \\ FOD_{cmpr} &= \frac{3\lambda^2}{4\pi^2 c^2} GDD_{cmpr}\left(1+8\lambda N\frac{\cos\,\alpha}{\sin^2\,\alpha}+\lambda^2 N^2[1+\tan^2(\alpha)(6+5\,\tan^2(\alpha))]\right), \end{aligned} \tag{2.4}$$

where β_0 is the diffraction angle for the central wavelength of the pulse. In many cases, it is more convenient to use the grating distance L for the central wavelength of the pulse instead of the perpendicular grating distance G. Their relationship is simply $L\,\cos(\beta_0) = G$.

When a grating is tilted and an off-plane angle is introduced, its diffraction plane is tilted with respect to the incidence plane. the incident and diffracted beam then no longer lie in the same "horizontal" plane. The footprint of the dispersed beam on the second grating is tilted and slightly curved with respect to the diffraction plane. This is illustrated in Fig. 2.5. Since the dispersed spectral components retain the vertical k_y-component and are dispersed in the xz plane, their k-vectors lie on the surface of a sphere centered at the incidence point. The intersection of the k-vectors of the dispersed pulse with the sphere creates a circle parallel with the horizontal xz plane. The footprint of the dispersed beam is then the projection of this circle onto the plane of the second grating. Simply put, the offplane angle is the same for all frequency components and since the grating normal is tilted with respect to the incident beam, higher frequency components have shorter optical path when they propagate between gratings. Therefore, they acquire smaller y-component than low frequency components with longer optical path.

There are two options how to introduce the offplane angle. The first way is to rotate the grating about an axis perpendicular to the grating grooves and parallel to the grating plane (pitch). The second way is to slightly rotate grating grooves in the grating plane (roll). When the grating is first tilted about the y-axis (yaw) by Y to set the incidence angle and then the offplane angle γ is introduced by either pitch Π or roll Ω, their relation can be expressed as[A4]:

$$\sin(\gamma_{Pitch}) = -\sin(\Pi)\,\cos(Y) \qquad \sin(\gamma_{Roll}) = -\sin(\Omega)\,\sin(Y) \tag{2.5}$$

The incidence angles in the diffraction plane $\alpha_{Pitch}, \alpha_{Roll}$ are then given by:

$$\begin{aligned} \cos(\alpha_{Pitch}) &= \frac{\cos(\Pi)\cos(Y)}{\sqrt{\sin^2(Y) + (\cos(\Pi)\cos(Y))^2}} \\ \cos(\alpha_{Roll}) &= \frac{\cos(\Omega)\cos(Y)}{\sqrt{\cos^2(Y) + (\cos(\Omega)\sin(Y))^2}} \end{aligned} \tag{2.6}$$

From Eq. (2.5), it follows that the desired off-plane angle can be induced by a smaller pitch angle when $\alpha < 45°$ and by smaller roll when $\alpha > 45°$. The suitability of either of these configurations is then driven by the particular design of the compressor. The effective aperture of the second grating is decreased as the amount of vertical spatial chirp and the orientation of the second grating varies for either of these configurations. Diffraction efficiency of the gratings can be influenced as well especially for narrow bandwidth high line density MLD gratings.

Compressor misalignments

We consider a grating compressor well-aligned if both gratings within the pair are parallel to each other, gratings have equal line densities, the angle of incidence on the first grating is equal to the negative value of the angle of incidence on the third grating and the distance L between both grating pairs is the same. In general, we can divide compressor misalignments into two categories. The first one is the variation of global parameters (while gratings within the pair remain aligned) - the angle of incidence on both grating pairs α, the grating distance within each pair L and line densities of the gratings N. These lead only to the deviation of the induced spectral phase $\varphi(\omega)$, which can be directly calculated using Eq. (2.4). The second category is the misalignment of individual gratings. Each grating has 4 degrees of freedom: 3 rotational: yaw, pitch

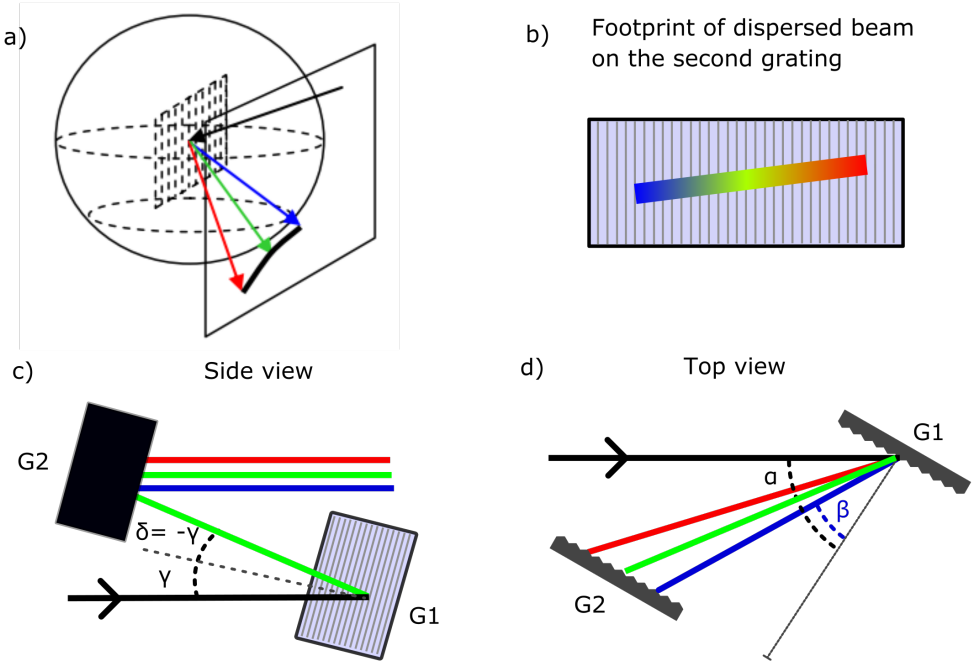

Figure 2.5: Offplane diffraction in a grating compressor. a) Visualization of the offplane diffraction taken from [42] b) Footprint of the dispersed pulse on the second grating c) Side view of the compressor d) Top view of the compressor

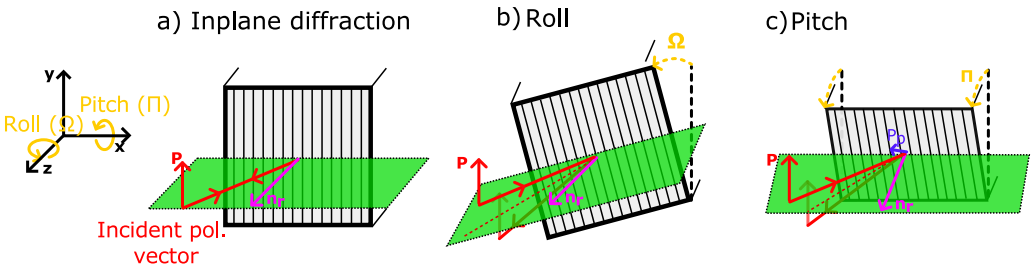

Figure 2.6: Illustration of pitch and roll rotation of a diffraction grating.

and roll (see Fig. 2.4); and line density variation. When any of these parameters differs from the designed value, the compressor yields spatio-temporal couplings of the compressed pulse. The couplings mainly manifest in the deviation of the spectral phase and a linear pulse front tilt which is equivalent to linear angular dispersion. The impact of each misalignment is summarized in Table 2.2.

For a compressor having an arbitrary grating orientation, the residual angular dispersion and the induced spectral phase deviation in terms of GDD and TOD can be calculated using analytical formulae derived in the article [43]. Here we show basic formulae for the case of a small misalignment in single degree of freedom and for $\gamma, \delta = 0$, which will be useful in the following chapter. The pointing deviation of the diffracted beam θ_x in the diffraction plane due to the yaw grating misalignment θ_{yaw} and the small line density variation ΔN can be derived using only the grating equation as:

$$\theta_x = \theta_{yaw} \frac{\cos\,\beta}{\cos\,\alpha} + \frac{\Delta N \lambda}{\cos\,\alpha} \tag{2.7}$$

From that, the residual angular dispersion in the diffraction plane $\frac{\mathrm{d}\theta_x}{\mathrm{d}\lambda}$ can be for the small yaw misalignment expressed as:

$$\frac{\mathrm{d}\theta_x}{\mathrm{d}\lambda} = \theta_{yaw} N \frac{\tan\,\beta}{\cos\,\alpha} + \frac{\Delta N}{\cos\,\alpha} \tag{2.8}$$

Therefore, the line density variation can be partly compensated by tilting the grating by $\theta_{yaw}^{\Delta N}$:

$$\theta_{yaw}^{\Delta N} = \frac{\Delta N}{N\,\tan\,\beta} \tag{2.9}$$

The Eq. 2.9 is valid only for small line density variations since it works with the linear term of the residual angular dispersion only and it neglects quadratic and cubic terms. For the small pitch misalignment θ_{pitch} and roll misalignment θ_{roll}, the residual angular dispersion in the plane perpendicular to the diffraction plane can be calculated as:

$$\frac{\mathrm{d}\theta_y}{\mathrm{d}\lambda} = \theta_{pitch} N \tan\,\beta + \theta_{Roll} N \tag{2.10}$$

Table 2.2: Impact of basic misalignments on the spectral phase and residual angular dispersion of the compressed pulse.

	ΔN	θ_{yaw}	θ_{pitch}	θ_{roll}	α	L	N
G1, G4	$\varphi(\omega), \frac{d\theta_x}{d\lambda}$	$\frac{d\theta_x}{d\lambda}$	$\frac{d\theta_y}{d\lambda}$	$\frac{d\theta_y}{d\lambda}$	-	-	-
G2, G3	$\varphi(\omega), \frac{d\theta_x}{d\lambda}$	$\varphi(\omega), \frac{d\theta_x}{d\lambda}$	$\frac{d\theta_y}{d\lambda}$	$\frac{d\theta_y}{d\lambda}$	-	-	-
G1+G2 or G3+G4	-	-	-	-	$\varphi(\omega)$	$\varphi(\omega)$	$\varphi(\omega)$

2.2 Phasing gratings and mirrors

2.2.1 Grating-Grating

Since the size of commercially available gratings is restrained to approximately 1 m diameter, a tiled grating scheme was proposed to overcome this limitation [10]. It follows the well-established design of segmented mirror telescopes used in astrophysics pioneered by J.Nelson in the design of Keck telescopes. A tiled grating is composed of an array of smaller diffraction gratings having parallel faces and grooves so that they behave like one large diffraction grating. However, it is necessary to align the gratings with sub-microradian and sub-micrometer accuracy in five degrees of freedom to reach sufficient quality of diffracted wavefront (Figure 2.7). The impact of individual misalignments on the spatial phase of a beam is summarized in Table 2.3.

Three degrees of freedom are angular, which represent the rotation of the face of the grating and yield a phase offset linear in $\vec{x}$ or $\vec{y}$. A yaw misalignment effectively changes the incidence angle and therefore it offsets the diffraction angle. Pitch and roll misalignments then deviate the beam pointing in the vertical direction. A piston misalignment represents a condition that the faces of all diffraction gratings within tiled grating have to lie in one plane. It yields spatially constant phase offset. For a monochromatic laser, the offset is periodic with period equal to the wavelength corrected for the angle of incidence and diffraction. For broadband pulses, the piston yields also temporal delay. A lateral shift safeguards that the periodicity of the groove spacing is retained even with the gaps between the individual gratings. Generally, each grating groove induces additional 2π phase shift in the spatial phase of the diffracted beam [44]. This phase can be recalculated into the tilt of the diffracted beam, which is represented by the grating equation. If one grating within a tile is offset by z_L,

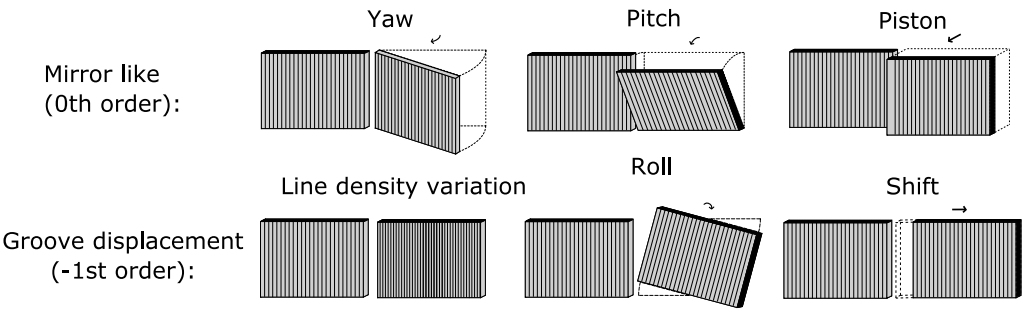

Figure 2.7: 6 degrees of freedom for the alignment of tiled gratings

Table 2.3: Spatial phase induced by the misalignment of a tiled grating pair. θ_{Yaw}, θ_{Pitch} and θ_{Roll} are the angles of the yaw, pitch and roll misalignment respectively, z_P is the distance between the grating faces, z_L is the shift misalignment, $\vec{\mathbf{y}}$ is the vector parallel with the grating grooves and perpendicular to propagation direction of the beam and $\vec{\mathbf{x}}$ is the vector that is perpendicular to $\vec{\mathbf{y}}$ and the beam propagation direction [45].

Misalignment	**0th order**	**1st order**
Yaw	$\frac{4\pi}{\lambda}\theta_{Yaw}\vec{\mathbf{x}}$	$\frac{2\pi}{\lambda}(1+\frac{\cos(\alpha)}{\cos(\beta)})\theta_{Yaw}\vec{\mathbf{x}}$
LDV	-	$\frac{2\pi\Delta N}{\cos\beta}\vec{\mathbf{x}}$
Pitch	$\frac{4\pi}{\lambda}\cos(\alpha)\theta_{Pitch}\vec{\mathbf{y}}$	$\frac{2\pi}{\lambda}(\cos(\alpha)+\cos(\beta))\theta_{Pitch}\vec{\mathbf{y}}$
Roll	-	$\frac{2\pi}{\lambda}(\sin(\alpha)+\sin(\beta))\theta_{Roll}\vec{\mathbf{y}}$
Piston	$\frac{4\pi}{\lambda}\cos(\alpha)z_p$	$\frac{2\pi}{\lambda}(\cos(\alpha)+\cos(\beta))z_p$
Shift	-	$2\pi N z_L$

the spatial phase of the part of the beam which is incident on this grating is offset by $2\pi N z_L$ with respect to the rest of the beam. This also means that compared to the piston, the shift misalignment is periodic with 1/N period even for broadband pulses and therefore it is sufficient to compensate it only within a groove period. The yaw, pitch and piston represent mirror-like misalignments and they influence the reflected and diffracted wavefront at both the zeroth and first diffraction orders. Line density variation, roll and shift represent misalignments of the grating grooves with respect to the other grating and they deviate the wavefront of the diffracted beams only.

The line density variation (LDV) is mostly determined by the technology of the grating manufacturer. It is possible to partly compensate the induced wavefront deviation from LDV by intentionally misaligning the grating in yaw since they are both present in the $\vec{x}z$ plane.

The concept of tiling multiple gratings together has been successfully tested in several laser facilities so far (LULI [45], POLARIS [14] or OMEGA-EP [13]). The mutual position of the gratings was determined either interferometrically [45, 46] or by far-field monitoring [47]. Both methods require to measure both the specular 0th order and diffracted 1st order to cover all possible misalignments.

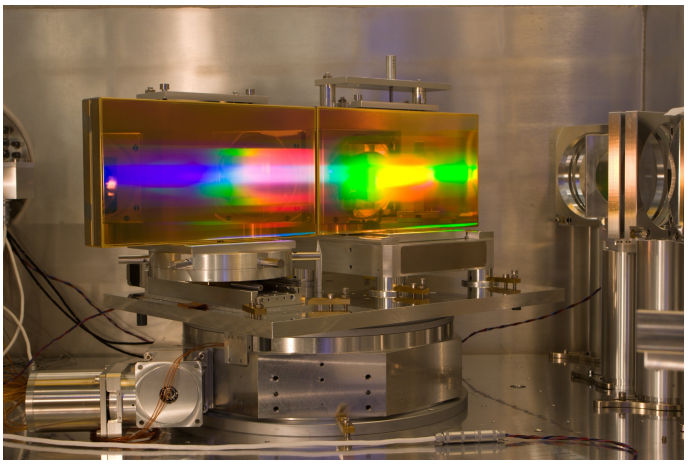

Figure 2.8: Photograph of a tiled grating assembly from the POLARIS laser system [14].

2.2.2 Grating-Mirror

Recently, a simplified scheme was proposed where a diffraction grating is phased with a perpendicularly positioned mirror (Fig. 2.9) [11, 12]. Such setup reduces the number of degrees of freedom to 3 and eliminates the need to set the piston absolutely. Two angular degrees of freedom - yaw and pitch - represent the ordinary degrees of freedom for the alignment of the mirror. While the yaw misalignment represents the yaw of the imaged grating, the pitch misalignment of the phased mirror is equivalent to the roll misalignment of the imaged grating. The third degree of freedom is called piston of the mirror (a movement along the normal axis of the mirror). It disrupts the periodicity of the grooves between the grating and its image and therefore it is equivalent to the shift misalignment between the real and imaged grating. However, due to the mirroring effect, the induced phase change of each of these misalignments is two times higher than for a tiled grating pair. The spatial phase difference between the splitted halves of the beam induced by the misaligned grating-mirror pair can be calculated as [48]:

$$\phi(x,y,z) = \frac{4\pi}{\lambda_0}(1+\frac{\cos(\alpha)}{\cos(\beta)})\theta_{Yaw}\vec{\mathbf{x}} + \frac{4\pi}{\lambda_0}(\sin(\alpha)+\sin(\beta))\theta_{Pitch}\vec{\mathbf{y}} + 4\pi N dz_{Piston} \tag{2.11}$$

For the grating-mirror configuration, it is sufficient to monitor the 1st diffraction order only as it covers all three degrees of freedom. For the specular 0th order reflection from the grating, the grating-mirror configuration behaves like ordinary rooftop mirror and therefore it is possible to detect the yaw misalignment only.

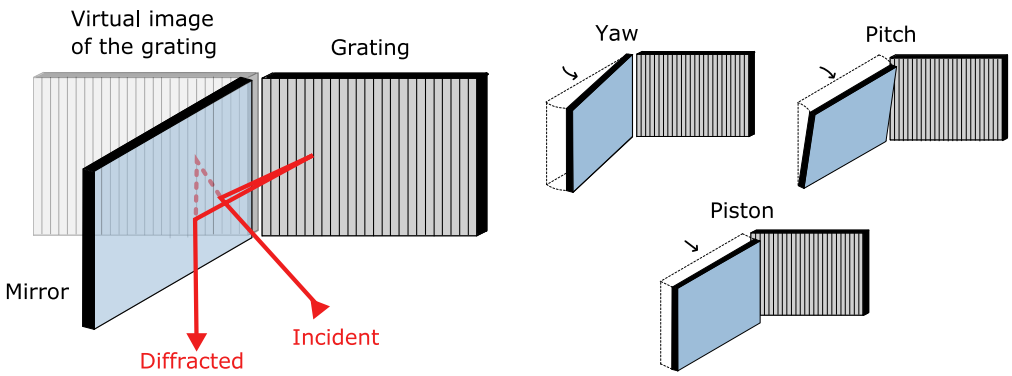

Figure 2.9: Sketch of a grating mirror assembly. One half of the incident beam is diffracted off the grating as the +1st diffraction order. The other half is reflected from the mirror and consequentially it is diffracted as the -1st diffraction order and reflected off the mirror again. Thereby the mirror creates a virtual grating by mirroring the real grating.

2.2.3 Measurement methods

Interferometry

For the monitoring of the mutual position of phased gratings and mirrors a Fizeau interferometer can be used (Figure 2.10). In the Fizeau interferometer, a high-quality reflection flat is placed in front of a tested surface and a nulled fringe pattern is recorded. The surface profile of the tested optic can be then obtained from the position of the maxima of the fringes. To enhance the accuracy of the extraction of the surface profile, there are two main types of fringe analysis methods.

In the phase-shifting interferometry, the tested optics has to be motorized and move in parallel direction with respect to the interferometric beam. The nulled fringe pattern

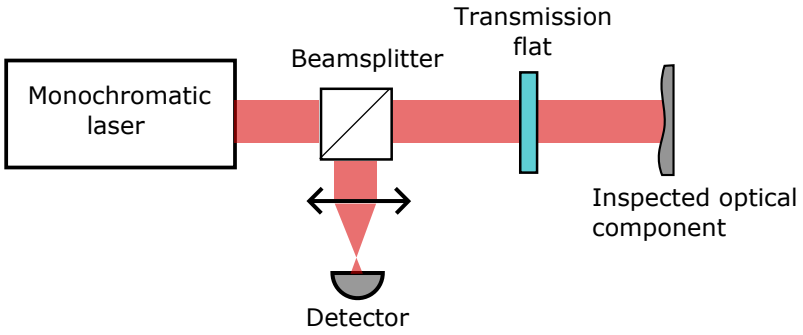

Figure 2.10: Schematic of a Fizeau interferometer

is recorded at four distinct positions being at $\lambda/4$ distance from each other . Using these four measurements, the surface profile can be analytically retrieved with precision better than $\lambda/100$. The phase shifting interferometry is susceptible to vibration and requires piezo-motorized mount of either of the optics. Contrarily, the Fourier fringe pattern analysis (FFA) [49] is an instantaneous method, where both the test and reference optics are static. In FFA, it is necessary to tilt the reference optics with respect to the test optics to introduce a linear fringe pattern. The measured intensity pattern $g(x, y)$ can be expressed as:

$$g(x, y) = a(x, y) + b(x, y)cos(2\pi\nu_0 x + \varphi(x, y)), \tag{2.12}$$

where $\varphi(x, y)$ is the phase profile, ν_0 is the spatial-carrier frequency representing the tilt angle between the reference and test optics and $a(x, y)$, $b(x, y)$ are slowly varying intensity fluctuations with respect to ν_0. These intensity fluctuations originate from the background illumination and non-uniformity of the transmission and reflection. Eq. (2.12) can be reformulated as:

$$\begin{gathered} g(x, y) = a(x, y) + c(x, y)\exp(i2\pi\nu_0 x) + c^*(x, y)\exp(-i2\pi\nu_0 x); \\ c(x, y) = 1/2\ b(x, y)\exp(i\varphi(x, y)) \end{gathered} \tag{2.13}$$

After computing the spatial 2D Fourier transform, the measured fringe pattern $G(x, y)$ consists of three terms separated by the carrier frequency ν_0:

$$G(x, y) = A(\nu, \xi) + C(\nu - \nu_0, \xi) + C^*(\nu + \nu_0, \xi) \tag{2.14}$$

Next, the first and the last term are filtered using bandpass filter and the remaining term is shifted to zero:

$$C(\nu - \nu_0, \xi) \rightarrow C(\nu, \xi) \tag{2.15}$$

Lastly, the inverse 2D Fourier transform of the remaining term is computed and its complex logarithm is calculated:

$$\log(c(x, y)) = \log(1/2\ b(x, y)) + i\varphi(x, y) \tag{2.16}$$

Following this procedure, the phase profile $\varphi(x, y)$ being in the imaginary part of the $c(x, y)$ is then separated from the intensity variation $b(x, y)$ and can be easily recovered. The procedure is summarized in Fig. 2.11. The phase profile has to be unwrapped to remove discontinuities occurring at 2π intervals. Generally, unwrapping of spatial phase in 2D is a complicated problem which is beyond the scope of this thesis. There are several well-established algorithms such as Itoh's [50] and Goldstein's [51], their stability

and accuracy mostly depends on the amount of the noise present in the data. The FFA method is more prone to errors than the phase-shifting interferometry performed in the controlled environment, nevertheless precision up to $\lambda/100$ has been reported with carefully processed data [52].

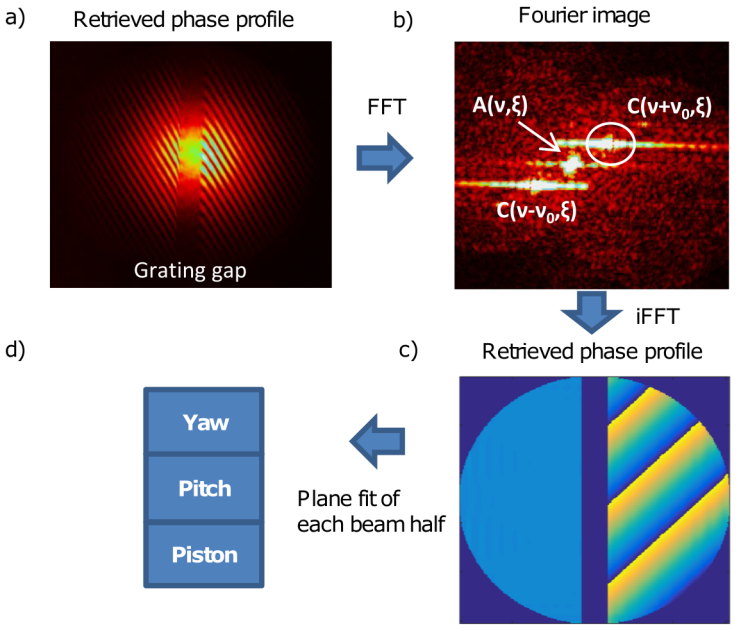

Figure 2.11: Phase extraction using the Fourier fringe pattern analysis method. The measured interference pattern (a) is Fourier transformed, a term with the carrier frequency ν_0 (b) is filtered, shifted to zero and inverse Fourier transformed. Its phase profile (c) is then extracted from its imaginary part and yaw, pitch and piston coefficients are retrieved from plane fit of each beam half (d).

Since the FFA method requires tilting the reference optics with respect to the measured one, the beam reflected from the reference and the beam reflected from the test optics no longer share the same optical path through the interferometer. Usually, an optical system decreasing the beam diameter and imaging the measured surface on the camera recording the fringe pattern is employed. A systematic "retrace" error is then induced by the aberrations of this optical system and therefore it increases with the carrier frequency of the interferogram. It can be calibrated in situ [53] by recording the fringe pattern for different carrier frequencies and comparing the calculating phase profiles. An easier but less robust option is to place a different "calibration" reference flat with known surface profile instead of the test surface without changing the pointing of the beam. The retrace error can be then obtained for this exact configuration (i.e. with the fixed carrier frequency). The impact of the retrace error can be calculated from the optical model of the imaging system and is usually bellow $\lambda/20$.

Another type of error originates from insufficient separation of the terms from Eq. (2.14). In the case of tiled gratings, there is always a gap between the optics and the interferometric beam is scattered by the chamfered edges of the optics. This increases the high spatial frequency content of the interferometric beam so that the high frequencies of the A and $C*$ terms can leak into the C term. Since the Fourier transform is performed numerically using the FFT algorithm, other errors can originate from its discrete nature. The picket fence effect manifests in a fact that the shift in Eq. (2.15) does not likely go to zero but in most cases some small residual carrier frequency ν_0 remains. This is due to the fact that the centroid of the C term is not likely exactly on

the sampling point of the FFT. This error introduces tip and tilt offset of the recovered phase. It is automatically subtracted when comparing the tip and tilt between the beams halves for phasing, however it can introduce artificial piston phase offset. In general, it can be compensated by fitting and subtracting tip and tilt phase for the whole aperture.

Farfield

The idea behind far-field monitoring of phased grating assemblies is that the perfect focal spot is obtained only when the phased gratings and mirrors are well aligned. A typical farfield monitoring setup is sketched in Fig. 2.12. A collimated monochromatic laser source is incident on the gap between the gratings, the specular reflection and the first diffraction order are focused and their focal spot profiles are recorded on CCD cameras. Fig. 2.13 illustrates possible farfield distribution in the presence of phasing misalignments. The resolution of the far-field method can be estimated from

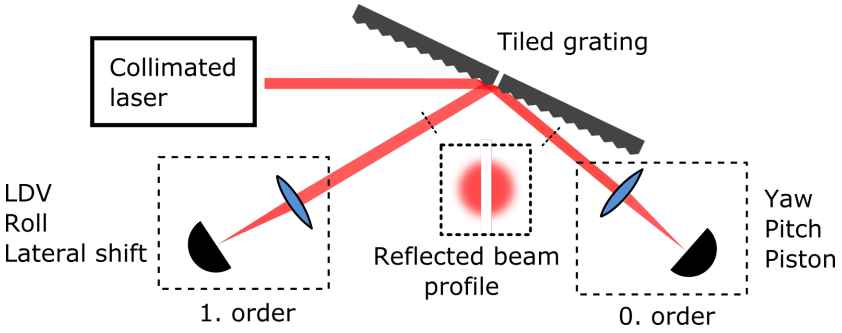

Figure 2.12: Typical farfield setup for the alignment of tiled gratings. A collimated laser beam is incident on the tiled grating and is centered on the grating-grating gap. A specular reflection is monitored to align the yaw, pitch and piston. The 1st diffraction order is measured to adjust the roll and lateral shift.

the Rayleight resolution criterion as the misalignment of the assembly can be measured only if we are able to resolve the individual focal spots. For an aberration-free focusing system, the angular resolution is $\sim \frac{\lambda}{2w_0}$.

For an initial alignment, the angular accuracy can be increased up to $\sim 0.2\frac{\lambda}{2w_0}$ by intentionally misaligning the phased grating in the perpendicular degree of freedom [47]. Focal spots are split in one plane and the centroids of both focal spots can then be accurately compared in the other plane where they no longer overlap (i.e. misaligned in the yaw to measure the pitch). After the intentional misalignment is corrected, the process can be repeated for the other plane. However, such accuracy cannot be achieved during the online measurement of the phasing alignment and it is not very beneficial for laser systems with high repetition rates. The method also requires to have the grating on a rotational stage with very good accuracy and repeatability to achieve sufficient precision when the intentional misalignment is corrected. Accuracy up to 0.2 μrad and 20 nm for piston has been reported with this method [54].

Compared to the interferometric method, the far-field method has a simpler setup and is less prone to systematic errors. However, since the split foci method is not suitable for online monitoring of the phasing, the accuracy of the interferometric method is superior. The interferometric method is also more resistant to random noise such as air fluctuation which can be averaged out to some extent.

Determination of absolute piston

One of the biggest challenges of the tiled grating configuration is the precise alignment of the absolute piston error due to the fact that the induced phase offset is periodic for monochromatic laser beams and therefore it is not possible to acquire its absolute value using a single wavelength laser and single angle of incidence. According to Table 2.3, the piston phase offset φ_0 is given by:

$$\varphi_0 = 4\pi \cos(\alpha)\frac{z_p}{\lambda}, \tag{2.17}$$

which is periodic for monochromatic beams with period $z_p^{\text{per}} = \frac{\lambda}{2\cos(\alpha)}$ within 2π phase range. The period z_p^{per} is in the order of μm for conventional systems, which is insufficient and below the mechanical accuracy of positioning of the assembly. Therefore, several methods have been proposed using either broadband laser or multiple monochromatic lasers to increase the period.

The spectrally resolved far-field method using broadband laser was reported to work within 2 μm - 100 μm range [54]. The method utilizes the fact that the spatial phase induced by the piston misalignment is wavelength dependent. Therefore the absolute value of the piston misalignment can be retrieved by monitoring of the spectrally dispersed far-field profile. A broadband beam is incident on the grating-mirror gap and the zeroth order is focused and then dispersed by a diffraction grating. The dispersed farfield profile is then recorded on the camera. Since the period of the piston misalignment varies with the wavelength, the farfield profile of each spectral component changes as well. If the absolute misalignment is big, the slope of the induced phase fast and the phase can go through 2π range several times within the bandwidth. The farfield profile gradually changes through all the possible farfield shapes sketched in

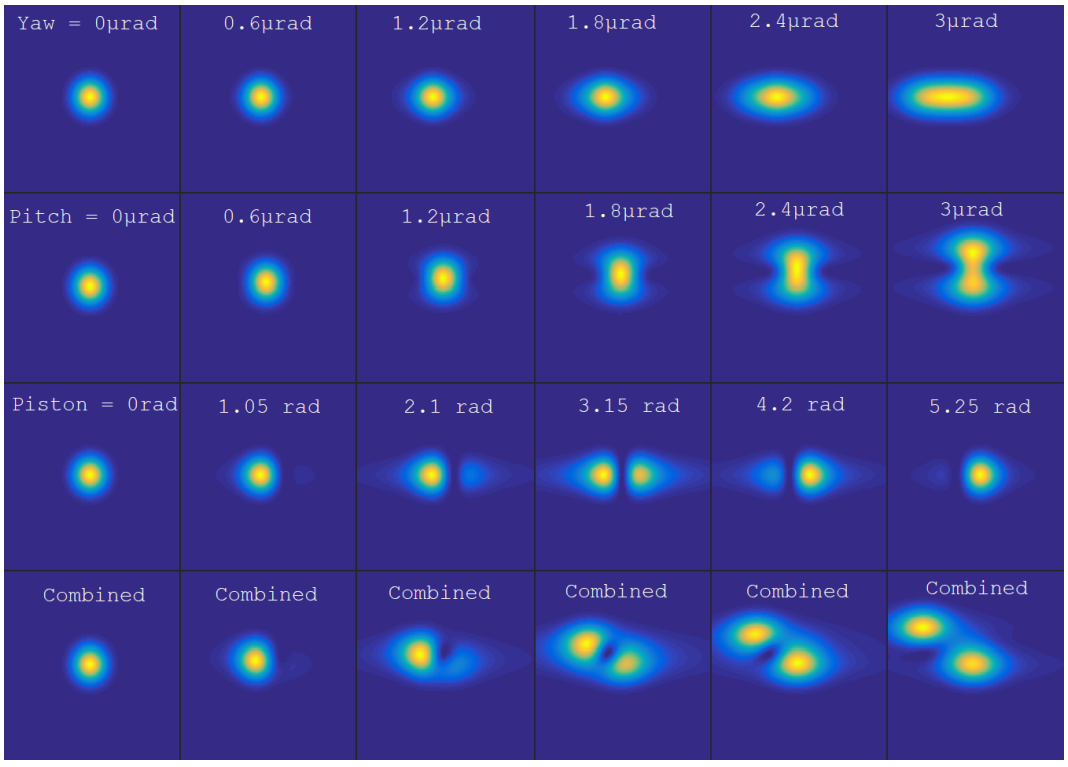

Figure 2.13: Spatial intensity distribution in focal spot for various yaw, pitch, piston and combined misalignments. The focal spots were numerically simulated in Matlab using FFT and the phase formulae from Table 2.3.

Figure 2.14. If the absolute misalignment is small, the farfield profile slowly changes within 2π period without changing its shape. The spectrally resolved farfield method can be also directly used to diagnose the main beam.

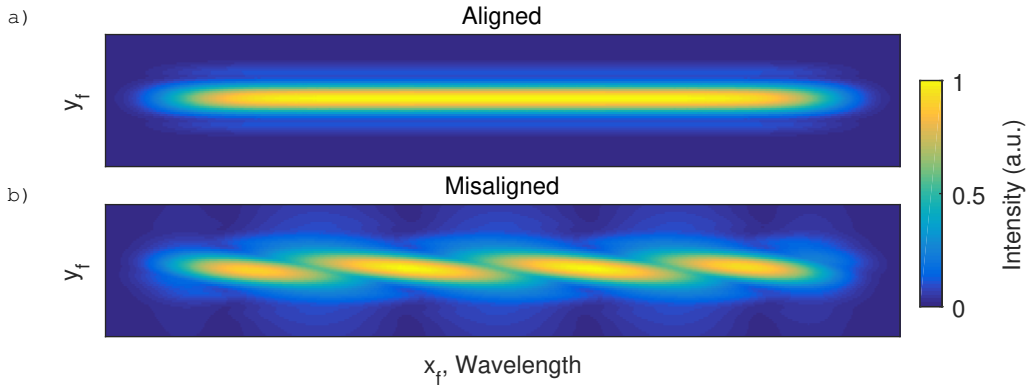

Figure 2.14: Simulated farfield profile in the case of no misalignment (a) and the absolute piston offset being tens of μm (b).

Other methods increase the piston period by using either directly two wavelengths [55] or two incidence angles [56] and comparing their farfield profiles while scanning the piston displacement z_p. Such then system exhibits a synthetic period z_p^s, which represents such displacement z_p^s for which both beams gain the same phase offset within 2π range, i.e. $\mathrm{mod}(\varphi_0^{\lambda_1,\alpha_1}, 2\pi) = \mathrm{mod}(\varphi_0^{\lambda_2,\alpha_2}, 2\pi)$:

$$z_p^{\lambda\alpha} = \left| \frac{2\cos(\alpha_1)}{\lambda_1} - \frac{2\cos(\alpha_2)}{\lambda_2} \right|^{-1}, \tag{2.18}$$

where α_1, α_2 and λ_1, λ_2 are the angles of incidence and central wavelengths of both beams. To further increase the synthetic period both zeroth and first diffraction orders can be monitored using both two beams. Using this method, the absolute piston error can be set-up with periodicity up to 40 μm. So, the initial positioning of the gratings in the compressor chamber has to be done with better than 40 μm accuracy by some other method. Since the spectrally resolved far-field method exhibits no periodicity and the determination of the absolute piston error has to be done only during the first alignment, it is generally less ambiguous and easier to implement.

2.3 Stretcher

In high peak power femtosecond CPA systems, design of the stretcher is usually based on the compressor. The stretcher is located at the beginning of the CPA chain, where the beam has small diameter and energy. Therefore, its design is more flexible. Ideally, the stretcher should yield exactly opposite chirp compared to the compressor and material dispersion in the CPA chain. A diffraction grating stretcher is usually preferred as it can induce almost exactly the opposite spectral phase change as the grating compressor, which is preferred for systems requiring high dispersion. However, different types of stretchers such as bulk material (long optical fibers), fiber Bragg gratings [57], grisms [58] and other can be employed in systems with shorter stretched pulse durations. The comparison of the stretcher types is summarized in Table 2.4.

Table 2.4: Comparison of basic parameters of basic stretcher types.

Type	**Dispersion**	**Tunability**	**Alignment**
Gratings	high	moderate	hard
Fiber Bragg grating	medium	small	easy
Bulk material	medium	none	easy
A-O modulator	low	high	easy
Prisms/Grisms	low	small	moderate

The idea of a grating pulse stretcher was firstly proposed by O.E. Martinez [40] motivated by the compensation of the negative group velocity dispersion in low loss region (1.3-1.6 μm) of telecommunication fibers. Soon it was recognized that it would be very useful in CPA systems where it could be used as the counterpart of the grating compressor since the existing systems had trouble with the compensation of high dispersion orders. A typical grating stretcher comprises a pair of diffraction gratings and a 1:1 telescope placed in between the gratings to reverse the sign of the group velocity dispersion (Fig. 2.15). Since the second grating is placed in front of the image of the first grating, the system is equivalent to a compressor having the negative distance between the first and the second grating. Ideally, the stretcher would yield exactly

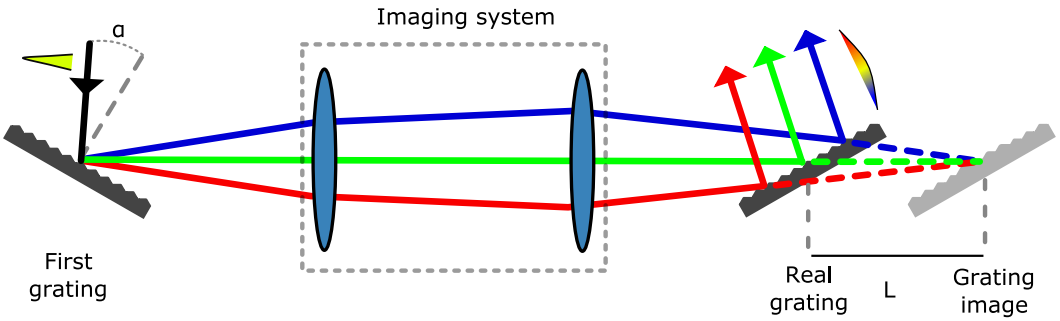

Figure 2.15: Schematic of a grating pulse stretcher. s is the distance between the first grating and the entrance pupil (the first lens), s_{img} is the distance between the last lens and the image of the first grating, L is the distance between the image plane and the second grating.

opposite dispersion (Eq. (2.4)). However, if aberrations are present in the stretcher imaging system, the spectral phase of the stretched pulse is deviated with respect to the ideal state. The phase profile of the grating stretcher has to be computed by numerical ray-tracing algorithms. Residual spatial chirp and angular dispersion appearing at the output of the stretcher are also induced by the aberrations. On the other hand, they can be also used to advantage to balance the dispersion of the whole chain when there is significant amount of material present. Recently, a new method for the analytic calculation of the induced spectral phase deviation and spatio-temporal couplings, when aberrations are present, has been published by our group [59] and it is described in the following section.

Since its invention, the stretcher design has undergone many innovations. In 1993, White et al. found that through the modification of chromatic and spherical aberrations of doublet lenses, TOD and FOD of the stretcher can be adjusted [60]. Around the same time, another group tried to eliminate the impact of the chromatic aberration and the lens material dispersion by replacing the lenses with cylindrical mirrors [61]. The main advantage of the cylindrical mirrors compared to spherical ones is that they introduce aberrations only in the diffraction plane and therefore do not introduce spatio-temporal couplings in the perpendicular plane. Nevertheless, the aberrations present in the diffraction plane which deviate the spectral phase making the design not ideal for the ultrashort laser systems with pulse durations below $\lesssim 20$ fs.

An aberration-free stretcher design was discovered three years later [62]. The aberration-free Offner stretcher is composed of 2 gratings with a reflective Offner triplet in between wherein the first grating lies at the center of curvature of the first concave mirror (Fig. 2.16). The Offner stretcher exhibits only very small deviation of the spectral phase since all Seidel aberrations are compensated by the design. However, to achieve separation between the input and output beams, the incidence point has to be offset from the optical axis of the imaging system. To compensate higher order aberrations originating from that offset, the concave mirrors can be replaced with cylindrical ones. The incidence point lies in the plane which is not imaged and the radius of curvature of the convex mirror can be adjusted [63]. The Offner stretcher offers the spectral phase profile closest to the ideal, on the other hand it compromises of many optical components, which has to be precisely manufactured and aligned to achieve good performance, and can have relatively large footprint. Nevertheless, this design is vastly preferred for all laser systems with few-cycle pulse duration.

Others attempted to find a more simple and compact configuration. Banks adapted the initial Martinez design and converted it to all-reflective single grating configuration using only one concave mirror [64] allowing to account for large material dispersion through the uncompensated spherical aberration. A similar effect was observed in the single-grating Offner stretcher [65], where the grating is shifted from the aberrations-free position towards the first concave mirror. Another, ingenious aberration-free stretcher design was implemented in Gemini laser [66]. The imaging system consists of a concave mirror and a plane mirror placed in its focal plane. The first grating is then placed in the center of curvature of the concave mirror. However, compared to the other designs, the second grating is placed in between the concave and the flat mirror where the beam is still converging. The simpler configuration compared to the 2-grating Offner is paid off by higher wavefront aberrations - especially chromatism and astigmatism. The individual simplified layouts of the stretcher designs are sketched in Fig. 2.16.

In recent years, it has been noted that the temporal intensity contrast of the pulse can be degraded by the stretcher itself even with the sufficient spectral bandwidth and high dispersion orders compensated. The coherent pedestal, which is the area in

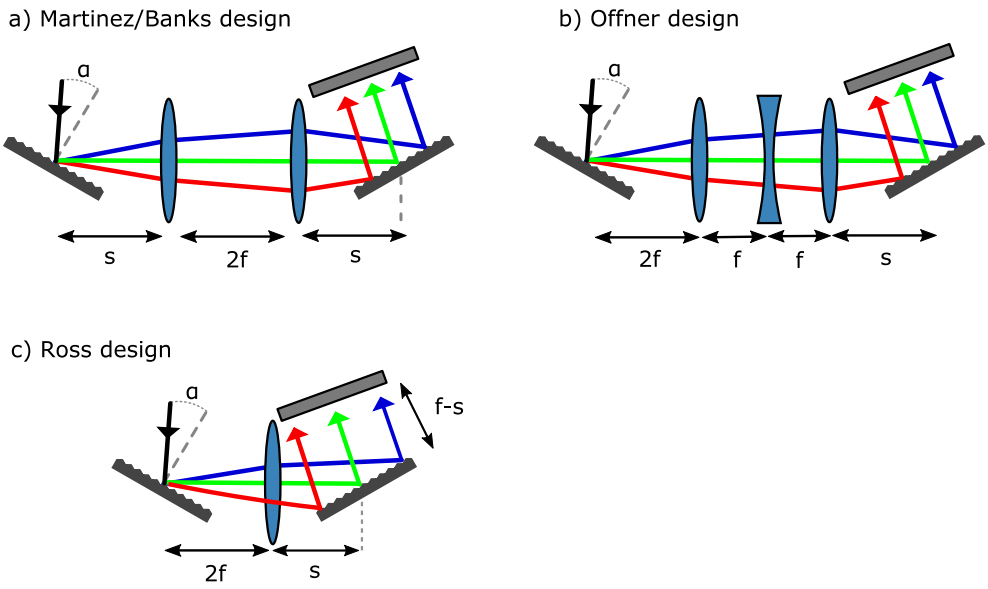

Figure 2.16: Simplified schematic of the common grating pulse stretcher designs. a) Martinez/Banks stretcher; b) Offner stretcher; c) Ross stretcher

the ps-scale around the main peak, can be induced through the scattering of the first grating [67]. A noticeable improvement has been achieved using etched fused silica transmission gratings instead of the reflective gold ones [68]. The transmission gratings have lower surface roughness and better groove quality due to simpler manufacturing process. The scattering model has been further explored by Li [23] who showed that multi-pass stretcher designs are theoretically more prone to the contrast degradation through multiple scattering. Temporal contrast of a focused pulse can be also degraded through the spatio-temporal couplings at the Fourier plane of the stretcher imaging system. This coupling is mostly noticable for stretcher designs having a mirror at the focal plane of a concave mirror. At the focal plane, the individual spectral components are spatially dispersed and they are incident on different parts of the mirror surface. High frequency surface imperfections of the mirror are then directly transferred to the spectral phase profile of the pulse at focus. General high-frequency noise of the spectral phase raises the noise-floor of temporal contrast [20]. The measurement by a spatio-temporal cross correlator confirmed that the stretchers without a mirror in the Fourier plane have superior on-axis farfield contrast [69].

2.4 Seidel aberrations in grating pulse stretchers

The following text is based on the article published in [A1].

As was stated before, the spectral phase of the stretcher is usually calculated using numerical ray-tracing when aberrations are present in the stretcher imaging system. The Offner stretcher with a grating placed near the center of curvature of the concave mirror is aberration-free. Eqs. (2.4) are then very close to the reality and no numerical modeling is necessary. However, for all the other cases the analytic formulae are very beneficial as they enable to choose the right stretcher design from scratch and crosscheck the results of numerical ray-tracing. In the following paragraph, the work in the field which has been done up to now is summarized.

First, Martinez calculated the spectral phase of a perfect stretcher [70]. Later, an extended ABCD formalism was introduced by Martinez [71] and expanded by Kostenbauder [72]. However, the linear nature of this formalism only allows for the calculation of GDD and not the determination of higher-order terms. Druon et al. proposed another extension of the ABCD formalism by using nonlinear operators instead of linear matrices [73] enabling calculation of the spectral phase in the general case. The spectral dependence of the group delay was also calculated by Zhang [74] using ray-tracing analytically. Even though the spectral phase and higher order dispersion terms for grating stretchers can be analytically obtained by the usage of the last two methods, the resulting formulae are not illustrative without numerical substitution and do not offer much physical insight. Here, we present an elegant analytical method which can be used to calculate the deviation of GDD, TOD and FOD with respect to the ideal state based on the Seidel aberration coefficients.

Transfer function

According to Goodman [75], we can express the relation between the object $U(x, y, \omega)$ and its image $U_{img}(x_{img}, y_{img}, \omega)$ using the amplitude transfer function $H(\nu_x, \nu_y)$, which acts as a spatial frequency filter and modifies the amplitude and phase of the input beam spatial spectrum as:

$$FT[U_{img}(x_{img}, y_{img}, \omega)](\nu_x, \nu_y, \omega) = H(\nu_x, \nu_y) FT[U(x, y, \omega)](\nu_x, \nu_y, \omega) \quad , \tag{2.19}$$

where x, y (x_{img}, y_{img}) are Cartesian coordinates in the object (image) plane, ν_x and ν_y are spatial frequencies and FT stands for a Fourier transform. The amplitude transfer function is a complex function and it can be expanded to:

$$H(\nu_x, \nu_y, \omega) = P(\xi(\nu_x), \eta(\nu_y)) e^{-ik\Phi(\xi(\nu_x), \eta(\nu_y), x, y)} \quad , \tag{2.20}$$

where P describes the amplitude transmittance and Φ is the aberration function, which represents a wavefront deviation with respect to a Gaussian reference sphere (see Figure 2.17).

For a grating pulse stretcher, the dependence of the pupil coordinates on ν_x, ν_y and ω can be expressed in the paraxial approximation as:

$$\xi = x_0 + s\lambda\nu_x; \qquad \eta = y_0 + s\theta(\omega) + s\lambda\nu_y \quad , \tag{2.21}$$

where s is the distance between the first grating and the entrance pupil, λ is the wavelength, $\theta(\omega)$ is the ray angular deviation coming from angular dispersion. We can expect that the position of a ray on the entrance pupil in grating stretchers is mostly given by its frequency, which comes from the Fourier transform of the temporal profile of the pulse and not the transform of its spatial profile [see Fig. 3]. In the following,

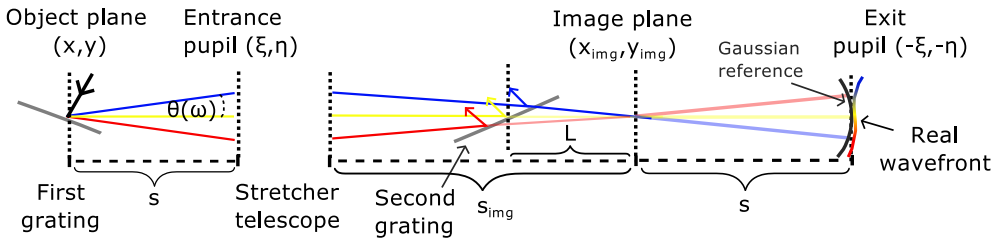

Figure 2.17: Schematic of a grating pulse stretcher. s is the distance between the first grating and the entrance pupil (the first lens), s_{img} is the distance between the last lens and the image of the first grating, L is the distance between the image plane and the second grating.

we will thus neglect the effect of a finite beam size ($s\lambda\nu_x \approx 0,\ s\lambda\nu_y \approx 0$) and proceed with the calculation for a plane wave. Pupil coordinates can then be expressed as:

$$\xi = x_0; \qquad \eta = y_0 + s\theta(\omega) \quad . \tag{2.22}$$

Assuming that the entrance pupil of the stretcher is large enough so that the spectrum of the pulse is not truncated, we can put $P(\xi, \eta) = 1$. If we substitute pupil coordinates Eq. (2.22) into Eq. (2.19), we get:

$$FT[U(x_{img}, y_{img}, \omega)](\nu_x, \nu_y, \omega) = e^{-ik\Phi(\xi(x_0),\eta(\omega,y_0,s),x_0,y_0)} FT[U(x, y, \omega)](\nu_x, \nu_y, \omega) \quad . \tag{2.23}$$

According to Eq. (2.23), the aberration function can be used to calculate the deviation of the spectral phase of the pulse $\varphi(\omega)$ at the image plane with respect to the ideal case without aberrations:

$$\varphi(\omega, s_{img}) = \frac{\omega}{c}\Phi(\xi(x_0), \eta(\omega, y_0, s), x_0, y_0). \tag{2.24}$$

To calculate the spectral phase at some other point, we can proceed the same way as for the ideal stretcher with the effective grating distance L_{eff} [41]. To our knowledge, the additional residual angular dispersion originating from the aberrations at the image point does not induce additional phase changes when the pulse is propagated from the image point to the position of the second grating. The total spectral phase of the pulse is then given by the sum of the spectral phase deviation coming from aberrations and the spectral phase of the ideal stretcher:

$$\varphi(\omega, L) = \frac{\omega}{c}\Phi(\xi(x_0), \eta(\omega, y_0, s), x_0, y_0) - L_{\text{eff}}\frac{\omega}{c}\cos(\theta(\omega)). \tag{2.25}$$

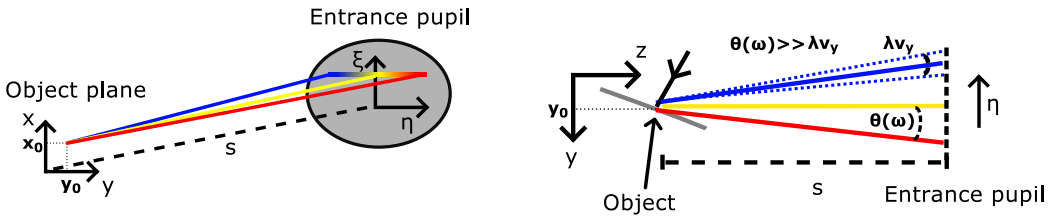

Figure 2.18: Coordinate system definition. We define the object as a place, where the laser pulse hits the diffraction grating with coordinates (x_0, y_0). To simplify calculation, it is convenient to choose coordinate-axis so that diffraction occurs in the horizontal yz plane (diffraction plane). We assume that the optical axis of the stretcher telescope is parallel with z-axis and the propagation direction of the central wavelength of the pulse and intersects the object plane at the point (0,0).

This theory can also be used to calculate the residual angular dispersion of the stretcher, which can generally lead to additional pulse broadening and reduces peak power in the focus [28]. The residual angular dispersion is present because rays with different frequencies propagate through the stretcher with different angles and acquire different angular deviation due to aberrations. In other words, the derivative of the wavefront at a given point corresponds to the propagation direction of the ray coming from that point. The aberration function represents a deviation of the real wavefront from a perfect wavefront. The derivative of the aberration function with respect to the pupil coordinate then expresses a variation in the propagation direction of aberrated rays. Since each pupil coordinate is assigned to a ray of different frequency, this variation of propagation direction is spectrally dependent. Residual angular dispersion can then be calculated as:

$$\begin{aligned} \mathrm{d}\theta_y(\omega) &= \frac{\cos(\beta)}{\cos(\alpha)} \frac{\mathrm{d}\Phi(\xi(x_0), \eta(\omega, y_0, s), x_0, y_0)}{\mathrm{d}\eta} = \frac{\cos(\beta)}{\cos(\alpha)} \frac{1}{\theta(\omega)} \frac{\mathrm{d}\Phi(x_0, y_0, s, \omega)}{\mathrm{d}s} \\ \mathrm{d}\theta_x(\omega) &= \frac{\mathrm{d}\Phi(\xi(x_0), \eta(\omega, y_0, s), x_0, y_0)}{\mathrm{d}\xi} = \frac{\mathrm{d}\Phi(x_0, y_0, s, \omega)}{\mathrm{d}x_0} \quad , \end{aligned} \tag{2.26}$$

where the $\frac{\cos(\beta)}{\cos(\alpha)}$ factor comes from the grating equation and rescales the angular dispersion in the diffraction plane as the pulse hits the second grating. In the rest of the article, the residual angular dispersion $\mathrm{d}\theta(\omega)$ is expressed as a function of wavelength, as it is more common, rather than frequency.

Aberration function

Following Welford [76], we can define a wave aberration function:

$$\begin{aligned} \Phi(\xi, \eta, x, y) = \; & B(\xi^2 + \eta^2)^2 + C(\xi x + y\eta)^2 + D(x^2 + y^2)(\xi^2 + \eta^2) \\ & + E(x^2 + y^2)(\xi x + y\eta) + F(\xi^2 + \eta^2)(\xi x + y\eta) \quad , \end{aligned} \tag{2.27}$$

where B is the spherical aberration, C is the astigmatism, D is the field curvature, E is the field distortion and F is the coma coefficient. In the following calculations, we deal with the impact of the fourth order aberrations only. The aberration function can be easily extended to include higher order aberrations as well, but in general their analytic calculation is very complicated. We also neglect tilt and defocus terms as they represent a shift of the center of the Gaussian reference sphere with respect to the image point and the aberrations are usually measured with respect to the sphere originating from the Gaussian image point.

If we substitute pupil coordinates ξ and η from Eq. (2.22) to Eq. (2.27) and put $x = x_0$ and $y = y_0$, we get:

$$\begin{aligned} \Phi(x_0, y_0, s, \omega) = \; & B s^4 \theta^4(\omega) + y_0 \, (4B + F) s^3 \theta^3(\omega) \; + y_0^2 \, (6B + C + D + 3F) s^2 \theta^2(\omega) \\ & + x_0^2 \, (2B + D + F) s^2 \theta^2(\omega) + ... \end{aligned} \tag{2.28}$$

In a grating stretcher, $\theta(\omega)$ is defined by the grating equation and can be linearly approximated by:

$$\theta(\omega) = \arcsin(mN\frac{2\pi c}{\omega} - \sin(\alpha)) - \arcsin(mN\frac{2\pi c}{\omega_0} - \sin(\alpha)) \doteq \frac{mN(2\pi c)}{\omega_0^2 \cos(\beta_0)}(\omega - \omega_0) \quad , \tag{2.29}$$

where ω_0 is the central frequency of the pulse, α is the angle of incidence on the grating, β_0 is the diffraction angle of the central frequency, m is the diffraction order and N

is the line density of the grating. The linear approximation of $\theta(\omega) \sim (\omega - \omega_0)$ allows for an estimation of the impact of each term from Eq. (2.28) on the spectral phase dispersion terms [Eq. (1.12)]. The first term from Eq. (2.28) is quartic in $\theta(\omega)$ and it deviates the FOD. The second term is cubic and deviates the TOD. The third and the fourth terms then deviate the GDD. In the following calculations, the terms that are linear or constant in $\theta(\omega)$ are neglected because they mostly introduce additional group delay or a constant phase offset respectively, and do not change the temporal profile of a pulse. The odd power terms in $\theta(\omega)$ are present only when the object has a y_0 offset as they originate from the middle term of $\eta^2 = (y_0 + s\theta(\omega))^2 = y_0^2 + 2y_0 s\theta(\omega) + (s\theta(\omega))^2$.

The linear approximation of $\theta(\omega)$ limits the accuracy of the method because it neglects the contribution of the terms of the lower powers to the given dispersion order. For example, the quadratic term of Eq.(2.28) also contributes to TOD through the nonlinear part of $\theta(\omega)$. In general, the contribution of terms derived within the linear approximation to the corresponding dispersion orders is a few orders of magnitude bigger than the contribution of these nonlinear corrections. Nevertheless, these corrections might be still required for systems with a high stretch ratio or broad bandwidth.

In general, x_0 and y_0 offsets are required for the separation of input and output beams in multi-pass stretchers. Usually, the x_0 offset is used for separation of the beams between subsequent passes while y_0 offset is required for the separation of the beams only in 4 and higher pass designs. In stretchers using only one grating and reflective optics, the x_0 offset is usually much bigger than y_0 because it also separates the beam between subsequent grating hits. In the following two sections, two possible setups will be discussed. First, we consider a situation when the object (i.e. the place where the pulse hits the grating) is on the optical axis of the stretcher telescope. This case is important for 2-pass stretchers and stretchers using cylindrical optics, where the x_0 offset does not matter because the beam is imaged only in the yz plane. Second, we consider a general situation when the pulse hits a grating at the arbitrary point (x_0, y_0), which is relevant for the majority of stretcher designs.

On-Axis object

First, let's assume that the object lies on the optical axis of the stretcher telescope ($x_0 = 0$ and $y_0 = 0$). Only spherical aberration is present because all the other coefficients from Eq. (2.28) vanish due to the cylindrical symmetry. The spectral phase deviation at the image plane φ_{on}^{ab} is then:

$$\varphi_{on}^{ab}(\omega, s_{img}) = \frac{\omega}{c}\Phi(s,\omega) = \frac{\omega}{c}Bs^4\theta^4(\omega) \doteq Bs^4\frac{m^4N^4(2\pi)^4c^3}{\omega_0^8\cos^4(\beta_0)}\omega(\omega-\omega_0)^4 \quad . \tag{2.30}$$

Because the first three derivatives with respect to frequency at the central frequency of the spectral phase defined by eq. (2.30) are zero, the spherical aberration induces FOD deviation FOD^{ab}:

$$\left.\frac{\mathrm{d}^4\varphi_{on}^{ab}}{\mathrm{d}\omega^4}\right|_{\omega_0} \doteq 24Bs^4\frac{m^4N^4(2\pi)^4c^3}{\omega_0^7\cos^4(\beta_0)} = FOD^{ab} \quad . \tag{2.31}$$

Higher order dispersion terms can be calculated when the linear approximation of $\theta(\omega)$ is not used.

Off-axis object

When the object does not lie on the optical axis, all terms from Eq. (2.28) are relevant. Combining Eq. (2.24) and Eq. (2.28), we can calculate the spectral phase deviation

φ_{off}^{ab} for any object position in the object plane as:

$$\varphi_{off}^{ab}(\omega, s_{img}) = \frac{\omega}{c}\Phi(x_0, y_0, s, \omega) = \varphi_{off}^{ab1} + \varphi_{off}^{ab2} + \varphi_{off}^{ab3} + \varphi_{off}^{ab4} + ..., \tag{2.32}$$

where the individual terms φ_{off}^{ab1}, φ_{off}^{ab2}, φ_{off}^{ab3} and φ_{off}^{ab4} originate from the terms on the right of Eq. (2.28) with preserved order.

The first term φ_{off}^{ab1} represents the on-axis term φ_{on}^{ab} from the previous section [Eq. (2.31)]. The second term φ_{off}^{ab2} varies linearly with the y_0 offset and it has an impact on TOD and higher order terms. If we substitute the linear approximation of $\theta(\omega)$ [Eq. (2.29)] into Eq. (2.32), we can derive TOD deviation TOD^{ab} at the image position:

$$\left.\frac{\mathrm{d}^3\varphi_{off}^{ab2}}{\mathrm{d}\omega^3}\right|_{\omega_0} = \frac{y_0(4B+F)s^3}{c}\frac{\mathrm{d}^3(\omega\theta^3)}{\mathrm{d}\omega^3} \doteq 6y_0(4B+F)s^3\frac{m^3N^3(2\pi)^3c^2}{\omega_0^5\cos^3(\beta_0)} = TOD^{ab} \quad . \tag{2.33}$$

The contribution of φ_{off}^{ab2} to FOD deviation FOD_{TOD}^{ab} can be obtained if we leave out the linear approximation of $\theta(\omega)$ from Eq. (2.29) and calculate the fourth derivative of φ_{off}^{ab2} with respect to frequency numerically:

$$\left.\frac{\mathrm{d}^4\varphi_{off}^{ab2}}{\mathrm{d}\omega^4}\right|_{\omega_0} = \frac{y_0(4B+F)s^3}{c}\frac{\mathrm{d}^4(\omega\theta^3)}{\mathrm{d}\omega^4} = FOD_{TOD}^{ab} \quad . \tag{2.34}$$

The last two terms φ_{off}^{ab3} and φ_{off}^{ab4} from Eq. (2.32) are quadratic in both $\theta(\omega)$ and either y_0 or x_0 and thus mainly introduce GDD deviation GDD^{ab}:

$$\left.\frac{\mathrm{d}^2(\varphi_{off}^{ab3}+\varphi_{off}^{ab4})}{\mathrm{d}\omega^2}\right|_{\omega_0} \doteq 2(y_0^2(6B+C+D+3F)+x_0^2(2B+D+F))s^2\frac{m^2N^2(2\pi)^2c}{\omega_0^3\cos^2(\beta_0)} = GDD^{ab} \quad . \tag{2.35}$$

The contribution of the φ_{off}^{ab3} and φ_{off}^{ab4} terms to TOD deviation TOD_{GDD}^{ab} cannot be calculated in the scope of the linear aproximation of $\theta(\omega)$, but it can be analytically derived with the help of the outcome of Eq. (2.35) and the known ratio between the TOD and GDD of the ideal stretcher [41]. The formula for the ratio between the GDD, TOD and FOD depends on the power of $\theta(\omega)$. φ_{off}^{ab3}, φ_{off}^{ab4} and the ideal stretcher phase (the second term of Taylor series of cosine in Eq. (2.25)) are all quadratic in $\theta(\omega)$ and thus they retain the same ratio between the GDD, TOD and FOD. Because we know the ratio between the individual dispersion orders for a perfect stretcher, we can easily calculate the induced TOD deviation from GDD^{ab}:

$$\left.\frac{\mathrm{d}^3(\varphi_{off}^{ab3}+\varphi_{off}^{ab4})}{\mathrm{d}\omega^3}\right|_{\omega_0} = -GDD^{ab}\frac{3\lambda}{2\pi c}\left(1+\frac{\lambda}{d}\frac{\sin(\alpha)}{\cos^2(\alpha)}\right) = TOD_{GDD}^{ab} \quad . \tag{2.36}$$

Table 2.5: Summary of the induced spectral deviation phase by the individual Seidel aberrations in the linear approximation.

Dispersion orders	**B** Spher.	**C** Astig.	**D** Field Cur.	**E** Dist.	**F** Coma
FOD	•				
TOD (y_0)	•				•
GDD (x_0)	•		•		•
GDD (y_0)	•	•	•		•

2.4.1 Martinez/Banks stretcher

As an example of how to apply this method, we can look into the impact of Seidel aberrations in the Martinez-type stretcher with spherical optics. The aberrations of this design are essentially the same as those of the Banks stretcher (depending on the conic constant of the optics). An imaging system of the Banks stretcher comprises a curved mirror and two plane mirrors; one located at the focal plane of the curved mirror to retro-reflect the beam; the second mirror serves to steer the focused beam from concave on the retro reflecting mirror (Fig. 2.19) without hitting the grating. In the original Banks design the grating has a stripe without grooves in the middle which serves instead of the second plane mirror. The design is all reflective to prevent chromatic aberration but it exhibits spherical aberration and therefore considerable FOD deviation. The arrangement of the imaging system allows it to reach high stretch ratios while the footprint of the stretcher remains small. Thanks to simple imaging system it is also very robust and easy to align. The Banks design has been successfully implemented in both 30 fs [77] and 150 fs [37] TW/PW CPA chains. Optically, the imaging system of the stretcher can be substituted with 2 spherical mirrors at 2f distance. Seidel aberration coefficients for such system are presented in Table 2.6. For the following calculations, it is convenient to introduce dimensionless variables which scale with the radius of curvature $R = 2f$:

$$s' = \frac{s}{R}; \qquad x_0' = \frac{x_0}{R}; \qquad y_0' = \frac{y_0}{R} \quad . \tag{2.37}$$

Table 2.6: Aberration coefficients of Martinez-type stretcher. Coefficients were derived using theory presented in [76].

Spherical	Astigmatism	Field curvature	Coma
B	C	D	F
$\frac{(R-s)^2}{2R^3s^2}$	$\frac{1}{Rs^2}$	$-\frac{1}{2Rs^2}$	$-\frac{R-s}{R^2s^2}$

On-axis

Using Eq. (2.31) and the spherical aberration coefficient from Table 2.6, the dependence of the FOD deviation on the distance of the first grating from the first lens of the

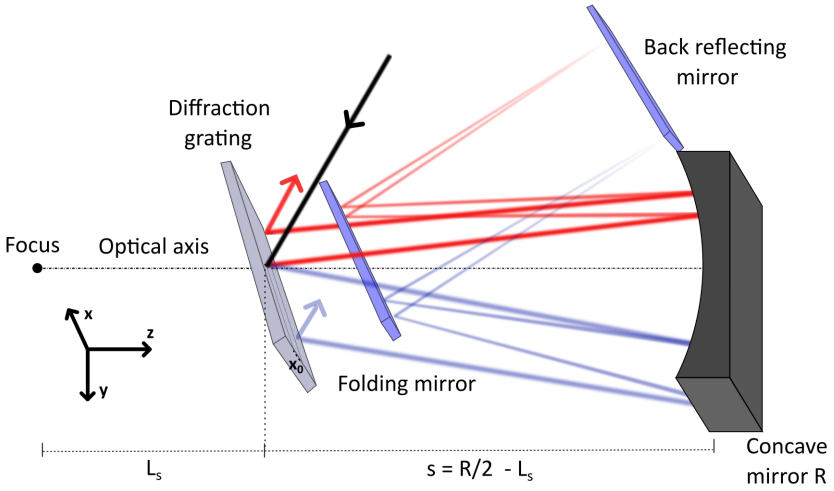

Figure 2.19: Banks stretcher scheme. A beam is incident on the diffraction grating with a vertical offset x_0 and is diffracted to the concave mirror. The mirror is curved and so it reflects the beam with a slight downward angle. The beam then strikes the smaller folding mirror centered in front of the grating. The folding mirror then reflects the beam to the back reflecting mirror located at the focal plane of the concave mirror. Reflection from the back refl+ecting mirror repeats this sequence in reverse order, only on the lower half of the optics. Finally, the beam diffracts of the grating with vertical offset $-x_0$ and is sent back for a second pass by a vertical roof. y_0 offset is introduced when it is necessary to add another 2 passes through the stretcher. As there is only single grating, one pass through the stretcher is equivalent to $L_{\text{eff}} = -2L_s$ compressor grating distance.

stretcher can be calculated:

$$FOD^{ab} = 12\frac{(R-s)^2}{R^3 s^2} s^4 \frac{m^4 N^4 (2\pi)^4 c^3}{\omega_0^7 \cos^4(\beta_0)} \sim R\left(s'^2 - 2s'^3 + s'^4\right) \quad . \tag{2.38}$$

The FOD deviation linearly increases with R and decreases as the object approaches the first lens. It reaches maximum when the object lies in the focal plane. It seems logical to put the object close to the first lens to minimize the FOD deviation. However, this can increase the residual angular dispersion $\mathrm{d}\theta_y(\lambda)$. Using Eq. (2.26) and the spherical aberration coefficient from Table 2.6, the residual angular dispersion can be expressed as:

$$\mathrm{d}\theta_y(\lambda) = \frac{\cos(\beta)}{\cos(\alpha)} \frac{1}{\theta(\lambda)} \frac{\mathrm{d}(Bs^4\theta^4(\lambda))}{\mathrm{d}s} = \frac{\cos(\beta)}{\cos(\alpha)} \left(s' - 3s'^2 + 2s'^3\right) \theta^3(\lambda) \doteq K_1 \cdot (\lambda - \lambda_0)^3 \quad , \tag{2.39}$$

where K_1 is a function of s'. Within the linear approximation of $\theta(\omega)$, the residual angular dispersion in the yz plane is cubic in $(\lambda - \lambda_0)$. Its value is given by the relative position of the grating within the stretcher s' regardless of the absolute value of R. Fig. 2.20 shows a comparison of FOD and $d\theta_y(\lambda)$ dependencies on s'. The results were verified by independent numerical ray-tracing calculations in Zemax OpticStudio.

Off-axis

When a laser pulse hits the grating at a point which is not on the optical axis of the telescope, aberrations introduce GDD and TOD deviations and increase residual angular dispersion in the xy and xz planes. By substitution of the respective aberration

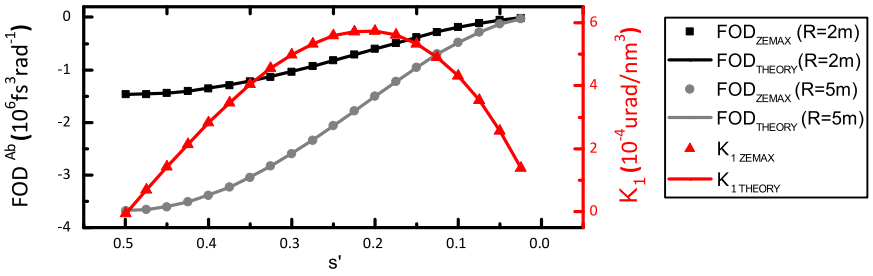

Figure 2.20: Comparison of FOD^{Ab} [Eq. (2.38)] and the residual angular dispersion [Eq. (2.39)] for different relative grating positions. Analytically calculated data are in solid lines, results obtained by numerical ray-tracing are marked with dots. The calculation was done for $N = 1480$ ln/mm, $\alpha = 48.19°$, $\lambda_0 = 0.82$ μm (parameters taken from [64]).

coefficients from Table 2.6 into Eq. (2.33), TOD deviation TOD^{ab} can be calculated as follows:

$$TOD^{ab} = 6y_0\left(4\frac{(R-s)^2}{2R^3s^2} - \frac{(R-s)}{R^2s^2}\right)\frac{m^3N^3(2\pi)^3c^2}{\omega_0^5\cos^3(\beta_0)} \sim y_0' R\left(s' - 3s'^2 + 2s'^3\right) \quad . \tag{2.40}$$

Analogously, GDD deviation GDD^{ab}_{PB} can be derived with the help of eq. (2.35) and Table 2.6 :

$$GDD^{ab} = R\left(x_0'^2(-1-2s'+2s'^2) + y_0'^2(1-6s'+6s'^2)\right)\frac{m^2N^2(2\pi)^2c}{\omega_0^3\cos^2(\beta_0)} \quad . \tag{2.41}$$

Both GDD^{ab} and TOD^{ab} linearly increase with R, their dependencies on the grating position s' are shown in Fig. 2.21. If we substitute the aberration coefficients from

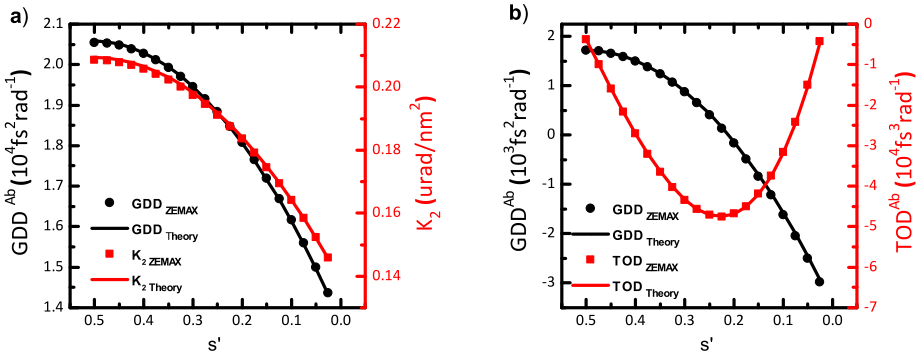

Figure 2.21: a) Comparison of GDD^{Ab} [Eq. (2.41)] and angular dispersion coefficient K_2 [Eq. (2.42)] for various grating positions with $x_0' = 1/20$. b) TOD^{Ab} [Eq. 2.40]) and GDD^{Ab} deviation (Eq. (2.41)) for various relative grating positions with $y_0' = 1/40$. The contribution of the φ^{ab3}_{off} phase term [Eq. 2.36] was included in the calculation of TOD^{Ab}. The calculation was done for $N = 1480$ ln/mm, $\alpha = 48.19°$, $\lambda_0 = 0.82$ μm (parameters taken from [64]) and $R = 2$ m. Analytically calculated data are in solid lines, results obtained by numerical ray-tracing are marked with dots.

Table 2.6 into Eq. (2.26) we can derive formulae for the residual angular dispersion:

$$\begin{aligned} \mathrm{d}\theta_x(\lambda) &= \frac{x_0'}{2}(1+2s'-2s'^2)\theta^2(\lambda) \doteq K_2\cdot(\lambda-\lambda_0)^2 \\ \mathrm{d}\theta_y(\lambda) &= \frac{\cos(\beta)}{\cos(\alpha)}((s'-3s'^2+2s'^3)\theta^3(\lambda)+y_0'(1-6s'+6s'^2)\theta^2(\lambda)+ \\ &+(3y_0'^2(2s'-1)+x_0'^2(2s'-1))\theta(\lambda)) \doteq \\ &\doteq K_1\cdot(\lambda-\lambda_0)^3+K_3\cdot(\lambda-\lambda_0)^2+(K_4+K_5)\cdot(\lambda-\lambda_0), \end{aligned} \tag{2.42}$$

where K_2, K_3, K_4 and K_5 are functions of s', x_0' and y_0'. The residual angular dispersion in the xz-plane is quadratic in (λ - λ_0) and it linearly increases as we put the object further from the optical axis. The angular dispersion in the yz plane constitutes three terms. The first term K_1, which is cubic in $(\lambda-\lambda_0)$, originates from the on-axis spherical aberration [Eq. ((2.39)]. The second term K_3 linearly increases with the object distance from the optical axis in the diffraction plane and is quadratic in $(\lambda-\lambda_0)$. The third and the fourth terms are quadratic in y_0 or x_0 respectively, while they are linear in $(\lambda-\lambda_0)$. Total angular dispersion in the yz plane is then given by the interplay of these terms. The dependencies of K_2, K_3 and K_4 on s' and the angular deviation of individual spectral components are shown in Fig. 2.22(a) and Fig. 2.22(b) respectively. For example, when a grating lies in the focal plane of the first lens, only the K_3 term is present which results in quadratic residual angular dispersion in the yz-plane. If we place the grating close to $s' = R/4$ in the given configuration then we can minimize residual angular dispersion because the individual terms from Eq.(2.42) almost cancel each other out.

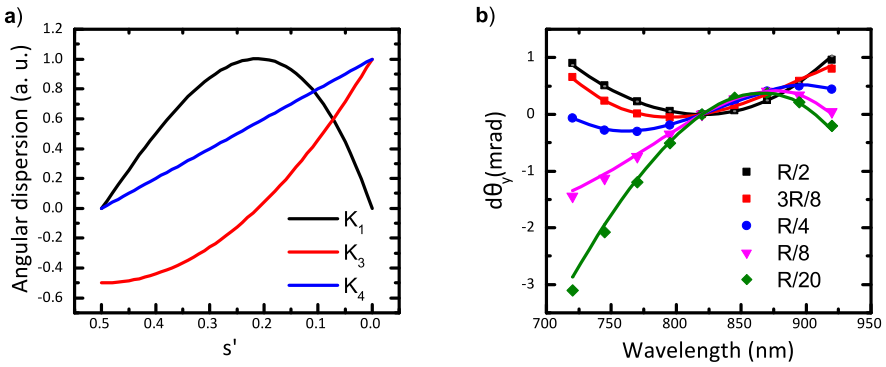

Figure 2.22: a) Comparison of normalized K_1, K_3 and K_4 dependencies on grating position s', their relative scaling depends mostly on y_0' and $\theta(\omega)$. b) Angular dispersion $\mathrm{d}\theta_x(\lambda)$ in the yz-plane for different s'. In this example, $\theta(\omega)$ was obtained directly from the grating equation without linear approximation [Eq. (2.26)] due to broad bandwidth. Analytically calculated data are in solid lines, results obtained by numerical ray-tracing are marked with dots. The calculation was done for $y_0' = 1/20$, $N = 1480$ ln/mm, $\alpha = 48.19°$, $\lambda_0 = 0.82$ μm and $R = 2$ m.

GDD, TOD and FOD deviations in a Martinez stretcher depend on the position of the first grating s' and linearly scale with R, while the residual angular dispersion depends on s' only. Spectral phase deviation tends to decrease if the grating is very close to the first lens which allows it to reach very high stretch ratios. Nevertheless, the deviation which depends on y_0' increase. As the x_0' offset is usually much bigger than y_0' offset (which can even be zero for the 2-pass design), the impact of the y_0' offset is for much smaller then the impact of the x_0' offset most cases. It is also interesting to

note that when the grating is placed into the focal plane of the concave mirror (hence the stretcher has zero stretch ratio), the Banks design induces biggest FOD deviation.

According to our calculations, there is no ideal grating position in the Martinez stretcher. However, with given space and spectral phase requirements Eqs. (2.38) - (2.42) may be used to find the ideal combination of R, s' and $\theta(\omega)$ to reach the ideal spectral phase profile with minimal angular dispersion. The calculation in the previous sections was done for a perfectly aligned stretcher, but it is possible to extend it to cases when there is some kind of misalignment present in the stretcher telescope.

2.4.2 Offner stretcher

Parts of the following text were published in [A2].
Offner stretcher is commonly employed in laser systems with pulse durations $\lesssim 20$ fs as its aberration-free nature make it suitable for systems with broad bandwidth [78, 79]. Compared to the Banks/Martinez stretcher, the Offner stretcher exhibits zero stretch ratio when the diffraction gratings are located in the center of curvature of the concave mirror. If the first grating is located at that point, the design is aberration-free in terms of Seidel aberrations and therefore it induces no spectral phase deviation in this approximation. Its stretch ratio is then increased by shifting the second grating towards the concave mirror. However, in some systems it is beneficial to introduce some spherical aberration to enable compensation of residual FOD originating from the material dispersion. In that case, the first grating has to be shifted as well and therefore it is more advantageous to convert the design into a single grating Offner stretcher (Fig. 2.23).

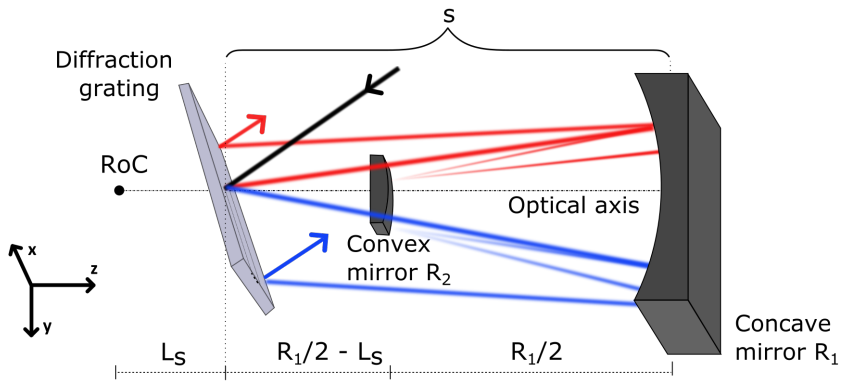

Figure 2.23: Schematic of a single grating Offner stretcher. A beam is incident on the diffraction grating with vertical offset x_0 and it is diffracted to the concave mirror with radius of curvature R_1. The concave mirror then reflects the beam downwards and focuses it on the convex mirror with radius of curvature R_2 and the sequence is repeated in reverse order on the lower half of the optics. Finally, the beam with spatial chirp leaves the grating with vertical offset $-x_0$ and is sent back for the second pass by a vertical roof mirror.

In the original Offner triplet design, the radii of curvature of the convex mirror R_2 has to be set to precisely $-R_1/2$ in order to compensate residual field curvature and astigmatism. However, if the first grating is shifted from the curvature center, the design is no longer aberration free and therefore it can be beneficial to adjust R_2 as well. This adds another degree of freedom which can improve the performance of the stretcher. The detuning of R_2 shifts the position of the image of the grating s_{img}, the effective distance L_{eff} equivalent to the negative compressor grating distance can be

Table 2.7: Aberration coefficients of an Offner triplet calculated according to the aberration theory presented in [76], where B is a coefficient of spherical aberration, C of astigmatism, D of field curvature and F of coma.

Ab.	$(\boldsymbol{R_1 = -2R_2})$
B	$\frac{(R_1-s)^4}{2R_1^3 s^4}$
C	$2\frac{(R_1-s)^2}{R_1 s^4}$
D	$\frac{(R_1-s)^2}{R_1 s^4}$
F	$-2\frac{(R_1-s)^3}{R_1^2 s^4}$
Ab.	$(\boldsymbol{R_1 \neq -2R_2})$
B	$\frac{R_1^8-3R_1^7R_2+8R_1^6R_2s+4R_1^5R_2^3-16R_1^5R_2^2s+24R_1^4R_2^2s^2-32R_1^3R_2^3s^2+32R_1^2R_2^4s^2+32R_1^2R_2^3s^3-64R_1R_2^4s^3+32R_2^4s^4}{8R_1^3R_2^4s^4}$
C	$\frac{R_1^6-3R_1^5R_2+4R_1^4R_2s+4R_1^3R_2^3-8R_1^3R_2^2s+4R_1^2R_2^2s^2+16R_2^4s^2}{16R_1R_2^4s^4}$
D	$-\frac{-R_1^6+3R_1^5R_2-4R_1^4R_2s-4R_1^3R_2^3+8R_1^3R_2^2s-4R_1^2R_2^2s^2+16R_1R_2^3s^2+16R_2^4s^2}{32R_1R_2^4s^4}$
F	$-\frac{R_1^7-3R_1^6R_2+6R_1^5R_2s+4R_1^4R_2^3-12R_1^4R_2^2s+12R_1^3R_2^2s^2-16R_1^2R_2^3s^2+16R_1R_2^4s^2+8R_1R_2^3s^3-16R_2^4s^3}{16R_1^2R_2^4s^4}$

then calculated as:

$$L_{\text{eff}} = s_{img} - s_2 = R_1 - \frac{R_1^2}{2R_2} - s - s_2, \tag{2.43}$$

where s_2 is the position of the second grating and $s = s_2$ for a single-grating Offner stretcher. Basically, as R_2 approaches ∞, the design is transformed from Offner to Banks. The individual Seidel aberration coefficients of the Offner triplet necessary for the evaluation of the general formulae from previous section are presented in Table 2.7. The coefficients for the Offner triplet with detuned R_2 are rather complicated and they are better understood graphically. By substitution of the corresponding aberration coefficients from Table 2.7 into Eqs. (2.31) and (2.35), we plot GDD^{ab} and FOD^{ab} profiles as functions of s and R_2 in Figure 2.24. With $R_2 = -R_1/2$ the results meet expectations as the aberrations are zero at the center of curvature of the concave mirror ($s = R_1$) and grow as s shifts away. Also, the decrease of the curvature of the convex mirror leads to the decrease of FOD^{ab} and vice versa. Changes in R_2 produce offsets in the GDD^{ab} curves. The dependence of the FOD^{ab}, TOD^{ab} and GDD^{ab} on the grating position can be easily analytically expressed for the original Offner triplet design using the second column from Table 2.7:

$$FOD^{ab} \overset{(R_1=-2R_2)}{=} \frac{(R_1-s)^4}{2R_1^3}\frac{m^4N^4(2\pi)^4c^3}{\omega_0^7\cos^4(\beta_0)} \sim R_1(1-s')^4 \tag{2.44}$$

$$TOD^{ab} \overset{(R_1=-2R_2)}{=} -y_0\frac{2(R_1-s)^3}{R_1^3}\frac{m^3N^3(2\pi)^3c^2}{\omega_0^5\cos^3(\beta_0)} \sim -R_1y_0'(1-s')^3 \tag{2.45}$$

$$\begin{aligned} GDD^{ab} \overset{(R_1=-2R_2)}{=} & \left(x_0^2\frac{(R_1-s)^2}{R_1^3} + 3y_0^2\frac{(R_1-s)^2}{R_1^3}\right)\frac{m^2N^2(2\pi)^2c}{\omega_0^3\cos^2(\beta_0)} \\ & \sim R_1\left(x_0'^2(1-s')^2 + 3y_0'^2(1-s')^2\right) \end{aligned} \tag{2.46}$$

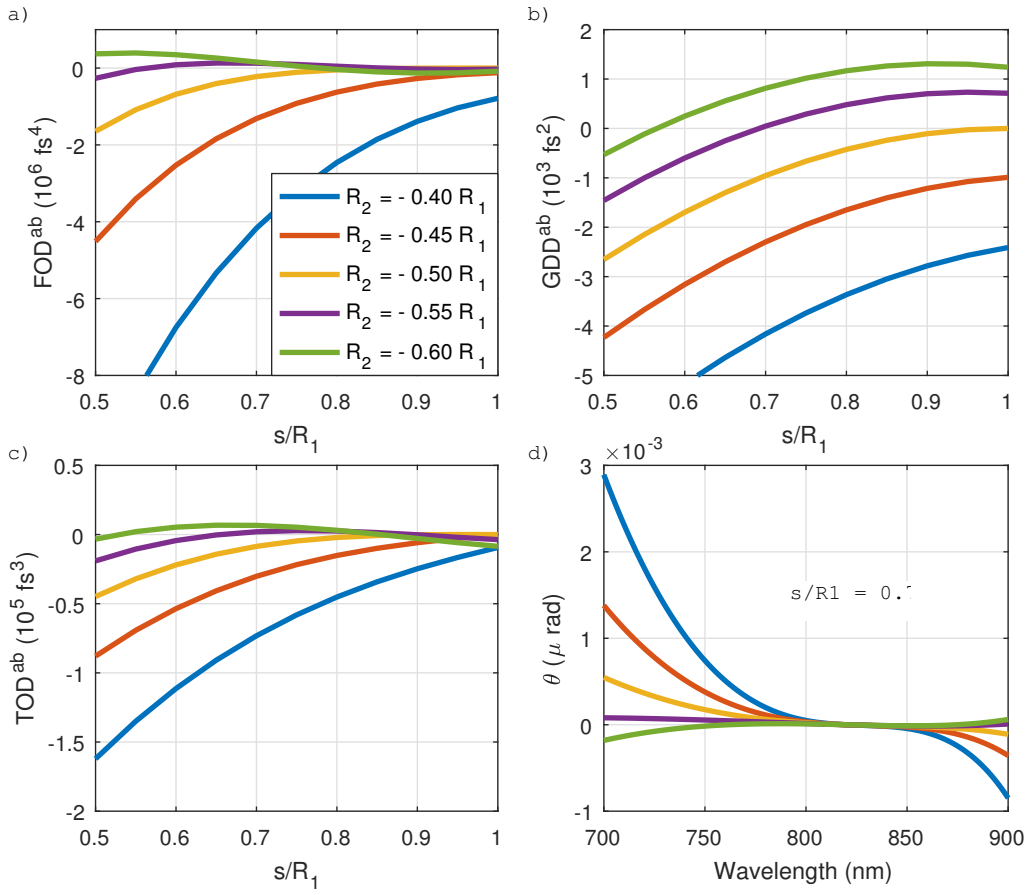

Figure 2.24: Dependence of FOD^{ab} (a), GDD^{ab} (b) and TOD^{ab} (c) deviation on the grating position s and the residual angular dispersion in diffraction plane at $s' = 0.7$ (d) for 1-grating Offner stretcher with various R_2 and $R_1 = 1.5$ m, $x_0 = 0.05$ m and $y_0 = 0.02$ m.

For the calculation of the residual angular dispersion of a system with broad bandwidth, it is necessary to abandon the linear approximation. Because there is no derivative with respect to the frequency in Eq. (2.26), the calculation is quite straightforward with $R_2 = -R_1/2$. The residual angular dispersion in the xz plane $\mathrm{d}\theta_x(\lambda)$ and yz plane $\mathrm{d}\theta_y(\lambda)$ can be obtained using aberration coefficients from Table 2.7:

$$\begin{aligned} \mathrm{d}\theta_y(\lambda) &= -2\frac{\cos(\beta_0)}{\cos(\alpha)}\left((x_0'^2 + 3y_0'^2)(1-s')\theta(\lambda) + 3y_0'(1-s')^2\theta^2(\lambda) + (1-s')^3\theta^3(\lambda)\right), \\ \mathrm{d}\theta_x(\lambda) &\overset{(R_1=-2R_2)}{=} 2x_0'(R_1 - s')^2\theta^2(\lambda), \end{aligned} \tag{2.47}$$

where α is the angle of incidence and $\theta(\lambda)$ is the angular deviation of the wavelength component with respect to the central wavelength of the pulse. The formulae for angular dispersion with arbitrary R_2 can be calculated in the same manner using coefficients from Table 2.7, but we omit them here for the sake of clarity as they are very long and do not offer much physical insight.

From Fig. (2.24a) it is evident that the aberrations which occur when the grating shifted towards the concave mirror are partly compensated by increasing the absolute value of R_2. When $s' \approx 0.7$ and $R_2 \approx -0.55\ R_1$, all GDD^{ab}, TOD^{ab} and FOD^{ab} are close to zero and the design is being almost aberration free. The residual angular dispersion vanishes at that point too. Consequently, for each grating position s there

is some R_2 for which the aberrations are minimized and where the design is close to the ideal stretcher (see Fig. 2.25). Moreover, if there is some residual FOD in the system, the combination of the grating position and R_2 can be adjusted to compensate it. Compared to the original two grating Offner stretcher, the single grating Offner stretcher offers two times higher stretch ratio while its footprint remains smaller as the grating is not located at the center of curvature of the concave mirror. This is mainly advantageous for systems with narrower bandwidth requiring high stretch ratios. The stretcher remains compact so it can be placed into a vacuum chamber to prevent spectral phase noise induced by air turbulence and to enhance its stability.

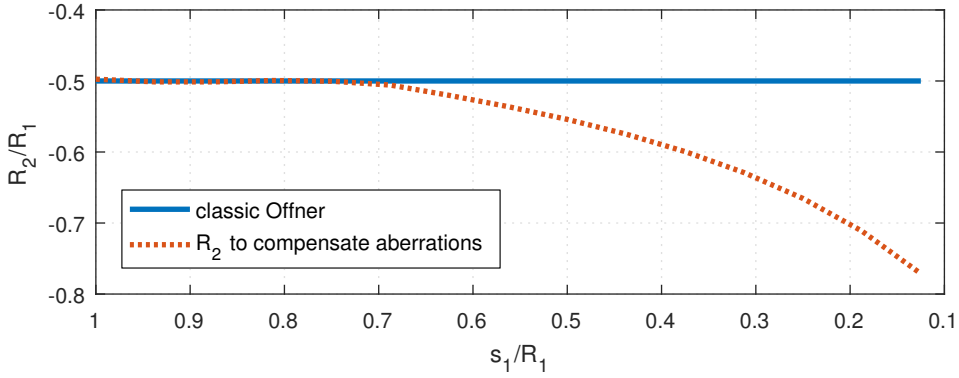

Figure 2.25: Dependence of R_2 on s_1 for a classic Offner stretcher versus for a single grating Offner stretcher with R_2 adjusted to compensate spherical aberration calculated according to Eq. 2.44 with coefficient from Table 2.7.

2.4.3 Discussion

In general, the accuracy of the analytical method can be considered to be equivalent to ray-tracing when there is a very small ($y_0' \lesssim 1/100$) offset and it is bounded to the accuracy of the linear approximation of $\theta(\omega)$. The most severe limitation of the accuracy originates in the terms with odd powers of $\theta(\omega)$ in Eq. (2.28). These terms occur only with the y_0' offset and they introduce errors in the calculation of higher dispersion orders within the linear approximation. For example, the neglected term that is linear in $\theta(\omega)$ mainly introduces group delay deviation but its higher derivatives, which are zero under the linear approximation, also partly contribute to GDD and higher order dispersion terms. However, the linear approximation does not restrict the usage of this method with respect to the bandwidth of the system as the individual dispersion terms are defined as local derivatives at the central wavelength of the pulse. For a precise calculation of the angular dispersion of a pulse with broad bandwidth (>30 nm), it is necessary to abandon the linear approximation and use the general grating equation. Nevertheless, this calculation is very straightforward as $\theta(\omega)$ can be calculated directly from the grating equation.

Residual angular dispersion can be suppressed in multi-pass setups by employing roof mirrors in the design. Roof mirrors flip the beam over either xz or yz plane which reverses the sign of the angular dispersion. Unfortunately, total compensation is not possible because of the fact that roof mirrors also change either the x_0' or the y_0' coordinate for the next pass, which according to Eq. (2.39) leads to uneven absolute values of residual angular dispersion between subsequent passes.

The method gives accurate results even for a full round trip and multi-pass setups. However, it should be noted that the residual angular dispersion acquired after each pass may lead to errors in the calculation of the spectral phase for the next pass as $\theta(\omega)$

is slightly different. These errors especially increase with y'_0 offset as it induces changes in the angular dispersion in the diffraction plane. They mainly distort the FOD and higher dispersion orders but they strongly depend on the profile of the residual angular dispersion and their impact is thus hard to generalize.

The deviation of the spectral phase dispersion terms obtained by this method coincided with a numerical ray-tracing algorithm with deviation less than 0.1% for "on-axis" and x'_0 "off-axis" terms and less than 5% for y'_0 "off-axis" terms. If the accuracy is not sufficient, it is possible to either expand $\theta(\omega)$ into the next Taylor term or use this method numerically and directly calculate the spectral phase from Eq. (2.28). Also, it might be necessary to consider higher order aberrations.

2.5 Dispersion management

To ensure that the compressed pulse retains transform limited profile and thus maximal intensity, the sum of the induced spectral phase changes at each CPA stage must be equal to zero (excluding group delay and constant phase offset):

$$\varphi_{stretcher}(\omega) + \varphi_{material}(\omega) + \varphi_{compressor}(\omega) = 0. \tag{2.48}$$

Usually, it is convenient to expand the spectral phase of each term from Eq. (2.48) into the individual dispersion orders using Taylor expansion from Eq. (1.12) and discuss them separately. Dispersion properties of the commonly employed components are compared in Table 2.8. Since dispersion of diffraction gratings is much higher than any of other components, a grating stretcher has to be used with a grating compressor in most cases. Other components are then usually employed to correct remaining spectral phase originating either from material dispersion or stretcher aberrations. Depending on the transform-limited pulse duration, dispersion orders up to the fifth order have to be precisely controlled. Which particular components are employed then depends on the number of degrees of freedom the system has. For the following discussion, it is assumed that the spectral phase induced by the material is much smaller than the spectral phase induced by the compressor. That is generally true for all high-power laser systems using a grating compressor.

When material is added into the CPA chain with an ideal stretcher and a compressor, the residual GDD and TOD is positive (Table 2.9). It can be then compensated by decreasing the stretcher grating spacing L and the angle of incidence α to tune GDD and to increase the GDD/TOD ratio of the stretcher. Since the material dispersion is small, the stretcher remains close to the nominal configuration. Through this adjustment the residual FOD is increased as the adjustment of the incident angle also increases the FOD/GDD ratio of the stretcher with respect to the compressor. The residual positive FOD originating from the mismatched stretcher compressor pair is usually much higher then the negative FOD of the material itself. Therefore, material dispersion mainly increases the residual FOD of the ideal CPA chain. Another degree of freedom is therefore necessary for its compensation.

According to the previous chapter, the spherical aberration in the stretcher imaging induces the FOD deviation with respect to the ideal case. Since the distance of the grating from the zero stretch point depends on two variables - R and s, the imaging system can be designed to have such spherical aberration so that the residual FOD is compensated. The dependency of the FOD profile on the position of the first grating within the Offner and Banks stretcher designs is compared in Fig. 2.26. The Banks

Table 2.8: Comparison of dispersion properties of different components. The sign of the spectral phase of components that induce angular dispersion can be reversed when they are used in stretcher-like configuration.

Type	**GDD**	**TOD**	**FOD**	**Typical $\Delta\tau$**
A-O modulator	+/-	+/-	+/-	1 ps
Bulk material	+	+	-	1-100 ps
Chirped mirrors	+/-	+/-	+/-	1 ps
Gratings	-	+	-	10-1000 ps
Grism	-	-	-	10 ps
Prism	-	-	-	1 ps

Table 2.9: Compensation of the material-induced spectral phase (mat) for a CPA system with a grating stretcher (s) and a grating compressor (c).

Setup	**Adjusted**	GDD	TOD	FOD
s+c	-	0	0	0
s+c+mat	-	+	+	-
s+c+mat	L	0	+	-
s+c+mat	L, α	0	0	+
s+c+mat	L, α, N | R	0	0	0

stretcher offers larger FOD deviation for small stretch ratios and it is therefore suitable for systems having large material dispersion such as systems with regenerative amplifiers. The FOD deviation induced by the Offner stretcher is smaller and it can be tuned to zero for an arbitrary grating position through the adjustment of the radius of the curvature of the convex mirror. The Offner stretcher design is more useful for systems demanding high stretch ratio and having relatively small material dispersion.

Another option is to decrease the line density of the stretcher gratings with respect to the compressor [80]. Gratings with lower line densities have small angular dispersion and according to Eq. (2.4) also smaller GDD/TOD and GDD/FOD ratios. The residual GDD, TOD and FOD can be therefore compensated through the optimization of L, α and N. When any of the above-discussed methods is not possible like for example for already operating systems, it also possible to implement a Dazzler for the active dispersion control or a grism pair compressor for the passive control of residual FOD [78].

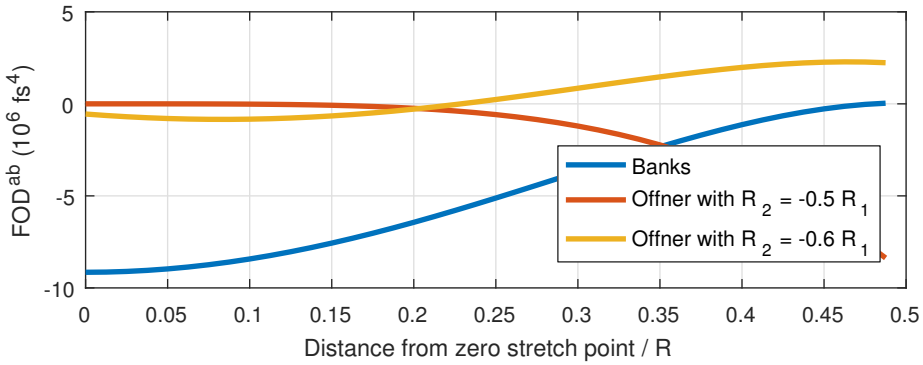

Figure 2.26: FOD as a function of s for the Banks stretcher, Offner stretcher with $R_2 = -R_1/2$ and the Offner stretcher with $R_2 = -0.6R_1$. The FOD curves were caculated according to Eqs. (2.38, 2.44).

3. ELI

Extreme light infrastructure (ELI) is an European project which aims to improve current state-of-the-art ultrashort high-power laser systems and is dedicated to fundamental study of laser matter interaction in ultrarelativistic regime (I¿10^{24} W/cm^2). Currently, ELI constitutes of 3 pillars. ELI-ALPS in Szeged, Romania focuses on the generation of attosecond pulses which could help to understand electron dynamics in atoms, molecules, plasmas and solids. ELI-NP located in Magurele, Romania is designed to further interrogate the structure of atomic nucleus and its dynamics. The ELI-Beamlines facility is in Dolní Břežany, Czech Republic and was opened for the first experiments in 2018. Altogether, 4 state-of-the-art laser systems (L1-L4) are currently being developed; each suited for specific experiments in dedicated experimental halls (E1-E6). The primary mission is generation of new secondary sources of radiation such as gamma, proton, heavy ion beams. The architecture of ELI-Beamlines allows to combine any of these sources into one target and to achieve unprecedented pump and probe experiments [A3]. A schematic of the ELI-beamlines facility is sketched in Fig. 3.1.

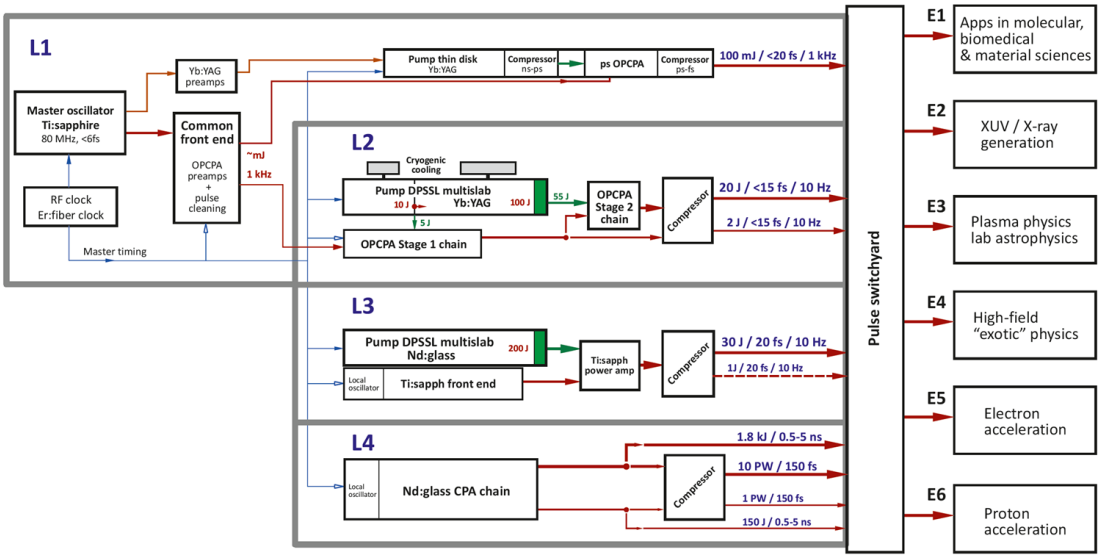

Figure 3.1: Schematic of ELI-Beamlines facility

The L1 laser system is fully based on the OPCPA technique [81]. Its pump lasers are amplified in Yb:YAG thin disk regenerative amplifiers. The 5 TW peak power, high repetition rate 1kHz and pulse duration shorter than 20 fs make it an excellent tool for the generation of secondary UV to soft X-ray radiation which will be used for the characterization of biomedical samples. The L2 system will be also based on the OPCPA technique. The pump lasers will be amplified using cryogenically cooled Yb:YAG multi-slab amplifiers developed by Rutherford Appleton Laboratory. The final output parameters are yet to be decided. The L3 laser system (also called HAPLS) is amplified in Ti:Sapphire crystals [79]. The majority of energy is extracted from two helium cooled multi-pass power amplifiers pumped by the second harmonic of diode-pumped Nd:glass pump laser. Each amplifier is pumped by high power laser diode arrays, each providing an 800-kW peak power and currently being the highest peak-power pulsed laser diode arrays in the world. 1 PW peak power with 10 Hz repetition rate make the L3 system an ideal tool for the broad range of experiments such as particle acceleration.

The L4 10 PW laser system is based on a hybrid OPCPA and mixed Nd:glass amplification techniques and was designed to deliver <150 fs pulses with 1500 J energy with the central wavelength of 1060 nm at 1 shot per minute [A8]. High pulse energy combined with focused intensity reaching 10^{24-25} W/cm^2 will enable new types of experiments for particle acceleration and exotic physics. The layout of the L4 laser is summarized in Fig. 3.2. The L4 system is developed by a consortium of National energetics and Ekspla, which provides pump lasers for the ns-OPCPA section and a flashlamp system for the main power amplifiers. The ELI-Beamlines participates in the design and implementation of the stretcher, the ns-OPCPA, the relay imaging system between the second power amplifier and the compressor, the compressor and temporal diagnostics.

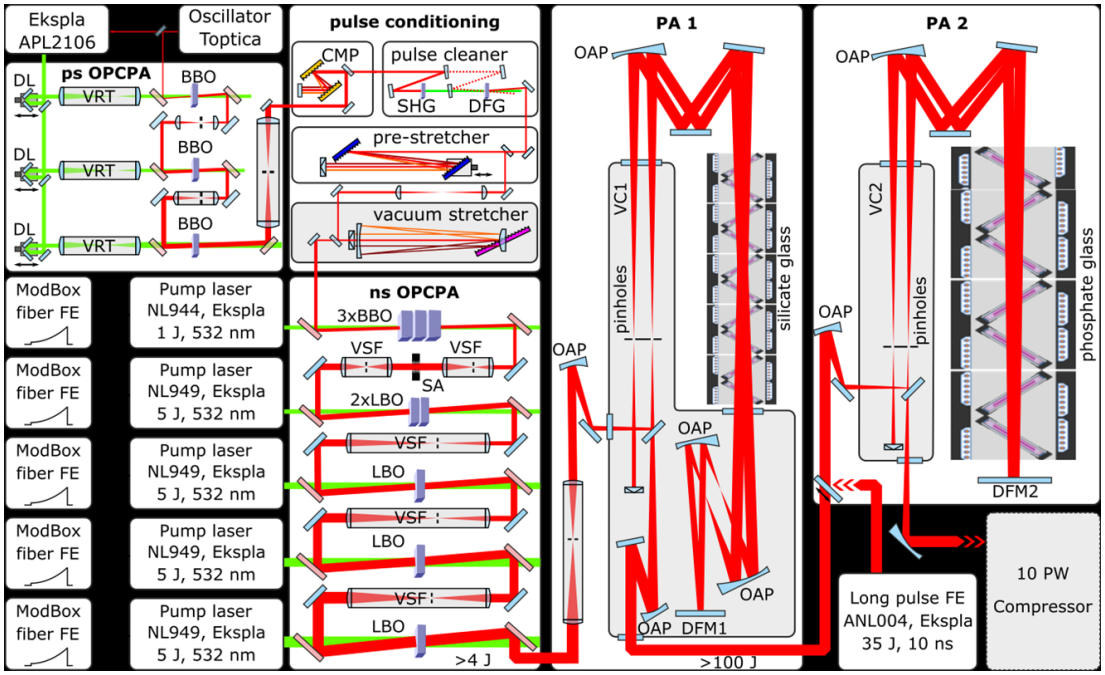

Figure 3.2: Layout of the L4 laser system.

L4

The design of the L4 system is mostly based on the Texas Petawatt Laser [37, 82]. The laser chain starts with a femtosecond mode-locked oscillator synchronized to the ELI-Beamlines master clock. A pulse from the oscillator is amplified in the 3-stage picosecond OPCPA section to 30 mJ and compressed to 100 fs in a small compressor (CMP). At this stage, the pulse has enough energy to undergo nonlinear pulse cleaning, which improves its temporal contrast by several orders of magnitude [83]. The pulse is then pre-stretched to picosecond duration by another grating compressor and it is transferred to a nanosecond grating pulse stretcher operating under vacuum. The design of the stretcher is discussed in the sixth chapter of this thesis. After the stretcher, the pulse retains only around 150 μJ energy and has roughly 8 ns duration with 40 nm spectral bandwidth. Subsequently, the pulse is amplified in 5 stage ns-OPCPA pumped by Nd:YAG lasers to 4 J (Figure 3.3). Spectral gain of the OPCPA stages is designed to pre-compensate spectral narrowing induced by the power amplifiers. This is accomplished by arbitrary shaping the temporal envelopes of the pump lasers [84]. The supergaussian square profile of the seed is generated using serrated aperture and

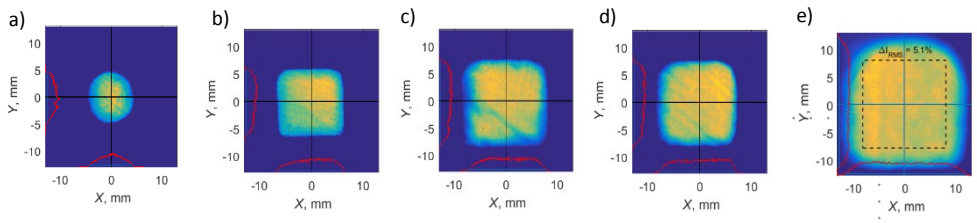

Figure 3.3: Output nearfield profile of the amplified beam of the system at each OPCPA stage [84].

further enhanced through the amplification process.

After the ns-OPCPA section, the pulse enters power amplifiers, where a combination of silicate and phosphate neodymium doped glass is employed to broaden the gain bandwidth. Both power amplifiers are 4-pass designs using liquid-cooled glass slab modules in a split-disc configuration and are pumped by flashlamps. The silicate glass has a generally lower damage threshold due to the presence of platinum inclusions compared to the platinum-free phosphate glass. So the first power amplifier mostly uses silicate slabs, while the second amplifier phosphate ones. The beam size is increased to 16 cm in the first amplifier and to 26 cm in the second amplifier to limit fluence. The beam is relay imaged during each pass using a parabolic mirror telescope from the center of the amplifier to a deformable mirror, which is used to correct residual wavefront aberrations. Spatial uniformity of the beam is further enhanced by far-field filtering through vacuum ceramic pinholes during each pass. In total, the pulse is amplified to 120 J by the first power amplifier and up to 2 kJ by the second amplifier.

The amplified pulse is then transported by a compressor imaging system (CIS) to a compressor floor. The CIS system consists of two keplerian telescopes using three off-axis parabolas, one spherical mirror and plane mirrors. The residual aberrations originating from the spherical mirror are corrected by an additional deformable mirror. To decrease the fluence on the compressor gratings, the square beam profile is expanded from 25 cm to 62.5 cm width. The CIS system relay images the deformable mirror of the PA2 onto the fourth compressor grating to avoid the spatial intensity modulations originating from the supergaussian profile of the beam. The compressor uses 1136 ln/mm gratings in the off-plane configuration. The aperture of the second and third grating is extended by phasing them with a perpendicularly positioned mirror. The detailed design and analysis of the compressor is discussed in the following chapter.

The L4 laser system is also able to operate in a different regime, where the power amplifier 2 is bypassed for the femtosecond beam. The femtosecond laser chain then

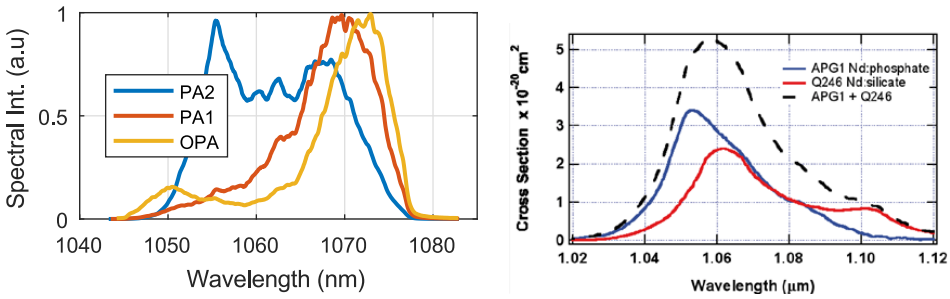

Figure 3.4: a) Simulated spectrum at the output of the OPA and power amplifiers [84] using the measured gain profiles of Nd:glasses b) Gain profile of phosphate and silicate Nd:glass

provides roughly 100 J PW-class 150 fs pulse using power amplifier 1 only. The power amplifier 2 is then seeded with a separate front end (called Long pulse front end) allowing variable temporal shaping in the ns-scale. The output $\sim$ 2 kJ amplified ns pulse can be then possibly combined with the compressed 1 PW beam for pump and probe experiments.

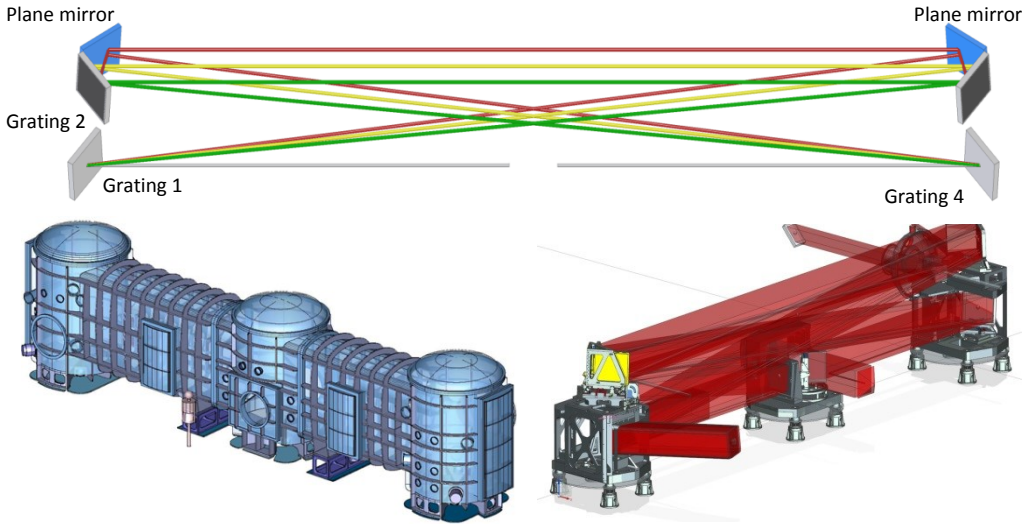

Figure 3.5: Optical layout and a visualisation of the compressor chamber

4. Compressor design

For the state-of-the-art laser systems with the highest peak powers, the design of the compressor is driven by the availability of diffraction gratings with sufficient aperture and laser induced damage threshold for the given beam-line parameters. The power amplification stages of the L4 system require at least 3 ns stretched pulse duration to avoid optical damage and to suppress the accumulation of nonlinear phase. Given 13 FWHM bandwidth of the Gaussian spectrum, the compression ratio has to be roughly 210 ps/nm. Due to the high energy of the pulse and large stretch ratio, the only viable way of the compression is to use diffraction gratings, preferably the multilayer dielectric (MLD) ones as they offer higher laser induced damage threshold (LIDT) and overall diffraction efficiency. At the time, only two grating designs were able to fulfill the high LIDT requirements - low line density 1136 ln/mm gratings or 1740 ln/mm gratings frequently used in similar laser systems. These two designs have to be used in completely different compressor configurations since the 1136 ln/mm gratings exhibit the best diffraction efficiency near Littrow angle of incidence, while the 1740 ln/mm gratings operate at 74° angle of incidence. Moreover, the 1136 ln/mm gratings have lower dispersion which results in much longer grating distance. The basic parameters of both compressor setups are summarized in Table 4.1 and will be discussed in more detail further in this chapter.

Table 4.1: Basic parameters of both pulse compressor designs. N is the groove density of diffraction gratings, λ_0 is the central wavelength of the pulse, L is the grating distance along the central wavelength, α is the angle of incidence, β_0 is the diffraction angle for the central wavelength, γ is the off-plane angle, w_x is the half-width of the spatial profile of the beam and dim describes approximate dimensions of the compressor.

N (ln/mm)	λ_0 (nm)	L (m)	α	β_0	γ	w_x (cm)	dim (m)
1136	1060	15.1	37°	37°	3.25°	30	18x3x4
1740	1060	2.25	74°	62°	0	20	12x3x3

For the safe operation of both compressor designs, it is desirable to limit the fluence of an ideal beam at the 4th grating below 400 mJ/cm^2 beam normal to avoid the risk of laser induced damage. Figure 4.1 shows the dependence of the fluence on the grating surface on the beam size. The beam size was set to minimize the fluence taking into account the fact, that the size of available diffraction gratings was restrained to approximately 1 m in diameter. For the 1136 system, the ideal beam size is 60 cm as it

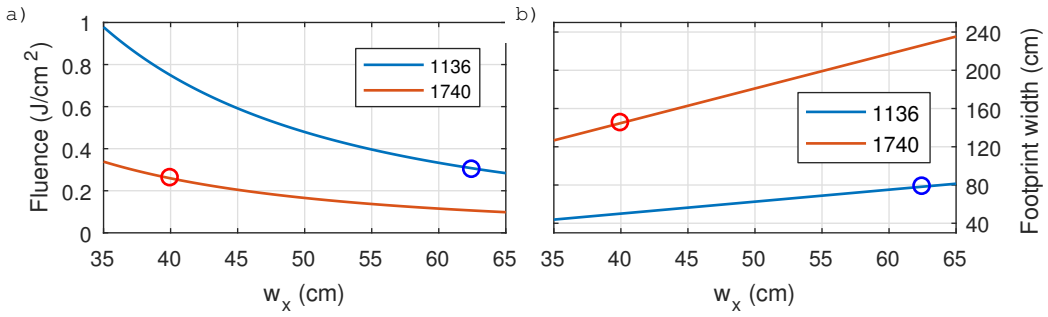

Figure 4.1: The fluence of the ideal pulse having top-hat spatial profile recalculated to the grating normal a) and the width of the beam on the grating for both grating designs. The operational position is marked with a circle.

fills the aperture of the 80x60 cm grating tilted at 37° having 1 m diameter. For 1740 system, due to the large angle of incidence, the beam footprint on the fourth grating must be bigger than 1 m to constrain the fluence. However, monolithic gratings with such dimensions were not commercially available. Hence, the configuration requires either alignment of two gratings side by side or the alignment of one grating with a perpendicularly positioned mirror to double the effective aperture. Nevertheless, the aperture of the second and third grating, where the individual frequencies are spatially separated, has to be doubled for both designs to avoid clipping of the dispersed spectra.

Tolerance budget

The aim of the tolerance analysis is to estimate the impact of each degree of freedom in the system on the focused intensity of the laser pulse. No wavefront or spectral phase compensation is possible after the compressor due to the high peak intensity of the compressed pulse. Residual spectral phase can be to some extent pre-compensated by the precompressor, strecher or Dazzler without any significant issues. Contrarily, the wavefront pre-compensation has to be very carefully applied since wavefront distortion at the compressor input could possibly introduce some spatiotemporal couplings or yield unwanted spatial modulation on the fourth grating. In general, the outcome of the tolerance analysis and the preliminary alignment procedure determines the opto-mechanical design of the grating mounts in the compressor - mostly their range, resolution and stability.

The simulation assumed either Gaussian or super-Gaussian spectrum of the fourth order having transformed limited pulse duration of 130 fs. The spatial profile was chosen to match the grating aperture. For both compressor configurations the super-Gaussian profile of the twentieth order was used to model spatial intensity with $w_x = 20$ cm for 1740 ln/mm and $w_x = 30$ cm for the 1136 ln/mm design. For the pulse with no spatio-temporal couplings, total Strehl ratio can calculated as the product of two terms. First, a spatial Strehl ratio can calculated as the ratio between the maximum of the spatial intensity of the real wavefront and the ideal wavefronts in the $k - \omega$ domain. Second, a temporal Strehl ratio is the ratio between the real and the transform limited temporal profile in the $k - t$ domain.

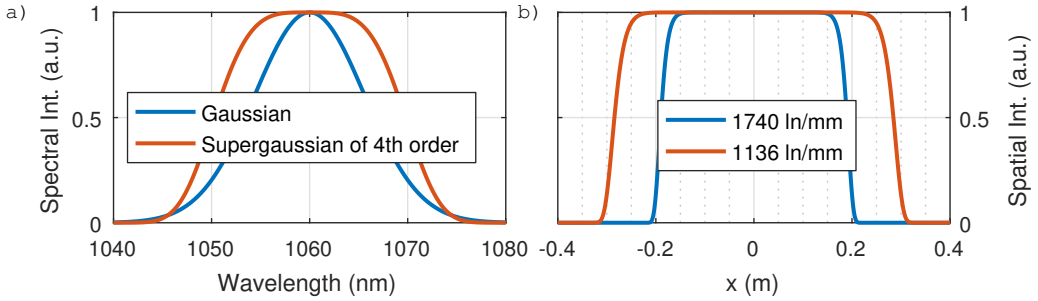

Figure 4.2: (a) The comparison of Gaussian and Supergaussian spectral profiles having transform limited pulse duration 130 fs; (b) Spatial intensity profiles for 1740 ln/mm and 1136 ln/mm designs.

Spectral Strehl ratio $S_\omega > 0.8$

The Strehl ratio in the spectral domain is mainly driven by the wavefront deviation induced by the misaligned gratings and mirrors within the grating assemblies (GA). However, it can be also degraded by the residual angular dispersion induced by the

non-parallel grating pairs. The wavefront error induced by the wavefront quality of the gratings was neglected at this stage. The simulation assumed perfect plane wavefront at the input of the compressor. Possibly, the wavefront error at the compressor output could be partly pre-compensated by the deformable mirror in CIS. However, it could increase the possibility of introducing spatial intensity modulations into the beam profile on the fourth grating. The deformable mirror is therefore assumed to be set so that the pulse has a plane wavefront at the compressor input.

Temporal Strehl ratio $S_t > 0.9$

The Strehl ratio in the temporal domain 0.9 is equivalent to 13 fs pulse broadening for approx. 130 fs transform-limited pulse duration. There are two major sources of the degradation of the temporal profile at focus - the residual angular dispersion and the spectral phase. They are independent and cannot compensate each other.

Spatio-temporal couplings

The residual angular dispersion decreases the peak intensity of the compressor pulse via two mechanisms. Different pointing of the individual spectral components leads to spatial broadening of the focal spot profile and it simultaneously narrows the spectral bandwidth at each point. This is illustrated in Figure 4.3 where the spatio-spectral Strehl ratio (the focused spectral intensity) is compared with spatio-temporal Strehl ratio (the focused temporal intensity). The impact of residual angular dispersion scales with the beam size as a larger beam can be focused to tighter focal spot. The maximal residual linear angular dispersion can be estimated to 30 nrad/nm. It is mainly induced by the non-parallel gratings in the compressor. It can be present both in the horizontal and the vertical plane, so the bounds for maximal residual AD in one plane have to be decreased by $\sqrt{2}$ factor to 20 nrad/nm.

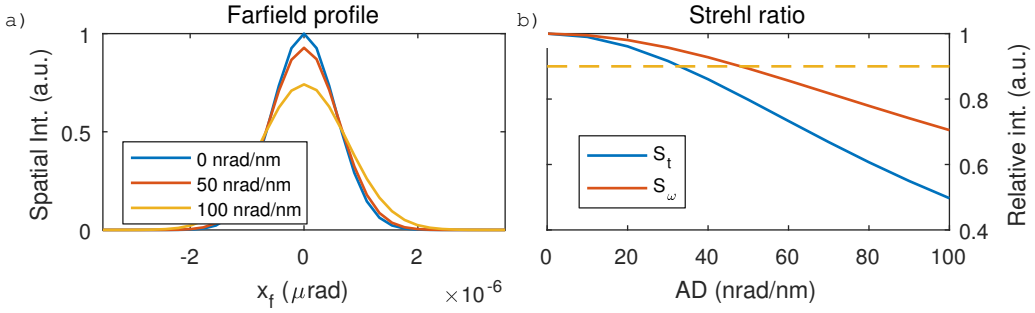

Figure 4.3: Degradation of the peak intensity due to residual linear angular dispersion defined in μrad/nm. The simulation was done for Gaussian pulse with transform-limited pulse duration 130 fs with super-Gaussian spatial profile of the twentieth order with 0.3 m half-width.

Uncompensated spectral phase

The impact of the residual phase on the temporal Strehl ratio is plotted in Figure 4.4. Assuming the Gaussian spectrum, the maximal residual spectral phase can be estimated to be 2500 fs^2 and 250 000 fs^3, 4 000 000 fs^4. The faster decay of the tails of the super-Gaussian spectra of the fourth order relaxes these parameters to 4000 fs^2 and 250 000 fs^3, 4 000 000 fs^4. The output spectrum of laser can be expected to lie in between. For the purpose of this tolerance analysis, the Gaussian spectrum is assumed to be the worst case scenario. According to Table 2.2, the residual spectral phase is mostly induced by the deviation in the grating spacing, incorrect angle of incidence

into the compressor and the yaw misalignment of the second and third grating.

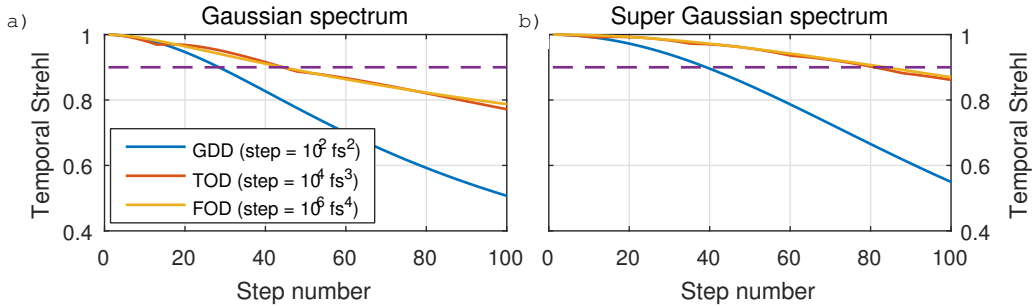

Figure 4.4: Degradation of the peak intensity due to residual spectral phase of a pulse with Gaussian (a) and super-Gaussian spectrum of the fourth order (b) having transform-limited pulse duration of 130 fs. The temporal Strehl ratio was calculated independently for the individual dispersion orders.

Budget

The maximum misalignment, which would breach the constraints for the Strehl ratio, was estimated for each parameter. Based on that a tolerance budget taking into account all the possible misalignments was established. The total error was uniformly distributed among the uncoupled degrees of freedom. The maximum possible contribution of the individual degree of freedom was then calculated:

$$individual\ error = \frac{Total\ error}{\sqrt{Degrees\ of\ freedom}} \tag{4.1}$$

Afterward, the results were verified by Monte Carlo analysis using optical model in ZEMAX Opticstudio.

Method

The tolerance analysis can be decoupled into two separate problems. The mutual alignment of the grating assemblies and the alignment of the gratings within the assembly can be studied independently. An optical model in ZEMAX Opticstudio was created to evaluate the sensitivity of the individual degrees of freedom with respect to the tolerance budget. The residual angular dispersion was obtained from the spectral dependence of ray pointing at the compressor output, spatial Strehl ratio was simulated using Huygens point spread function and the residual spectral phase was calculated using user developed macro based on principles discussed in Section 1.6. The simulated values were also verified with theoretical formulae where possible [43]. The temporal Strehl ratio was calculated as follows. The studied compressor configuration was phase-traced. The retrieved spatial profile for each spectral component was then exported into Matlab using ZOSAPI link. In Matlab, far-field distribution was numerically calculated using the 2D FFT algorithm according to Eq. (1.36). The far-field points with the highest spatial intensity were then transformed into the temporal domain using the 1D FFT algorithm (Eq. 1.2). The peak temporal intensity of the examined case was then compared with the peak temporal intensity of the ideal system having constant phase in the $x - \omega$ domain.

4.1 1740 ln/mm compressor

The 1740 ln/mm grating design has been successfully implemented in high energy laser systems such as Texas Petawatt [37] or OMEGA EP [46]. The operational angle of the gratings is set to 74° for 1060 nm central wavelength with diffraction efficiency better than 95% within the whole bandwidth [85]. To constrain the fluence on the last grating, the beam size has to be enlarged to 40 x 40 cm resulting in 145 cm footprint width of the beam on the first and the last grating (Figure 4.1). Since monolithic gratings with such aperture were not commercially available, a tiled grating and a grating-mirror scheme allowing to increase the effective grating aperture were considered. The compressor is composed of 4 gratings assemblies (GA) in the typical Treacy configuration (Figure 2.4). Due to large incidence angle, each grating assembly has to be either in the tiled grating (G-G) or grating-mirror (G-M) configuration. The overall schematic of the first half compressor for both tiled grating and grating-mirror configuration is shown in Figure 4.5. The second half of the compressor is arranged symmetrically.

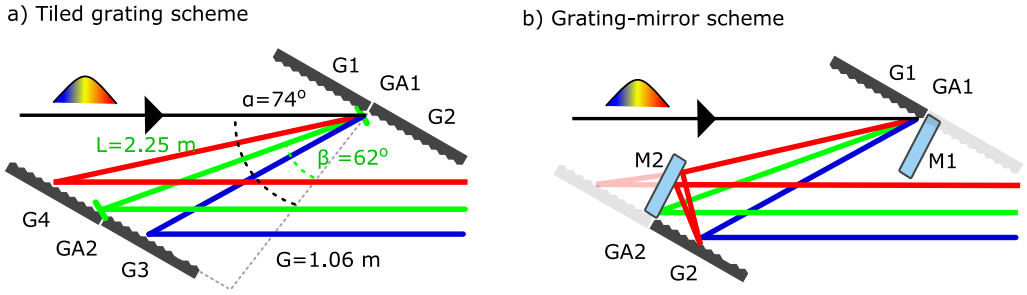

Figure 4.5: Schematic of the compressor in tiled-grating (a) and grating-mirror configuration (b).

Spectral throughput

The nominal model of the compressor was designed so that the ray with 1060 nm wavelength incident on the center of the GA1 is diffracted to the center of the GA2. Since the gratings have limited aperture, the edges of spectra are truncated depending on the spatial coordinate of the beam. The grating gap at the GA1&4 creates a dip in spatial amplitude for all spectral components around x=0, whereas the position of the grating gap at the GA2&3 depends on the wavelength. The spatio-spectral intensity profile of the beam after the compressor is shown in Figure 4.6a. The overall transmissivity curve of the compressor with a super-Gaussian spectrum and the spatial offset on the GA2 of the individual spectral components is shown in Figure 4.6b. The overall transmittance of the compressor due to truncation was estimated to be 96% (Figure 4.2).

GA-GA tolerances

An analysis of the required alignment accuracy for the individual grating assemblies was performed under the assumption that the gratings and the mirror within each assembly are perfectly aligned. The simulated sensitivities of the individual degrees of freedom to residual angular dispersion, output Strehl ratio and spectral phase deviation are summarized in Table 4.2.

The compressor is the most sensitive to misalignments within the horizontal (diffraction) plane, namely to the yaw and line density variation. These misalignments change

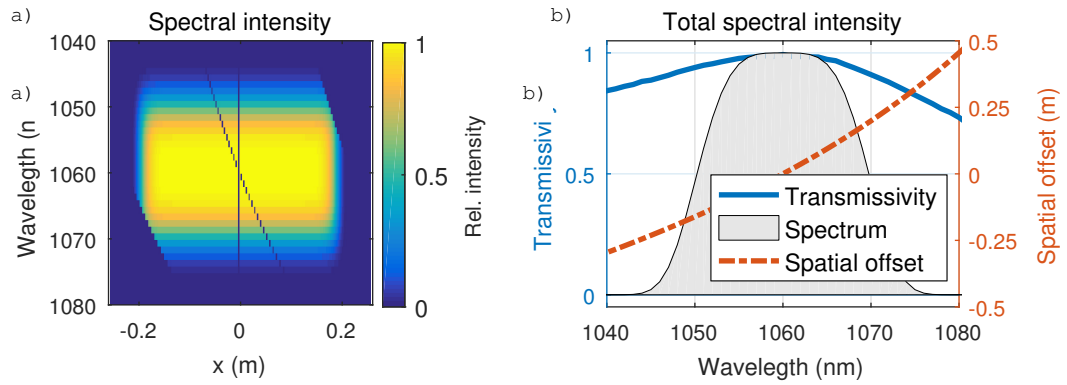

Figure 4.6: a) Spectral truncation induced by the compressor. b) Transmissivity curve compared with the expected spectral profile of the pulse and the spatial offset on the GA2 of the individual spectral components. The simulation was made Matlab assuming 0.8 m width of the gratings in the diffraction plane, a 6 mm grating-grating gap and no clipping in the vertical plane.

Table 4.2: GA-GA alignment tolerances to meet values from tolerance budget, the spectral phase error is induced through the misalignment of the GA2 or GA3 only

DoF	**AD**	S_ω	**Spectral phase**
Target	20 nrad/nm	> 0.80	2500 fs^2
Yaw (μrad)	2	13	6
Pitch (μrad)	6	46	3000
Roll (μrad)	12	87	700
LDV (ln/mm)	$6 \cdot 10^{-3}$	$2 \cdot 10^{-2}$	$3 \cdot 10^{-3}$
ΔL (μm)	-	-	85
$\Delta\alpha$ (μrad)	-	-	15

the magnitude of the angular dispersion (AD) so that the AD of the first grating does not match the AD of the second grating. The pitch and roll misalignments effectively tilt the diffraction plane of one of the gratings with respect to the other one and a small vertical component of AD then remains uncompensated. The residual spectral phase is then mostly induced by the yaw misalignment of the GA2 and GA3. When the GA2 or GA3 is slightly rotated by several μrad, the optical path of the dispersed spectral components is also changed in the μm scale for meter sized gratings. So, the individual spectral components acquire different group delay than intended which results in pulse broadening.

The other parameters are the error in the angle of incidence $\Delta\alpha$ into the compressor (assuming perfectly parallel gratings) and the incorrect spacing ΔL between the gratings. These two parameters can be partly corrected after the alignment of the compressor. Usually, the grating spacing is mechanically set up to be approximately the same for both grating pairs with mm accuracy and then the grating distance of one pair is fine-tuned to minimize pulse duration. Consequently, the grating pairs do not have exactly the same grating spacing. But since the spatial chirp linearly scales with the propagation distance, the residual spatial chirp is negligible. Small errors in the incidence angle can be easily corrected by a slight adjustment of the stretcher incidence angle or the grating spacing (Eq. 2.4).

The required alignment precision is therefore driven by minimization of the residual angular dispersion for the angular degrees of freedom. That also corresponds to

the operational needs since the residual spectral phase can be to some extent pre-compensated by the Dazzler or stretcher. A small adjustment of the order of tens of fs does not influence the temporal profile of the chirped pulse with nanosecond duration. On the contrary, the residual angular dispersion is mostly induced by wedged windows and other optics and it should be kept minimal throughout all the chain. Moreover, it inversely scales with the magnification of the beam. Therefore, it is not feasible to tune the angular dispersion prior to the compressor. It is therefore critical to align the compressor so that the corresponding GA pairs are parallel in the first place.

There are altogether 4 grating assemblies, each one has one adjustable degree of freedom in the horizontal plane (yaw) and two degrees of freedom in vertical plane (pitch, roll). Since the tolerance values are driven by the angular dispersion, the tolerance budget for each grating will be driven by the second column of the Table 4.2. The yaw tolerance value will be therefore divided by $\sqrt{4 \cdot 1}$ and the pitch and roll tolerance values by $\sqrt{4 \cdot 2}$. The tolerance budget representing the target alignment precision of each grating is presented in Table 4.3. The piston error can be treated separately as it can be easily adjusted after the alignment.

Table 4.3: Tolerance budget for the alignment precision of each individual grating

Yaw	**Pitch**	**Roll**	**Piston**
1 μrad	2 μrad	4 μrad	42 μm

Phasing tolerances

Generally, the misalignment of the gratings within the GA yields a wavefront deviation. In the presence of misalignment, the wavefront of one beam half is tilted or gains a constant phase offset with respect to the other half. This wavefront offset is achromatic when the GA1 or GA4 are misaligned. The situation is a bit different on the GA2 and GA3 where the individual spectral components are spatially offset. However, since the spatial offset is much smaller then the overall width of the beam on the tiled grating (see position of grating gap in Figure 4.6), the impact of their misalignment is very similar to the GA1.

There are altogether six degrees of freedom for the alignment of the tiled gratings and three degrees of freedom for the grating-mirror configuration. The sensitivity to misalignments is two times bigger for the grating-mirror configuration according to the theoretical prediction. Since there are four GAs, there are altogether $4 \cdot 6 = 24$ degrees of freedom for tiled G-G configuration and only $4 \cdot 3 = 12$ degrees of freedom for the G-M configuration. According to Eq. 1.20, the total Strehl ratio can be estimated as the product of the individual Strehl ratios of each misalignment. The misalignments in horizontal (yaw, piston, LDV, shift) and vertical (pitch, roll) planes are independent and cannot compensate each other. Contrarily, the misalignments within one plane can partly compensate each other even if they originate from a different GA. The target Strehl ratio S_{GG} and S_{GM} for a single misalignment can be derived as :

$$0.8 = S_{GG}^{(\sqrt{4\cdot4}+\sqrt{4\cdot2})} \qquad 0.8 = S_{GM}^{(\sqrt{4\cdot2}+\sqrt{4\cdot1})}, \tag{4.2}$$

where the first term in the exponent represents horizontal misalignments and the second one vertical misalignments. Eq. 4.2 has solution $S_{GG} = 0.97$ and $S_{GM} = 0.95$ respectively. Tolerance values for each degree of freedom were simulated using a non-sequential model in Zemax Opticstudio and confirmed by numerical analysis in Matlab using analytic expressions from Table 2.3. The results were then employed as bounds

in a Monte Carlo analysis performed in ZEMAX with an uniform distribution of misalignments. The simulation was run 500 times and yielded a 0.87 mean value of the Strehl ratio with 0.8 reached in 80% of cases.

Table 4.4: Estimation of the maximal misalignment within GAs leading to 0.8 Strehl ratio after the compressor assuming a normal distribution of the errors within the compressor. The tolerance values in the table represent 0.97 Strehl ratio of a single misalignment for the G-G configuration and 0.95 Strehl ratio for the G-M configuration.

DoF	**Tiled G-G**		**G-M**	
Yaw	0.3	μrad	0.2	μrad
Pitch	0.7	μrad	0.2	μrad
Piston	70	nm	40	nm
Line density variation	$2 \cdot 10^{-4}$	ln/mm		
Roll	0.3	μrad		
Lateral shift	70	nm		

Diffraction on grating gaps

The beam clipping on the grating gaps induces spatial intensity modulations as the beam propagates through the compressor. Since the gratings in the GA4 operate close their LIDT as the pulse retains its minimal duration there, the estimation of the magnitude of the modulations is crucial to establish a sufficient safety margin. The simulation was performed in Matlab using the Fresnel propagation algorithm in the diffraction plane (1D spatially). The spatial amplitude of each spectral component was propagated through four apertures representing the individual GAs. Their mutual distances were set according to the GA-GA distance in the compressor (Table 4.1). Figure 4.7a shows the spatial intensity profiles at the GA4 of the individual spectral components, Figure 4.7b represents the resulting spatial intensity modulation of the beam, which is calculated as a spectral sum of the spatial intensities. The modulation maxima reach up to 1.5 times of the maximum of the input intensity profile.

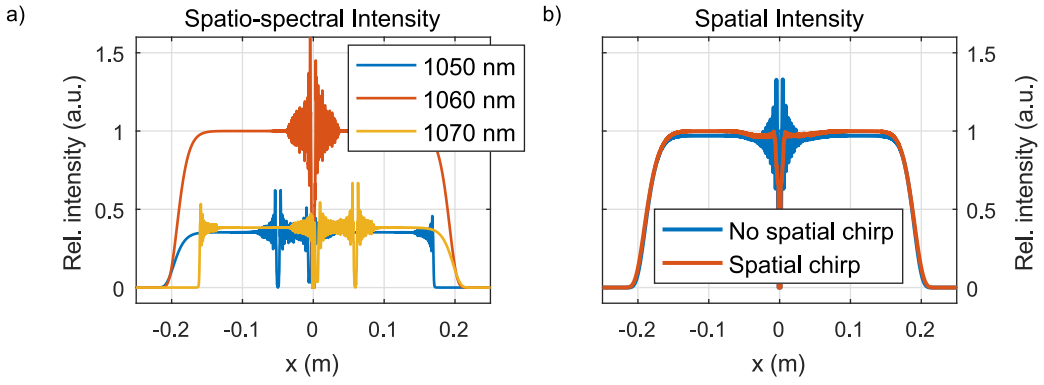

Figure 4.7: Diffraction induced intensity modulations on the GA4.

The side modulations induced by the grating gap at the GA2&3 are not present in the spatial profile because they are averaged out as their position varies with wavelength. The modulation induced by the GA1 gap can be suppressed by leaving slight ($\sim$0.0005 m/nm) spatial chirp at the compressor output [86]. The spatial chirp shifts the modulation maximum in dependence on the wavelength so that the modulation is

smeared out in the same way as the modulations from the GA2&3. Such small spatial chirp influences the pulse duration and the focused peak intensity only marginally as it represents only 1 cm sweep between the edges of 20nm bandwidth in the nearfield. Nevertheless, the modulations induced by the GA4 gap cannot be suppressed this way as all the spectral components overlap and are collimated there. The modulation then increases the risk of damaging subsequent optics. The modulation could be theoretically suppressed by apodization the part of the beam incident on the gap prior to the compressor.

Line density variation

Since the line density variation (LDV) of the grating is determined through the manufacturing process highly sensitive to the refraction index of the air, the grating producer is able to restrict it only to certain intervals. Line densities of the compressor gratings may then differ. According to Table 2.2, the LDV in compressors generally induces both residual angular dispersion and spectral phase deviation. To compensate it, the grating can be tilted in yaw so that it matches the linear angular dispersion of its counterpart according to Eq. 2.9. Such compensation then leads to even bigger detuning of the output spectral phase. That can be compensated through the adjustment of the incidence angle α and the grating spacing L of the both grating pairs to tune the output GDD and TOD and to minimize spatial chirp. The impact of the higher dispersion orders on pulse broadening is then minimal. However, the quadratic term of angular dispersion remains uncompensated, which can decrease the Strehl ratio for systems with large LDV or broad bandwidth. A simulation in ZEMAX confirmed that the impact of LDV in the order of 0.1 ln/mm on the Strehl ratio is negligible (Table 4.5).

Table 4.5: Compensation of line density variation in the 1740 ln/mm compressor; $\theta_{Yaw}^{\Delta NC}$ stands for the yaw adjustment necessary to suppress residual angular dispersion, ΔL and $\Delta\alpha$ stand for the adjustments of the grating spacing and the angle of incidence to compensate the residual spectral phase.

LDV ln/mm	$\boldsymbol{\theta_{Yaw}^{\Delta NC}}$ μrad	**Δ L** μm	**Δα** μrad	$\boldsymbol{S_\omega}$ -
0.1	31	636	209	1
1	305	3840	2093	0.94

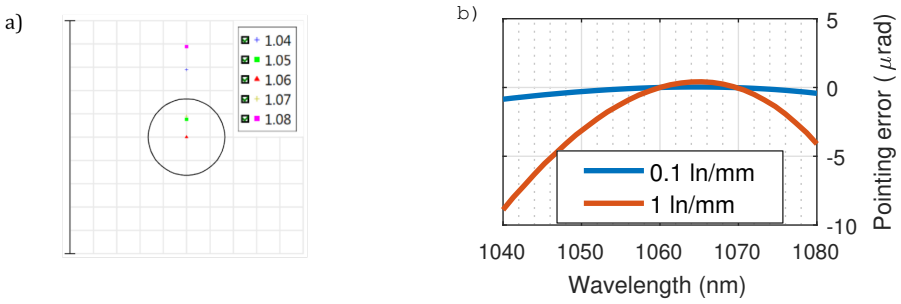

Figure 4.8: Residual quadratic angular dispersion present when the LDV is compensated by the GA yaw. a) Farfield profile in ray approximation; b) The dependence of pointing deviation on wavelength

Line density variation within GAs (G-G)

For tiled grating assemblies, the compensation is more complicated since the LDV also influences the diffracted wavefront from the GA. Because the sensitivity to the LDV within GAs is bigger than to the LDV between the opposite GAs (compare Table 4.2 and 4.4), the LDV within GA has to be compensated first. That can be achieved by tilting one of the gratings within the GA with respect to the other in the yaw by θ_{Yaw}^{GA} equal to:

$$\theta_{Yaw}^{GA} = \frac{-\Delta N \lambda}{\cos\,\alpha + \cos\,\beta}. \tag{4.3}$$

The residual angular dispersion can be minimized by tilting whole GAs with respect to each other. However, as the spectral components propagate by one of the four possible paths sketched in Figure 4.9, the exact compensation of residual AD is possible only for a single path.

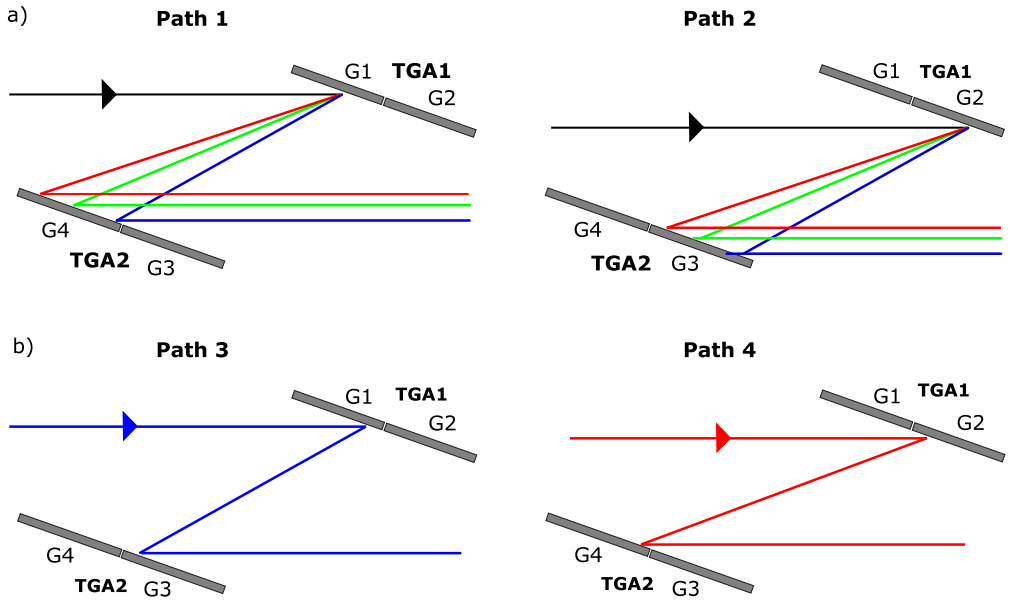

Figure 4.9: Possible optical paths through tiled grating assembly. Paths 1 and 2 are the most frequent ones (a); Paths 3 and 4 are propagated only by the rays incident near the grating gap with eligible wavelength.

Because the majority of the rays propagate along paths 1 and 2, it is advisable to minimize their AD. To do that, three steps must be followed. First, the gratings should be grouped into the pairs with the closest line densities to achieve the smallest line density variation ΔN_{GA} possible for all GAs. This minimizes θ_{Yaw}^{GA} which mainly results in the difference in the residual angular dispersion between the path 1 and 2. Second, the gratings on the opposite sides of the compressor (G1-G4, G2-G3) must be arranged to have the closest line density difference (ideally $|N_1 - N_4| = |N_3 - N_2|$). If the line density difference is the same for both paths, it can be entirely compensated by tilting whole GA. Third, GA2 has to be tilted by $\theta_{Yaw}^{\Delta N_C} + \theta_{Yaw}^{GA}/2$ in order to minimize the residual angular dispersion for both ray paths. The angle $\theta_{Yaw}^{\Delta N_C}$ is given by the average line density variation $\Delta N_C = \frac{N_1+N_2-N_3-N_4}{2}$ and can be calculated as:

$$\theta_{Yaw}^{\Delta N_C} = \frac{\Delta N_C}{N\ \mathrm{tg}\ \beta} \tag{4.4}$$

Fourth, the second half of the compressor should be populated with gratings in a such way that its residual AD has the opposite value compared to the first compressor half.

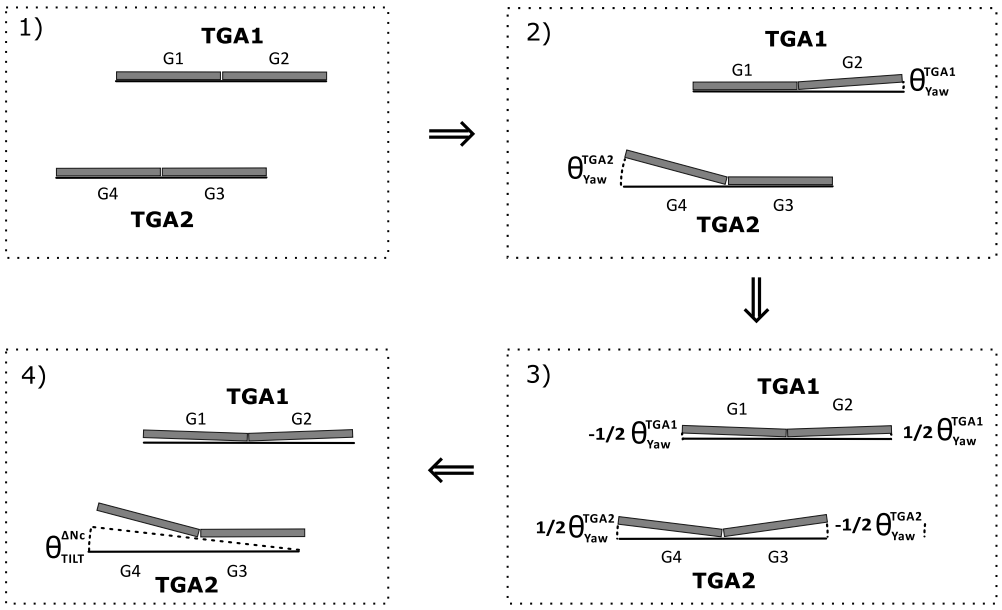

Figure 4.10: Procedure of the compensation of the line density variation in a tiled grating compressor. First, gratings within a GA are tilted by θ_{Yaw}^{GA} to compensate for the wavefront error of the diffracted beam. Second, the angle between the GAs is adjusted to minimize the residual angular dispersion.

The whole procedure is sketched in Figure 4.10. The residual angular dispersion of the corrected system can be expressed with the help of Eq. (2.8) using the angles from Eqs. (4.3) and (4.4). Since the tilts are symmetric, paths 1&2 and 3&4 retain the same residual angular dispersion. The residual AD $\frac{\mathrm{d}\theta_x}{\mathrm{d}\lambda}|_{P1\&2}$ ($\frac{\mathrm{d}\theta_x}{\mathrm{d}\lambda}|_{P3\&4}$) for beam paths 1&2 (3&4) can be calculated as:

$$\begin{aligned}\frac{\mathrm{d}\theta_x}{\mathrm{d}\lambda}|_{P1\&2} &= K(\lambda)\cdot(N_1 - N_2 + N_3 - N_4) = K(\lambda)\cdot(\Delta N_{GA1} - \Delta N_{GA2})\\ \frac{\mathrm{d}\theta_x}{\mathrm{d}\lambda}|_{P3\&4} &= K(\lambda)\cdot(N_1 - N_2 - N_3 + N_4) = K(\lambda)\cdot(\Delta N_{GA1} + \Delta N_{GA2})\end{aligned} \tag{4.5}$$

with

$$K(\lambda) = \frac{1}{2\cos(\alpha)} + \frac{1}{2(\cos(\alpha)+\cos(\beta))}\frac{\mathrm{tg}(\beta)}{\cos(\alpha)}N\lambda, \tag{4.6}$$

with $\Delta N_{GA1} = N_1 - N_2$ and $\Delta N_{GA2} = N_4 - N_3$. Following Eq. (4.5), it can be deduced that the compensation of paths 1&2 goes against the compensation of path 3&4. The worst-case scenario for paths 1&2 happens when all gratings have same line densities except for one having LDV difference δN. Otherwise, it should be possible to arrange the gratings in such way that δN is at least partly compensated (assuming that G1 to G4 are interchangeable). The right side of Eq. (4.5) is then equivalent to $K(\lambda)\ \delta N$ with $K = 10$ for 1060 nm wavelength and the simulated compressor setup. The 20 nrad/nm requirement from the tolerance budget then determines the condition for the maximal LDV $\delta N < 0.002$ ln/mm.

Theoretical prediction was cross-checked with spatio-temporal simulation in ZEMAX OpticStudio combined with Matlab. The compressor aligned according to Figure 4.10 was ray-traced; the optical path and output pointing of the rays were extracted in dependence on their entrance pupil position and wavelength. The residual angular dispersion, GDD and TOD were then calculated. The output profile was also focused using Fraunhofer approximation and the temporal Strehl ratio was obtained. The gratings were then aligned according to Figure 4.10. A simple simulation where only one grating had line density variation was performed. The results from Table 4.6 confirm that only 0.003 ln/mm line density variation can result in ten percent decrease of the focused intensity.

Table 4.6: Simulation with line density variation of only one grating. Path 3 and 4 are neglected as there is only one grating with LDV. ΔGDD describes GDD difference between path 1 and 2.

$\boldsymbol{\Delta N}$ ln/mm	$\boldsymbol{\theta_{Yaw}^{GA}}$ μrad	$\boldsymbol{\theta_{Yaw}^{\Delta N_C}}$ μrad	**AD Path1** μrad/nm	**AD Path2** μrad/nm	**ΔGDD** fs^2	$\boldsymbol{S_\omega}$	$\boldsymbol{S_t}$
0.003	4.3	0.5	0.03	-0.03	1200	0.95	0.93
0.01	14.2	1.5	0.1	-0.1	3800	0.91	0.87

To generalize results, the compressor was populated with gratings having uniformly distributed LDV ±0.01 ln/mm. Three methods for the arrangement of the gratings and two methods for the alignment of the compressor are compared in Table 4.7. In the first case the compressor was randomly populated with generated gratings. In the second case, gratings were sorted to minimize LDV within the GAs. In the third case, the gratings were again sorted to minimize LDV within GA but they were also swapped within the GAs to mutually compensate the LDV of the other GAs according to the procedure discussed above. For each case, two alignment methods were studied. In each alignment method one of the gratings within GA was tilted to suppress the phasing wavefront error (Eq. 4.3), the mutual angle between GA1&2 and GA3&4 and grating spacing was optimized to limit residual angular dispersion and GDD. For the alignment method number 1, the optimization was done for path 1 (Figure 4.9). The alignment method number 2 followed the procedure sketched in Figure 4.10 leaving even angular dispersion and GDD for both paths 1&2. The effective line density variation ΔN_{eff} is generally a value comparable with a compressor having only one grating with LDV ΔN (assuming that the minimization procedure is undertaken) and it was calculated as:

$$\begin{aligned} \Delta N_{eff} &= \Delta N_{GA1} - \Delta N_{GA2} + \Delta N_{GA3} - \Delta N_{GA4} \\ &= N_1 - N_2 + N_3 - N_4 + N_5 - N_6 + N_7 - N_8 \end{aligned} \tag{4.7}$$

Simulation results confirm that it is critical to arrange gratings in a way that minimizes the LDV within the GA and that also mutually compensates the residual LDV between the different GAs. The alignment method number 2 described in Figure 4.10 yields better results as the residual AD is uniformly distributed between paths 1&2 compared to the alignment method number 1. On the other hand, the alignment method number 1 is more feasible experimentally since it requires measurement of AD and GDD for only one path. In the alignment method number 2, the GDD and AD would have to be adjusted for both paths in successive steps. Nevertheless, the arrangement ("Optimized") and the alignment method number 2 described above allow to considerably minimize the impact of LDV within tiled grating compressor. Still, the mutual compensation of LDV is possible only when the LDV of the gratings are

Table 4.7: Comparison of the impact line density variation in the compressor. ΔN_{eff} represents the effective line density variation being equivalent to a compressor having only a single grating with LDV ΔN_{eff}. AD and GDD are marked with corresponding path number. The Strehl ratio of the ideal system in this simulation was reduced to $S_t = 0.96$ and $S_\omega = 0.97$ due to the clipping of the spectral edges on GA2&3.

Grating	**Random**		**Sorted**		**Optimized**	
N1 (ln/mm)	1739.991		1739.991		1739.991	
N2 (ln/mm)	1739.995		1739.991		1739.991	
N3 (ln/mm)	1739.992		1739.992		1739.995	
N4 (ln/mm)	1740.006		1739.995		1739.992	
N5 (ln/mm)	1740.004		1739.996		1739.996	
N6 (ln/mm)	1739.996		1740.004		1740.004	
N7 (ln/mm)	1739.991		1740.006		1740.009	
N8 (ln/mm)	1740.009		1740.009		1740.006	
ΔN_{eff} (ln/mm)	**-0.028**		**-0.014**		**-0.002**	
Alignment method	**1**	**2**	**1**	**2**	**1**	**2**
S_t	0.34	0.58	0.53	0.83	0.92	0.95
S_ω	0.46	0.68	0.66	0.88	0.95	0.97
AD_1 (nrad/nm)	0	-280	0	-140	0	-20
AD_2 (nrad/nm)	560	280	280	140	40	20
GDD_1 (fs^2)	0	1300	0	-2400	0	1000
GDD_2 (fs^2)	-2600	-1300	-4700	2400	-2100	-1000

comparable. If one grating has remarkably bigger LDV, it determines the Strehl ratio after the compressor.

In Figure 4.11 the pulse-front of the output pulse is compared for the alignment methods for the second case. The residual linear AD leads to pulse front tilt in general. The alignment method number 1 results in no AD for the one beam half and constant AD for the other beam half (Table 4.7). However, for the alignment method number 2 the sign of the angular dispersion is flipped at the grating gap and therefore the sign of the pulse front tilt delay is opposite as well. The pulse front profile then resembles reversed V-shape. The alignment method number 2 clearly leads to smaller maximal deviation of the group delay across the beam profile and therefore yields higher Strehl ratio.

Retro-reflections (G-M)

Since the zeroth diffraction order of the grating-mirror configuration is equivalent to a specular reflection from a roof mirror, the grating-mirror assembly horizontally retro-reflects the beam back with relative intensity equal to the zeroth order efficiency of the grating ($\sim 1\%$). The retro-reflections pose a risk to a laser system as they cannot not be filtered by the relay pinholes. They can be also further amplified during back propagation (Nd:glass lifetime is in the order of microseconds) which can lead to their damage. The summary of three most risky retro-reflections is presented in Table 4.8.

The first retro-reflection originates from the GA1 (Figure 4.12a) but since the beam is not yet dispersed, the reflected pulse has the same duration as the incoming pulse. The second back-reflection originates from the GA2 (Figure 4.12b). Firstly, the beam is diffracted off the GA1 and its spectrum is dispersed. The dispersed beam then hits

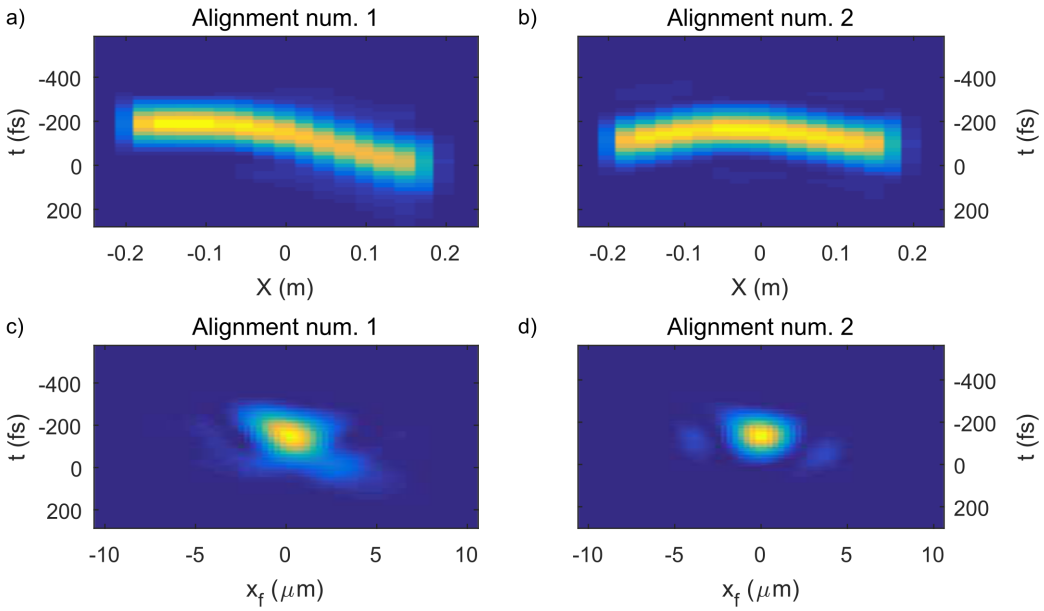

Figure 4.11: Comparison of the pulse front profiles (a-b) and focal spot profiles (c-d) in the diffraction plane after the compressor with an uniform LDV of the gratings for both alignment methods with normalized z-scale. The simulation was performed for the "sorted" case from Table 4.7 in ZEMAX OpticStudio linked with Matlab. The pulse front and focal spot profile in the plane perpendicular to the diffraction plane are not aberrated.

the GA2 and is reflected back as the zeroth diffraction order. Since the pointing of each spectral component is preserved, the beam is then collimated as it is diffracted again from the GA1. The beam travels $2L$ distance between the gratings and therefore the temporal chirp of the pulse is compensated. Because the zeroth order reflection off the GA2 inverses the spatial coordinates of the beam in the diffraction plane, the spatial chirp is doubled and can be estimated to be 1 cm/nm. The L4 beam has 40 cm diameter at the compressor input with 20 nm bandwidth. The overlap of the spectra is therefore sufficient to obtain a few hundred fs pulse even in the nearfield. A ¡200 fs pulse can be expected in te farfield where the spatial chirp has no effect. Assuming 1500 J at the input and 1% zeroth order efficiency, the retro-reflection can reach 100 TW peak power. The third back-reflection comes from the GA3 (Figure 4.12c). The beam propagates through the first half of the compressor and is incident on the GA3. It is again diffracted as the zeroth order, back reflected and its spatial coordinates are inverted in the diffraction plane. After it propagates back through the first half of the compressor its spatial chirp is doubled and it is temporal chirp is compensated. The back reflected pulse has therefore the same properties as the back-reflected pulse from GA2.

Table 4.8: The summary of back reflections originating from the zeroth diffraction order from grating-mirror assemblies in the compressor.

0th order at	**GA1**	**GA2**	**GA3**
Pulse duration	∼3 ns	∼130 fs	∼130 fs
Energy	1 %	1%	1%
Delay	0 ns	20 ns	40 ns

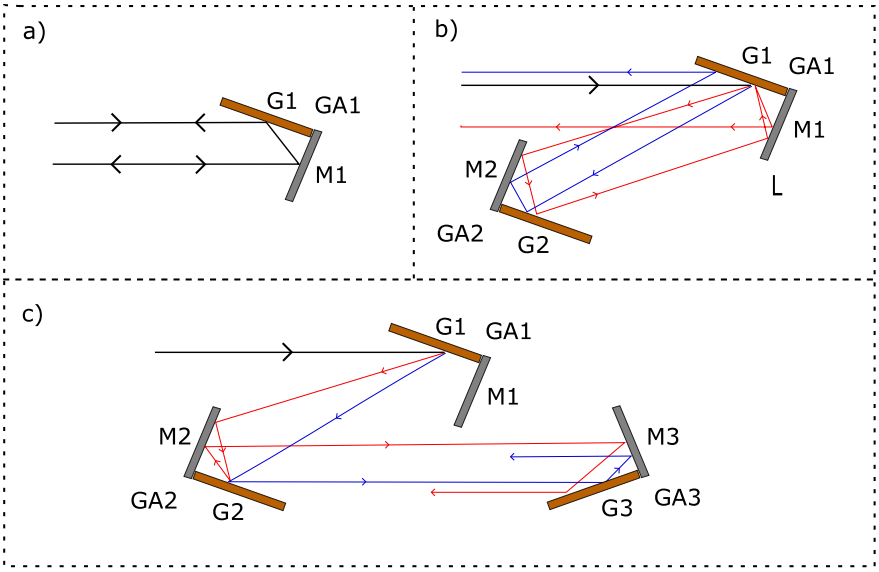

Figure 4.12: Retro-reflections for the grating mirror configuration coming from the zeroth order diffraction of the GA1 (a), GA2 (b) and GA3 (c).

The retro-reflections can be filtered when the gratings are vertically tilted to deviate the pointing of the retro-reflection in the vertical plane. When the tilt is small, the retro-reflection can be possibly filtered at the relay pinholes. However, since the peak power of the retro-reflections approaches 100 TW, pinhole filtering is not advisable as it can lead to pinhole drilling and contamination of vacuum. A preferable approach would be to introduce a larger vertical tilt so that the zeroth order from the GA2 (GA3) misses the GA1 or preferably some optics upstream and is guided to a beam dump.

Postpulses (G-M)

When the beam is diffracted as the zeroth order two times, it has the same propagation direction as the main beam but it is delayed with respect to ti. Generally, properties of these post-pulses are very similar to the pre-pulses mentioned above. Their characteristics is summarized are Table 4.9. The most intense post-pulse is created when the beam is reflected as the zeroth diffraction order subsequently from the GA3 and GA2 respectively. Such a post-pulse is delayed by 40 ns with respect to the main beam and has only 0.01% energy. Otherwise, it has exactly the same properties as the main pulse. Contrarily, the other two post-pulses are temporarily chirped and exhibit large spatial chirp as the dispersed beam propagates three times longer distance between the GA1 and GA2 or GA3 and GA4 compared to the main pulse.

Table 4.9: The summary of post-pulses originating from the double zeroth order diffraction of the beam.

0th order at	**GA4, GA3**	**GA3, GA2**	**GA2, GA1**
Pulse duration	4.5 ns	130 fs	4.5 ns
Energy	0.01 %	0.01 %	0.01 %
Delay	20 ns	40 ns	20 ns

Discussion

The 1740 ln/mm compressor design poses several challenges. For a grating-grating configuration, line density variation of the gratings has to be precisely determined during the manufacturing process with 0.003 ln/mm precision, otherwise it would lead to complex spatio-temporal couplings. In the grating-mirror configuration, line density variation is not present since the grating is imaged by a mirror. On the other hand, the zeroth order diffraction order from the GA2 and GA3 configuration are retro-reflected and compressed during their back-propagation. The peak power of these retro-reflections can reach up to 100 TW, they cannot be easily relay filtered and therefore they pose a risk to the laser system. In both configurations, diffraction at the grating gaps has to be mitigated. Diffraction induced modulations at the GA4 (having highest LIDT requirements) can be possibly smoothed out by spatial chirp smoothing. Still, the modulation originating from the GA4 gap cannot be suppressed and it tightens the requirements on damage threshold of all subsequent optics. Both configurations have strict tolerances for the accuracy of GA-GA alignment in the order of microradians. The grating-mirror configuration offers slightly better opto-mechanical requirements than the tiled grating configuration because the number of degrees of freedom is limited to three. Nevertheless, sub-microradian alignment accuracy is necessary for both types of assemblies.

4.2 1136 ln/mm compressor

The multilayer dielectric 1136 ln/mm grating design offers the best diffraction efficiency near the Littrow angle in the 1040-1080 nm region. To separate the incident and diffracted beams, the gratings have to be vertically tilted and can be then arranged in a "butterfly" configuration sketched in Figure 4.13. The gratings are tilted by 37.0° in the horizontal (diffraction) plane to operate near the Littrow angle for the central wavelength 1060 nm. The incident and the diffracted beam are then separated in the vertical plane by 4.07° pitch yielding 3.25° off-plane angle. The off-plane angle was chosen with regard to the CIS design, which transports the beam from the last amplifier into the compressor, and the physical dimension of the compressor hall. The grating spacing for the central wavelength of the pulse was set to 15.1 m to reach the target compression ratio. Thanks to the small incidence angle, only a 75x60 cm clear aperture of the first and the last grating is required for a square beam with 60 cm width. To increase the aperture of the GA2&3, the grating-mirror configuration was favoured as it is more cost effective and the retro-reflections discussed in the previous chapter are filtered due to the off-plane angle. Mirrors with 75x65 cm dimensions were selected. The clear aperture of the mirrors is equivalent to 56 cm grating width, since they are tilted at 53° with respect to the incoming beam. The mirrors have to exhibit flat spectral reflectivity close to 100%, since a part of the dispersed beam is incident four times on the mirrors and two times on the gratings in total whereas the other part is incident only two times on the grating. The multilayer dielectric 1136 ln/mm gratings with 85x65 cm clear aperture and more than 98% reflectivity in 1040-1080 nm region are to be produced in Lawrence Livermore National Laboratory.

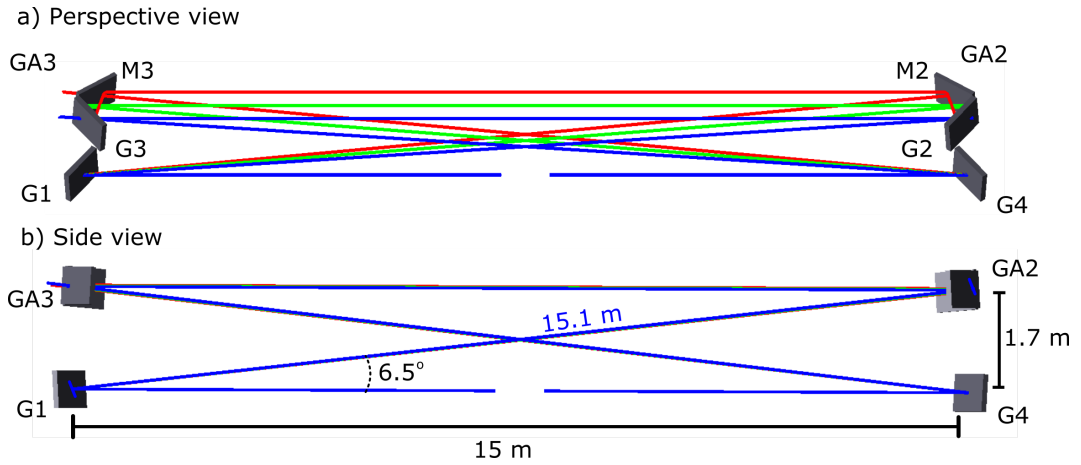

Figure 4.13: Drawing of the compressor in the grating mirror configuration exported from a ZEMAX model.

Spectral truncation

Since the 1136 ln/mm compressor configuration employs an off-plane angle, the calculation of the compressor throughput is more complicated as it is a 3D problem. The diffracted components gain both horizontal (21 mm/nm) and vertical (1 mm/nm) spatial chirp as they propagate towards GA2. Since the GA2&3 can be either tilted by either pitch (4.07°) or roll (5.45°), its effective aperture is also rotated with respect to the classical compressor configuration and the dispersed beam can be clipped also in vertical plane as it is shown in Figure 4.14.

For a numerical analysis, the vertical position of the GA2&3 was fixed and pitch

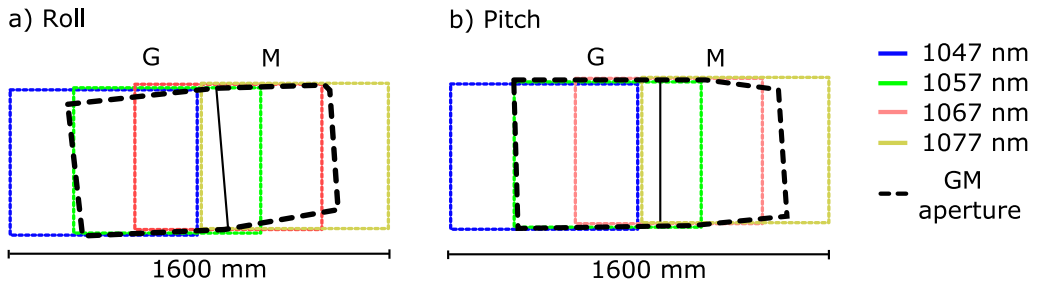

Figure 4.14: Effective aperture of the grating mirror assembly compared with the spatial profile of the dispersed beam at the GA2 for roll (a) and pitch (b) configurations.

and roll tilts were adjusted to maximize the compressor throughput. The output beam profiles of the individual spectral components and the overall transmissivity of the compressor for both configurations are presented in Figure 4.15. The pitch tilt leads to better overall transmissivity as the aperture of GAs is filled better for all wavelengths.

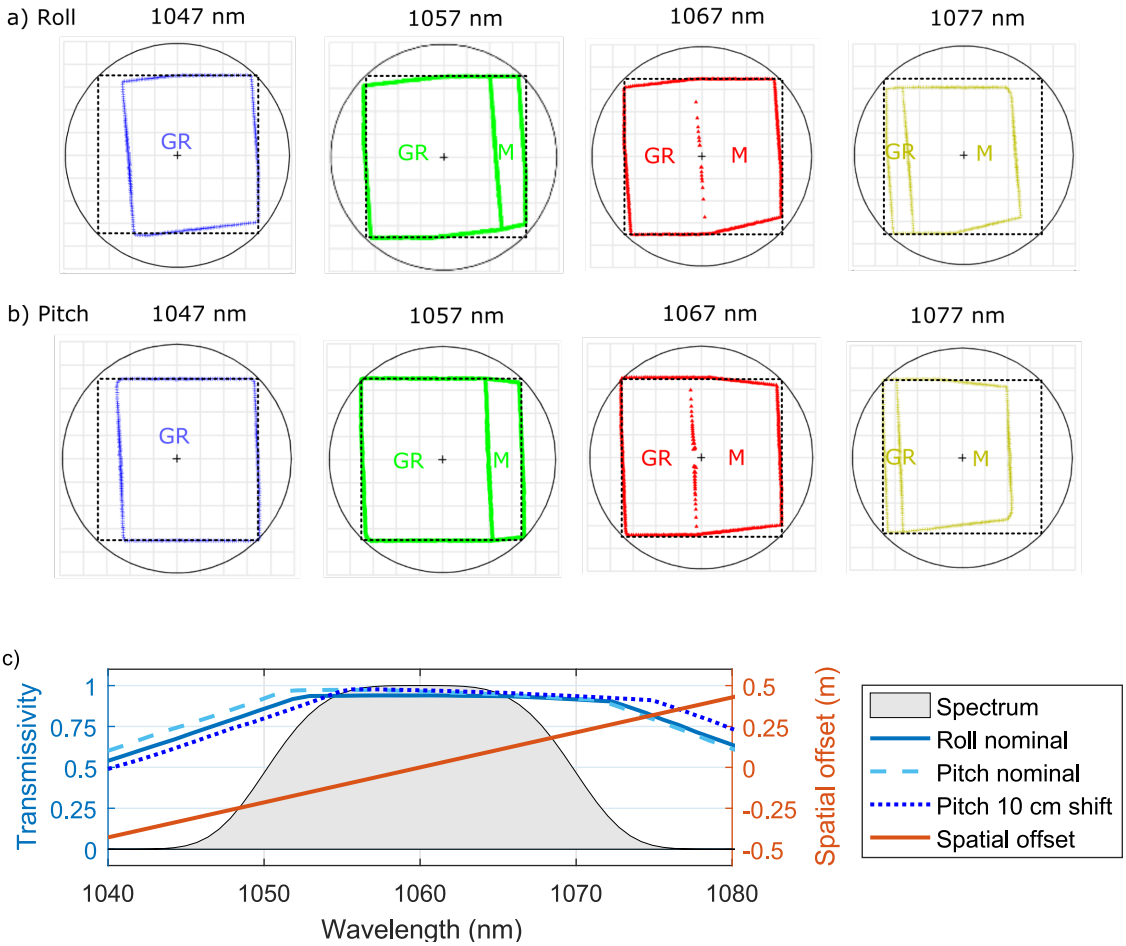

Figure 4.15: Spectral truncation in the 1136 ln/mm compressor. Footprints of the individual spectral components in the nominal configuration with roll (a) and pitch (b) tilts compared with the input beam profile (black dashed square). GR and M sign mark the beam part incident on the grating and mirror within GAs respectively. c) The compressor transmissivity for roll and pitch configurations and the spatial offset on the GA2 for the individual spectral components.

At the roll configuration, the spectral components are clipped mostly by the grating because the roll angle of the grating aperture is much bigger than the vertical angle of the spatially dispersed beam. At the pitch configuration, the dispersed beam is clipped mostly on the mirror from both sides. The transmissivity curve can be shifted to either sides of the spectra by moving the GA assembly horizontally in the perpendicular direction to the input beam. The overall spectral throughput of the compressor due to truncation can be estimated to be 95% for the nominal pitch and 92% for the roll configuration and hence the pitch configuration was favoured.

GA - GA alignment tolerances

The simulated sensitivity of the individual degrees of freedom calculated from the numerical ZEMAX model are presented in Table 4.10. The tolerances were cross-checked using analytical formulae wherever possible.

Table 4.10: GA-GA alignment toleraces for the 1136 ln/mm design

DoF	**AD**	S_ω	**Spectral phase**
Target	20 nrad/nm	> 0.80	2500 fs^2
Yaw (μrad)	20	69	17
Pitch (μrad)	23	90	280
Roll (μrad)	18	70	200
LDV (ln/mm)	0.016	0.6	0.011
ΔL (μm)	-	-	600
$\Delta\alpha$ (μrad)	-	-	17

The tolerance values are again mostly driven by the residual AD induced by the angular misalignments (yaw, pitch, roll). The maximal yaw misalignment leading to pulse broadening due to spectral phase deviation is very close to the value given by the residual AD. The piston error has a very small impact on residual spectral phase due to the low line density of the gratings. AD originating from the line density variation (LDV) has to be compensated by tilting the grating by respective angle and will be discussed in following section.

The tolerance budget closely follows the argumentation presented in the corresponding section of the 1740 ln/mm compressor. The maximal allowable yaw misalignment is driven by the spectral phase error closely followed by the horizontal angular dispersion. The spectral phase error is induced only through the misalignment of GA2 and GA3 where the individual spectral components are spatially dispersed, whereas the residual AD si present for all degrees of freedom. The misalignment of the angle of incidence $\Delta\alpha$ of the grating pairs and the piston error ΔL can be corrected using Dazzler or by tuning the stretcher, so they are not included. The yaw tolerance value will be therefore divided by $\sqrt{4 \cdot 1}$ and the pitch and roll tolerance values by $\sqrt{4 \cdot 2}$. The tolerance budget representing target alignment precision of each grating is presented in Table 4.11.

Table 4.11: The tolerance budget for the misalignment values of each individual grating

Yaw	**Pitch**	**Roll**	**Piston**
10 μrad	8 μrad	6 μrad	400 μm

Phasing tolerances

The 1136 ln/mm configuration has 1.5 times bigger beam size but it uses only two phased grating assemblies, so it can be expected that the tolerance values will be close to the 1740 ln/mm design. There are altogether 12 degrees of freedom for the tiled grating and only 6 for grating-mirror configuration. The target Strehl ratio S_{GG} and S_{GM} for a single misalignment can be again derived as:

$$0.8 = S_{GG}^{(\sqrt{2\cdot4}+\sqrt{2\cdot2})} \qquad 0.8 = S_{GM}^{(\sqrt{2\cdot2}+\sqrt{2\cdot1})}, \tag{4.8}$$

where the first term in the exponent represents horizontal misalignments and the second one vertical misalignments, which cannot mutually compensate each other. Eq. 4.8 leads to $S_{GG} = 0.95$ and $S_{GM} = 0.94$ respectively. The tolerance values for each degree of freedom were simulated in a non-sequential model in Zemax Opticstudio and confirmed by numerical analysis in Matlab using analytic expressions from Table 2.3. The results are shown in Table 4.12 and were then employed as bounds in a Monte Carlo analysis performed in ZEMAX with an uniform distribution of misalignments within the bounds. The simulation run 500 times with random misalignments and it yielded 0.91 mean value of Strehl ratio with 0.86 reached in 80% of cases for the grating-mirror configuration.

Table 4.12: Estimation of the maximal misalignments within the GAs leading to 0.8 Strehl ratio after the compressor assuming a normal distribution of the errors within the compressor. The tolerance values in the table represent 0.95 Strehl ratio of single misalignment for a G-G configuration and 0.94 Strehl ratio for G-M configuration.

DoF	**Tiled**	**G-G**	**G-M**	
Yaw	0.2	μrad	0.1	μrad
Pitch	0.3	μrad	0.2	μrad
Piston	80	nm	50	nm
Line density variation	$2 \cdot 10^{-4}$	ln/mm		
Roll	0.4	μrad		
Lateral shift	100	nm		

Diffraction on grating gaps

Because G1 and G4 are single gratings there are no diffraction induced intensity modulations at the fourth grating. The modulations induced by the gap at GA2&3 are

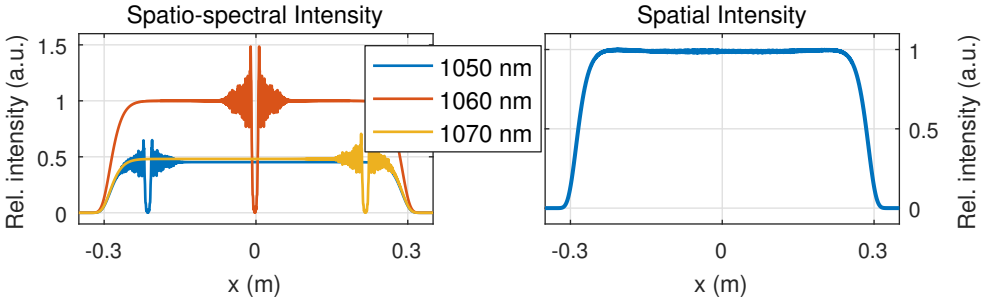

Figure 4.16: Diffraction induced intensity modulations of each spectral component (a) are averaged out on G4 where all spectral components overlap (b).

averaged out as the position of the gap within the beam aperture is dependent on the wavelength (see Figure 4.16).

Line density variation

The process of the compensation LDV is again analogous to the 1740 ln/mm configuration. One grating within the pair is tilted to suppress the residual AD, and the overall angle of incidence and grating spacing has to be then adjusted to tune the spectral phase. Since 1136 ln/mm gratings have lower dispersion, looser tolerance values can be expected. The tilts and piston required for the compensation of the residual AD and residual GDD, TOD with respect to the nominal configuration are summarized in Table 4.13. The residual quadratic angular chirp is illustrated in Figure 4.17. The impact of 1 ln/mm LDV is indeed very low compared to 1740 ln/mm design.

Table 4.13: Compensation of line density variation in the 1136 ln/mm compressor; $\theta_{Yaw}^{\Delta NC}$ stands for the yaw adjustment needed to suppress residual angular dispersion, ΔL and $\Delta\alpha$ stand for the adjustments of the grating spacing and the angle of incidence needed for the compensation of residual spectral phase.

LDV ln/mm	$\boldsymbol{\theta_{Yaw}^{\Delta N_C}}$ mrad	**Δ L** mm	**Δα** mrad	$\boldsymbol{S_\omega}$ -
1	1.1	18.9	2.5	0.99
5	5.5	71.9	11	0.9

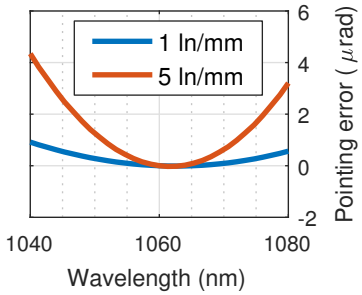

Figure 4.17: The residual quadratic angular dispersion present when LDV is compensated by GA yaw.

Pre/post-pulses (GM)

Since only the GA2&3 are in the grating-mirror configuration and all assemblies are vertically tilted, there are no retro-reflection into the laser as in 1740 ln/mm design. However, as the compressor operates near the Littrow angle, the specular reflection from the GA2&3 is reflected in the same direction as the diffracted beam. In the horizontal plane, the GAs operate as a roof mirror. Therefore they retro-reflect the incoming beam back and spatially inverse the beam in the horizontal plane with respect to the GA gap. Similarly, the diffracted and reflected beams are mirror-like reflected and propagate under the same angle in the vertical plane but since they have slightly different optical paths, they are vertically offset. The process is illustrated in Figure 4.18.

When the beam is diffracted as the zeroth order from either GA2 or GA3, it is diffracted off the gratings only 3 times in total as the first diffraction order. It has

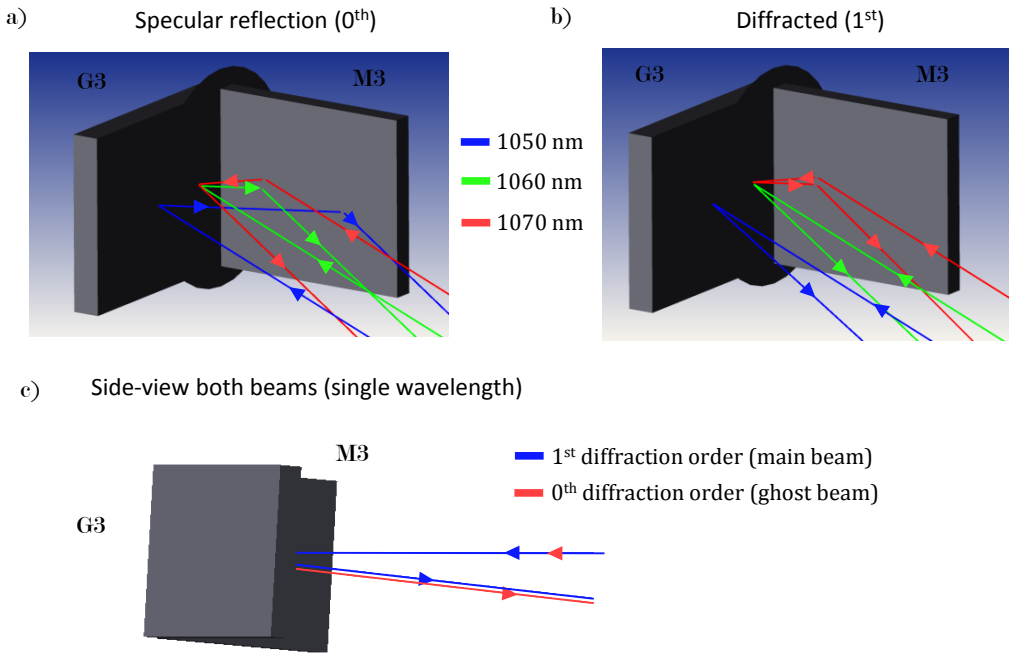

Figure 4.18: Optical path of the main vs the ghost beam at the GA3 exported from ZEMAX; a) Comparison of the optical path of various wavelengths for the specular reflection b) Comparison of the optical path of various wavelengths for the diffraction c) Side view on the GA3

residual angular chirp equal to the grating dispersion at the compressor output. Therefore, there is a wavelength λ_p for which the incidence angle α is equal to its Littrow angle at the off-plane configuration so that this wavelength propagates in a parallel direction with the main beam after both beams are diffracted at G4. If we substitute the incidence and the off-plane angles using known yaw and pitch rotations of the gratings from Eq. (2.5, 2.6) into the grating equation Eq. (2.2), λ_p can be estimated to 1059.5 nm. After the compressor, both beams will propagate approximately 30 m to the experimental chamber with a 0.9 m diameter focusing parabolic mirror. Since the ghost beam propagates with the residual AD, it gains residual spatial chirp. A part of the spectrum is then clipped at the G4 and the aperture of the parabolic mirror. Also, only a narrow part of the spectrum centered at λ_p is focused to the same spot as the main beam. Determination of the arrival time of this specular reflection with respect to the main pulse and the estimation of its energy is very important to prevent possible ionization of the experimental targets.

The estimation of the arrival times is a very intricate task. Generally, it depends on the position of the grating mirror gap with respect to λ_p, the input temporal chirp and the sign of the (λ_p-λ_0) (i.e. whether is λ_p delayed with respect to the λ_0 in the compressor). Nevertheless, the delay of the specular reflection with respect to the main beam can be partly estimated through the comparison of the optical path at each grating. A spatio-temporal simulation was performed in ZEMAX and Matlab to verify the results. To decrease sampling requirements originating from the linear (angular dispersion) and quadratic (temporal chirp) phase dependence in the x-ω domain only a 6 cm beam diameter and 1 nm bandwidth centered at λ_p were employed. Such simplification offers sufficient resolution without losing any significant information. The nominal configuration of the compressor was ray-traced to calibrate the time axis (set

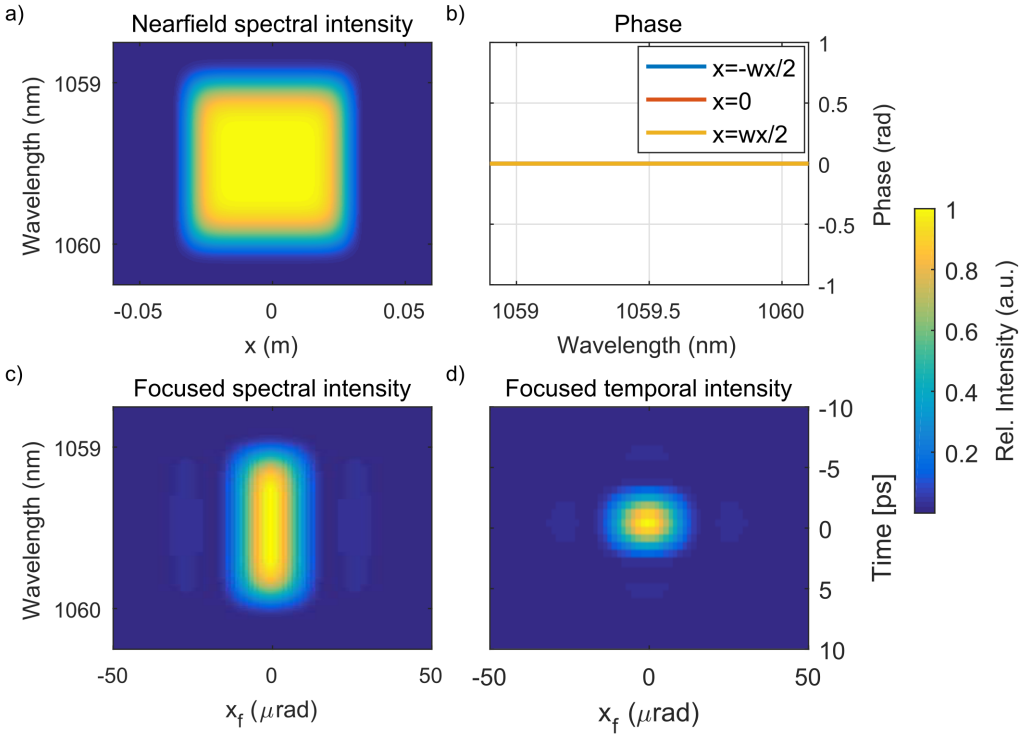

Figure 4.19: Simulated spatio-temporal profile of the nominal configuration. The simulation used only a 6 cm diameter and 1 nm spectral bandwidth to limit sampling requirements. a) Near-field spectral intensity profile; b) Near-field spectral phase profile; c) Focused spectral intensity; d) Focused temporal intensity

up the zero arrival time). The diffraction order of either GA2 or GA3 was then changed to zero and the compressor was ray-traced again. At the parabola, the nearfield profile of the beam was transformed to farfield using Fraunhofer diffraction integral for each spectral component (Eq. 1.36). The temporal profile was then calculated through the temporal Fourier transform at each far-field point (Eq. 1.2). A virtual compressor in the exactly same configuration with negative distances was placed in ZEMAX before the examined compressor model. The beam propagating through the nominal configuration therefore exhibited zero OPD and zero GDD in total at the image plane. This helped to suppress uncertainty of the arrival time of the ghost pulse due to reflections in Fourier domain and also to reduce the sampling requirements. A simulated spatio-temporal profile of the nominal configuration is shown in Figure 4.19. The duration of the focused pulse is around 2 ps due to narrow bandwidth employed in the simulation. However, since the ghost beam has residual angular dispersion, the spectral overlap in the focal plane is much smaller. The pulse duration of the focused ghost beam then mostly depends on the simulated beam size which is inversely proportional to the focused spot size which influences the spectral overlap in focus. Two scenarios will be examined here. First, the delay of the specular reflection of GA3 and second the specular reflection of GA2 will be discussed.

GA3 Zeroth order

In this scenario, the first half of the compressor operates as usual. The beam incident on the GA3 has regular spatial chirp present after the GA2 and no residual AD, it is collimated and half of its temporal chirp is compensated. The specular reflection off the GA3 then only inverses the spatial chirp and sends the beam towards the G4.

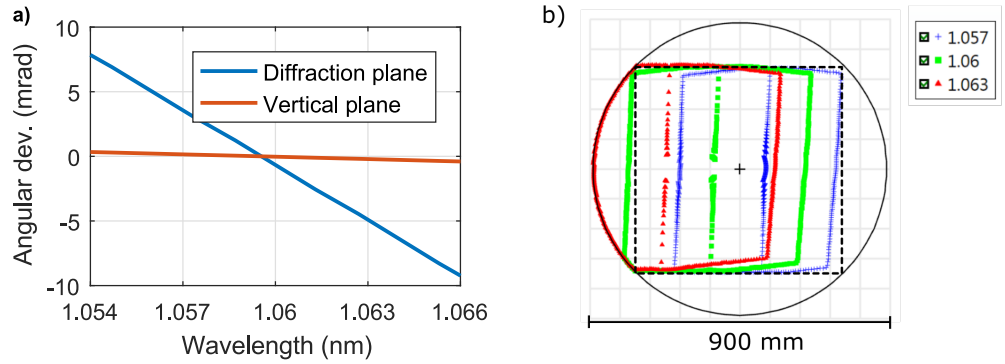

Figure 4.20: Residual angular dispersion (a) and the spatial chirp (b) of the ghost beam at the position of the focusing parabola exported from the Zemax model. The profile of the main beam is marked with dashed black curve.

Because the G4 diffracts the beam as its first order, the beam is angularly dispersed and its spatial chirp is further increased during its propagation towards the parabolic mirror. The simulated profile of the residual angular dispersion (Figure 4.20a) at focus confirms that the propagation direction of 1059.5 nm component is parallel with the beam. The nearfield profile (Figure 4.20b) shows that there is no significant clipping of the spatial profile of λ_p at the aperture of the focusing parabola.

To determine the arrival time of the ghost beam with respect to the main beam, their optical path at the GA3 and G4 were compared for λ_p. The top view of the GA3 (Figure 4.21a) shows that the ghost beam has approximately 10 cm longer optical path since it travels from the G3 to the M3 in the rooftop configuration whereas the main beam diffracts solely from the G3. Contrarily, since the ghost beam is horizontally shifted with respect to the main one due to its specular reflection off the GA3, the optical path of the ghost beam at the G4 is 16 cm shorter compared to the main beam. In total, that means that the ghost beam has 6 cm shorter optical path then the main pulse and therefore it should arrive approximately 200 ps prior to the main pulse. The numerical simulation presented in Figure 4.22 confirms that the ghost reflection is a pre-pulse with arrival time 250 ps prior to main pulse. Its pulse duration is around 300 ps at each point due to spectral narrowing induced by residual angular dispersion at focus. However, in simulation the ghost beam has bigger spectral overlap in focus since the beam diameter was limited to 6 cm. In reality, the beam size is 10 times bigger, so 10 times longer pulse duration can be expected assuming aberration free focusing system and perfect flat wavefront of each spectral component. The arrival time of the ghost

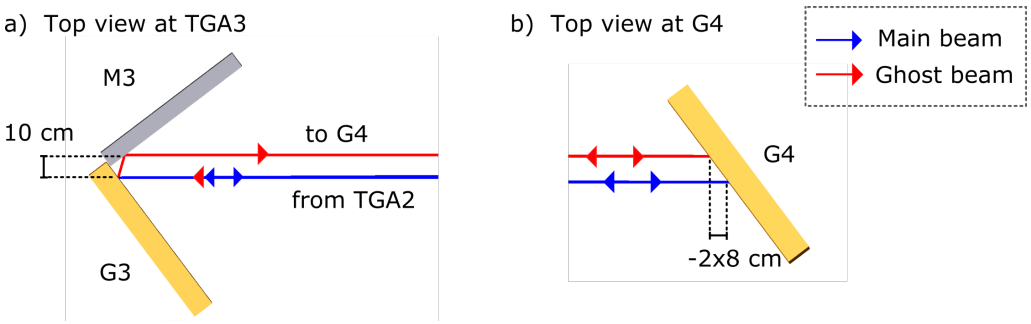

Figure 4.21: Comparison of the optical path of the ghost reflection and the main beam at GA3 (a) and G4 (b).

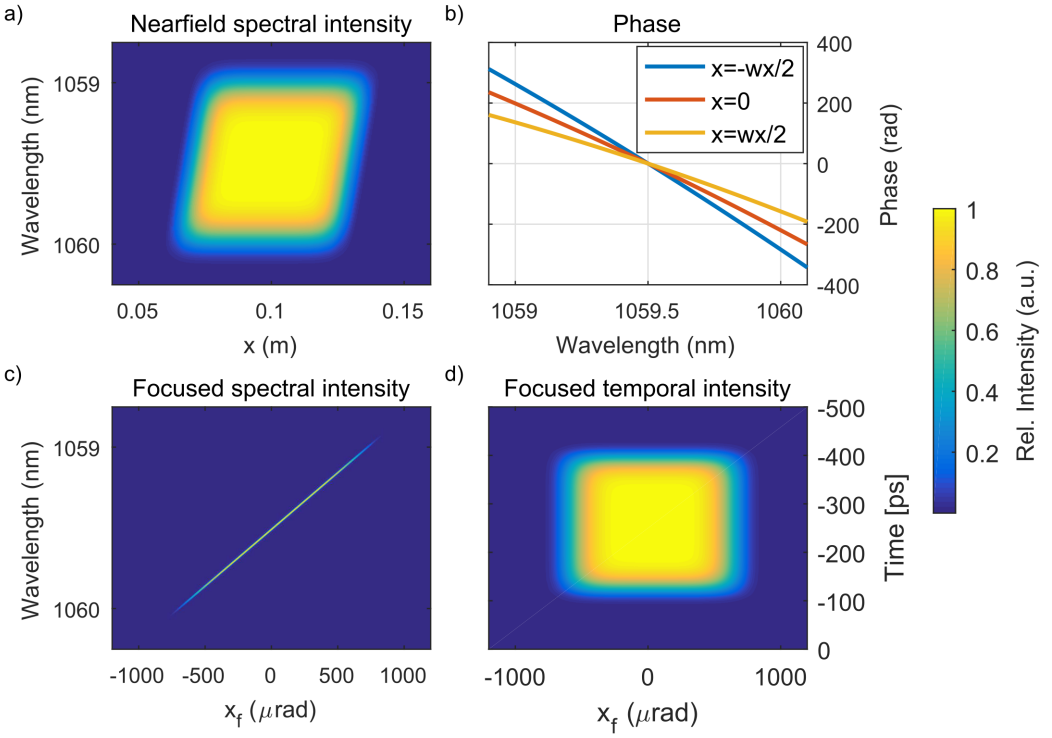

Figure 4.22: Simulated spatio-temporal profile of the configuration with specular reflection of GA3. a) Nearfield profile; b) Nearfield phase profile; c) Focused spectral intensity; d) Focused temporal intensity

pulse can be possibly adjusted by moving the GA gap towards the point of incidence of the input beam (intersection of the grating front surface and the blue line in Figure 4.21). Nonetheless, it is not feasible to filter the prepulse entirely as the movement of GA gap also shifts the compressor spectral transmissivity. The prepulse duration is expected to be several ns. According to Figure 4.21, -10 cm shift of the grating mirror gap induces 200 ps change in the delay of the ghost pulse. Filtering the prepulse would then require more than -50 cm shift of the grating mirror assembly which would significantly reduce the compressor transmissitivity for the higher wavelengths.

The relative intensity of the postpulse can be estimated as follows: First, due to the angular dispersion only a subset of spectra is focused into the same spot as the beam. Here, we assume that the light incident within 15 μm radius from the focused beam can influence the contrast of the focused main pulse (10 times the spot size). Since the residual angular dispersion is 1.4 mrad/nm, only 10 pm bandwidth of the ghost pulse is encircled in the target radius having only $2 \cdot 10^{-3}$ relative energy. Second, the geometrical vignetting of the rays leads to truncation of 30% of the rays within the encircled bandwidth. Third, the encircled bandwidth corresponds to $\sim ns$ pulse duration. The residual temporal chirp can be neglected as the compression factor is -200 ps/nm. Fourth, the diffraction efficiency into zeroth order is estimated to be approximately 1%. Altogether, the relative intensity 10^{-9} can be obtained. In reality, the relative intensity of the pre-pulse will be further reduced by tighter focusing which will mainly result in additional pulse broadening.

GA2 Zeroth order

The scenario where GA2 diffracts as the zeroth order is more complicated. The beam is diffracted of the G1 and incident on the GA2. The specular reflection at the GA2

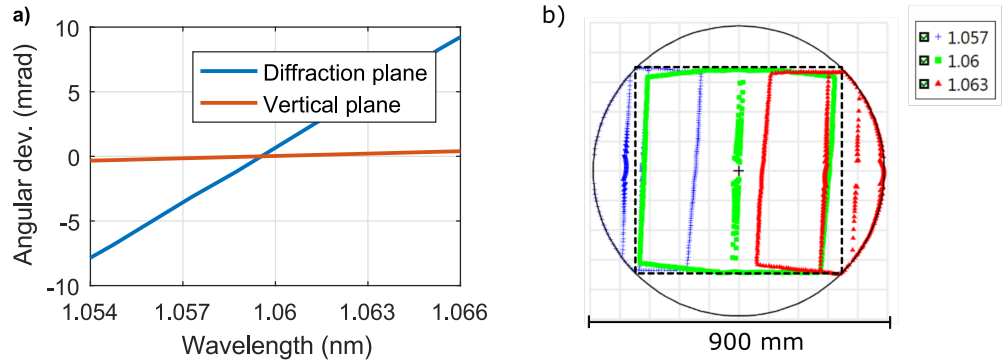

Figure 4.23: Residual angular dispersion (a) and the spatial chirp (b) of the ghost beam at the position of the focusing parabola exported from the Zemax model. The profile of the main beam is marked with the dashed black curve.

flips the horizontal coordinates but retains the angular dispersion. The reflected beam therefore gains additional spatial chirp as it propagates towards the GA3. The GA3 diffracts the beam and since its spatial coordinate was inversed, the angular dispersion is doubled by diffraction. At the G4 the ghost beam has approximately four times bigger spatial chirp than at the GA2. Diffraction at then G4 reduces the residual AD of the ghost beam to half - i.e. it is only flipped with respect to the GA3 scenario (Figure 4.23a). The simulation confirms that even for this scenario, λ_p is equal to 1059.5 nm. At the focusing parabola, the ghost beam has much bigger spatial chirp than in the previous scenario and therefore more energy is clipped there (Figure 4.23b). Nevertheless, the narrow bandwidth centered at λ_p propagates through the compressor without significant losses.

The ghost beam has approximately 10 cm longer optical path at the GA2 compared to the main one as it travels from the G2 to the M2 in the rooftop configuration (Figure 4.24). The optical path between the GA3 and G4 is the same for both beams because the optical path difference at the GA3 is opposite to the optical path difference at the G4 as the effective apertures of the GA3 and G4 are parallel. It follows that 9 cm longer optical path of the ghost beam leads to approximately 300 ps delay with respect to the main pulse, which agrees with the results from the numerical simulation presented in Figure 4.25.

The relative intensity of the post-pulse can be estimated to 10^{-9} analogously to the previous scenario since the residual angular dispersion has the same absolute value and

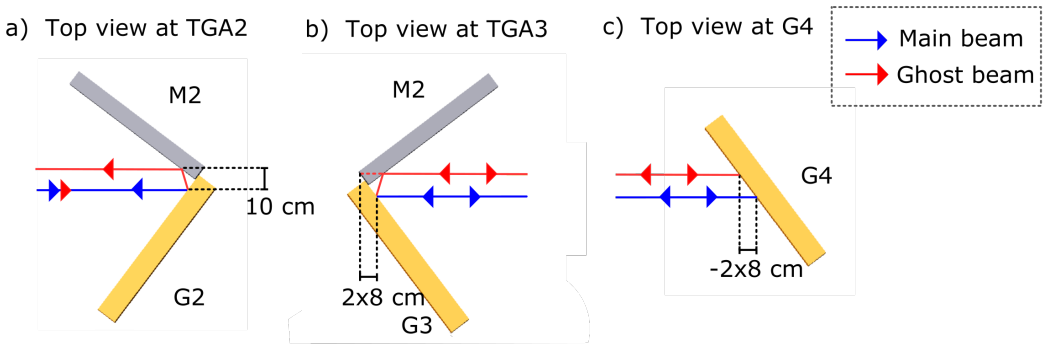

Figure 4.24: Comparison of the optical path of the ghost reflection and the main beam at GA2 (a), GA3 (b) and G4 (c).

there is no significant clipping of λ_p spectral component.

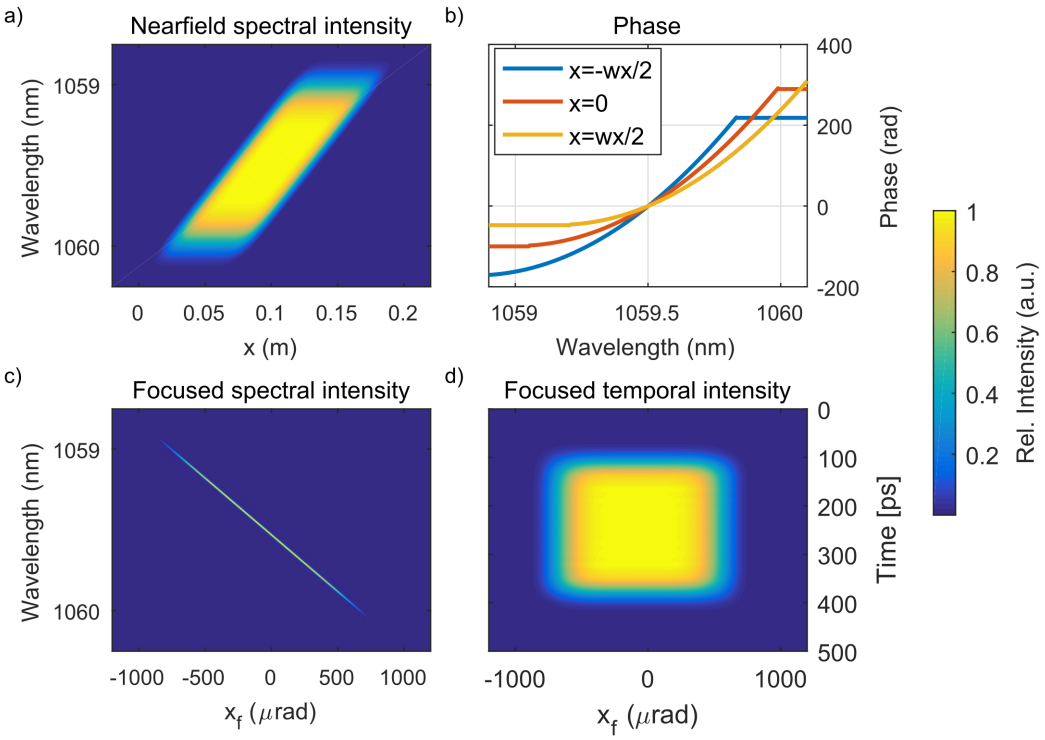

Figure 4.25: Simulated spatio-temporal profile of the configuration with specular reflection of GA3. a) Nearfield profile; b) Nearfield phase profile; c) Focused spectral intensity; d) Focused temporal intensity

Discussion

Thanks to the low line density of the gratings, the 1136 ln/mm compressor design offers looser alignment tolerances compared to the 1740 ln/mm design. The grating-mirror configuration of the GA2&3 suppresses line density variation issues and since the first and the last grating comprises a single grating, there is no diffraction induced intensity modulation at the compressor output. The simulation results confirm that the grating-mirror configuration is feasible as it has a smaller number of degrees of freedom and avoids the determination of the absolute piston misalignment. Still, it requires almost two times better alignment precision for the alignment of the mirrors with respect to the gratings. The pre-pulses and post-pulses originating from the zeroth diffraction orders at the second and third grating-mirror assemblies will have to be examined experimentally. Their delay with respect to the main beam can be partly adjusted by moving the grating mirror gap which modifies also compressor spectral throughput. Nevertheless, the entire filtration of the pre-pulses might not be possible due to their long temporal duration. These pre and post pulses might introduce a ns-pedestal around the main pulse with relative intensity lower then 10^{-9}. The relative intensity of the pedestal is mostly dependent on spectral overlap in the focal plane and therefore it will be given by the focusing setup and the aberrations of the real beam. To summarize, the 1136 ln/mm design exhibits generally looser alignment tolerances, it avoids diffraction induced intensity modulations at the compressor output and line density variation issues and it was therefore selected for the implementation of the L4 compressor.

5. Phasing

This chapter encompasses design and testing of the alignment system for grating-mirror assemblies for the 1136 ln/mm compressor. It will mostly focus on the means of optical alignment of the assemblies as optical methods directly monitor the mutual position of the optical surfaces. The other methods such as the ones using displacement sensors are able to provide sub-nm precision but they measure displacement towards some reference which is not directly coupled with the optical surface. Therefore such sensors cannot be employed for the first alignment of the grating mirror assembly. Moreover, position of their reference can drift in time with respect to the optical surface due to thermal effects and introduce additional systematic errors.

Tolerance values from Table 4.12 demand sub-microradian resolution for the mutual alignment of the grating and mirror in the 1136 ln/mm compressor design. Resolution better than $\lambda/50$ is required from interferometric methods for a beam with $w_0 = 25$ mm at a 1 μm wavelength. Such resolution is achievable for relative measurements monitoring the mutual position of the grating and mirror using the Fourier fringe analysis method [87]. For an absolute measurement required for the first alignment, a careful calibration is necessary as the interferometric method posses some systematic errors even when for an ideal surface figure of the measured component.

The resolution of the farfield method can be roughly estimated from the Rayleigh criterion. Using the same beam parameters mentioned above, the angular resolution can be estimated to 10 μrad. With the help of numerical processing, the resolution can be further improved by comparing the fitted width of the measured focal spot with some ideal spot reflected off some reference optics. The dependency of the beam width on yaw, pitch and piston misalignments are shown in Figure 5.1. Simulation shows that 0.1 μrad yaw misalignment yields only 0.1% increase of the measured beam width. Such precision is hardly achievable due to noise-induced through the air turbulence and dark noise induced by the thermal heating of the camera. The resolution could be improved using split foci method reported in [47], where the assembly is intentionally misaligned in one angular degree of freedom (pitch), while the centroid position is measured for the other angular degree of freedom (yaw). Since the focal spots do not overlap, the coordinates of centroid can be compared with high accuracy. However, such a method cannot be employed for the online measurement of the assembly as it would require to misalign the assembly between shots. The interferometric method clearly offers better resolution at fixed beam size. Also, a calibration taking into account the surface figures of optics, retrace and other types of errors can be implemented into the interferometric method more easily. The resolution of both methods cannot be improved by lowering the wavelength of the alignment laser due to the reflectivity of the MLD coatings of

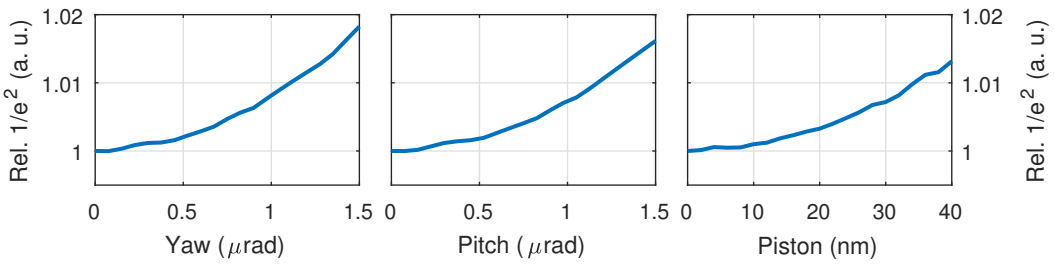

Figure 5.1: Sensitivity of the far-field phasing method. Graphs a)-c) show the dependence of the relative increase of the $1/e^2$ width of the focus on the indvidual misalignments.

the gratings and mirrors as it is discussed later.

During operation, an alignment setup will be used to maintain the mutual position of grating and mirror within the assembly. Since an alignment beam will probe only a part of the total GA aperture, it is expected that the final fine tuning of the alignment will be done based on the full aperture measurement of the main beam. Such measurement cannot distinguish which GA induces the error, but since only GA2&3 are tiled, their small misalignments can be mutually compensated. Nevertheless, the alignment system will be designed and calibrated to eliminate absolute errors as much as possible. These errors are relevant for the first alignment of the GA but not for the relative measurement required to fix the position of GAs during operation.

Configuration

The setup is based on a Fizeau interferometer with additional far-field diagnostics and it will be settled on an optical table placed next to the compressor chamber. A fiber coupled Bragg grating diode is split by a 50/50 beamsplitter. Each branch then serves for diagnostics of one grating assembly. Both branches are collimated to a w_0=2.5 mm and the beam then passes through two more beam-splitters. The first BS1 and the second BS2 beamsplitter serve for far-field and near-field diagnostics of the back-reflected beam respectively. The beam diameter is further expanded ten times by a Keplerian telescope composed of f200 and f2000 planoconvex lenses. The vertical coordinate of the beam is increased by a periscope to fit it vertically in between G1/GA3 and G2/GA4. Afterward, the beam passes through a vacuum window into the compressor chamber. Inside, 40% is back-reflected by a transmission flat with a slight pointing deviation to introduce a carrier frequency into the interferogram. The rest of the beam passes through the flat and is reflected off the motorized mirror oriented at 45°. The mirror steers the beam towards the grating-mirror assembly with a slight vertical angle so that it is incident at the exact Littrow angle with no off-plane deviation. The beam is then diffracted and it propagates the exactly same path backwards to the BS2 where it is further demagnified by a 2:1 Keplerian telescope and an interferogram is recorded on a camera. Both telescopes are designed so that the grating-mirror gap is imaged on the NF camera CCD chip. An intermediate image plane will be located 10 cm in the front of the f200 lens. The back-reflected beam is also reflected off the BS1 and it is focused by a f700 lens onto a camera. The focused spot diameter is expected to be roughly 200 μm to achieve sufficient resolution using a regular camera with few

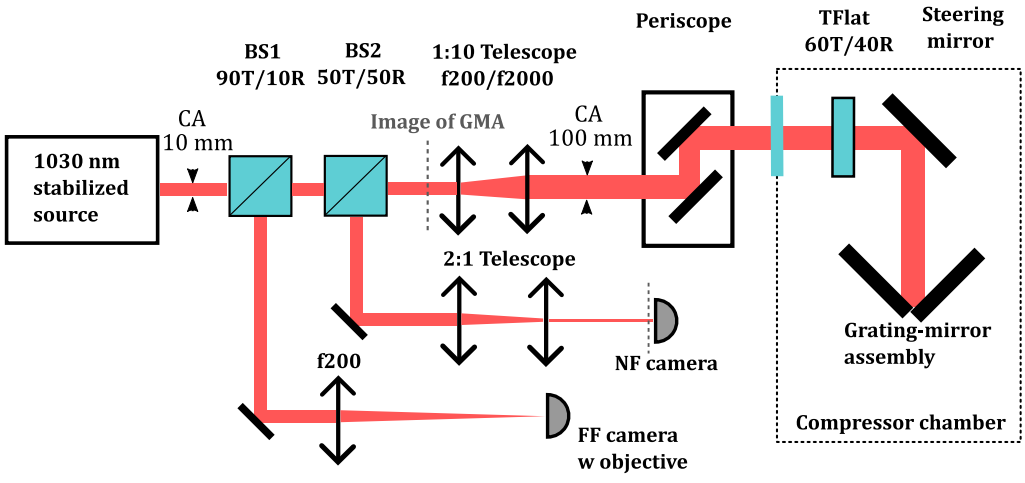

Figure 5.2: Layout of the Fizeau interferometer for grating-mirror phasing

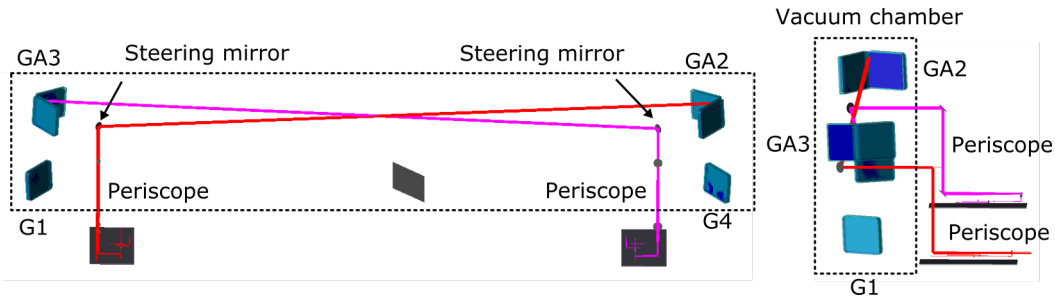

Figure 5.3: Layout of the phasing beams within the compressor exported from a ZEMAX model. Most parts of the interferometer will be located on a separate optical table located close to the compressor chamber. The probe and interferometric beams will be injected to the compressor using periscope and a dedicated flange.

μm pixel size.

The best visibility of fringes is achieved with a 40R/60T coating with diffraction efficiency of the grating-mirror assembly better than 90%. All the large aperture optics after the f2000 lens is planned to have $\lambda/20$ PV at 633 nm surface figure to reduce systematic errors. The expected layout of the interferometric beams within the compressor is illustrated in Figure 5.3.

Systematic Errors

Uncertainties discussed in this section are mainly relevant for the measurement of the initial mutual position of the grating and mirror. There are three main types.

The most significant error comes from the surface figure of the back side of the transmission flat and the front side of the steering mirror. The reference beam reflected off transmission flat gains wavefront deviation equivalent to two times the surface figure of the back side compared to the probe beam. The surface figure steering mirror induces the error equivalent to three times surface figure since the beam hits the mirror two times and the mirror is tilted at 45°. The deviation in the retrieved coefficients is then given by the symmetry of surface figures of the measured optics. For example, a defocus and vertical astigmatism introduce deviation in the yaw coefficient. An oblique astigmatism deviates the pitch. A coma aberration then deviates the piston only.

Another systematic error originates from the fact that the alignment beam samples only a sub-aperture of the grating and mirror. The local gradient of the surface figure then does not have to match the overall gradient of the full surface figure. The difference between these gradients induces an alignment error. However, since the part of the beam which is incident on the mirror also hits the grating, a part of this error is self-compensated due to the mirror symmetry. The grating induced wavefront gradient in the vertical plane is exactly mirrored and therefore it does not induces any pitch error. The same applies for the piston error. The grating induced wavefront gradient in the horizontal plane is doubled and introduces the yaw error. The errors induced by the mirror surface figure are all doubled. To estimate the impact of the sub-aperture error, a full grating surface figure was simulated in Matlab using Zernikes polynomials of the 2-8 order. The top right corner of the grating aperture with 5x10 size was selected as the sub-aperture. A copy of the grating sub-aperture was mirror inversed. Both sub-apertures were fitted with a plane and their coefficients were compared. The simulation was performed 20 times with $\lambda/3$ PV grating surface figure and yielded maximal PV error of the grating sub-aperture $\lambda/20$ with 2μrad yaw coefficient.

Another major systematic error is called retrace error and it can be explained as follows. Since the reference beam, reflected off the transmission flat, and the probe

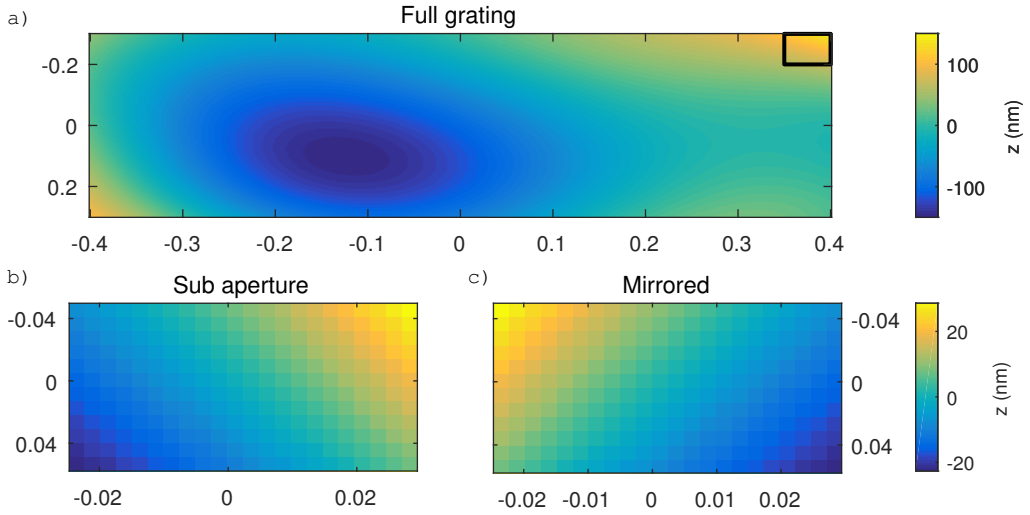

Figure 5.4: Example of the subaperture error. In the shown example, the Peak-To-Valley ratio wavefront error of the full grating was set to 300 nm, while the Peak-To-Valley ratio of the subaperture yielded only 40 nm resulting in 1 μrad yaw difference.

beam, diffracted at the grating-mirror assembly, do not share exactly the same path during back propagation, their wavefront deviation gained during back-propagation can differ. The retrace error is a systematic error which increases with a carrier frequency of the interferogram and is induced via two mechanisms. First, the reference beam has slight angular deviation and therefore it passes through the lenses under different angles. Second, as the reference beam propagates back it becomes spatially offset with respect to the probe beam within the aperture of the optics. Surface figures of the mirrors and lenses are not ideal and therefore the induced wavefront deviation of both beams is spatially shifted with respect to each other and no longer compensate each other entirely. To estimate the impact of the retrace error, an optical analysis was performed in ZEMAX using randomly generated surface figures using the spherical, astigmatism and coma aberration with a peak to valley ratio according to the previous section. The angular deviation of the beam reflected off the transmission flat was set to 250 μrad and the wavefront of the probe and the reference beams was subtracted. The PV of the retrace error was smaller then $\lambda/50$ in each of 20 cases with the wavefront PV of the individual beams smaller then $\lambda/3$. The surface figure of the transmission flat and steering mirror was neglected in the simulation to separate the retrace error.

The errors originating from surface figures of the optics can be numerically subtracted assuming that the surface figures are accurately characterized and that the interferometric beam is centered within their aperture. The sub-aperture error can be

Table 5.1: Systematic errors of the interferometric measurement. The table shows the maximal possible errors induced by surface figures of optics for a given PV.

Error source	**Est. PV**	**Yaw** μrad	**Pitch** μrad	**Piston** nm
Tranmission flat	$\lambda/15$	3	3	60
Steering mirror	$\lambda/11$	4	4	90
Subaperture grating ($\lambda/3$ full ap.)	$\lambda/20$	2	-	-
Subaperture mirror ($\lambda/10$ full ap.)	$\lambda/50$	1	1	40
Retrace error	$\lambda/50$	1	1	20

included in a similar fashion if the surface and holographic errors of the grating are known. The retrace error can be calibrated using one of the established methods [88]. It also possible to set up the whole system at the working position and place a high quality reflection flat in between the steering mirror and the grating-mirror assembly. The retrieved phase profile should correspond to the overall systematic error of the system. The accuracy of this approach is mostly limited by the surface figure of the additional reflection flat.

Laser source

A laser used for the alignment has to operate near the central wavelength of the laser. Compared to the tiled grating setup, the grating-mirror configuration is bound by the following condition. Since one part of the beam is reflected straight off the grating, the other part undergoes additional two reflections from the mirror. Both farfield and nearfield phasing methods require to have roughly the same intensity of both beam halves (even though interferometric method is more flexible in this aspect). The alignment laser has to therefore operate in the wavelength region, where the mirror is close to 100% reflectivity, to get similar intensity of the both beam halves. According to the expected reflectivity plots of the MLD mirrors, the working region is 1020 - 1100 nm. The alignment laser should also meet following criteria. First, it should preferably operate at the Littrow angle to avoid the placement of the additional back reflecting mirror. Second, the beam path should not collide with the existing beam paths in the compressor. Third, it should have sufficient coherence length. Since the transmission flat has to be positioned at the other half of the compressor than the measured grating assembly to avoid the optical path of the main beam, the laser coherence length should be at least 30 m which corresponds to a 4 MHz linewidth. Fourth, it should be preferably fiber-coupled and temperature stabilized to avoid pointing and wavelength drifts.

The operating wavelength around 1030 nm meets all these requirements, since the 35.8° Littrow angle has suitable beam path through the compressor (Fig. 5.3). The selected laser diode QFBGLD-1030-5 [89] is a fiber bragg grating wavelength stabilized single mode laser. The diode is operated by an Arroyo 6305 ComboSource laser diode driver with integrated temperature control. Since the diode has only 5 mW output, the output power will be too low for a pre-alignment of the inteferometric setup due to larger beam size. This pre-alignment will be done with a separate 400mW fibre-coupled laser diode with the same central wavelength having shorter coherence length. After the prealignment the diodes will be swapped and therefore the output pointing should be preserved.

5.1 Fizeau interferometer

To evaluate experimental accuracy of the phasing methods, a Fizeau interferometer with farfield diagnostics was built (Figure 5.5). A frequency stabilized He-Ne laser is collimated to 2 cm diameter. After passing through a beamsplitter cube, a part of the beam is back-reflected by a high quality transmission-flat, while the rest of the beam is incident on the measured surface and is retro-reflected back. Both beams are then down-collimated by a 7:1 telescope and their interference pattern is measured by a 12-bit Bassler ACA camera. A far-field profile of the beam is also monitored by an 8-bit U-Eye camera.The spatial phase profile is extracted from the interference pattern by the Fourier fringe pattern analysis method discussed in Section 2.2.3. Compared to the more established phase-shifting technique, the Fourier fringe pattern analysis

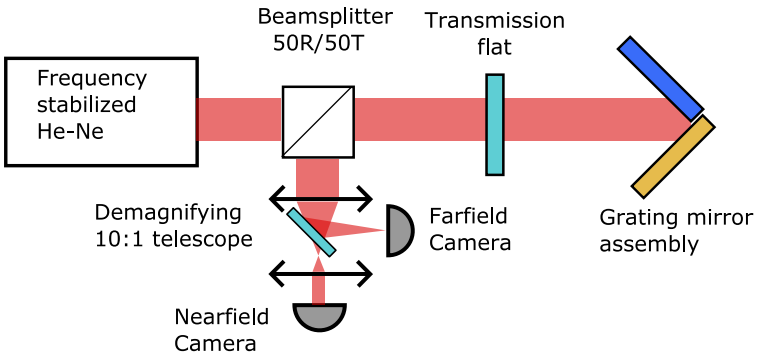

Figure 5.5: Layout of the constructed Fizeau interferometer

method allows to obtain phase at real-time without the need of additional moving actuators on either transmission flat or measured object. The procedure of the phase extraction was programmed in Labview to allow easy portability and broad hardware compatibility. The individual steps of the algorithm are sketched in Figure 2.11. Firstly, a mask defining the region of interest is created. The masked intensity pattern is Fourier transformed to a spatial frequency domain. The term with the induced carrier frequency is then Hanning filtered to reduce spectral leakage, moved to zero and inverse Fourier transformed back to the spatial domain. The resulting complex field contains the measured wrapped phase profile. The phase profile is unwrapped by the Goldstein algorithm [51]. Both beam halves are then fitted with a plane and the coefficients of the plane fit are then compared to retrieve the relative yaw, pitch angles and the relative piston according to Eq. (2.11). The farfield intensity distribution calculated from the retrieved coefficients can be then compared to the measured one.

5.2 Testing

The following text is based on [A5].

Initial laboratory tests were conducted on an in-house developed mount equipped with flexible joints offering sub-microradian precision for the positioning the mirror with respect to the grating. The mount was developed to prove the validity of the

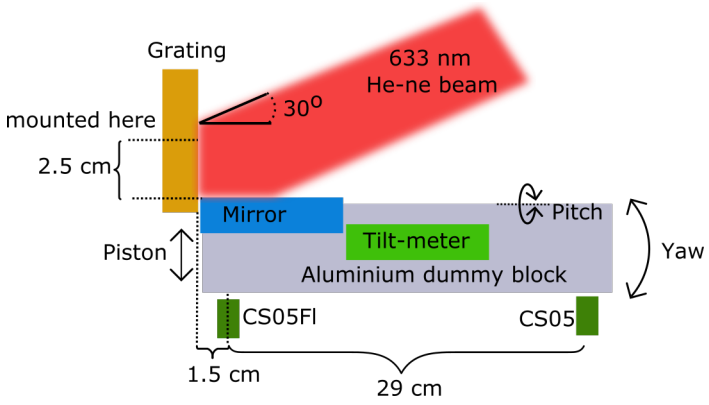

Figure 5.6: Experimental setup: 633 nm He-Ne beam is incident on a grating-mirror assembly under the Littrow angle, the position of the mirror is also monitored by capacitive sensors and a tilt-meter.

grating-mirror concept and was then employed in the sub-aperture compressor. For the testing, the mount was fitted with smaller sized optics - a Spectrogon 1740 ln/mm gold grating and a flat silver mirror. The mirror was attached in an aluminium block to fit the mount designed for a long striped mirror. The experimental scheme is sketched in Figure 5.6 and photos of the setup are shown in Figure 5.7.

For the measurement of yaw and piston misalignments, the mount was equipped with capacitive sensors. CS05 and CS05Fl probes with CapaNCDT6200 driver were provided by MicroEpsilon for the testing. The sensors measure the distance between their front face and a conductive surface in 500 μm range with few nm resolution. Readout positions of the sensors were zeroed at the beginning of the measurement. The yaw coefficient was calculated as the relative position difference of the sensors divided by their distance. The piston coefficient was obtained from the position of the CS05Fl sensor, which was located close to the grating-mirror gap, where the piston is defined. However, it was necessary to add a small correction term due to the fact that the sensor was not located exactly at the interface of the mirror and the grating but was shifted by 1.5 cm (see Fig.5.6a). The correction factor was calculated as: $\mathrm{CS05FL_{pos}} + \mathrm{Yaw} \cdot 1.5$ cm. The pitch misalignment of the mirror was monitored by a Jewell 755-series high gain inclinometer sensor. The sensor contains conductive liquid, an air bubble and three platinum electrodes. When the sensor is tilted, the area where the liquid touches the electrodes changes due to the movement of the air bubble. That in turn modifies the ratio of the resistivity of the electrode pairs which can be further processed to calculate the tilt of the sensor with respect to the gravitational vector. The sensor is capable of measurement of the tilts about two-axis - one representing the pitch of the mirror, the other representing the roll (rotation about the normal of the mirror). The resolution is 1 μrad at low-gain mode with 16 mrad range and 0.1 μrad

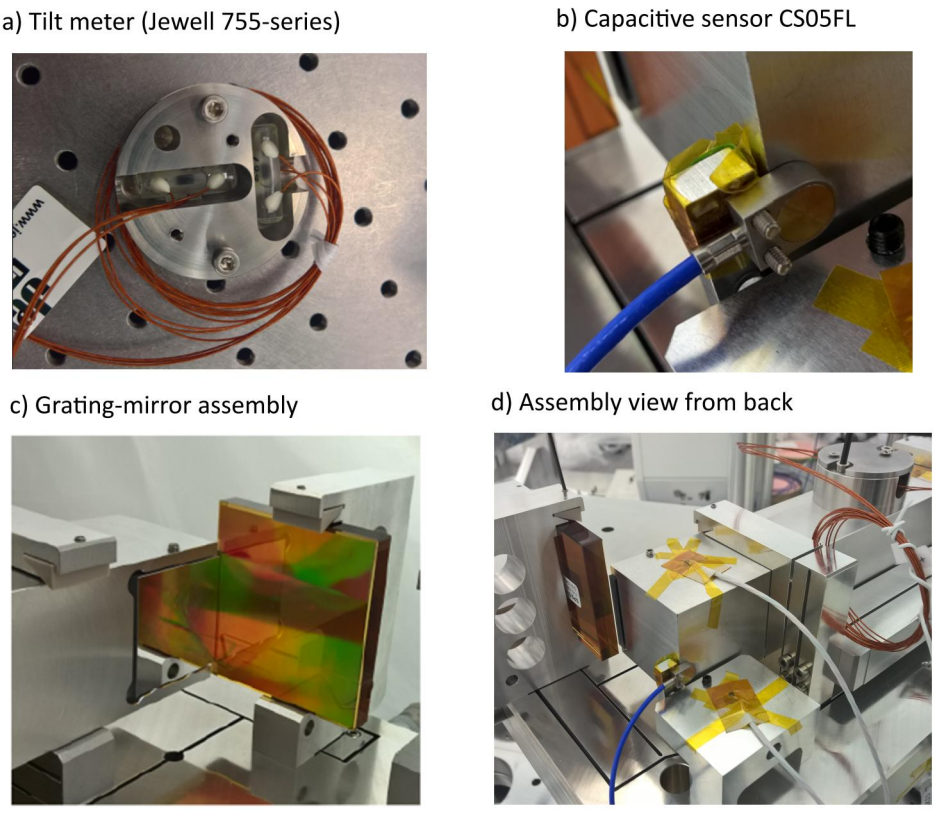

Figure 5.7: Grating-mirror compressor mount with the attached sensors

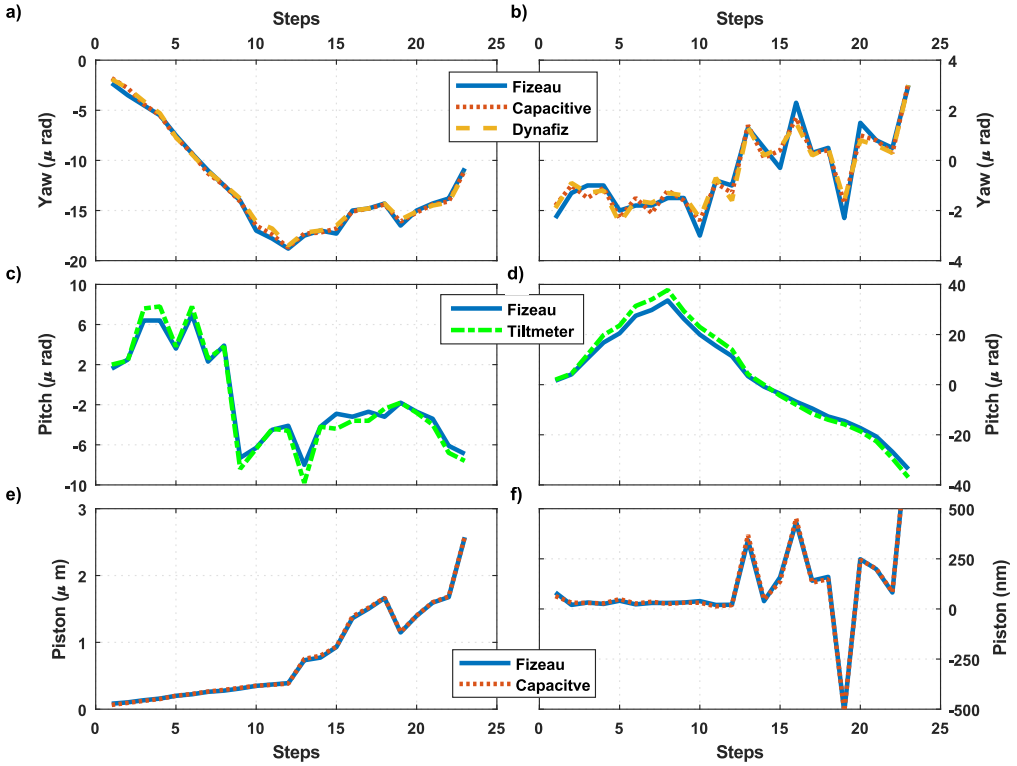

Figure 5.8: Short-term measurement, where the mirror was intentionally misaligned each step. a) shows the absolute value of the yaw misalignment, b) shows the relative value between the individual steps of yaw, c) shows the absolute value of the pitch misalignment, d) shows the relative value between the individual steps of pitch, e) shows the absolute value of the piston misalignment, f) shows the relative value between the individual steps of piston

at high gain mode with 2 mrad range. The sensor requires a first-order temperature correction. Temperature of the mount and air was monitored by RTD OMEGA sensors with 0.001° C resolution.

Firstly, we conducted a short-term measurement in which the mirror was intentionally misaligned in few consecutive steps and its position was monitored using all the methods described above. Fig.5.8a,b show excellent agreement of the yaw misalignment measurement between the ELI-developed Fizeau interferometer, Zygo Dynafiz and capacitance sensors. The standard deviation between the individual methods was calculated to be 0.2 μrad. The measurement of the mirror piston by capacitive sensors also coincides with the interferometric measurement with standard deviation of 15 nm (Fig.5.8e,f). The interferometrically measured mirror pitch misalignment was compared to the output of Jewell tiltmeters with a standard deviation within the resolution of the tilt-meter 0.4 μrad (Fig.5.8c,d). The graph also shows small systematic error as the magnitude of the tilt calculated by the tiltmeter is bigger than the tilt obtained from the interferometric measurement.

The accuracy of the measurement was mostly limited by the interferometric measurement because the beam diameter was only 2 cm. 0.2 μrad yaw misalignment then represents only 0.02 rad phase difference between the beam edges. On the other hand, the measurement was not influenced by the absolute error because only relative phase changes were calculated. The accuracy could be increased by using larger sized optics which would allow to increase the beam diameter.

Several long-term measurements were carried over the period longer than 12 hours

(Fig. 5.9, 5.10). During the long-term measurements, the yaw and piston measured by the capacitive sensors were usually much smaller than the actual displacement measured by the interferometry. The interferometric pitch measurement had slightly different gradient due to the temperature sensitivity of the tilt sensor. The deviation could have been also induced by thermal movement of the mirror since the tilt sensor was attached to the aluminium block while the intereferometer measured the optical surface of the mirror attached within the block.

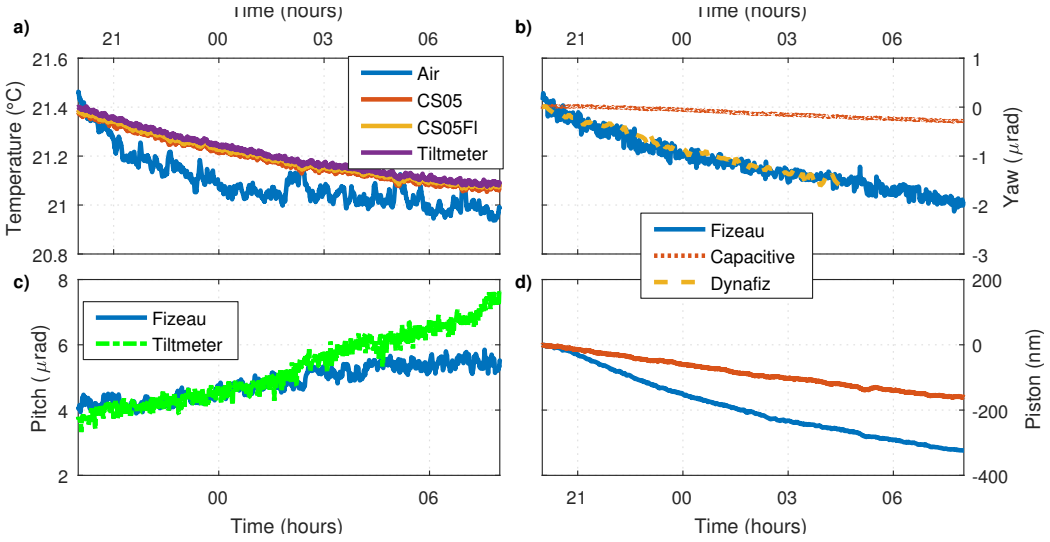

Figure 5.9: Selected long-term measurement of the grating-mirror alignment stability. a) Temperature at several positions, b) Yaw misalignment, c) Pitch misalignment and d) Piston misalignment.

The discrepancy between the short-term and long-term measurements of the piston was probably induced by the temperature expansion/shrinking of the aluminium desk on which the grating and the mirror were mounted. It can be explained as follows. The grating has a zerodur substrate and was attached to the mount at its center. There was 2.5 cm distance between the middle of the grating and the front plane of

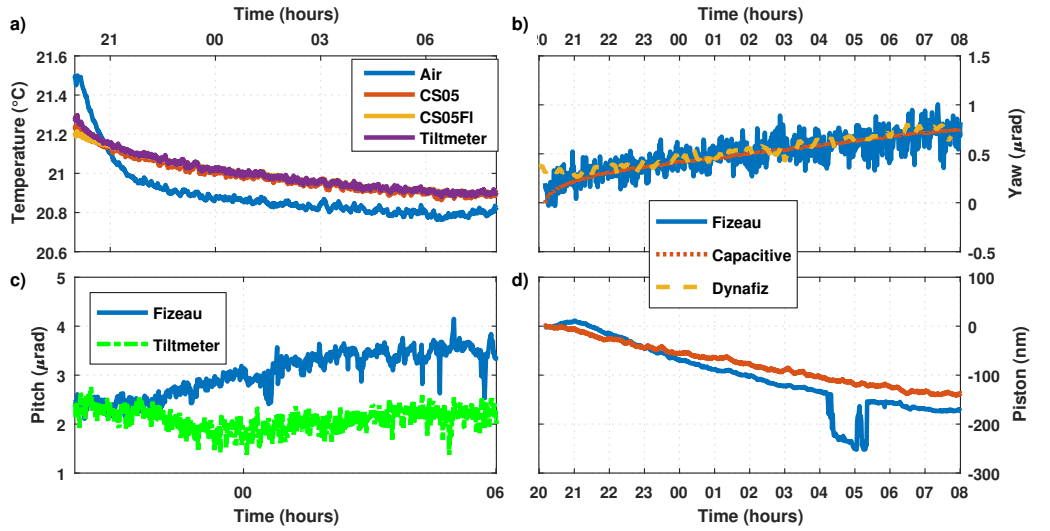

Figure 5.10: Selected long-term measurement of the grating-mirror alignment stability. a) Temperature at several positions, b) Yaw misalignment, c) Pitch misalignment and d) Piston misalignment.

the mirror. With decreasing temperature, the grating size remained almost constant (0.5 ppm change per °C), while the 2.5 cm part of the aluminium desk between the mirror and the place where the grating is attached shrank faster (20 ppm per °C). The edge of the grating then approached the front side of the mirror and therefore the piston drifted with the temperature change as it was measured interferometrically. On the other hand, the capacitive sensors were mounted on the desk from behind of the mirror and they thermally drifted with it. Therefore, they could not measure this temperature-induced drift. In Fig.5.11 the piston difference between the capacitive sensors and the interferometric measurement is compared with the thermal expansion of a 2.5 cm long aluminium slab according to Fig.5.9a. The data show good agreement. To avoid this effect, it is necessary to attach the capacitive sensors directly to the optics or, at least, attach the sensors to the mount/frame holding the optics which has the thermal expansion coefficient very close to the one of the grating substrate.

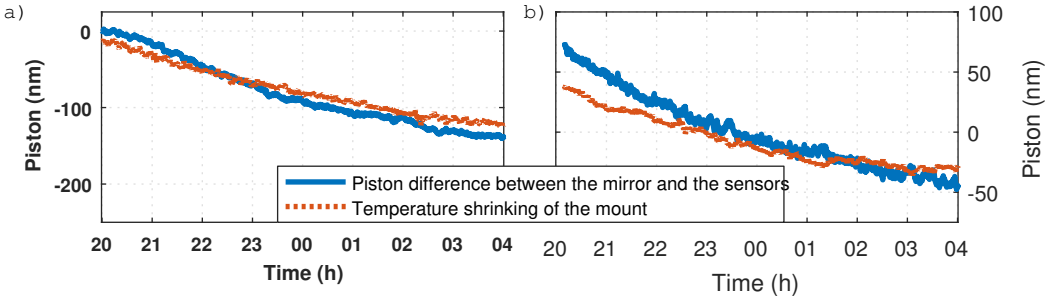

Figure 5.11: Comparison of the temperature expansion of the aluminium mount and the piston difference between the interferometric and capacitive sensor measurement for two longterm measurements. a) data from Fig.5.9, b) data from Fig.5.10.

The validity of the interferometric method was also crosschecked by comparing the simulated farfield profile (obtained from the measured yaw, pitch and piston coefficients) with the measured one. The beam profiles shown in Figure 5.12 show good agreement.

5.3 Discussion

The testing was conducted with 2 cm beam diameter incident on a small scale model of the grating-mirror assembly. The data measured by the ELI-developed Fizeau interferometer were compared with the output of the capacitance sensors for yaw and piston misalignments and tilt-meter for the pitch misalignment. Since there were no other means of the measurement of the absolute alignment of the grating mirror assembly than the interferometry itself, the measurement did not include possible systematic errors. Their impact was also lower due to the smaller aperture of the system. Short-term, these measurements show excellent agreement with accuracy better than 0.2 μrad for yaw, 0.4 μrad for pitch and 15 nm for piston. The resolution of the interferometer scales with the beam size, which was the main factor limiting its resolution. Therefore, the results point out that 10 cm beam aperture of the alignment beam for the main compressor should provide sufficient resolution. Also, since the reference and probe beam will be separated in vacuum, lower impact of the noise induced by air turbulence is expected.

The long-term measurements were influenced by the thermal expansion/shrinking of the aluminium desk to which the grating and the mirror were attached. Due to these thermal effects, piston and yaw measured by the capacitive sensors were always smaller

than piston and yaw obtained from the interferometric measurement. The measurement of pitch using tilt-meters also yielded deviation with respect to the interferometer and it could be improved by placing the tilt-meter on the optics substrate. The results will be comprehended in the design and positioning of the mounts for the capacitive sensors in the main compressor.

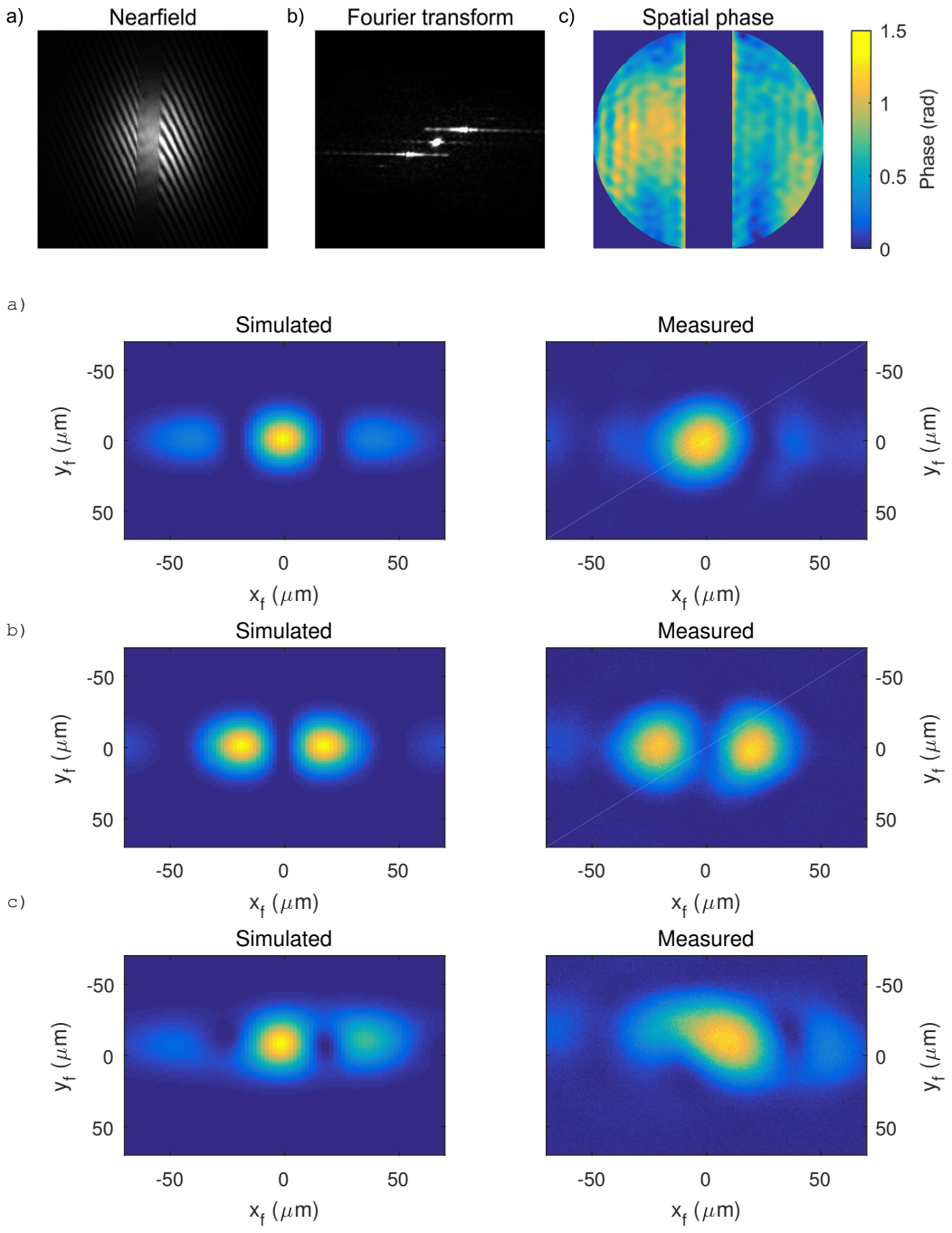

Figure 5.12: The comparison of the measured farfield with farfield distribution simluated according to yaw, pitch piston coefficients obtained the interferograms. a) Recorded interferogram; b) Fourier transform of the interferogram; c) Retrieved phase profile for the perfect alignment; d) Perfect alignment; e) piston = 3 rad; f) yaw,pitch = 30 μrad; piston = 1.5 rad

6. Stretcher design

The design of the stretcher of the L4 beamline is based on the design of the compressor which was bound by the fluence and aperture requirements. Thanks to relatively narrow spectral bandwidth of the system, it is beneficial to employ a single grating stretcher having an aberrated imaging system. The single grating stretcher eliminates the need to measure parallelism of the first and second grating, it has a smaller footprint and allows easy tuning of the angle of incidence on the grating position in order to adjust the GDD and TOD. In the single grating stretcher design, output beam pointing is not influenced by the translation or rotation of the grating. The aberrations present in the imaging system can be then used to tune the stretcher FOD deviation to match the residual FOD originating from material dispersion.

The design goals were to allow transmittance of 40 nm bandwidth without clipping to avoid degradation of time intensity contrast, to limit wavefront aberrations, to minimize residual spatio-temporal couplings and to entirely compensate residual spectral phase in the CPA chain. Also, it was preferred to keep the footprint of the stretcher as small as possible so it could be placed inside a vacuum chamber. Evacuating the stretcher chamber limits the spectral phase noise originating from air non-homogenities and turbulence and therefore it enhances stability of temporal profile and contrast. An acousto-optic modulator (Dazzler) is included in the CPA chain to control higher dispersion orders. However, its efficiency decreases when larger group delays have to compensated. So, it is advisable to design the system to have theoretically flat spectral phase and use Dazzler to compensate the real-world deviation only.

The individual dispersion orders of the L4 system are summarized in Table 6.1. The material section comprises mostly fused silica windows and amplifier glass and was modeled using Sellmeier coefficients. Since the material dispersion is several orders of magnitude smaller than the compressor dispersion, it can be expected that the optimal configuration of an ideal stretcher should be very close to the compressor. It is therefore advantageous, if possible, to employ the same MLD 1136 ln/mm grating design in the stretcher to reduce its cost and to enhance its transmittance. However, as it will be shown later, it was also advantageous to consider 1300 ln/mm line density for the Banks design due to its inherent aberrations.

Table 6.1: Dispersion of the L4 laser system

Dispersion term	**GDD (fs^2)**	**TOD (fs^3)**	**FOD (fs^4)**
Material	78 256	126 581	−245 067
Compressor 1136	−128 135 131	462 792 672	−2 663 047 191
Stretcher target	128 056 875	−462 916 581	2 663 292 258

With line density of the gratings fixed, a stretcher optimization procedure was done as follows. First, the ideal grating spacing and the angle of incidence to suppress the material GDD and TOD was calculated (Table 6.2). Based on these values, the optimal radii of curvature and number of passes through the stretcher were guessed and subsequently implemented into a ZEMAX model. The model was then optimized to meet the design goals according to Fig. 6.2. In general, an adjustment of the radii of curvature influences the amount of the spherical aberration in the stretcher imaging

Table 6.2: The residual FOD originating from the material dispersion and configuration of the ideal aberration-free stretcher having fixed line density with L and α selected to compensate GDD and TOD from Table 6.1.

Line density (ln/mm)	$\boldsymbol{L_{\mathrm{tot}}}$/ $\boldsymbol{L_{4\mathrm{pass}}}$/$\boldsymbol{L_{8\mathrm{pass}}}$ **(m)**	$\boldsymbol{\alpha}$**(°)**	**Δ FOD (fs^4)**
1136	30/7.5/3.8	36.95	$4 \cdot 10^6$
1300	24.5/6.1/3.1	54.45	$6 \cdot 10^7$

system and it helps to compensate the residual FOD according to Eq. (2.31). With a fixed number of passes in the Banks design, there is only one combination of the grating position, incidence angle and radii of curvature for which the GDD, TOD and FOD are compensated. A single grating Offner stretcher is more flexible in this regard as it offers another degree of freedom which is the radius of curvature of the convex mirror R_2. Therefore, for any arbitrary value of the radius of the concave mirror R_1 there is such radius of the convex mirror R_2 so that the FOD is compensated. That is again achieved through the adjustment of the spherical aberration of the imaging system (see Fig. 2.26 for comparison). Nonetheless, due to aberration induced spatio-temporal couplings, it is practical to keep R_2 close to the position which minimizes the Seidel aberrations (see Fig. 2.25 for reference). Of course, the same versatility can achieved in the Banks stretcher through the adjustment of line density of gratings [80]. The impact of the residual FOD from Table 6.2 on the temporal profile of a pulse is illustrated in Fig. 6.1.

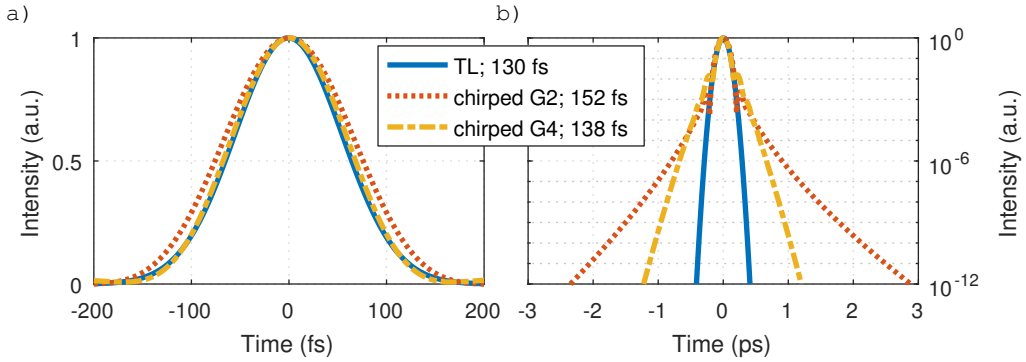

Figure 6.1: Pulse broadening (a) and time intensity contrast degradation (b) due to the residual FOD $6 \cdot 10^7$ fs^4 in the system. The simulation was made for Gaussian and super-Gaussian spectrum of the order 4 having a transform limited pulse duration of 130 fs. The residual FOD of the 1136 ln/mm system with an ideal stretcher is negligible.

Retro-reflecting elements are useful design tools for the compensation of residual spatio-temporal couplings in stretchers. There are multiple possible setups such as a plane mirror, a roof mirror, a staircase like structure [61] or a beam inverter [90] (Fig. 6.3). Their effectiveness depends on the symmetry of the imaging system and the symmetry of their configuration with respect to the optical axis of the system. Generally, if the beam is retro-reflected back and it is incident on the grating approximately under the same angle as during its previous pass, spatial chirp is compensated. Moreover, if the individual spectral components propagate exactly the same path backwards after the reflection like with a corner-cube retro-reflector, the residual angular

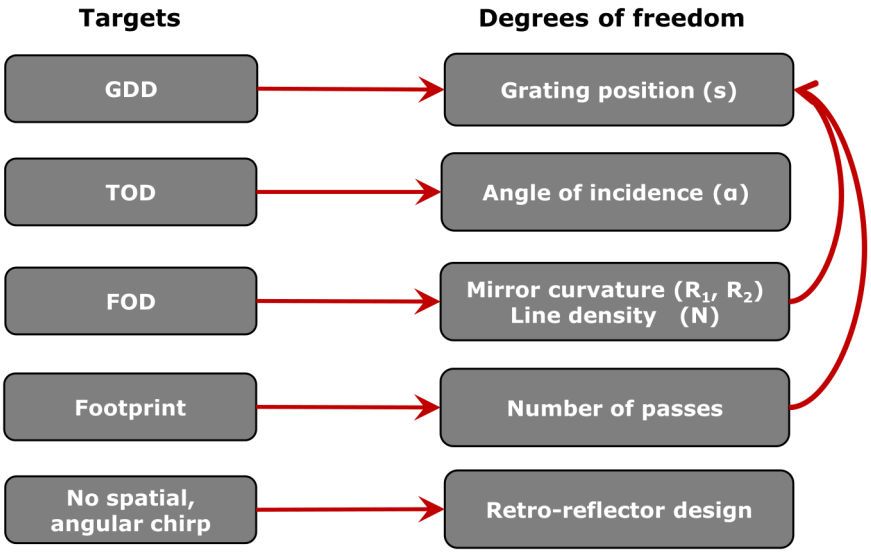

Figure 6.2: Diagram of a stretcher optimization process.

dispersion can be canceled as well. However, to separate the input and output beams, the beam is usually spatially offset and the beam profile is also often inversed. According to Eqs.(2.42, 2.47), the magnitude of the residual angular dispersion varies between subsequent passes having different x_0 and y_0 offsets. Furthermore, when the beam is spatially inversed, spatial chirp changes its sign and it is then doubled during back-propagation. Therefore there are no simple rules which could be valid in every situation. However, the individual properties of each retro-reflecting structure working at most situations are summarized in Table 6.3.

A plane mirror positioned perpendicularly to the central wavelength of the beam cancels the spatial chirp but doubles the angular chirp in both planes. If the spatial separation of the beams at the output is necessary, the mirror can be vertically tilted (assuming diffraction plane being horizontal). The tilt then results in slightly different dispersion of the grating along the vertical plane yielding some vertical spatial chirp at the output. For this reason, a vertical roof mirror is usually placed after the first pass in stretchers and compressors. The vertical roof mirror retro-reflects, inverses and

Table 6.3: Compensation of residual spatio-temporal couplings by retro-reflector design in stretchers. $\vec{x}, \vec{x}$ denotes horizontal vs vertical axis, $0\vec{x}$ means compensation of a spatio-temporal coupling and $2\vec{x}$ means that the spatio-temporal coupling is doubled. There are two possible configurations for a roof mirror and staircase structure; $\vec{x}$ and $\vec{y}$ axis can be therefore swapped.

	Plane	**Roof**	**Staircase**	**Beam inverter**
Beam inversion	-	$\vec{x}$	$\vec{x}$	$\vec{x}$ & $\vec{y}$
Beam offset	-	$\vec{x}$	$\vec{y}$	$\vec{x}$ | $\vec{y}$
Spatial chirp	$0\vec{x}$, $0\vec{y}$	$2\vec{x}$, $0\vec{y}$	$2\vec{x}$, $0\vec{y}$	$2\vec{x}$, $2\vec{y}$
Angular dispersion (no offset)	$2\vec{x}$, $2\vec{y}$	$0\vec{x}$, $2\vec{y}$	$0\vec{x}$, $2\vec{y}$	$0\vec{x}$, $0\vec{y}$

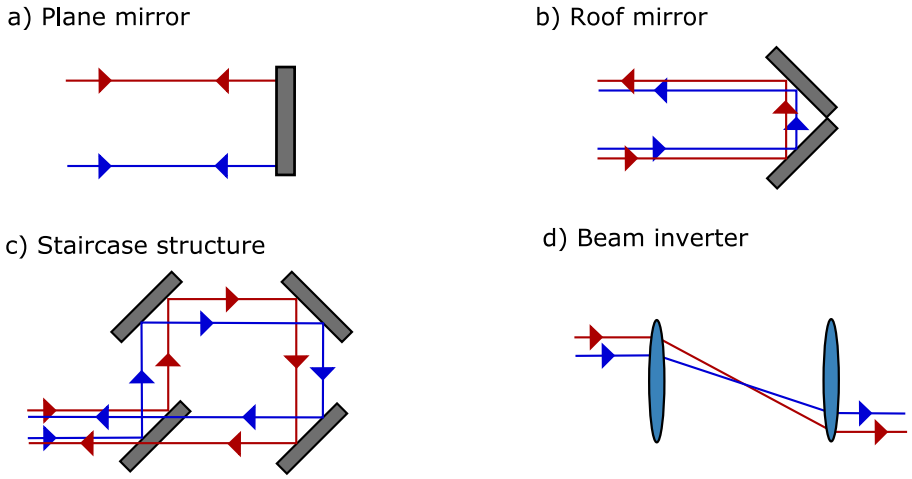

Figure 6.3: Comparison of various retro-reflecting elements. a) Plane mirror; b) Roof mirror; c) Staircase structure; d) Lens beam inverter

offsets the beam along the vertical axis. Therefore, it helps to compensate the vertical angular dispersion as it retains the vertical pointing of each spectral component. But since the beam is inversed along the vertical axis, the vertical spatial chirp is doubled. In the horizontal plane the vertical roof can be substituted with a plane mirror. It cancels the spatial chirp and doubles the angular dispersion.

A horizontal staircase structure operates in a similar way as the roof mirror. It comprises four plane mirrors tilted horizontally at 45°. The first and the last mirror is also slightly vertically tilted to separate the input and output beams. Compared to the roof mirror the staircase structure offsets the beam vertically while the beam coordinates are inversed horizontally (or vice versa). It therefore retains similar properties regarding the compensation of the spatio-temporal couplings as the roof mirror. However, as it offsets and inverses the beam in different planes, it can provide better compensation of the residual angular chirp than the roof mirror in some situations. A staircase-like structure or a horizontal roof mirror or are usually used after the second pass to suppress the residual vertical spatial chirp and horizontal angular dispersion.

A beam inverter can be composed of either one lens with a plane mirror positioned in its focal plane or a 1:1 keplerian telescope. It spatially inverses the beam along both axis and retains the pointing of the beam like corner-cube reflector. In general, the residual angular dispersion in both planes is canceled and the spatial chirp is doubled. The beam inverter also allows to arbitrarily offset the output with respect to input in x-y plane. The beam inverter is advantageous to use only when there is no residual spatial chirp. It can help to completely suppress the residual angular chirp in dependence on the x_0 and y_0 offsets.

6.1 FOD, footprint optimization

Banks design

Since the MLD 1136 ln/mm gratings have to operate very close to the Littrow angle to have good diffraction efficiency, it is necessary to introduce an offplane angle to separate the incident and diffracted beam. Unfortunately, the Banks design is not well suited for the off-plane Littrow angle setup. The radius of curvature of the concave mirror, the grating position and the off-plane angle have to be precisely matched otherwise the beam is clipped or cannot be injected or extracted from the stretcher. This is illustrated in Fig. 6.4, where back reflecting (BM2), horizontal roof (RM) and injection and extraction (I/O) mirrors are located in between the beam trajectories through the stretcher. Such positioning would require very ingenious opto-mechanical design and would make the stretcher very hard to align properly without any beam clipping. Generally, it is therefore not possible to entirely compensate the FOD through the adjustment of the radius of curvature in the off-plane Banks design as its length can be adjusted only within a very small interval without any significant clipping of the beam. Given the required stretch factor, it was necessary to choose 12.8 m radius of

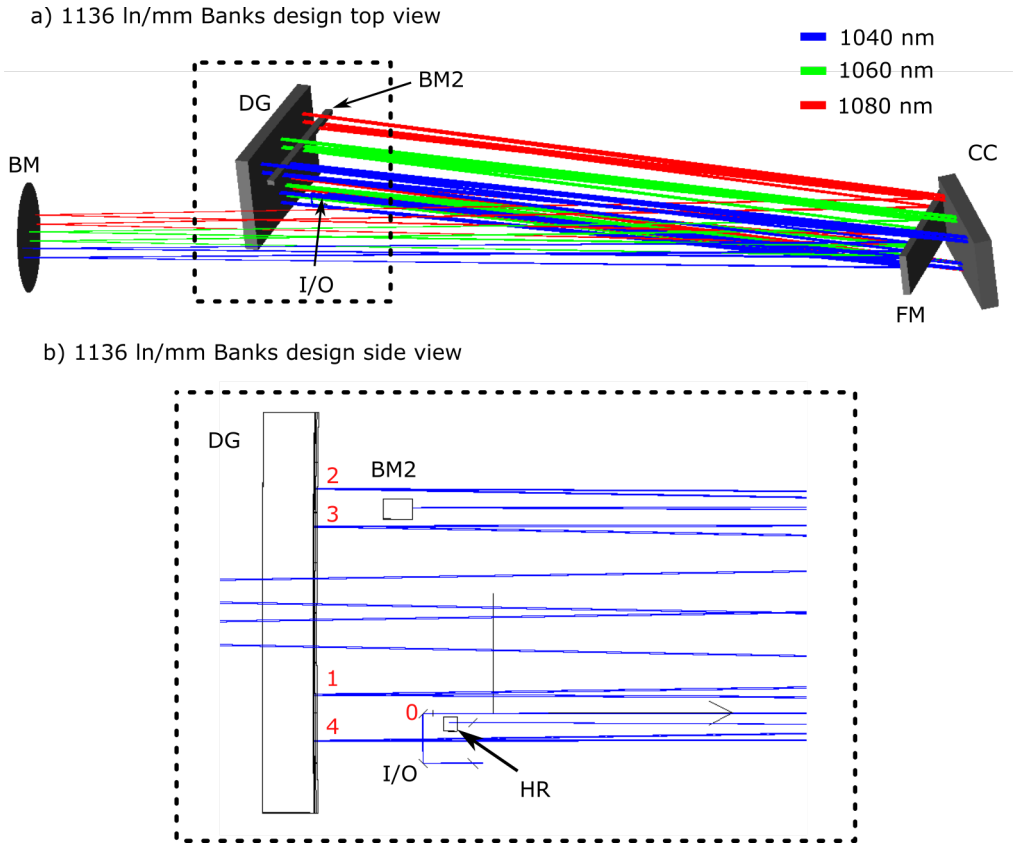

Figure 6.4: Schematic of the 4-pass Banks stretcher using 1136 ln/mm gratings in the off-plane configuration. I/O stands for an Input/Output, DG for a diffraction grating, CC for a concave mirror, FM for a folding mirror located near the grating, BM for a plane mirror located at focal plane of the concave, BM2 for a plane mirror reflecting the beam back for the second/fourth pass and HR for a small horizontal roof reflecting the beam for the third pass. The red number describes the number of times the beam hits the grating during its first two passes though the system. After the fourth hit, the beam is reflected to the horizontal roof mirror and it propagates upwards in the opposite direction.

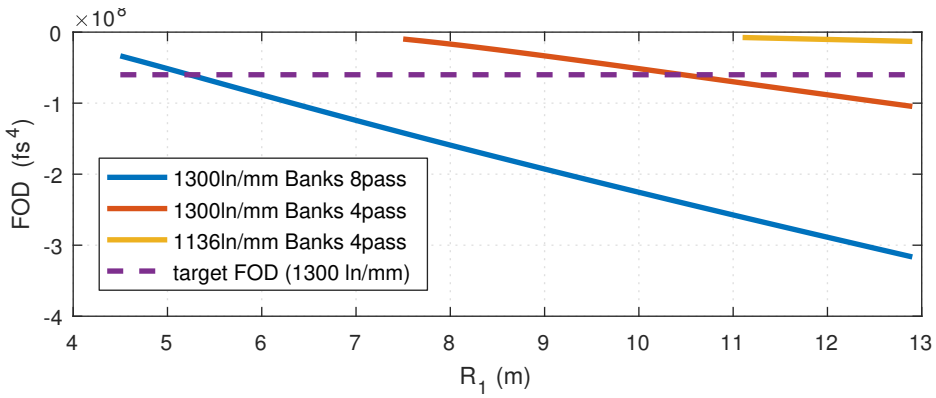

Figure 6.5: Dependence of the FOD deviation on the radius of curvature of the concave mirror for the simulated Banks designs calculated according to Eq. (2.38). A stretch ratio remained fixed during the calculation to meet the GDD and TOD from Table 6.1.

the concave mirror due to the beam clipping issues. The stretcher then exhibits very large spherical aberration leading to the residual FOD $5 \cdot 10^7$ fs^4 and a large footprint. To summarize, the off-plane Banks design was therefore considered to be unsuitable for the L4 beamline.

Another option was to increase the line density of the stretcher gratings to shift the operating angle further from the Littrow angle so that the off-plane configuration would not be necessary for the separation of the incident and diffracted beam. The combination of the angle incidence, the line density and the position of the grating was selected to enable such separation and to match the target GDD and TOD. The radius of curvature of the concave mirror was then adjusted to tune the FOD. Commercially available gratings with predefined line densities were preferred to reduce possible cost. A 1300 ln/mm grating design was found suitable as the operating angle of incidence 54.35° is far enough from the Littrow angle 43.5° at 1060 nm. Higher line density of the

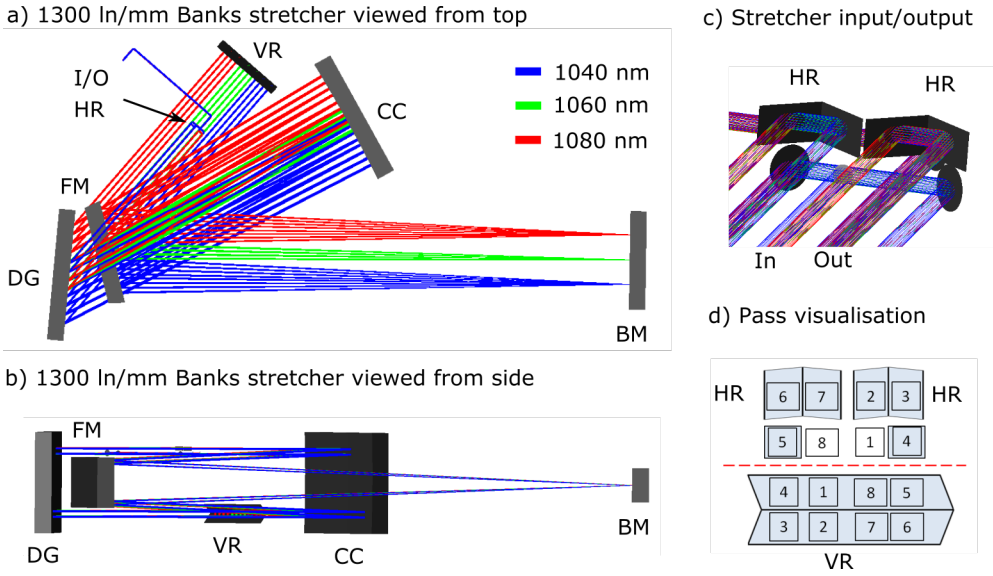

Figure 6.6: 8-pass 1300 ln/mm Banks schematic. I/O stands for Input/Output, DG for a diffraction grating, CC for a concave mirror, FM for a folding mirror located near the grating, BM for a back reflecting mirror located at focal plane of the concave, VR for a large vertical roof, HR for a small horizontal roof.

gratings increases dispersion and therefore the grating spacing required for the GDD compensation is decreased from 30 m to 25 m. The residual FOD of the system with an aberration-free stretcher would be then increased to $6 \cdot 10^7$ fs^4. A typical 4-pass Banks design using a vertical and a horizontal roof mirror would therefore require ~3.5 m distance of the grating from the focal plane of the concave mirror. According to Figure 6.5, such design would require more than 10 m long radius of curvature of the concave mirror to suppress the residual FOD. That would result in the footprint of the stretcher that is larger than 4 m since a plane mirror has to be placed in the focal plane of the concave mirror in the Banks design. To decrease the footprint, it is possible to include two additional horizontal roof mirrors to add four more passes through the stretcher. The layout of the 8-pass stretcher and its roof mirror system is shown in Figure 6.6. The additional four passes enabled to significantly reduce the radius of curvature of the concave mirror to half (5 m) and therefore to shrink the overall footprint of the stretcher to 2.5 m. The simulated dependence of the residual group delay of a pulse at the output of the full CPA chain is sketched in Figure 6.7. The residual group delay is induced by the higher order aberrations from the stretcher imaging system. The simulation also exhibits slight wavefront distortion at the stretcher output (mainly astigmatism with P-V $\lambda/50$) and negligible spatio-temporal couplings. The residual angular dispersion is well within the natural divergence of the beam with 7 mm diameter. In this design, gratings with gold coating would have to be employed. Typical reflectivity of gold coated gratings is expected to be around 90% and reflectivity of the other optics is expected to be 99%. In total, 16 reflections off the grating and 64 reflections off the other optics would yield overall transmission less than 10%.

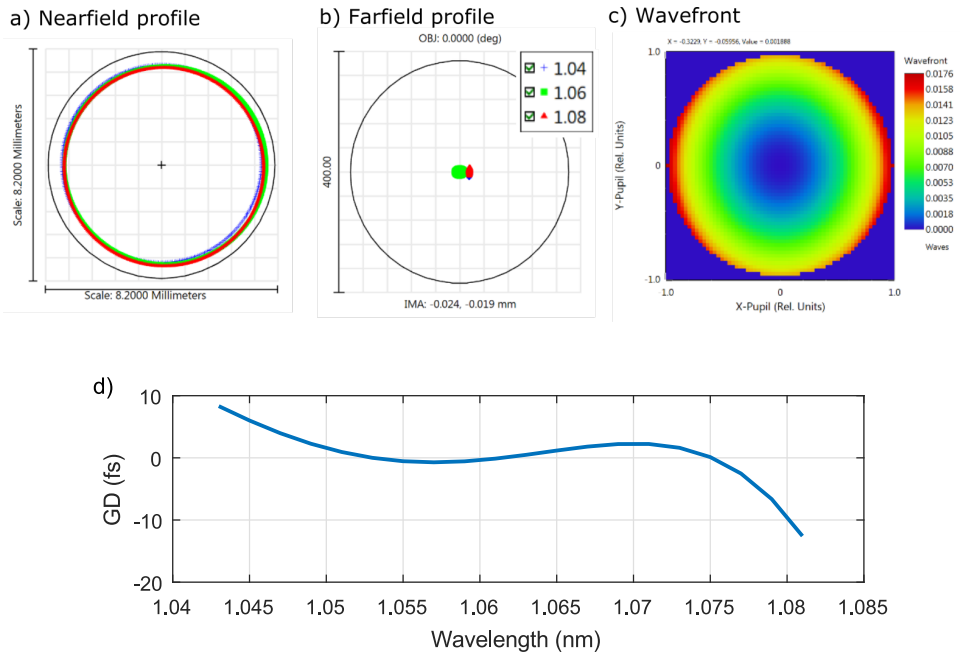

Figure 6.7: Simulated output beam parameters for the 8 pass 1300 ln/mm Banks design. a) Nearfield profile having 7 mm beam diameter; b) Farfield profile encircled by 184 μrad Airy ring c) Wavefront of the central wavelength; d) Output group delay profile after the compressor

Offner

Next, a single grating Offner stretcher design in the off-plane configuration was considered (Figure 6.8). The off-plane incidence angle offers an advantage over the in-plane incidence for a single grating configuration as the grating can be easily positioned in between the concave and the convex mirror thanks to the vertical separation of the beams. In the in-plane configuration this is not possible because a single grating would obstruct the convex mirror as they are vertically at the same level. Therefore, the off-plane configuration can be more compact as it allows to place the grating further away from the zero stretch point which in turn enables to reduce the radii of curvature of the mirrors. On the other hand, since the concave mirror is tilted with respect to the convex mirror, their curvature centers no longer overlap. The imaging system is then aberrated even for the object positioned at the center of curvature of the concave mirror. However, as the grating is moved towards the concave mirror to increase the stretch ratio, the "in-plane" aberrations increase and the contribution of this off-plane term has less weight. The off-plane incidence on the diffraction grating yields angular dispersion in the vertical plane which results in vertical spatial chirp after the first pass. Because the vertical roof mirror inverses the beam vertically, the spatial chirp is then doubled after the second pass. It is therefore necessary to add a horizontal roof mirror to compensate the vertical spatial chirp making the design four passed at least.

Compared to the Banks design, a single grating Offner stretcher offers an additional degree of freedom - the radius of curvature of the convex mirror R_2. Since it was preferred to keep the line density of the stretcher fixed, the radii of curvature of the convex and the concave mirrors was adjusted to optimize the residual FOD and minimize the stretcher footprint. By substituting the residual FOD of the system from Table 6.1, the ideal ratio of the curvatures of the concave and convex mirror was calculated according to Eq. (2.24) and it is sketched in Figure 6.9). The optimal R_1 and the offplane angle were then selected to reach sufficient vertical spacing between the optics and the beam according to a ray-tracing model.

A single pass through the Offner stretcher with the grating at L distance from the center of curvature is equivalent to $L_{\text{eff}} = -2L$ distance between the pair of diffraction gratings. For the 4-pass design the grating has to be almost 4 m away from the center of curvature of the concave mirror to meet target GDD and TOD values from Table 6.1. When the diffraction grating is too close to the concave mirror, the beam reflected

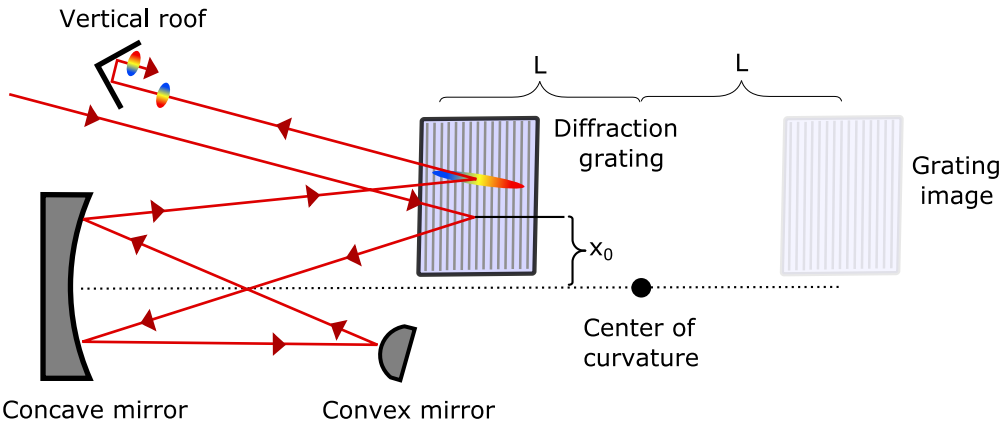

Figure 6.8: Single grating Offner stretcher in the off-plane configuration. To achieve separation of the input and output beams, the diffraction grating and the concave mirror have to be tilted with respect to the input beam.

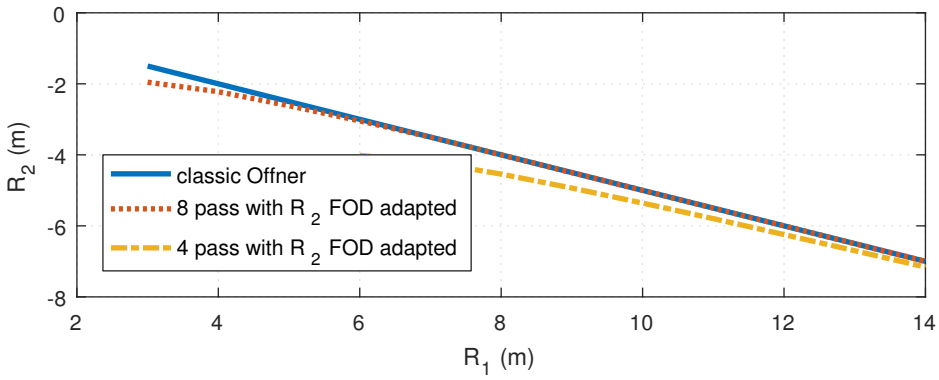

Figure 6.9: FOD compensation through the adjustment of the R_2 in the Offner stretcher design. For the R_1 close to 14 m (7 m), the adjustment of R_2 is no longer necessary for 4 pass (8 pass), respectively. The FOD using was calculated using Eq. (2.24) with the offplane angle neglected. The stretch ratio remained fixed during the optimization to meet the GDD, TOD and FOD from Table 6.1

off the concave mirror starts to get clipped by the bottom edge of the grating in the vertical plane (see Figure 6.8). In order to avoid it, the grating has to be positioned at least 1 m away from the concave mirror which bounds R_1 to be longer than 5 meters with $R_2 = -R_1/2$. But when the absolute value of R_2 is increased, the position of the grating image shifts towards the real grating, The effective stretcher grating distance L_{eff} is then decreased according to Eq. (2.43). For $R_1 = 6$ m and $R_2 = -4$ m, the grating image is shifted by 1 meter. The grating has to be moved 1 m closer to the concave mirror to compensate this effect. $R_1 = 6$ was therefore chosen as a starting point for the FOD curve in Fig. 6.9. Consequently, the FOD compensated 4-pass design has a footprint bigger than 3 m, since the convex mirror has to be placed at the focal plane of the concave mirror.

With the eight pass design, L is reduced to 1.9 m which in turn enables to further decrease R_1. However, R_1 is closely linked with the off-plane angle. With short R_1, the distance between the grating and the concave mirror is decreased. That in turn makes necessary to increase the offplane angle to reach sufficient vertical separation between

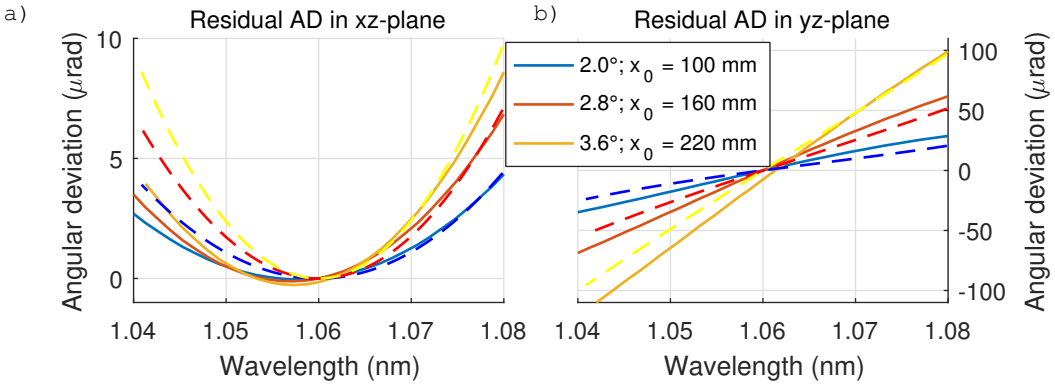

Figure 6.10: Dependence of the residual angular dispersion in xz and yz planes on the offplane angle of a single pass through the single grating Offner stretcher with $R_1 = 3.8$ m, $R_2 = 2.225$ m and $s = 2$ m. Dashed curves are calculated according to Eq. (2.26) for a stretcher with no off-plane angle. Seidel aberration coefficients can be calculated only for systems without tilts so we assumed zero off-plane angle and used coefficients from Table 2.7

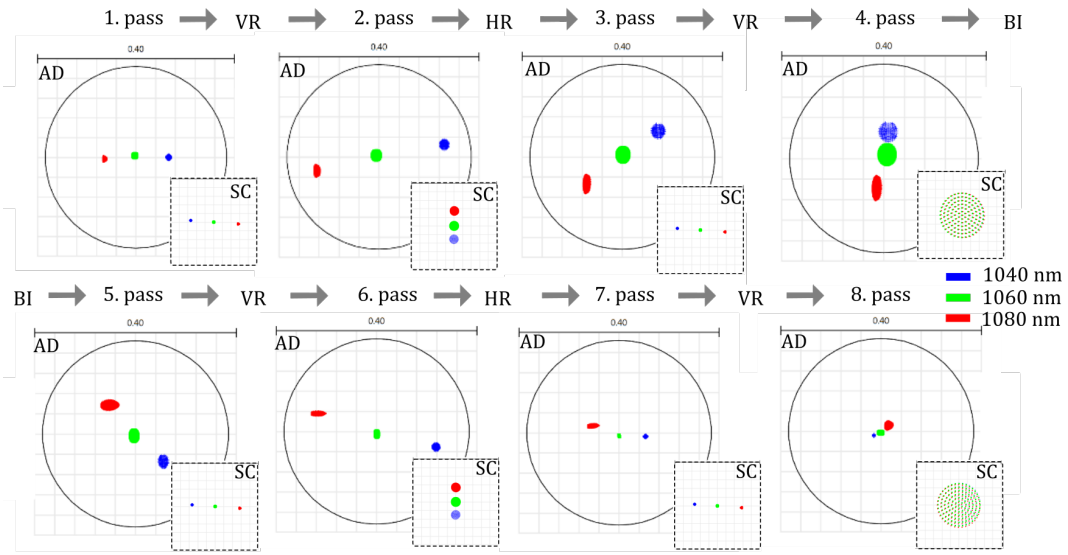

Figure 6.11: Residual angular dispersion (AD) and spatial chirp (SC) after each pass, the black circle represents Airy ring with 184 μrad radius (7 mm circular aperture). VR stands for a vertical roof, HR for a horizontal roof and BI for a beam inverter

the convex mirror and diffraction grating to prevent beam clipping. A x_0 spacing has to be adjusted as well as the beam diffracted off the grating has to be incident on the lower part of the concave mirror during each pass. The increase of x_0 combined with higher aberrations of the system due to shorter R_1 of the eight pass system then yield bigger residual angular dispersion (Figure 6.10). The term linear in λ and quadratic in x_0 from Eq. (2.47) is dominant which is confirmed by approximate theoretical calculation using Eq. (2.26) with an arbitrary R_2. Nevertheless, the calculated values are still very close to the simulated ones and share similar profile. For $R_1 = 3.8$ m, $R_2 = 2.225$ m

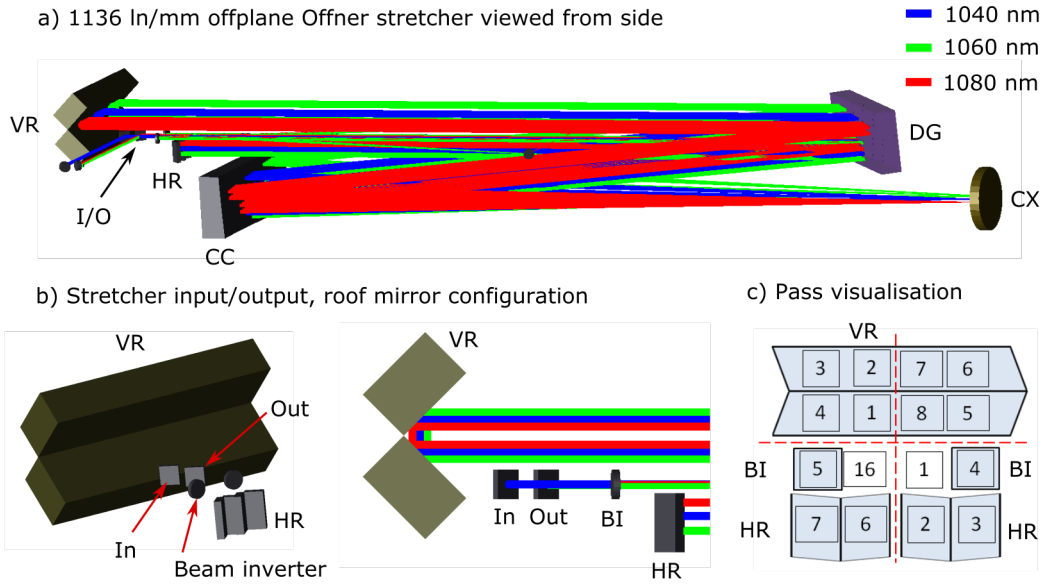

Figure 6.12: 8 pass 1136 ln/mm Offner schematic. I/O stands for Input/Output, DG for a diffraction grating, CC for a concave mirror, CX for a convex mirror, VR for a large vertical roof, HR for small horizontal roofs.

and $\gamma = 2.8°$, the angular deviation of the individual spectral components is within 60 μrad for single pass, which is smaller than the natural divergence of a Gaussian beam with $w_x = 3$ mm (expected input beam size). Such configuration had sufficient vertical separation of the beams and it was selected as a good compromise between the output beam quality and small footprint.

The residual angular dispersion and spatial chirp can be further effectively reduced with the roof mirror design. To compensate horizontal spatial chirp a vertical roof has to be installed after the first pass. After the second pass, there is vertical spatial chirp due to the off-plane diffraction and therefore a horizontal roof mirror has to be used. After the first four passes, spatial chirp in both planes is completely suppressed, but slight residual angular dispersion in both planes remain. In that situation, it is advantageous to employ a beam inverter which reverses the profile of the angular dispersion. The beam then undergoes the same sequence as during the first four passes. The beam inverter comprises two spherical mirrors with 2 m focal distance used in a Keplerian telescope configuration. The beam inverter helped to reduce the residual angular deviation to less than 20 μrad within the target bandwidth. The pass-to-pass evolution of the residual angular dispersion is shown in Figure 6.11.

The configuration of the final stretcher design is sketched in Figure 6.12. The initial design was performed in a non-sequential mode of ZEMAX. Once the design was fixed, it was converted to a sequential mode to enable more detailed analysis of the system. The output beam profile shown in Figure 6.13 exhibits minimal spatial and angular chirp. Wavefront deviation of the system with ideal optics is mainly astigmatic with $\lambda/100$ PV for the central wavelength. The group delay is well compensated within the whole bandwidth. The residual term originates from the higher order aberrations. The beam undergoes 16 reflection off the grating and 64 reflections off the mirrors, the expected throughput of the stretcher was simulated to be approximately 40%. The entire stretcher can be fitted into a 2500x800x500 mm chamber.

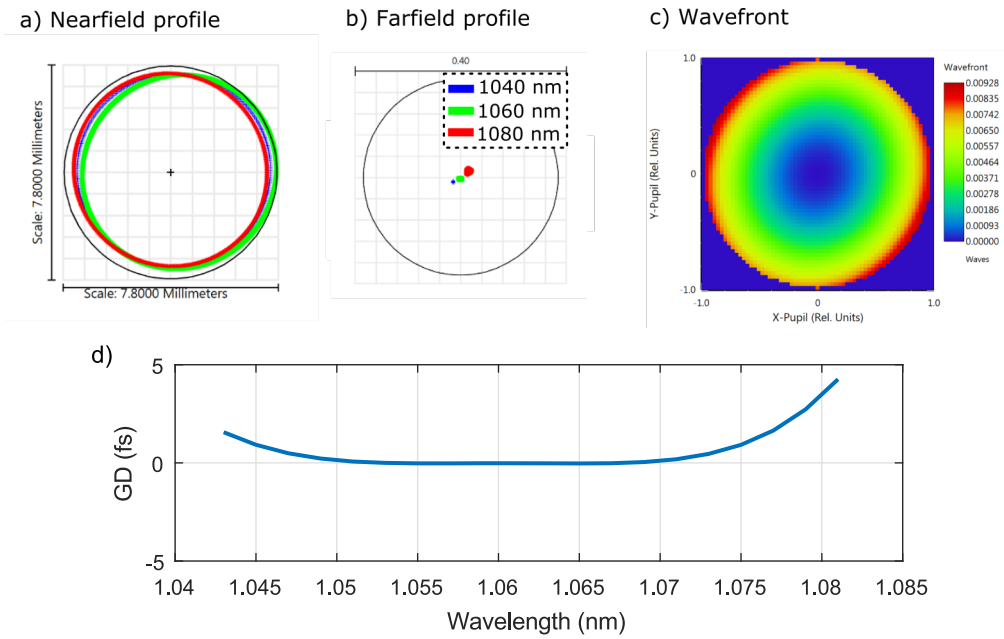

Figure 6.13: Output beam parameters for the 8 pass 1136 ln/mm Offner stretcher. Spatial chirp (a), residual angular dispersion enclosed within the Airy ring of a 7 mm aperture (b) and the wavefront of the central wavelength of the pulse (c); d) The simulated output group delay profile after the compressor.

6.2 Installation and alignment

The 8-pass single grating Offner design was selected to be implemented into the L4 beamline since the 1136 ln/mm MLD gratings offer better diffraction efficiency with lower scattering compared to the gold gratings employed in the Banks design. The MLD coating has 99% diffraction efficiency at the offplane Littrow configuration within the target bandwidth. Also, its optomechanical design can be more robust as no optical component is vertically surrounded by beams. An independent tolerance analysis of the stretcher made by Matt Kepler from National Energetics confirmed that the stretcher offers sufficient flexibility for the real application with non-ideal optics. The stretcher can accommodate line density variation (± 5 ln/mm), compressor grating spacing change (± 0.2 m) or different grating incidence angles (± 0.2°). As was mentioned before, the big advantage of a single grating design is that the output beam pointing and centering is retained when the grating is rotated or translated. This allows to easily match the dispersion of the stretcher with the compressor. An FOD deviation is induced by the aberrations of the imaging system and material dispersion. When the grating spacing/incidence angle of both compressor and stretcher is changed, the residual FOD remains unchanged and therefore the compensation still works. To prevent possible spatio-temporal couplings and contrast degradation, high quality optics were procured with max irregularity $\lambda/10$ peak to valley of the reflected wavefront, surface gradient $\lambda/20$/cm at 633 nm and less than 0.5 nm rms surface roughness. The grating and concave mirror have a rectangular aperture with 420x150 mm dimension, the convex mirror has a circular aperture with 6 inch diameter. The width of the vertical roof mirror was set to 340 mm to match the effective aperture of the tilted grating.

Alignment

The apex angle of roof mirrors was preliminarily aligned using an autocollimator. All the optics were then mounted and placed at their appropriate position into a vacuum chamber according to a CAD model with few mm uncertainty. The autocollimator was then moved in to set up the grating roll angle. Its vertical pointing was set-up

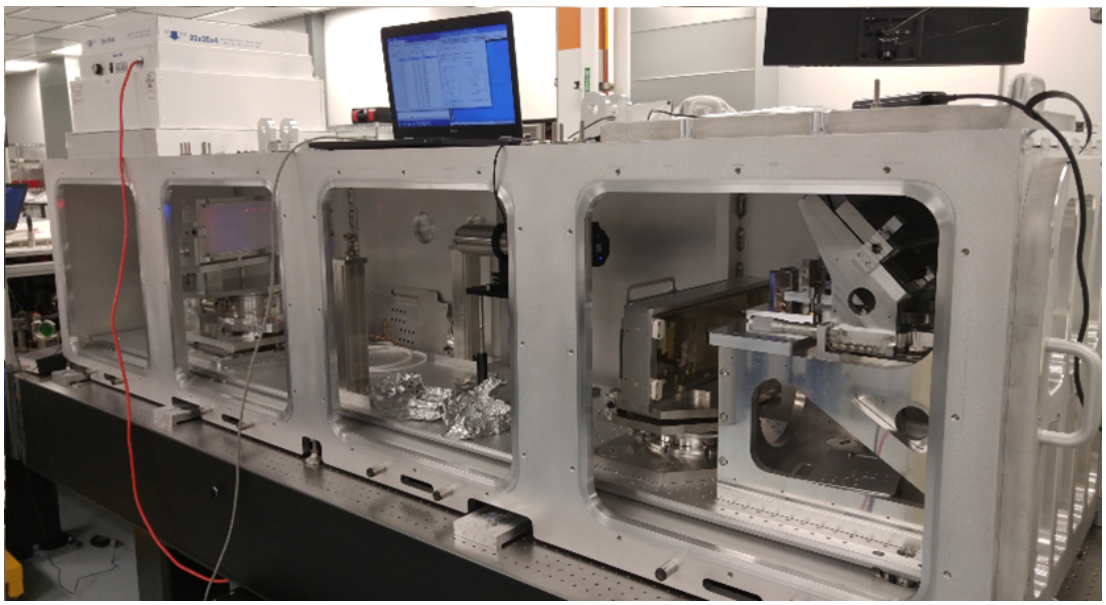

Figure 6.14: Opened stretcher chamber during the alignment.

using a penta-prism and a liquid mirror having horizontal surface (water filled cup). The penta-prism deviates the beam vertically by 90° and so the beam is back-reflected from the water level only when the input vertical pointing is perpendicular to the gravity and thus perfectly horizontal. The autocollimator was then pointed at the grating normal and the grating pitch angle was adjusted to retrieve a back-reflection. Afterward, the grating was rotated to the Littrow angle and the roll angle was set-up in the same manner. The procedure was then repeated to minimize possible systematic error introduced by crosstalk of the grating mount. Nevertheless, the roll angle can be set-up only approximately since the Offner triplet is cylindrically symmetric and there is only a single grating used.

The stretcher was initially prealigned using a narrow-band 1064 nm Nd:Yag laser and in-house alignment plates (Figure 6.16). Three alignment plates were used - one in the front of the roof mirrors (input plate), one at the grating and one at the concave mirror. Each plate consists of sixteen holes with a 1 cm diameter, each one centered at the position of the 1064 nm ray according to the ZEMAX model combined with the optomechanical CAD model. The corresponding number of the pass through the plate is engraved near each hole to avoid ambiguity. The alignment procedure using the plates is identical to the setting up beam centering and pointing with two pinholes. The tilts of each optical component and the vertical position of the large roof mirror were adjusted so that the beam propagated through all the holes to the output mirror. The alignment plates were then removed and beam pointing of each pass was fine-tuned by monitoring the beam scatter on the convex mirror with an IR viewer. Since the convex mirror lies in the focal plane of the concave mirror, focal spots of all eight passes should overlap there if they have parallel propagation direction. Their mutual position can be adjusted by tilting the individual roof mirrors. The roof mirrors should be subsequently blocked to observe a perfect overlap of each pass during the procedure. The beam pointing into the stretcher is monitored by a far-field measurement at the stretcher input.

The alignment of the stretcher was verified using a fiber-coupled broadband superluminescent diode. The spectrum of the diode is centered at 1055 nm with 20 nm bandwidth and the diode was collimated to 2 mm half-width. The yaw angle of the vertical roof can be fine-tuned through the compensation of the residual spatial chirp with a broadband source. The vertical roof should be positioned so that it is perpendicular in the yaw to the input beam incident on the grating. If there is some slight

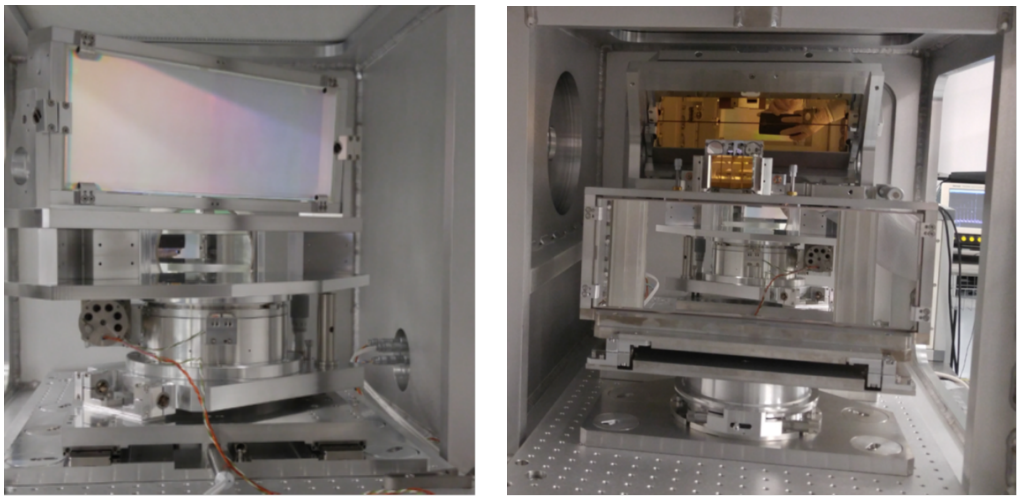

Figure 6.15: Diffraction grating, concave and roof mirror in the stretcher

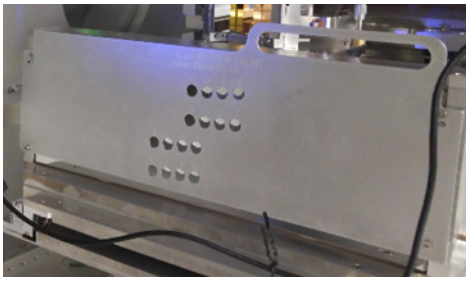

Figure 6.16: Aluminum alignment plate placed in front of the concave mirror. Each hole represents one reflection off the mirror.

deviation, the incidence angle on the grating slightly differs between the first and the second pass. Consequently, horizontal spatial chirp is not entirely compensated after the second pass. This residual horizontal spatial chirp is then doubled after the beam is reflected from the horizontal roof mirror (the third, fourth pass) and it can be observed at the input of the beam inverter (the fifth pass). Analogously, it is necessary to set up the output beam pointing from the beam inverter by measuring the spatial chirp at the stretcher output. The output of the beam inverter has to be aligned to be parallel with the input beam. To increase the resolution of the measurement of the residual spatial chirp it is advantageous to close an iris at the stretcher input to limit the beam size. Degradation of the beam quality due to diffraction is limited because the beam is imaged through the stretcher. The position of the convex mirror can be fine-tuned through the minimization of the residual horizontal angular dispersion after the third or fifth pass.

After the alignment, the output near-field and far-field diagnostic cameras were installed at the stretcher input and nearfield and farfield profiles of the superluminescent diode were recorded in Figure 6.17. A subtle near field modulation was induced through the clipping of the beam tails on a square input and output mirror. To prevent this size of the mirrors was increased from half inch to one inch. Different size of the input and output farfield is due to different combination of the focusing lenses and objectives on the cameras which was changed for the OPA beam. The measurement of the diode output spectrum confirmed a flat spectral response of the stretcher (Figure 6.18). Total transmittance of the stretcher was measured to be roughly 25% using the diode. This corresponds to approximately 98% reflectivity of each optical component as there is 72 reflections in total. The major source of losses is expected to be the coating of optics and the scattering on the grating.

Finally, the L4 beam was injected into the stretcher by matching its input farfield

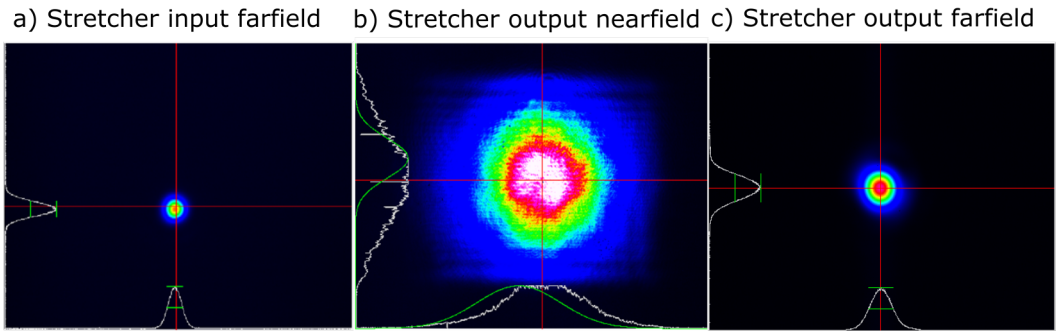

Figure 6.17: Input and output beam profile of the superluminsecesnt diode from the stretcher.

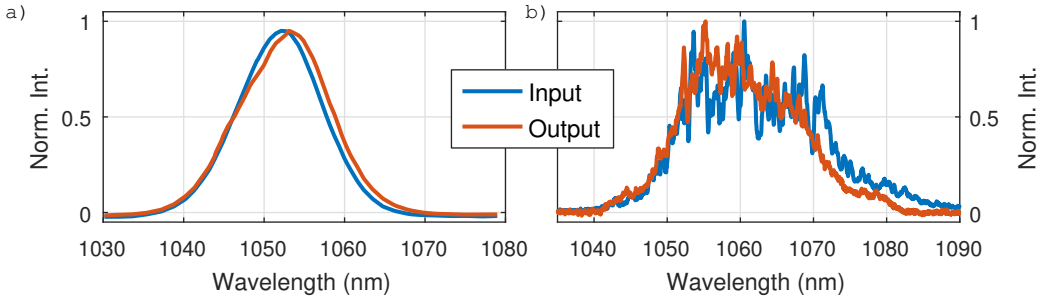

Figure 6.18: Comparison of the input/output spectrum of the SLD diode (a) and the L4 beam (b) from the stretcher measured using a fiber tip, which confirms that the transmitted bandwidth is wider than 37 nm.

and centering with the superluminescent diode. After the propagation through the stretcher both farfield and nearfield profiles are retained (Figure 6.19). The inhomogeneity of the NF profile originates from the pulse cleaner and it is completely suppressed by the ns-OPA amplification. The measurement of the output spectra confirmed transmitted bandwidth wider than 37 nm (Figure 6.18). The operational bandwidth of the stretcher was shifted towards lower frequencies (1047-1085 nm) to enhance the gain profile of the power amplifiers (Figure 3.4). The input and output spectrum were sampled by a tip of multi-mode fiber coupled into a spectrometer. The input and output spectrum differs within 37 nm bandwidth due to the spatial inhomogeneity imprinted by the pulse cleaner and stretcher itself and the interference effects in the fiber itself.

For a day-to-day operation the stretcher chamber was evacuated to ¡1 mbar. The robust design of the chamber prevented any deformation inside and after the pump-down the output beam pointing and centering remained well within the beam spot size. Transition from the air to vacuum shifts the effective line density of the stretcher grating by 0.2 ln/mm a decreases the grating spacing L by 6 mm approximately and was later compensated.

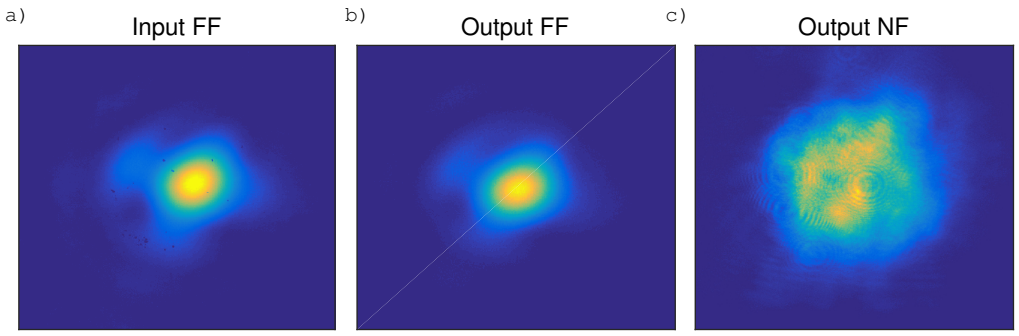

Figure 6.19: Input (a) and output beam profile (b,c) after the stretcher with the L4 beam.

7. Subaperture compressor

The subaperture compressor is a miniaturized version of the main L4 compressor which was designed to measure the temporal profile of a pulse throughout the amplification and to test the feasibility of grating-mirror phasing. It has the same dispersion properties as the main compressor. An input beam diameter is decreased to approximately 1 cm to minimize the size of the gratings. The layout of the subaperture compressor exported from a CAD/ZEMAX model is shown in Figure 7.1. It comprises four 1136 ln/mm diffraction gratings with two folding mirrors in between which serve to decrease the overall footprint of the compressor. The second and the third grating are phased with a plane mirror. The compressor uses one horizontal and one vertical roof mirror and it is four passed altogether.

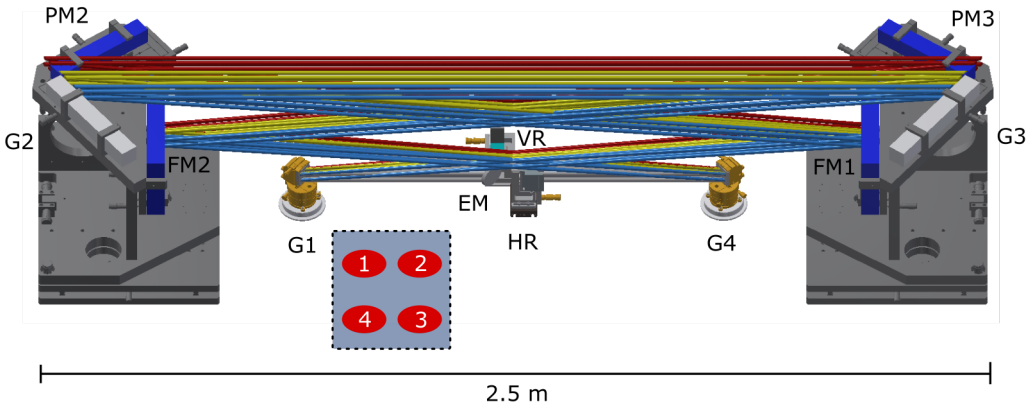

Figure 7.1: Layout of the subaperture compressor. G1-4 stands for the first to fourth grating, FM1-2 for the first and the second folding mirror, PM1-2 for phasing mirrors, EM for an elliptical plane mirror, HR for a horizontal roof mirror and VR for a vertical roof mirror.

The beam propagates through the compressor as follows. It hits G1 at the top left corner close to the Littrow angle ($\alpha = 37°$) and it is deviated upwards with offplane angle ($\gamma = 4°$). The beam is then reflected off the first folding mirror FM1 (positioned perpendicularly to the input beam) and is incident on the G2 and the PM2. The G2 collimates the angularly dispersed beam and diffracts the beam horizontally to the G3 and PM3. From the G3 the beam is diffracted with slight downward angle, it is reflected off the second folding mirror FM2 and finally hits G4. The horizontal roof mirror HR horizontally offsets and retro-reflects the beam which then repeats the sequence up to G1 in reverse order. Afterwards, the beam is incident on G1 in top left corner and is diffracted to the elliptical mirror which steers the beam to vertical roof mirror VR. The VR again retro reflects the beam and offsets it downwards. The whole sequence is then repeated for the lower part of G1-4 aperture. The total optical path through the compressor is almost 45 m. The four pass design enabled to reduce the grating distance L for single pass from 15 m to 3.75 m. It employs two small 5 x 5 cm diffraction gratings, two large 35 x 5 cm gratings phased with 30 x 5 cm mirrors. The upper part of both towers holding G2 and G3 is designed so that the phasing assembly can be replaced with a single grating to improve its stability and to eliminate possible phasing errors when it will be used simultaneously with the main compressor. The compressor is placed inside an enclosure to prevent spectral phase

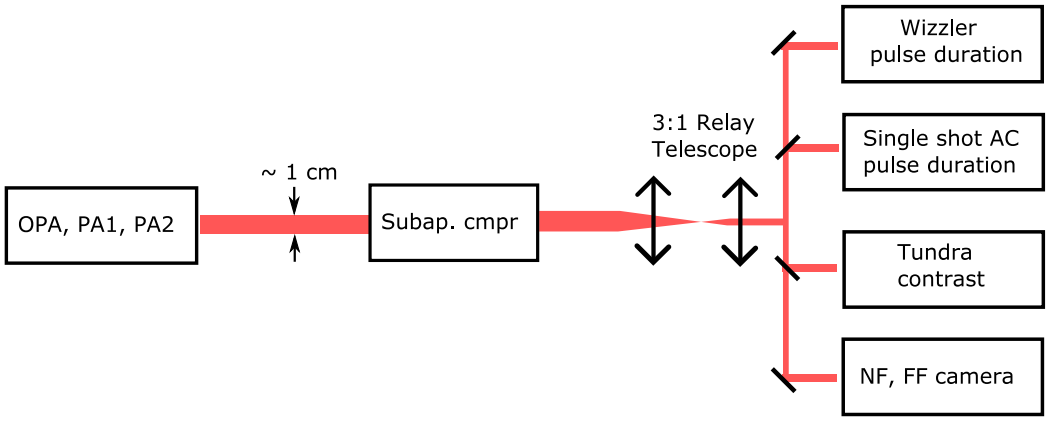

Figure 7.2: Schematic of the diagnostics of the subaperture compressor

noise originating from air turbulence. Under normal laboratory conditions, this noise prevents from measuring pulse duration shorter than few hundred femtoseconds due to long optical path in the compressor.

The schematic of temporal diagnostics layout is shown in Figure 7.2. The output beam from the OPA/PA1/PA2 sections is reflected off AR coated wedged window (∼0.5%) and it is routed into the subaperture compressor. The input beam is clipped to 1 cm diameter using an iris and possibly de-magnified beforehand to get better energy throughput. After the compressor the beam is downsized three times to 3 mm diameter and distributed to a single shot autocorellator, Wizzler, Tundra and spatial diagnostics.

Alignment

For the initial alignment of the subaperture compressor all mounts were positioned according to CAD and Zemax models. The folding mirrors FM1 and FM2 were aligned by autocollimation through two pinholes of the same height centered on the holes of the optical table with better than miliradian precision. The orientation of the gratings was tuned using monochromatic alignment laser with central wavelength of 1064 nm according to ZEMAX/CAD model. Since the beam propagates 3.8 m in between the gratings and since the folding mirrors were pre-aligned, such alignment has miliradian accuracy as well. Grating parallelism was then fine tuned to minimize residual angular dispersion. To measure it, a beam sampler monitoring both input and output farfield beam profile was installed at the compressor input. First, a plane mirror was placed after the G2 to retro-reflect the dispersed beam and the tilts of the G1 were adjusted. Second, a plane mirror was placed in between the G4 and the HR and the procedure was again repeated for tilts of the G4. The orientation of the roof mirrors was ten adjusted to retrieve an unclipped beam profile at the output and to match the footprint position of the individual passes on the G1 according to Figure 7.1.

Next, the angle and the position of the gratings was readjusted to retrieve the pulse duration in the ps-scale using a single shot autocorrelator (working in the scanning mode). The alignment procedure was reverified after each angular adjustment. Afterward, the shortest pulse duration was fine-tuned by motorized translation and rotation of the stretcher grating. The compressed beam spatial profile shows good quality with negligible angular and spatial chirp (Figure 7.4). Since the setup comprises vertical and horizontal roof mirrors, the residual angular dispersion is partly self-compensated during retro propagation in both planes. The beam profile at the output of the OPCPA

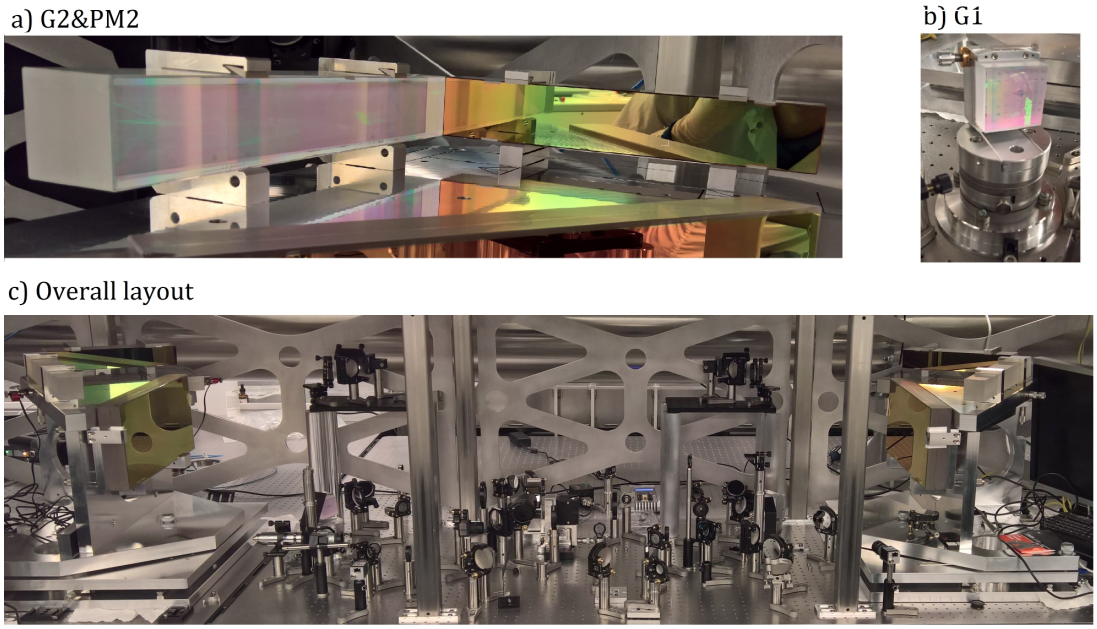

Figure 7.3: Photos of the installed subaperture compressor with phasing diagnostics

section having a top-hat shape was clipped at the relay plane by a circular iris to reduce the beam size. Even though the relay plane was imaged through the compressor on the last grating, the high spatial frequencies were smeared out. A very long imaging distance combined with relatively small apertures (1 inch diameter) of the lenses and mirrors induced the beam profile that resembles a Gaussian profile at the compressor output.

Pulse duration measurement

For initial measurements, only the first OPCPA section was active to limit the pulse energy. At this stage, DAZZLER wasn't implemented into the system to check the dispersion management. The measured output spectrum confirms that the compressor exhibits flat spectral response with a 3 nm dip centered at 1062 nm (Figure 7.5 vs 7.6a.). The spectral dip is induced through the clipping of the dispersed beam on the grating-mirror gap. The grating was aligned with mirror to have chamfers as close as

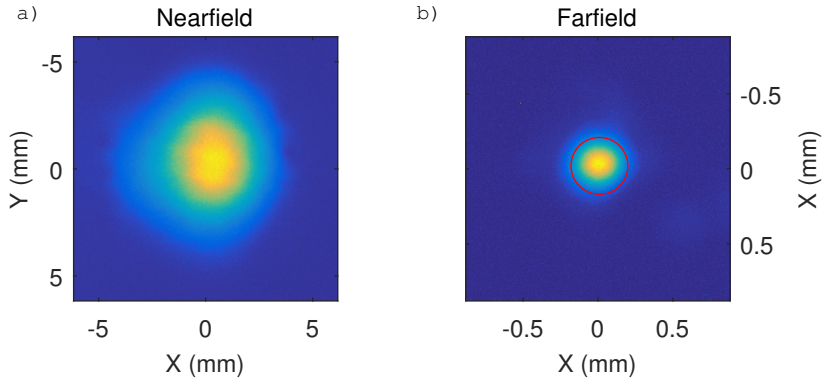

Figure 7.4: Output beam nearfield profile (a) and farfield profile using f2000 lens (b) measured after the sub-aperture compressor. The red circle marks the position of $1/e^2$ relative intensity calculated from the nearfield profile.

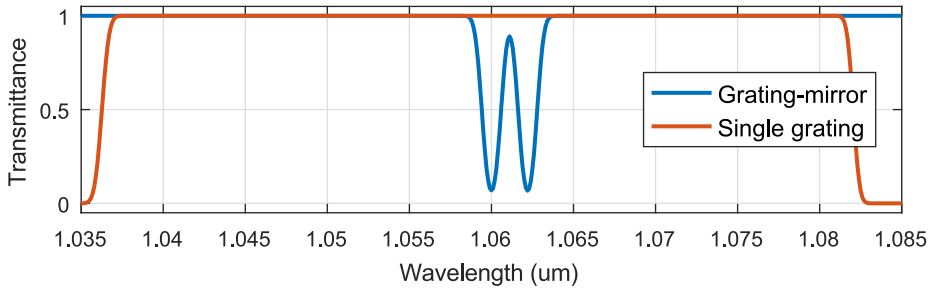

Figure 7.5: Simulated tranmission profile of the subaperture compressor in the single grating and grating-mirror configurations. The simulation was calculated with a Gaussian beam profile with $w_0 = 3.5$ mm (according to Figure 7.4a) with an 8 mm gap between the grating and mirror.

possible to each other. The effective size of the gap was mostly influenced by the fact that the grating was not coated to the edge of the substrate.

The compressed pulse duration was measured with an in-house developed single shot autocorrelator having calibration error ±10 fs. A comparison of the AC trace calculated from the recorded spectrum with the measured one is shown in Figure 7.6d. The recorded spectrum corresponds to the 150 fs Fourier transformed pulse duration and the autocorrelation constant $k = 1.48$ (i.e. the ratio between the duration of the

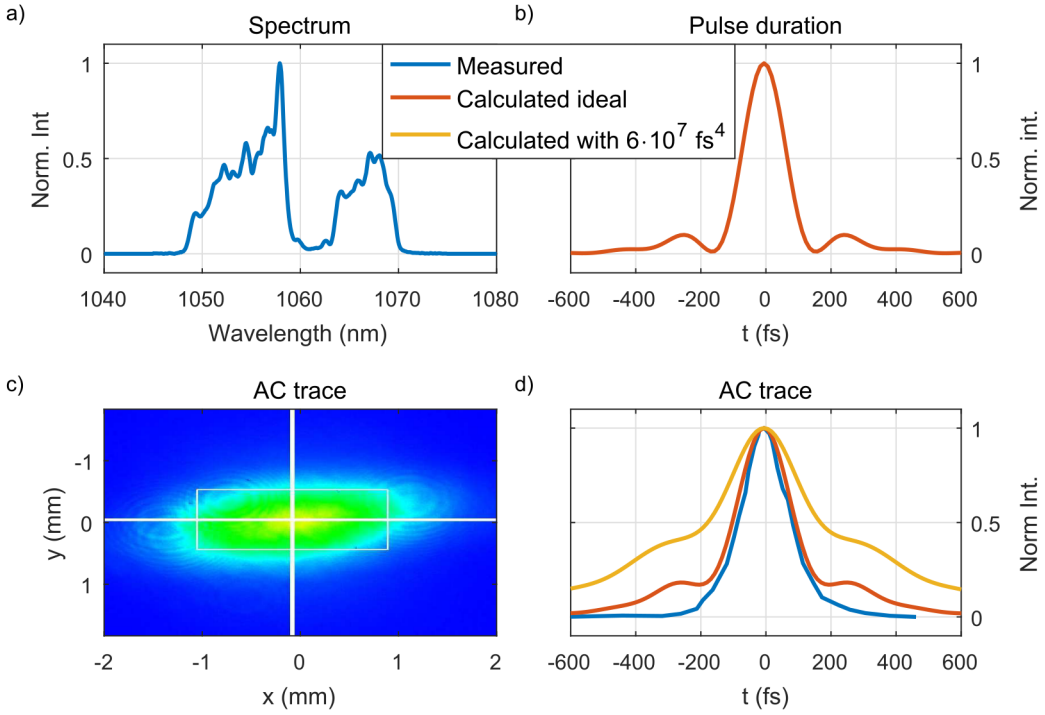

Figure 7.6: Compression of the OPA amplified beam using object-image-grating self-tiling method. Measured spectrum using a fiber tip (a), the simulated temporal profile from the spectrum (b), the measured autocorrelation trace (c) and the comparison between the measured and the simulated autocorrelation profile (d). The blue curve is the trace measured by a single short autocorrelator, the red and yellow AC trace were calculated from the measured spectra. The red curve is transform limited pulse profile, while the yellow curve represents additional pulse broadening due to residual FOD $6 \cdot 10^7 \text{fs}^4$ discussed in the previous chapter.

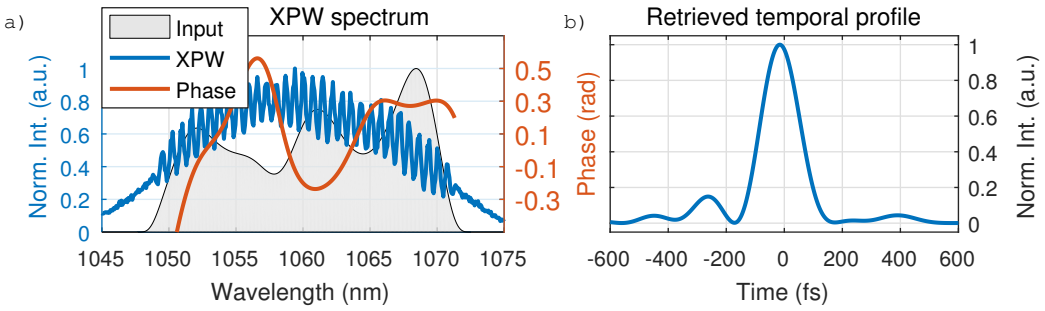

Figure 7.7: Compression of the OPCPA amplified beam using the single grating configuration with only OPCPA stage 1 active. The recorded ipnut and XPW spectrum (a) and retrieved temporal profile having the pulse duration of 151 fs FWHM (b) using Fastlite Wizzler with Fourier limit of 149 fs.

pulse and its autocorrelation). The side lobes are induced through the clipping of the middle part of the spectra. However, the measured profile of the spectral intensity is not entirely accurate as the position of the spectral dip varies with spatial coordinate of the beam. The measurement also confirms that the residual FOD originating from the aberrations in the stretcher and material dispersion is well compensated by the adjustment of the stretcher imaging system. The AC trace is slightly tilted due to a small misalignment of the autocorrelator which does not influence the measured pulse

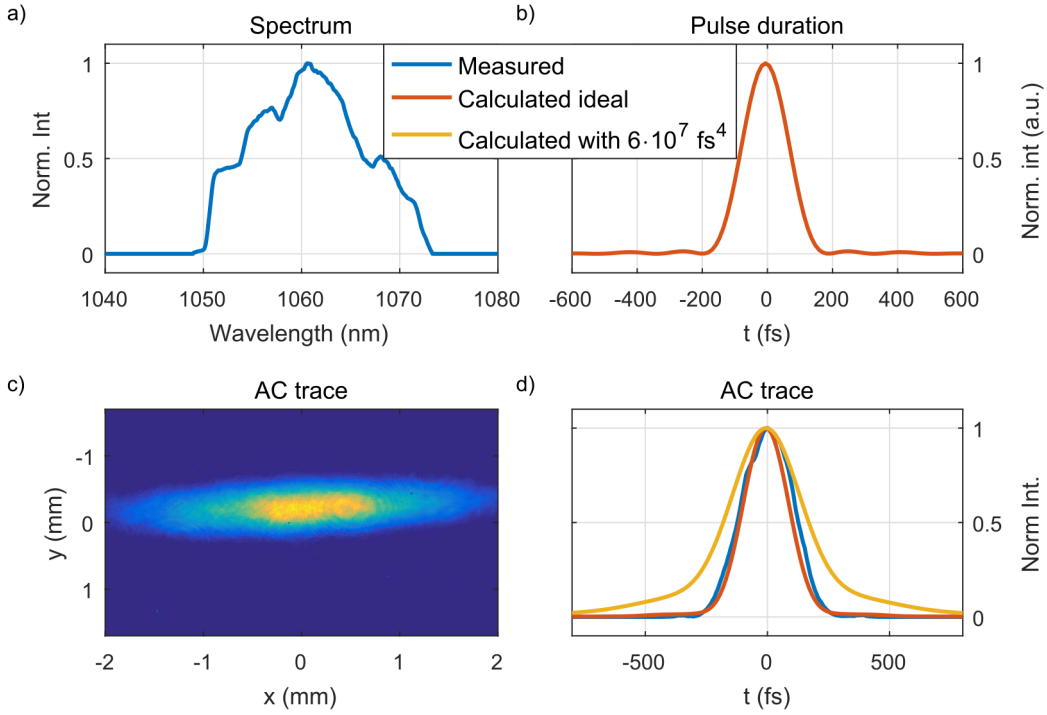

Figure 7.8: Compression of the pulse amplified to 30J using the OPCPA and PA1 sections. Measured spectrum from scatter(a), the simulated temporal profile from the spectrum having 158 fs FWHM transform limit (b), the measured autocorrelation trace corresponding to 166 fs FWHM (c) and the comparison between the measured and the simulated autocorrelation profile (d). The blue curve is the autocorrelation trace measured by a single short autocorrelator, the red and yellow AC trace were calculated from the measured spectra. The yellow curve represents additional pulse broadening due to residual FOD of $6 \cdot 10^7 \mathrm{fs}^4$ discussed in the previous chapter.

profile.

Later, the laser system was reinstalled in the ELI Beamlines, the subaperture compressor was modified to a single grating configuration and tested with full OPCPA chain. The compressibility was then also verified using Fastlite Wizzler. Figure 7.7 presents the recorded XPW spectrum and the retrieved temporal profile of the pulse having 174 fs FWHM with the Fourier limit of 170 fs FWHMs.

Next, the output of the first power amplifier (PA1) was routed to the compressor to measure compressibility of the amplified pulses. Figure 7.8 shows a retrieved spectrum, single-shot autocorrelation trace and corresponding pulse duration of the pulse amplified to $\sim$ 30J. The measured pulse duration 166 fs is close to the transform limit of the measured spectra 158 fs.

The preliminary measurement of temporal contrast (Figure 7.9) shows no pre-pulses and post-pulses and a low noise floor of 10^{-10} at -80 ps which is currently limited by the dynamic range of the Ultrafast Innovations TUNDRA+ device. The measurement was done with the stretcher and the subaperture compressor on air. Coherent pedestal likely originates from the scattering and surface quality of the optics in the strecher and sub-aperture compressor due to their multi-pass design. It might also come from the saturation of the first OPCPA stage. These assumptions will be tested in the contrast measurement at the output of the main compressor next year.

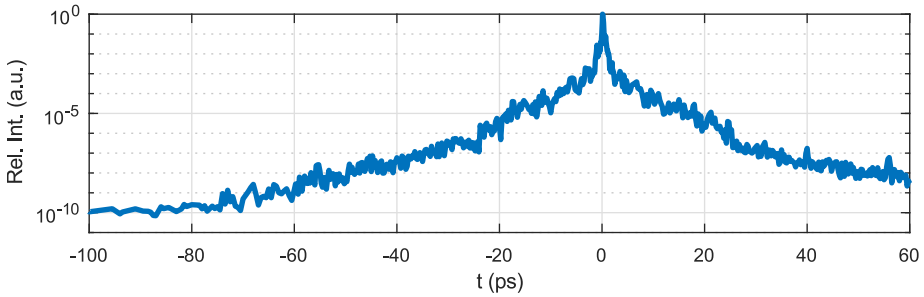

Figure 7.9: Preliminary temporal contrast of the OPCPA chain measured during testing of the TUNDRA+ device

Phasing

A phasing setup was employed to align the gratings within the sub-aperture compressor. To ensure correct positioning of the PM2 (PM3) with respect to the G2 (G3), a Fizeau interferometer was set up. A detailed layout is provided in Figure 7.10. A frequency stabilized He-Ne laser is fiber coupled and collimated to 2 cm diameter by f40 fiber collimator. After the collimator the beam is split by a 50:50 beamsplitter and each branch is propagated towards the grating-mirror assembly. A two inch uncoated wedge with $\lambda/15$ PV surface quality was used as a reference surface (transmission flat) and was slightly tilted with respect to the incoming beam to introduce carrier frequency into the interferogram. After the retro-reflection, the beam is downsized five times by a keplerian telescope which simultaneously images the grating-mirror gap on the camera. The interferogram is processed by an in-house developed LABVIEW program using fourier fringe analysis method [49], which provides the relative yaw, pitch and piston coefficients. To verify the results, farfield distribution is recorded as well. Systematic errors were neglected at this stage they have a very small impact due to the small beam size. Figure 7.11 shows an interferogram and a retrieved phase profile of the aligned assembly. Small misalignments in the order of μrad had no impact on the measured pulse duration. The setup exhibited good longterm stability in ambient conditions in both

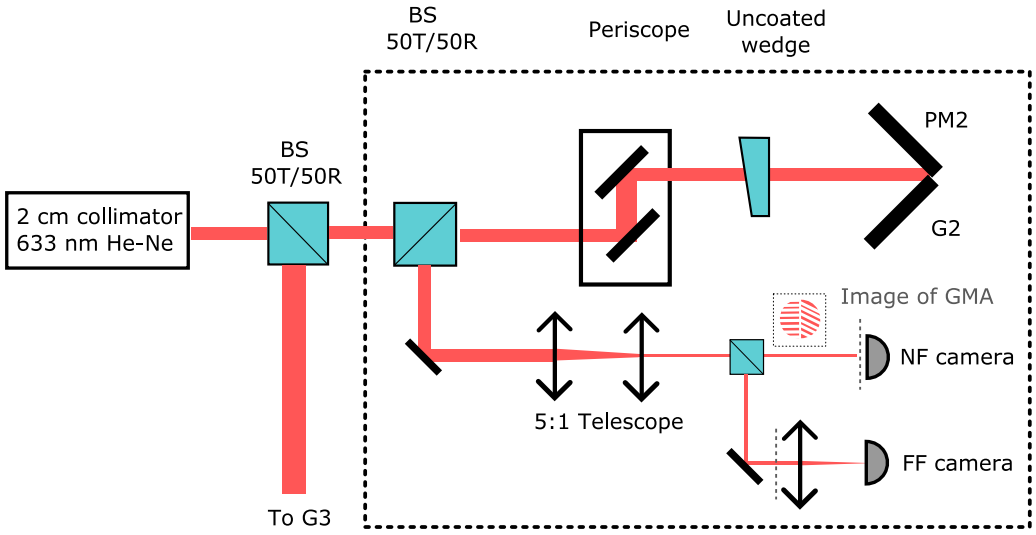

Figure 7.10: Layout of the phasing setup for the subaperture compressor.

angular degrees of freedom (Figure 7.12). The stability of the current optomechanic design is very susceptible to temperature changes as was discussed in Chapter 5.2 and therefore the piston drifted several periods during the five hour stability measurement. The period of the piston can be calculated as the half of the groove period which is 440 nm for 1136 ln/mm gratings. In this measurement, full aperture optics were installed compared to the previous experiment and therefore the distance between the front side of the mirror and the point where the grating is attached increased to 10 cm approximately. The laboratory where the measurement was conducted was stabilized to ± 1°C which yields ± 2 μm shift of the mirror with respect to the grating. That also corresponds to Figure 7.12c, where the piston drifts through five periods in total, which is equivalent to 2.2 μm shift. The grating-mirror assemblies of the main compressor will be housed in the evacuated chamber in the environment with better temperature stability to suppress temperature gradients as much as possible. The standard deviation of the measured values with respect to their moving average was determined to be 0.1 μrad for yaw, 1 μrad for pitch and 20 nm for piston. The resolution of the measurement was again mainly limited by the air turbulence between the transmission flat and the grating-mirror assembly. The worse stability of the pitch measurement might have been caused by the fact that a different type of actuator was temporarily employed to drive the flexible joints and it might not have been sufficiently pushing the flexible joints to constrain their movement and enhance their stability.

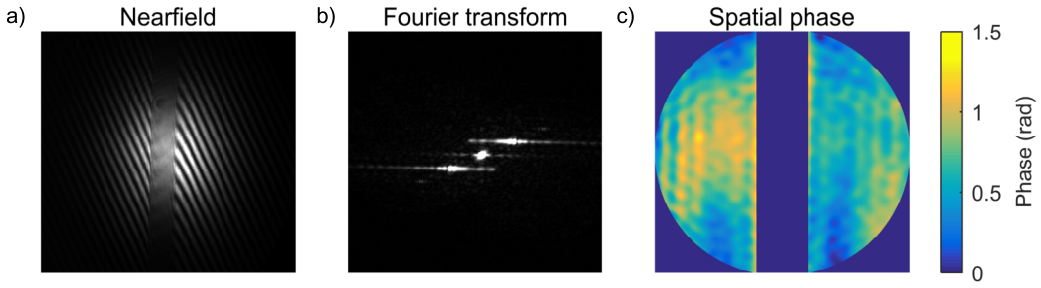

Figure 7.11: Interferogram (a), its spatial Fourier transform (b) and the retrieved phase (c) by the Fourier fringe pattern analysis method.

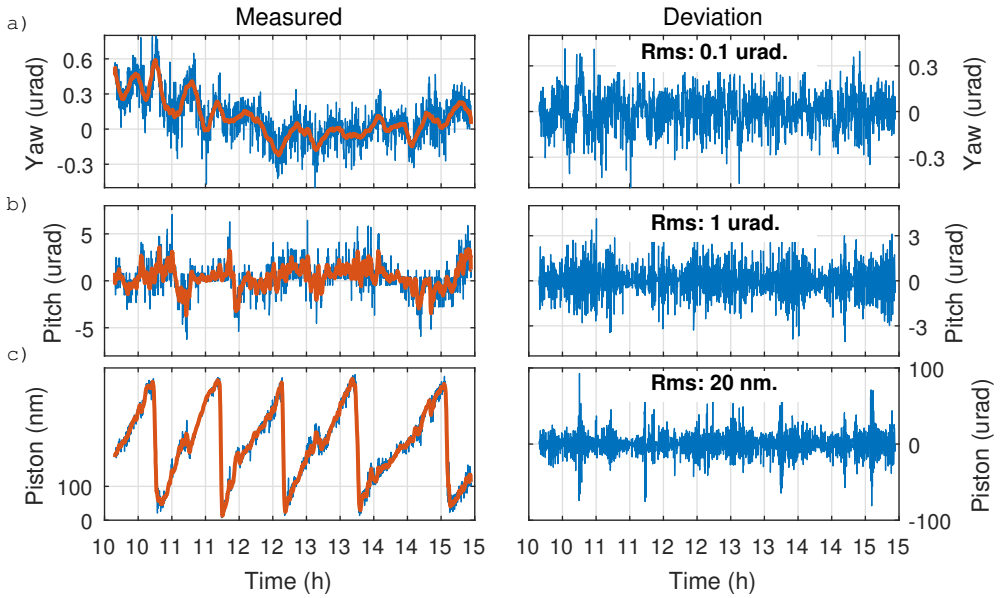

Figure 7.12: Measurement of phasing stability of the subaperture compressor for yaw(a), pitch(b) and piston(c) over a 5 hour period using an in-house build Fizeau interferometer. The red curve represents a moving average of 10 samples. Data were acquired once per 10 seconds.

Discussion

We have demonstrated the feasibility of the object-image-grating self-tiling-method for the main L4 compressor. The measured pulse duration is close to its transform limit which confirms that the pulse is compressed with low residual phase and which also points out that the residual fourth order dispersion should be compensated by the design of the stretcher. This proves that dispersion management was correctly implemented.

The resolution of the interferometric method meets the values specified in Table 4.11 for yaw and piston misalignment with a slight deviation in the pitch misalignment. The results indicate that the resolution of the interferometer should be well bellow the target values from Table 4.11 for the main compressor since both transmission flat and the measured grating-mirror assembly will be in vacuum and since the resolution will be improved 3.5 times by increasing the beam size to a 7 cm clear aperture.

Conclusion

Currently, a 10 PW kJ-class laser system is being re-assembled in the ELI-Beamlines[A3, A5]. The L4 system is based on the direct chirped pulse amplification technique and aims to deliver 1500 kJ pulses with 150 fs duration with wavelength centered at 1060 nm. This thesis dealt with the dispersion management of this system which mostly encompasses the design and analysis of the stretcher and compressor. The work presented here aimed to combine the analytical and numerical approaches to provide physical insight, detailed explanation of phenomena while using the benefits of numerical simulation.

The limited aperture and damage threshold of the compressor gratings remains one of the bottlenecks in reaching higher peak powers for the current state-of-the-art laser systems. The work presented here provides a detailed analysis of methods enabling to increase the effective aperture of the compressor. Currently, these methods seem to be the only ones viable method for reaching 100 PW or EW peak powers for the forthcoming laser systems. The analysis is also crucial for the implementation of the compressor into the L4 system as the grating-mirror configuration will be used for the first time in a TW-PW class laser system.

Generally, the conceptual design of the compressor of the L4 system was mostly driven by the availability of diffraction gratings with sufficient damage threshold and aperture. However, there were no monolithic gratings applicable due to high fluence of the beam. Therefore, the compressor has to use an existing multilayer dielectric grating design with high damage threshold and the effective aperture of the gratings has to be increased using either tiled grating or object-image-grating self-tiling (grating-mirror) configurations. In this thesis, compressor designs employing 1740 ln/mm and 1136 ln/mm gratings were compared for both configurations.

The 1740 ln/mm compressor design required to extend the aperture of all four gratings due to high incidence angle. We showed that it is advantageous to avoid tiling the first and the last grating in the compressor and, if possible, to keep them monolithic. The grating gap introduces amplitude modulations which can be suppressed by leaving slight spatial chirp at the compressor output. We also demonstrated that the line density variation of diffraction gratings in tiled grating compressors can become one of the limiting factors of such systems if it is not precisely controlled. Line density variation induces both wavefront error and residual angular dispersion of the output beam which cannot be entirely compensated. Only 0.01 ln/mm variation (5 ppm) could then lead to more than 10% decrease of the focused peak intensity for the L4 system. The impact of the line density variation will be further examined for < 30 fs systems and published. This issue was not present for the grating-mirror configuration as the grating is self-imaged by the mirror. Nevertheless, zeroth diffractions orders from the grating-mirror configuration retro-reflect back into the laser chain and they also create post-pulses with propagation direction parallel to the main beam.

In the 1136 ln/mm compressor design it was necessary to extend the aperture of the second and the third grating only. Because the compressor is in the off-plane configuration with Littrow angle incidence on the gratings, the grating-mirror configuration is preferred over the tiled grating configuration as there are no back-reflections. However, zeroth diffraction orders from the second and third grating propagate in parallel direction with the main beam and can reach the experimental target. They are expected to form a nanosecond pedestal with relative intensity smaller than 10^{-9} around the main pulse. Nevertheless, the 1136 ln/mm compressor design requires generally looser tolerances for the alignment, it avoids the line density variation issues and diffraction

induced modulations and it was therefore favoured against the 1740 ln/mm design.

A system for the mutual alignment of the grating-mirror assemblies was proposed for the 1136 ln/mm compressor. We showed that an interferometric method provides better resolution and is more suitable for the online diagnostics than a farfield method. To test it, we built a Fizeau interferometer and we extracted the phase profile from the interferogram by the Fourier fringe analysis method using an in-house developed Labview Program. The resolution of the interferometer was then compared experimentally with the commercial capacitive sensors, a tilt-meter and an interferometer Zygo Dynafiz [A5]. The experiment confirmed the feasibility and applicability of the proposed system for the main compressor of the L4 laser system.

Next, the design of a stretcher matching the 1136 ln/mm compressor design was presented. Banks and Offner all reflective designs in the off-plane configuration were compared [A6]. Generally, because the stretcher has to introduce very high stretch ratio, aberrations present in the stretcher imaging system induce spectral phase deviation with respect to the ideal stretcher. To understand it, a theory which connects the residual spectral phase with Seidel aberration coefficients was deduced [A1]. The theory comprises analytical formulae for the calculation of the deviation of individual dispersion orders and residual angular dispersion. Using this theory we showed that the residual FOD can be independently controlled in the Offner stretcher by adjusting the radius of curvature of the convex mirror [A2]. Such control is also very useful for passive compensation of material dispersion. It can be simply implemented during the design through the modification of the stretcher imaging system and it eliminates the need to insert additional optical components such as a grism pair or Dazzler. Generally, the theory may be used for the optimization of the spectral phase of CPA chains without extensive numerical ray-tracing and it can be utilized in the design of the upcoming laser systems requiring high stretch ratios while keeping the stretcher dimensions compact.

Based on the theory, a single grating Offner stretcher was designed in the 8-pass configuration. The radii of curvature of the convex and concave mirror were adjusted to minimize the footprint and to fine-tune the spectral phase deviation to exactly match the compressor and material dispersion properties. The stretcher was then successfully implemented into the L4 system. The stretcher has only 3 m footprint, while it provides stretch ratio equivalent to 30 m grating distance. It exhibits >38 nm transmission bandwidth without measurable spatiotemporal couplings at the output. To check the compressibility of the stretched amplified pulses, a miniaturized version of the compressor yielding the same dispersion properties was installed. The measured pulse duration corresponded to the transform limit of the measured spectra and confirms that the residual FOD is well compensated by the stretcher. The compressor was also used to test the developed interferometric method for phasing of the grating-mirror assemblies.

The author's personal responsibility was to perform all the analytical and numerical simulations regarding the stretcher and the compressor presented in this thesis, to develop the interferometer with the phase extraction algorithm and to experimentally test it. The author was also responsible for the alignment of the stretcher and sub-aperture compressor and for the characterization of the compressed pulse. The compressibility of the entire L4 laser chain was recently demonstrated to be nearly 150fs using the diagnostic compressor. Dazzler wasn't operated during the test. This proves that the dispersion management was correctly implemented.

References

[1] Ed Gerstner. Laser physics: Extreme light. *Nature*, 446(7131):16–18, March 2007.

[2] Eli whitebook, https://www.eli-beams.eu/o-eli-beamlines/eli-white-book/, 2018.

[3] Artem V. Korzhimanov, A. A. Gonoskov, Efim A. Khazanov, and Aleksandr M. Sergeev. Horizons of petawatt laser technology. *Phys.-Usp.*, 54(1):9, January 2011.

[4] S. V. Bulanov and V. S. Khoroshkov. Feasibility of using laser ion accelerators in proton therapy. *Plasma Phys. Rep.*, 28(5):453–456, May 2002.

[5] Donna Strickland and Gerard Mourou. Compression of amplified chirped optical pulses. *Optics Communications*, 56(3):219–221, December 1985.

[6] E. B. Treacy. Compression of picosecond light pulses. *Physics Letters A*, 28(1):34–35, October 1968.

[7] Alexander S. Pirozhkov, Yuji Fukuda, Mamiko Nishiuchi, Hiromitsu Kiriyama, Akito Sagisaka, Koichi Ogura, Michiaki Mori, Maki Kishimoto, Hironao Sakaki, Nicholas P. Dover, Kotaro Kondo, Nobuhiko Nakanii, Kai Huang, Masato Kanasaki, Kiminori Kondo, and Masaki Kando. Approaching the diffraction-limited, bandwidth-limited Petawatt. *Opt. Express, OE*, 25(17):20486–20501, August 2017.

[8] Junming Chen, Haopeng Huang, Yibing Zhang, Yonglu Wang, Fanyu Kong, Yanzhi Wang, Yunxia Jin, Peng Chen, Jiao Xu, and Jianda Shao. Reducing electric-field-enhancement in metal-dielectric grating by designing grating with asymmetric ridge. *Scientific Reports*, 8(1):5228, March 2018.

[9] M. Mero, J. Liu, W. Rudolph, D. Ristau, and K. Starke. Scaling laws of femtosecond laser pulse induced breakdown in oxide films. *Phys. Rev. B*, 71(11):115109, March 2005.

[10] Tiejun Zhang, Motoki Yonemura, and Yoshiaki Kato. An array-grating compressor for high-power chirped-pulse amplification lasers. *Optics Communications*, 145(1–6):367–376, January 1998.

[11] Dr Hein Joachim. Optische Beugungsanordnung großer Apertur, November 2008.

[12] Zhaoyang Li, Guang Xu, Tao Wang, and Yaping Dai. Object–image-grating self-tiling to achieve and maintain stable, near-ideal tiled grating conditions. *Opt. Lett.*, 35(13):2206–2208, July 2010.

[13] J. Qiao, A. Kalb, T. Nguyen, J. Bunkenburg, D. Canning, and J. H. Kelly. Demonstration of large-aperture tiled-grating compressors for high-energy, petawatt-class, chirped-pulse amplification systems. *Opt. Lett.*, 33(15):1684–1686, August 2008.

[14] M. Hornung, R. Bödefeld, M. Siebold, A. Kessler, M. Schnepp, R. Wachs, A. Sävert, S. Podleska, S. Keppler, J. Hein, and M. C. Kaluza. Temporal pulse control of a multi-10 TW diode-pumped Yb:Glass laser. *Appl. Phys. B*, 101(1-2):93–102, October 2010.

[15] Zhaoyang Li, Tao Wang, Guang Xu, Xiaoping Ouyang, Dawei Li, Hui Wei, Jianwei Yu, Lei Chen, and Yaping Dai. Demonstration of chirped-pulse compression with an object-image-grating self-tiling grating compressor. *Journal of Modern Optics*, 61(6):495–499, March 2014.

[16] Zhaoyang Li, Shuai Li, Cheng Wang, Yi Xu, Fengxiang Wu, Yanyan Li, and Yuxin Leng. Stable and near Fourier-transform-limit 30fs pulse compression with a tiled grating compressor scheme. *Opt. Express, OE*, 23(26):33386–33395, December 2015.

[17] Hans W. Mocker and R. J. Collins. Mode competition and self-locking effects in a q-switched ruby laser. *Appl. Phys. Lett.*, 7(10):270–273, November 1965.

[18] Jean-Claude Diels and Wolfgang Rudolph. *Ultrashort Laser Pulse Phenomena.* Elsevier, July 2019.

[19] Mark Trentelman, Ian N. Ross, and Colin N. Danson. Finite size compression gratings in a large aperture chirped pulse amplification laser system. *Appl. Opt.*, 36(33):8567–8573, November 1997.

[20] J. Bromage, C. Dorrer, and R. K. Jungquist. Temporal contrast degradation at the focus of ultrafast pulses from high-frequency spectral phase modulation. *J. Opt. Soc. Am. B*, 29(5):1125–1135, May 2012.

[21] Christophe Dorrer and Jake Bromage. Impact of high-frequency spectral phase modulation on the temporal profileof short optical pulses. *Opt. Express*, 16(5):3058–3068, March 2008.

[22] N. V. Didenko, A. V. Konyashchenko, A. P. Lutsenko, and S. Y. Tenyakov. Contrast degradation in a chirped-pulse amplifier due to generation of prepulses by postpulses. *Opt. Express*, 16(5):3178–3190, March 2008.

[23] Zhaoyang Li, Shigeki Tokita, Satoshi Matsuo, Keiichi Sueda, Takashi Kurita, Toshiyuki Kawasima, and Noriaki Miyanaga. Scattering pulse-induced temporal contrast degradation in chirped-pulse amplification lasers. *Opt. Express, OE*, 25(18):21201–21215, September 2017.

[24] M Born and E. Wolf. *Principles of Optics: Electromagnetic Theory of Propagation, Interference and Diffraction of Light.* Cambridge University Press, Cambridge ; New York, 7th edition edition, October 1999.

[25] Selcuk Akturk, Xun Gu, Pablo Gabolde, and Rick Trebino. The general theory of first-order spatio-temporal distortions of Gaussian pulses and beams. *Opt. Express*, 13(21):8642–8661, October 2005.

[26] K. Varjú, A. P. Kovács, K. Osvay, and G. Kurdi. Angular dispersion of femtosecond pulses in a Gaussian beam. *Optics Letters*, 27(22):2034, November 2002.

[27] J. Hebling. Derivation of the pulse front tilt caused by angular dispersion. *Opt Quant Electron*, 28(12):1759–1763, December 1996.

[28] K. Osvay, A.P. Kovacs, Z. Heiner, G. Kurdi, J. Klebniczki, and M. Csatari. Angular dispersion and temporal change of femtosecond pulses from misaligned pulse compressors. *IEEE Journal of Selected Topics in Quantum Electronics*, 10(1):213–220, 2004.

[29] Z. L. Horváth, K. Osvay, and Z. Bor. Dispersed femtosecond pulses in the vicinity of focus. *Optics Communications*, 111(5–6):478–482, October 1994.

[30] Lectures on ultrafast optics, http://www.physics.gatech.edu/gcuo/lectures/index.html, 2018.

[31] Selcuk Akturk, Xun Gu, Erik Zeek, and Rick Trebino. Pulse-front tilt caused by spatial and temporal chirp. *Opt. Express*, 12(19):4399–4410, September 2004.

[32] Eugene Hecht and Alfred Zajac. *Optics*. Addison-Wesley Pub. Co., 1974.

[33] Ulrike Fuchs, Uwe Zeitner, and Andreas Tünnermann. Ultra-short pulse propagation in complex optical systems. *Opt. Express*, 13(10):3852–3861, May 2005.

[34] https://www.wyrowski-photonics.com/.

[35] Donald C. O'Shea. Group velocity dispersion using commercial optical design programs. *Appl. Opt.*, 45(19):4740–4746, July 2006.

[36] I. Z. Kozma, G. Almási, and J. Hebling. Geometrical optical modeling of femtosecond setups having angular dispersion. *Appl Phys B*, 76(3):257–261, March 2003.

[37] Erhard W. Gaul, Mikael Martinez, Joel Blakeney, Axel Jochmann, Martin Ringuette, Doug Hammond, Ted Borger, Ramiro Escamilla, Skylar Douglas, Watson Henderson, Gilliss Dyer, Alvin Erlandson, Rick Cross, John Caird, Christopher Ebbers, and Todd Ditmire. Demonstration of a 1.1 petawatt laser based on a hybrid optical parametric chirped pulse amplification/mixed Nd:glass amplifier. *Appl. Opt.*, 49(9):1676–1681, March 2010.

[38] Jae Hee Sung, Hwang Woon Lee, Je Yoon Yoo, Jin Woo Yoon, Chang Won Lee, Jeong Moon Yang, Yeon Joo Son, Yong Ha Jang, Seong Ku Lee, and Chang Hee Nam. 4.2 PW, 20 fs Ti:sapphire laser at 0.1 Hz. *Opt. Lett., OL*, 42(11):2058–2061, June 2017.

[39] E. Treacy. Optical pulse compression with diffraction gratings. *IEEE Journal of Quantum Electronics*, 5(9):454–458, 1969.

[40] O. E. Martinez, J. P. Gordon, and R. L. Fork. Negative group-velocity dispersion using refraction. *J. Opt. Soc. Am. A*, 1(10):1003–1006, October 1984.

[41] Ian Walmsley, Leon Waxer, and Christophe Dorrer. The role of dispersion in ultrafast optics. *Review of Scientific Instruments*, 72(1):1–29, January 2001.

[42] M. Divoký. Dizertace Martin Divoký, 2011.

[43] Karoly Osvay and Ian N. Ross. On a pulse compressor with gratings having arbitrary orientation. *Optics Communications*, 105(3–4):271–278, February 1994.

[44] Stacy Wise, V. Quetschke, A. J. Deshpande, G. Mueller, D. H. Reitze, D. B. Tanner, B. F. Whiting, Y. Chen, A. Tünnermann, E. Kley, and T. Clausnitzer. Phase Effects in the Diffraction of Light: Beyond the Grating Equation. *Phys. Rev. Lett.*, 95(1):013901, June 2005.

[45] A. Cotel, M. Castaing, P. Pichon, and C. Le Blanc. Phased-array grating compression for high-energy chirped pulse amplification lasers. *Opt. Express*, 15(5):2742–2752, March 2007.

[46] J. Qiao, A. Kalb, M. J. Guardalben, G. King, D. Canning, and J. H. Kelly. Large-aperture grating tiling by interferometry for petawatt chirped-pulse?amplification systems. *Opt. Express*, 15(15):9562–9574, July 2007.

[47] Marco Hornung, R. Bodefeld, M. Siebold, M. Schnepp, J. Hein, R. Sauerbrey, and Malte C. Kaluza. Alignment of a tiled-grating compressor in a high-power chirped-pulse amplification laser system. *Appl. Opt.*, 46(30):7432–7435, October 2007.

[48] Zhaoyang Li, Tao Wang, Guang Xu, Dawei Li, Jianwei Yu, Weixin Ma, Jian Zhu, Lei Chen, and Yaping Dai. Research on potential problems of object image grating self-tiling for applications in large aperture optical systems. *Appl. Opt.*, 52(4):718–725, February 2013.

[49] Mitsuo Takeda, Hideki Ina, and Seiji Kobayashi. Fourier-transform method of fringe-pattern analysis for computer-based topography and interferometry. *J. Opt. Soc. Am.*, 72(1):156–160, January 1982.

[50] Kazuyoshi Itoh. Analysis of the phase unwrapping algorithm. *Appl. Opt., AO*, 21(14):2470–2470, July 1982.

[51] R. M. Goldstein, H. A. Zebker, and C. L. Werner. Satellite radar interferometry: Two-dimensional phase unwrapping. *Radio Science*, 23(4):713–720, July 1988.

[52] M. Kujawinska, A. Spik, J. Wojciak, M. Kujawinska, A. Spik, and J. Wojciak. Fringe Pattern Analysis Using Fourier Transform Techniques. volume 1121, pages 130–135, 1990.

[53] Daniel M. Sykora and Kuechel. In situ calibration of interferometers. Mezinárodní klasifikace G01B9/02, G01B11/24, G01B11/02; Klasifikace CPC G01B9/0201, G01B9/02068, G01B9/02032, G01B11/2441, G01B9/02057, G01B9/02072.

[54] Marco Hornung, Ragnar Bodefeld, Alexander Kessler, Joachim Hein, and Malte C. Kaluza. Spectrally resolved and phase-sensitive far-field measurement for the coherent addition of laser pulses in a tiled grating compressor. *Opt. Lett.*, 35(12):2073–2075, June 2010.

[55] Yanlei Zuo, Xiaofeng Wei, Xiao Wang, Qihua Zhu, Rui Ren, Zheng Huang, Hongjie Liu, and Chuntong Ying. Eliminating the longitudinal piston error between tiled gratings by angle tuning. *Opt. Lett.*, 32(3):280–282, February 2007.

[56] Yao Hu, Lijiang Zeng, and Lifeng Li. Method to mosaic gratings that relies on analysis of far-field intensity patterns in two wavelengths. *Optics Communications*, 269(2):285–290, January 2007.

[57] G. Imeshev, I. Hartl, and M. E. Fermann. Chirped pulse amplification with a nonlinearly chirped fiber Bragg grating matched to the Treacy compressor. *Opt. Lett., OL*, 29(7):679–681, April 2004.

[58] S. Kane, J. Squier, J. V. Rudd, and G. Mourou. Hybrid grating–prism stretcher–compressor system with cubic phase and wavelength tunability and decreased alignment sensitivity. *Opt. Lett., OL*, 19(22):1876–1878, November 1994.

[59] Štěpán Vyhlídka, Daniel Kramer, Galina Kalinchenko, and Bedřich Rus. Seidel aberrations in grating pulse stretchers. *Opt. Express, OE*, 24(26):30421–30432, December 2016.

[60] W. E. White, F. G. Patterson, R. L. Combs, D. F. Price, and R. L. Shepherd. Compensation of higher-order frequency-dependent phase terms in chirped-pulse amplification systems. *Opt. Lett.*, 18(16):1343–1345, 1993.

[61] B. E. Lemoff and C. P. J. Barty. Quintic-phase-limited, spatially uniform expansion and recompression of ultrashort optical pulses. *Optics Letters*, 18(19):1651, October 1993.

[62] G. Cheriaux, P. Rousseau, F. Salin, J. P. Chambaret, Barry Walker, and L. F. Dimauro. Aberration-free stretcher design for ultrashort-pulse amplification. *Optics Letters*, 21(6):414, March 1996.

[63] W A. Molander, A J. Bayramian, R Campbell, R R. Cross, G Huete, N Schenkel, C A. Ebbers, J Caird, C W. Siders, and C P. Barty. A Large-Bandwidth, Cylindrical Offner Pulse Stretcher for a High-Average-Power, 15 Femtosecond Laser. page MB1. OSA, 2009.

[64] P.S. Banks, M.D. Perry, V. Yanovsky, S.N. Fochs, B.C. Stuart, and J. Zweiback. Novel all-reflective stretcher for chirped-pulse amplification of ultrashort pulses. *IEEE Journal of Quantum Electronics*, 36(3):268–274, March 2000.

[65] Zhigang Zhang, Yanrong Song, Darui Sun, Lu Chai, Hong Sun, and Ching-yue Wang. Compact and material-dispersion-compatible Offner stretcher for chirped pulse amplifications. *Optics Communications*, 206(1–3):7–12, May 2002.

[66] P. Taday I. N. Ross, A. J. Langley. A simple achromatic pulse stretcher. *Central Laser Facility Annual Report 1999/2000*, pages 201–203, 2000.

[67] Chris Hooker, Yunxin Tang, Oleg Chekhlov, John Collier, Edwin Divall, Klaus Ertel, Steve Hawkes, Bryn Parry, and P. P. Rajeev. Improving coherent contrast of petawatt laser pulses. *Opt. Express*, 19(3):2193–2203, January 2011.

[68] Yunxin Tang, Chris Hooker, Oleg Chekhlov, Steve Hawkes, John Collier, and P. P. Rajeev. Transmission grating stretcher for contrast enhancement of high power lasers. *Optics Express*, 22(24):29363, December 2014.

[69] Jingui Ma, Peng Yuan, Jing Wang, Yongzhi Wang, Guoqiang Xie, Heyuan Zhu, and Liejia Qian. Spatiotemporal noise characterization for chirped-pulse amplification systems. *Nat Commun*, 6:6192, February 2015.

[70] O.E. Martinez. 3000 times grating compressor with positive group velocity dispersion: Application to fiber compensation in 1.3-1.6 #181;m region. *IEEE Journal of Quantum Electronics*, 23(1):59–64, January 1987.

[71] O.E. Martinez. Matrix formalism for pulse compressors. *IEEE Journal of Quantum Electronics*, 24(12):2530–2536, December 1988.

[72] A.G. Kostenbauder. Ray-pulse matrices: A rational treatment for dispersive optical systems. *IEEE Journal of Quantum Electronics*, 26(6):1148–1157, June 1990.

[73] Frédéric Druon, Marc Hanna, Gaëlle Lucas-Leclin, Yoann Zaouter, Dimitris Papadopoulos, and Patrick Georges. Simple and general method to calculate the dispersion properties of complex and aberrated stretchers-compressors. *Journal of the Optical Society of America B*, 25(5):754, May 2008.

[74] Zhigang Zhang, Takashi Yagi, and Takashi Arisawa. Ray-tracing model for stretcher dispersion calculation. *Applied Optics*, 36(15):3393, May 1997.

[75] J. Goodman. *Introduction to Fourier Optics*. Roberts and Company Publishers, Englewood, Colo, 3rd edition edition edition, December 2004.

[76] Welford, W.T. *Aberrations of Optical Systems*. CRC Press, Bristol, Eng. ; Philadelphia, 1 edition edition, January 1986.

[77] V. Yanovsky, V. Chvykov, G. Kalinchenko, P. Rousseau, T. Planchon, T. Matsuoka, A. Maksimchuk, J. Nees, G. Cheriaux, G. Mourou, and K. Krushelnick. Ultra-high intensity- 300-TW laser at 0.1 Hz repetition rate. *Opt. Express*, 16(3):2109–2114, February 2008.

[78] Shuai Li, Cheng Wang, Yanqi Liu, Yi Xu, Yanyan Li, Xingyan Liu, Zebiao Gan, Lianghong Yu, Xiaoyan Liang, Yuxin Leng, and Ruxin Li. High-order dispersion control of 10-petawatt Ti:sapphire laser facility. *Opt. Express, OE*, 25(15):17488–17498, July 2017.

[79] E. Sistrunk, T. Spinka, A. Bayramian, S. Betts, R. Bopp, S. Buck, K. Charron, J. Cupal, R. Deri, M. Drouin, A. Erlandson, E. S. Fulkerson, J. Horner, J. Horacek, J. Jarboe, K. Kasl, D. Kim, E. Koh, L. Koubikova, R. Lanning, W. Maranville, C. Marshall, D. Mason, J. Menapace, P. Miller, P. Mazurek, A. Naylon, J. Novak, D. Peceli, P. Rosso, K. Schaffers, D. Smith, J. Stanley, R. Steele, S. Telford, J. Thoma, D. VanBlarcom, J. Weiss, P. Wegner, B. Rus, and C. Haefner. All Diode-Pumped, High-repetition-rate Advanced Petawatt Laser System (HAPLS). In *Conference on Lasers and Electro-Optics (2017), Paper STh1L.2*, page STh1L.2. Optical Society of America, May 2017.

[80] S. Kane and J. Squier. Fourth-order-dispersion limitations of aberration-free chirped-pulse amplification systems. *J. Opt. Soc. Am. B*, 14(5):1237–1244, May 1997.

[81] František Batysta, Roman Antipenkov, Jakub Novák, Jonathan T. Green, Jack A. Naylon, Jakub Horáček, Martin Horáček, Zbyněk Hubka, Robert Boge, Tomáš Mazanec, Bedřich Himmel, Pavel Bakule, and Bedřich Rus. Broadband OPCPA system with 11 mJ output at 1 kHz, compressible to 12 fs. *Opt. Express, OE*, 24(16):17843–17848, August 2016.

[82] E. Gaul, T. Toncian, M. Martinez, J. Gordon, M. Spinks, G. Dyer, N. Truong, C. Wagner, G. Tiwari, M. E. Donovan, T Ditmire, and B. M. Hegelich. Improved pulse contrast on the Texas Petawatt Laser. *J. Phys.: Conf. Ser.*, 717(1):012092, 2016.

[83] Rahul C. Shah, Randall P. Johnson, Tsutomu Shimada, Kirk A. Flippo, Juan C. Fernandez, and B. M. Hegelich. High-temporal contrast using low-gain optical parametric amplification. *Opt. Lett., OL*, 34(15):2273–2275, August 2009.

[84] František Batysta, Roman Antipenkov, Teddy Borger, April Kissinger, Jonathan T. Green, Robertas Kananavičius, Gilles Chériaux, Dave Hidinger, Jonas Kolenda, Erhard Gaul, Bedřich Rus, and Todd Ditmire. Spectral pulse shaping of a 5 Hz, multi-joule, broadband optical parametric chirped pulse amplification frontend for a 10 PW laser system. *Opt. Lett., OL*, 43(16):3866–3869, August 2018.

[85] Plymouth grating laboratory mld data sheet, 2018.

[86] H. Huang and Terrance Kessler. Tiled-grating compressor with uncompensated dispersion for near-field-intensity smoothing. *Opt. Lett.*, 32(13):1854–1856, July 2007.

[87] M. Kujawinska and J. Wójciak. High accuracy Fourier transform fringe pattern analysis. *Optics and Lasers in Engineering*, 14(4):325–339, January 1991.

[88] C. J. Evans and J. B. Bryan. Compensation for Errors Introduced by Nonzero Fringe Densities in Phase-Measuring Interferometers. *CIRP Annals - Manufacturing Technology*, 42(1):577–580, January 1993.

[89] http://www.qphotonics.com/wavelength-stabilized-single-mode-fiber-coupled-laser-diode-5mw-1030nm.html.

[90] http://texaspetawatt.ph.utexas.edu/img/stretcher-layout-large.jpg, 2018.

List of Abbreviations

Abrreviations

AD	Angular dispersion
CPA	Chirped Pulse Amplification
ELI	Extreme Light Infrastructure
EM	Eliptical mirror
FFA	Fourier Fringe pattern Analysis
FM	Folding mirror
FOD	Fourth Order Dispersion
FWHM	Full Width at Half Maximum
GA	Grating Assembly
GDD	Group Delay Dispersion
HR	Horizontal roof mirror
LDV	Line Density Variation
LIDT	Laser Induced Damage Threshold
MLD	Multi-Layer Dielectric
OPCPA	Optical parametric chirped pulse amplification
PA1	Power Amplifier 1 of the L4 laser
PA2	Power Amplifier 2 of the L4 laser
PM	Phasing Mirror
PV	Peak to Valley ratio
TOD	Third Order Dispersion
VR	Vertical roof mirror

Symbols Greek

α	angle of incidence
β	diffraction angle
γ	off-plane angle of incident wave
δ	off-plane angle of diffracted wave
ϵ_0	vacuum permittivity
η	entrance pupil coordinate
θ_{pitch}	pitch misalignment
θ_{roll}	roll misalignment
θ_{yaw}	yaw misalignment
λ	wavelength
λ_0	central wavelength
ξ	entrance pupil coordinate
π	3.1415 ...
σ	wavefront rms
τ_{e^2}	pulse duration half width at $1/e^2$
τ_{FWHM}	pulse duration full width at half maximum
τ_{0FWHM}	transform-limited pulse duration half width at $1/e^2$
$\varphi(\omega)$	spectral phase of a pulse
Φ	aberration function
ω	frequency
ω_0	central frequency of a pulse

Symbols Roman

c	speed of light
c_n	normalization constant
c_p	pulse profile constant
k	scalar k-vector
i	imaginary unit
$\vec{k}_i$	incident k-vector
$\vec{k}_d$	diffracted k-vector
m	diffraction order
n	refraction index
s	grating distance from the entrance pupil
s'	dimensionless parameter s/R
w_x	beam diameter
x	spatial coordinate
x_f	spatial coordinate in focus
x_0	x-offset from the optical axis in stretcher
y	spatial coordinate
y_f	spatial coordinate in focus
y_0	y-offset from the optical axis in stretcher
z	spatial coordinate along the propagation direction
z_r	Rayleigh length
$A(\omega)$	absorptivity
B	spherical aberration coefficient
B_0	B-integral
C	field curvature coefficient
D	astigmatism coefficient
E	distortion coefficient
F	coma coefficient
FOD^{ab}	FOD deviation in stretcher due to aberrations
G	perpendicular grating distance
G_1, G_2, G_3, G_4	first to fourth grating in the compressor
GDD^{ab}	GDD deviation in stretcher due to aberrations
$H(\omega)$	optical transfer function
$\vec{K}$	grating k-vector
$I(t), I(\omega)$	temporal intensity, spectral intensity
L	propagation distance for the central wavelength
N	line density of diffraction grating
ΔN	line density variation
$R(\omega)$	Reflectivity
R	radius of curvature
R_1	radius of curvature of concave mirror in the Offner stretcher
R_2	radius of curvature of convex mirror in the Offner stretcher
S_t	Strehl ratio in the temporal domain
S_ω	Strehl ratio in the spectral domain
TOD^{ab}	TOD deviation in stretcher due to aberrations

Related author publications

Here we list all publications of the author relevant to the scope of this work.

Peer-reviewed journals

[A1] **Štěpán Vyhlídka**, Daniel Kramer, Galina Kalinchenko, and Bedřich Rus, "Seidel aberrations in grating pulse stretchers," Opt. Express 24, 30421-30432 (2016)

[A2] **Štěpán Vyhlídka**, Daniel Kramer, Alexander Meadows and Bedřich Rus; "Offner stretcher aberrations revisited to compensate material dispersion", Optics Communications 414, 207-211 (2018)

Conference proceedings

[A3] B. Rus, P. Bakule, D. Kramer, J. Naylon, J. Thoma, J. T. Green, R. Antipenkov, M. Fibrich, J. Novák, F. Batysta, T. Mazanec, M. A. Drouin, K. Kasl, R. Baše, D. Peceli, L. Koubíková, P. Trojek, R. Boge, J. C. Lagron, **Š. Vyhlídka**, J. Weiss, J. Cupal, J. Hřebíček, P. Hříbek, M. Durák, J. Polan, M. Košelja, G. Korn, M. Horáček, J. Horáček, B. Himmel, T. Havlíček, A. Honsa, P. Korouš, M. Laub, C. Haefner, A. Bayramian, T. Spinka, C. Marshall, G. Johnson, S. Telford, J. Horner, B. Deri, T. Metzger, M. Schultze, P. Mason, K. Ertel, A. Lintern, J. Greenhalgh, C. Edwards, C. Hernandez-Gomez, J. Collier, T. Ditmire, E. Gaul, M. Martinez, C. Frederickson, D. Hammond, C. Malato, W. White, and J. Houžvička, "ELI-Beamlines: development of next generation short-pulse laser systems," in Proc. SPIE (G. Korn and L. O. Silva, eds.), p. 95150F, May 2015.

[A4] Galina Kalinchenko, **Štěpán Vyhlídka**, Daniel Kramer, Alexander Lerer, Bedřich Rus, "Positioning of Littrow mounted gratings in pulse compressors", Proc. SPIE 9626, Optical Systems Design 2015: Optical Design and Engineering VI, 96261R (23 September 2015); doi: 10.1117/12.2191304

[A5] **Štěpán Vyhlídka**, Pavel Trojek, Daniel Kramer, David Snopek, Martin Šolc, Erhard Gaul, Bedřich Rus, "Precision control of mirror-grating phasing for a large aperture pulse compressor", Proc. SPIE 10238, High-Power, High-Energy, and High-Intensity Laser Technology III, 102381A (16 May 2017); doi: 10.1117/12.2270479

[A6] **Štěpán Vyhlídka**, Daniel Kramer, Matt Kepler, Erhard Gaul, Bedřich Rus, "Optimization of a grating pulse stretcher suitable for kJ class 10PW laser system", Proc. SPIE 10238, High-Power, High-Energy, and High-Intensity Laser Technology III, 102380T (11 May 2017); doi: 10.1117/12.2270477

[A7] B. Rus, P. Bakule, D. Kramer, J. Naylon, J. Thoma, M. Fibrich, J. T. Green, J. C. Lagron, R. Antipenkov, J. Bartoníček, F. Batysta, R. Baše, R. Boge, S. Buck, J. Cupal, M. A. Drouin, M. Ďurák, B. Himmel, T. Havlíček, P. Homer, A. Honsa, M. Horáček, P. Hribek, J Hubáček, Z. Hubka, G. Kalinchenko, K. Kasl, L. Indra, P. Korous, M. Košelja, L. Koubíková, M. Laub, T. Mazanec, A. Meadows, J. Novák, D. Peceli, J. Polan, D. Snopek, V. Šobr, P. Trojek, B. Tykalewicz, P.

Velpula, E. Verhagen, **Š. Vyhlídka**, J. Weiss, C. Haefner, A. Bayramian, S. Betts, A. Erlandson, J. Jarboe, G. Johnson, J. Horner, D. Kim, E. Koh, C. Marshall, D. Mason, E. Sistrunk, D. Smith, T. Spinka, J. Stanley, C. Stolz, T. Suratwala, S. Telford, T. Ditmire, E. Gaul, M. Donovan, C. Frederickson, G. Friedman, D. Hammond, D. Hidinger, G. Chériaux, A. Jochmann, M. Kepler, C. Malato, M. Martinez, T. Metzger, M. Schultze, P. Mason, K. Ertel, A. Lintern, C. Edwards, C. Hernandez-Gomez, J. Collier, "ELI-beamlines: progress in development of next generation short-pulse laser systems," Proc. SPIE 10241, Research Using Extreme Light: Entering New Frontiers with Petawatt-Class Lasers III, 102410J (26 June 2017);

[A8] E. Gaul, G. Chériaux, R. Antipenkov, F. Batysta, T. Borger, G. Friedman, J. T. Greene, D. Hammond, J. Heisler, D. Hidinger, A. Jochmann, M. Kepler, A. Kissinger, D. Kramer, J. C. Lagron, A. Meadows, B. Rus, P. Trojek, **Štěpán Vyhlídka**, and T. Ditmire, "Hybrid OPCPA/Glass 10 PW laser at 1 shot a minute," in Conference on Lasers and Electro-Optics, OSA Technical Digest (online) (Optical Society of America, 2018), paper STu3M.2.

[A8] E. Gaul, G. Chériaux, R. Antipenkov, F. Batysta, T. Borger, G. Friedman, J. T. Greene, D. Hammond, J. Heisler, D. Hidinger, A. Jochmann, M. Kepler, A. Kissinger, D. Kramer, J. C. Lagron, A. Meadows, B. Rus, P. Trojek, **Štěpán Vyhlídka**, and T. Ditmire, "Hybrid OPCPA/Glass 10 PW laser at 1 shot a minute," in Conference on Lasers and Electro-Optics, OSA Technical Digest (online) (Optical Society of America, 2018), paper STu3M.2.

[A9] **Štěpán Vyhlídka**, Pavel Trojek, Daniel Kramer, Davorin Peceli, Frantivsek Batysta, Jan Bartoníček, Jan Hubávcek, Ted Borger, Roman Antipenkov, Erhard Gaul, Todd Ditmire, Bedvrich Rus, "Temporal diagnostics for kJ class laser using object-image-grating self-tiling compressor," Proc. SPIE 11034, Short-pulse High-energy Lasers and Ultrafast Optical Technologies, 1103409 (9 May 2019);

Other

[B1] **Štěpán Vyhlídka**, Galina Kalinchenko, Daniel Kramer, Alexander Lerer, Bedřich Rus, "All-dielectric diffraction grating for multi-petawatt laser systems", Proc. SPIE 9442, Optics and Measurement Conference 2014, 94421J (7 January 2015); doi: 10.1117/12.2086800;

[B2] Galina Kalinchenko, **Štěpán Vyhlídka**, Daniel Kramer, Alexander Lerer, Bedřich Rus, "High reflective diffraction grating for ultrafast pulse compression", Proc. SPIE 9513, High-Power, High-Energy, and High-Intensity Laser Technology II, 95130K (12 May 2015); doi: 10.1117/12.2185696; https://doi.org/10.1117/12.2185696